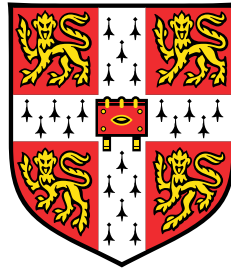


El Niño Southern Oscillation teleconnections and their effects on the Amundsen Sea region



Yu Yeung Scott YIU

Supervisor: **Dr. A.C. Maycock**

Prof. J.A. Pyle

Prof. P. Braesicke

Centre for Atmospheric Science, Department of Chemistry
University of Cambridge

This dissertation is submitted for the degree of
Doctor of Philosophy

Churchill College

May 2018

I would like to dedicate this thesis to my parents, Patrick Yiu and Amy Chiang.

Declaration

This dissertation is the result of my own work and includes nothing which is the outcome of work done in collaboration except as specified in the text.

It is not substantially the same as any that I have submitted, or, is being concurrently submitted for a degree or diploma or other qualification at the University of Cambridge or any other University or similar institution. I further state that no substantial part of my dissertation has already been submitted, or, is being concurrently submitted for any such degree, diploma or other qualification at the University of Cambridge or any other University or similar institution. This thesis does not exceed 60,000 words.

Yu Yeung Scott YIU

May 2018

Acknowledgements

I would like to thank my supervisors Dr Amanda Maycock, Professor John Pyle and Professor Peter Braesicke for their support and guidance throughout my PhD. I am especially grateful for their continual and unwavering support even after becoming head of department, moving to Leeds and Germany, respectively. I could not have asked for better supervisors for my PhD project.

This PhD was funded by Natural Environment Research Council and European Research Council and I wish to thank them for the opportunity to work on this project for the last four years. Furthermore, I also grateful to the University of Cambridge, Department of Chemistry, British Antarctic Survey and the Department of Applied Mathematics and Theoretical Physics for hosting me during my PhD.

I also owe thanks to my colleagues in the Centre for Atmospheric Sciences, British Antarctic Survey and the Department of Applied Mathematics and Theoretical Physics for their support and company during my PhD. I am especially thankful to Dr Luke Abraham for his help in initially setting up the HadGEM3 model. I would also like to thank Dr Marie-Estelle and Dr Maria Russo for helping me get started with my work on UPSCALE and model resolution. I would also like to show my gratitude to Professor Peter Haynes, Dr Scott Hosking and Dr John Turner for helping me get started with my PhD. I am also thankful to Dr Paul Griffiths and Dr James Keeble for their encouragement during these years. I would also like to thank my colleagues in room 101 for their support throughout these four years and also for putting up with my air conditioning and heater shenanigans where the indoor temperature has a six months lead-lag relationship with the outdoor temperature.

I am indebted to friends and previous teachers who have all helped me immensely in the past. I am especially grateful to Dr Christian Boehmer for his unwavering support. I would also like to thank Mr Kieran Ryan, Mr Anthony George, Dr Tong Tak Cheung, Mr Derek Chiu and Fr Joseph So. Additionally, I am thankful to thank Dr Peer Nowack and Mr Chun Hei Chow for sparking my interest in data science and machine learning. You have possibly made a significant change in my future career path!

Finally, I would like to thank my family and relatives for their support. I especially would like to thank Dr Charles Cheung for inspiring me to do a PhD. Lastly, but definitely not

least, I want to thank my parents, Mr Patrick Yiu and Mrs Amy Chiang, for their support and encouragement in the last 26 years. Thank you very much!

Abstract

El Niño Southern Oscillation events have global implications both climatologically and socio-economically. One such climatological teleconnection is manifested in the Amundsen Sea region (ASR). The Amundsen sea low (ASL) is the dominant low pressure system located around the ASR and is important to the climate of Western Antarctica. Therefore, it is important to understand the ASL and any phenomena that may affect it. This thesis focuses on the ENSO–ASR teleconnection under El Niño conditions and the mechanism behind it.

The ENSO–ASR teleconnection was explored using the UM version 8.4 (HadGEM3) model. Time–slice experiments with various magnitudes of idealised perpetual ENSO events are imposed. Two sets of ‘switch on’ experiments in which tropical Pacific SSTs were ramped up were also carried out to investigate the transient nature of the teleconnection.

The seasonality of the ENSO–ASR teleconnection is known from previous studies to be stronger in winter compared to summer. The mechanism behind the seasonality was explored using the time–slice experiments. The seasonality is found to originate from the seasonal differences in the Southern Hemispheric jets. As the subtropical jet is only present in austral winter, Rossby wave source anomalies can only be generated in the mid–latitudes in winter. Furthermore, the propagation of the Rossby waves is not possible in summer due to the strong polar front jet. The lack of the source and propagation in summer explains the weaker ENSO–ASR teleconnection. A flowchart summarising the mechanism was created and then verified by the transient runs.

The linearity of the ENSO–ASR teleconnection within El Niño has not been previously investigated. This is mainly due to insufficient reanalysis data available to overcome the high internal variability in the ASR. In this thesis, the linearity of the teleconnection under El Niño is studied using the time–slice runs. The results indicate linearity (within errorbars) for both the summer and winter seasons up to historically maximum El Niños. However, under extreme El Niños (beyond historic records) in winter, the teleconnection is no longer linear.

The UPSCALE dataset was used to investigate the effects of horizontal resolution on the simulation of the ASL climatological state and the ENSO–ASR teleconnection. The UPSCALE dataset consists of ensembles of HadGEM3 simulations at three different horizontal

resolutions. The high resolution model was found to better simulate the ASL while the low resolution model was found to better simulate the ENSO–ASR teleconnection.

Table of contents

List of figures	xv
List of abbreviations	xxi
Prologue	1
1 Introduction	5
1.1 Amundsen Sea Low	5
1.1.1 Climatology, annual cycle and recent trends	5
1.1.2 Role of the Amundsen Sea Low for Antarctic climate	8
1.2 El Niño Southern Oscillation	13
1.2.1 What is the El Niño Southern Oscillation?	13
1.2.2 ENSO indices	16
1.2.3 El Niño Southern Oscillation types	18
1.2.4 Global teleconnection impacts	19
1.3 Circulation of the atmosphere	21
1.3.1 The Hadley cell and the ITCZ	21
1.3.2 Jets	23
1.3.3 Circulation and patterns in the southern hemisphere	27
1.4 Teleconnections involving the Amundsen Sea Low	31
1.4.1 ASR teleconnections	32
1.4.2 Mechanisms of ENSO–southern hemisphere teleconnection	33
1.4.3 Rossby waves and teleconnections	33
1.5 Scientific aims	41
2 Model, setup and methods	43
2.1 Existing datasets	43
2.2 Model description	45
2.3 Experimental setup	45

2.4	Model evaluation	48
2.5	Methods	61
2.6	Concluding remarks	70
3	The seasonality of El Niño teleconnections to the Amundsen Sea region	73
3.1	Overview	73
3.2	Effect of the teleconnection	74
3.3	ENSO and tropical circulation	77
3.4	Jet movement	80
3.5	Rossby Wave Source	83
3.5.1	Quantifying the changes in the Rossby wave source	83
3.5.2	Explaining the changes in the Rossby wave source	86
3.6	Propagation of the teleconnection	91
3.7	Sea level pressure anomaly in austral summer (DJF)	96
3.8	Concluding remarks	97
4	Seasonality of El Niño teleconnections – transient response	101
4.1	Overview	101
4.2	Transient response of the teleconnection in JJA	103
4.3	Transient response of the teleconnection in DJF	110
4.4	Concluding remarks	112
5	The linearity of El Niño teleconnections to the Amundsen Sea region	115
5.1	Overview	115
5.2	Linearity of the teleconnection in austral winter under El Niño conditions	116
5.2.1	Response of key variables under various El Niño magnitudes	117
5.2.2	Combination of the Rossby wave source and propagation	127
5.3	Linearity of the teleconnection in austral summer under El Niño conditions	130
5.4	Concluding remarks	133
6	Model resolution dependence and the Amundsen Sea Low	135
6.1	Overview and previous literature	135
6.2	Model resolution and the climatology of the ASL	137
6.3	Model resolution and the ENSO–ASR teleconnection	140
6.4	Concluding remarks	142

7	Conclusions and future work	143
7.1	Chapter 3: The seasonality of the ENSO–ASR teleconnection	143
7.2	Chapter 4: Seasonality of the ENSO–ASR teleconnection – transient response	145
7.3	Chapter 5: The linearity of ENSO–ASR teleconnection	145
7.4	Chapter 6: Model resolution dependence and the ASL	147
7.5	Overall conclusions and brief discussions	147
7.6	Future work: additional runs	148
7.6.1	Eastern Pacific versus central Pacific El Niños	148
7.6.2	Comparison of real world La Niñas to ‘flipped’ El Niños	148
7.6.3	Atlantic Ocean–ASR and Indian Ocean–ASR teleconnections	150
7.6.4	Chemistry–interaction with the ENSO–ASR teleconnection	153
7.7	Future work: additional analysis	154
7.7.1	Understanding differences in the ENSO–ASR teleconnection in UP-SCALE	154
7.7.2	Inter–model comparison of the ENSO–ASR teleconnection	154
7.7.3	Predicting ASR SLP anomaly using statistics and machine learning techniques	155
	References	159
	Appendix A The ITCZ and the ‘energy flux equator’	175
	Appendix B Extreme historical El Niño events	177
	Appendix C Seasonality of the southern annular mode	183
	Appendix D Limitations of implementing Rossby wave ray tracing	185
	Appendix E Rossby wave ray tracing using different wavenumbers	187
	Appendix F Rossby wave ray tracing using different radius of filters	189
	Appendix G Tropical circulation changes and clouds	193
	Appendix H Absolute wave flux	195
	Appendix I Comparison of wave flux between ERA–40 and Karoly et al. (1989)	197
	Appendix J Ray tracing from the weaker negative RWS anomaly	199

Appendix K Preliminary results using machine learning techniques	201
---	------------

List of figures

1.1	Map of the seas around western Antarctica	6
1.2	The Amundsen Sea Low and the Amundsen sea region.	7
1.3	Seasonal MSLP maps of the Amundsen Sea Low	9
1.4	Trend in depth of the ASL by month over 1979–2008	9
1.5	Seasonal difference of surface variables in western Antarctica according to seasonal Amundsen Sea low longitude	11
1.6	Seasonal difference of surface variables in western Antarctica according to seasonal Amundsen Sea low depth	12
1.7	Anomalies in sea ice extent in the Antarctic between 1979–2017	13
1.8	Schematic of the ocean and tropical circulation under neutral and El Niño conditions.	14
1.9	Evolution of strong historic El Niños	15
1.10	Locations of different Niño regions	16
1.11	Histogram of the Niño3.4 index from 1979–2016	17
1.12	The evolution of the Niño3.4 index from 1982–2016	17
1.13	Tropical SST anomalies for eastern and Central Pacific El Niños	19
1.14	Map of the global teleconnections found during El Niño and La Niña in summer and winter	20
1.15	Zonal mass streamfunction of the Hadley and Ferrel cells	22
1.16	The subtropical and polar front jet	24
1.17	The wind speed, tropopause, the subtropical jet and polar front jet	24
1.18	Monthly location and detection frequencies of the jets	25
1.19	Zonal wind in the summer and winter	27
1.20	Southern Annular mode and the Pacific–South America pattern	29
1.21	First, second and third EOF in HadGEM3	30
1.22	Rossby wave ray tracing from the Atlantic	37
1.23	Atlantic–high latitude teleconnection flowchart	38

1.24	Rossby wave ray tracing from each of the different ocean sectors	39
1.25	Total Rossby wave number showing reflection and termination zones for the multi oceanic run	39
1.26	Simulated sea level pressure response to the four tropical SST anomalies . .	40
2.1	Maps of varying horizontal resolution	44
2.2	Idealised SST anomaly in the Pacific	47
2.3	Absolute SST in the Pacific for the HadGEM3 model experiments.	48
2.4	Evolution of Niño3.4 temperature anomaly in the transient runs.	49
2.5	Evolution of mean tropical precipitation in transient runs.	50
2.6	Comparison of the SST of ERA–Interim to the HadGEM3 runs.	51
2.7	Comparison of the zonal mean zonal wind for ERA–Interim and HadGEM3 runs under El Niño conditions.	53
2.8	Comparison of the zonal mean zonal wind between ERA–Interim and HadGEM3 runs under La Niña conditions.	54
2.9	Comparison of the Pacific zonal mean zonal wind for ERA–Interim and HadGEM3 runs under El Niño conditions.	55
2.10	Comparison of the Pacific zonal mean zonal wind between ERA–Interim and HadGEM3 runs under La Niña conditions.	56
2.11	Comparison of the sea level pressure in the high latitudes between ERA–Interim and HadGEM3.	57
2.12	Comparison of the sea level pressure anomalies under El Niño conditions in ERA–Interim and HadGEM3	58
2.13	Difference in sea level pressure anomaly between the HadGEM3 and ERA scaled under El Niño conditions	59
2.14	Comparison of the sea level pressure anomalies under La Niña conditions in ERA–Interim and HadGEM3	60
2.15	Difference in sea level pressure anomaly between the HadGEM3 and ERA scaled under La Niña conditions	60
2.16	Example of the Rossby wave ray tracing.	66
2.17	Comparison of ray tracing performed on 54 year climatologically or individual seasons.	67
2.18	Rossby wave ray tracing performed on the 0.0 K, 1.5 K and 3.0 K El Niño runs for DJF with baseline and perturbed climatologies.	68
2.19	Rossby wave ray tracing performed on the 0.0 K, 1.5 K and 3.0 K El Niño runs for JJA with baseline and perturbed climatologies.	69

3.1	Anomalous annual mean sea level pressure under El Niño.	74
3.2	Seasonal sea level pressure anomalies under El Niño conditions.	75
3.3	Sea level pressure in different seasons under various El Niño magnitudes.	76
3.4	The seasonal standard error of the sea level pressure.	77
3.5	<i>Absolute</i> annual precipitation rate under baseline (0.0 K) and El Niño conditions.	78
3.6	Seasonal outwards longwave radiation <i>anomaly</i> at the top of the atmosphere under El Niño conditions in DJF and JJA.	79
3.7	Seasonal mass streamfunction under El Niño conditions in DJF and JJA.	80
3.8	Seasonal zonal–meaned zonal wind under El Niño conditions in DJF and JJA.	81
3.9	Seasonal 200 hPa zonal wind under El Niño conditions in DJF and JJA.	83
3.10	Seasonal tropical 200 hPa zonal wind under El Niño conditions in DJF and JJA.	84
3.11	Seasonal Rossby wave source under El Niño conditions in DJF and JJA.	85
3.12	Contributions of each Rossby wave source terms to the overall Rossby wave source anomaly in JJA under El Niño conditions.	86
3.13	Zonal wind, meridional wind, divergence, absolute vorticity and ζD in JJA under baseline and El Niño conditions.	87
3.14	Zonal wind, meridional wind, divergence, absolute vorticity and ζD in DJF under baseline and El Niño conditions.	88
3.15	Contributions of $\zeta_0 D'$, $\zeta' D_0$ and $\zeta' D'$	90
3.16	Rossby wave ray tracing performed on the 1.5 K and 3.0 K El Niño runs for DJF and JJA.	92
3.17	Meridional gradient of absolute vorticity (β^*) and absolute vorticity under El Niño conditions in DJF and JJA.	94
3.18	Curvature of zonal wind with respect to latitude (U_{yy}) under El Niño conditions in DJF and JJA.	95
3.19	Wave flux anomaly following Plumb (1985) under El Niño conditions in DJF and JJA.	96
3.20	Flowchart showing the ENSO teleconnection mechanism to the Amundsen Sea Low	97
3.21	RWS anomaly, SLP anomaly and longitude of peak zonal mean zonal wind by month	99
4.1	Transient precipitation anomaly in JJA	105
4.2	Transient 200 hPa zonal wind anomaly in JJA	106
4.3	Transient 200 hPa RWS anomaly in JJA	107
4.4	Peak transient 200 hPa wave flux anomaly in JJA	108

4.5	Transient 200 hPa wave flux anomaly maps in JJA	108
4.6	Transient SLP anomaly in JJA	110
4.7	Peak transient SLP anomaly in DJF	111
4.8	Peak transient wave flux anomaly in DJF	111
4.9	Reaction times of critical variables in JJA	113
5.1	Sea level pressure anomaly during JJA under four different El Niño magnitudes.	118
5.2	200 hPa zonal wind during JJA under four different El Niño magnitudes. . .	120
5.3	Rossby wave source in JJA under four different El Niño magnitudes.	122
5.4	Absolute vorticity, divergence and ζD in JJA under baseline and four different El Niño magnitudes.	123
5.5	Rossby wave ray tracing under four different El Niño magnitudes in JJA. . .	124
5.6	200 hPa U_{yy} under in the four El Niño runs during JJA by longitude.	126
5.7	200 hPa RWS under in the four El Niño runs during JJA by longitude.	128
5.8	Amount of Rossby waves reaching and passing through the ASR under four different El Niño magnitudes in JJA.	129
5.9	Sea level pressure anomaly (in the Amundsen sea region) in the four El Niño runs during DJF.	131
5.10	zonal mean zonal wind by latitude–height in the four El Niño runs during DJF.	132
6.1	Sea level pressure of ERA–Interim and UPSCALE in JJA	137
6.2	Root mean squared error of sea level pressure between UPSCALE and ERA–Interim in JJA	138
6.3	Sea level pressure of ERA–Interim and UPSCALE in DJF	139
6.4	Root mean squared error of sea level pressure between UPSCALE and ERA–Interim in DJF	139
6.5	Sea level pressure composites of El Niño minus neutral conditions during JJA under ERA–Interim and UPSCALE	141
6.6	Sea level pressure composites of El Niño minus neutral conditions during DJF under ERA–Interim and UPSCALE	141
7.1	Peak sea level pressure anomaly under El Niño and La Niña conditions. . .	150
7.2	Mean zonal wind at 200 hPa between 25–35°S, 240–270°E under El Niño and La Niña conditions.	151
7.3	Peak outwards longwave radiation under El Niño and La Niña conditions. .	152
7.4	Regression of sea level pressure onto Niño3.4 temperature for the atmosphere only models (AMIP) in DJF.	156

7.5	Regression of sea level pressure onto Niño3.4 temperature for the atmosphere only models (AMIP) in JJA.	157
A.1	Change in latitude of the ITCZ over the seasons	175
B.1	SST anomalies during December and July for the three historical extreme El Niños	177
B.2	The evolution of the Oceanic Niñoindex and the Southern Oscillation index for the three extreme historic El Niños	178
B.3	Ranking of October–December El Niño episodes since 1950 by ONI	179
B.4	The list of Easterly wind bursts and Westerly wind burst of 2014 and 2015	181
C.1	First and second EOFs in HadGEM3 for DJF and JJA	184
D.1	Potential technical problems of implementing ray tracing.	186
E.1	Rossby wave ray tracing performed on the 1.5K El Niño run for DJF and JJA for wavenumber 2 and 4.	188
F.1	Rossby wave ray tracing performed on the 1.5K El Niño run for DJF and JJA with zonal filter sizes of approximately 21 degrees, 30 degrees, 39 degrees, 51 degrees and 60 degrees.	190
F.2	Rossby wave ray tracing performed on the 1.5K El Niño run for DJF and JJA with zonal filter sizes of approximately 21 degrees, 30 degrees, 39 degrees, 51 degrees and 60 degrees.	191
G.1	Pacific–meaned cloud bulk fraction under baseline (0.0K) and El Niño conditions.	194
H.1	Absolute wave flux anomaly following Plumb (1985) under 1.5 K El Niño conditions in DJF and JJA.	195
I.1	Geopotential height and absolute wave flux anomaly from ERA–40 and Karoly et al. (1989)	198
J.1	Rossby wave ray tracing performed on the 1.5K El Niño run for DJF and JJA initialised from the ‘second source’.	199

List of abbreviations

AMIP	Atmosphere only Climate Model Intercomparison Project
AMOC	Atlantic meridional overturning circulation
ASL	Amundsen Sea low
ASR	Amundsen Sea region
CBH	Cloud bottom height
CCM1	Community Climate model version 1
CMIP	Climate Model Intercomparison Project
CP	Central Pacific
CTH	Cloud top height
DJF	December–January–February
ECMWF	European Centre for Medium-Range Weather Forecasts
ENSO	El Niño southern oscillation
EOF	Empirical orthogonal function
EP	Eastern Pacific
HadGEM	Hadley Centre Global Environment Model
ITCZ	Intertropical convergence zone
JJA	June–July–August

MAM	March–April–May
MZWL	Maximum zonal wind location
NCAR	National Centre for Atmospheric research
OLR	Outwards longwave radiation
ONI	Oceanic Niño Index
PFJ	Polar front jet
PSA	Pacific–South–American
RWS	Rossby wave source
SAM	Southern annular mode
SLP	Sea level pressure
SOI	Southern oscillation Index
SON	September–October–November
SST	Sea surface temperature
STJ	Subtropical jet
T100	Timescale needed to reach 100% of peak value
T25	Timescale needed to reach 25% of peak value
TOA	Top of the atmosphere
UM	Unified model
UPSCALE	UK on PRACE – weather–resolving simulations of climate for global environmental risk
WKBJ	Wentzel, Kramers, Brillouin and Je

Prologue

Mark Twain around 1880 supposedly remarked¹ “The coldest winter I ever experienced was a summer in San Francisco” (Ahrens, 2009). He was probably referring to the climate impacts from a strong El Niño Southern Oscillation (ENSO) event that happened around that time. Such events have been known to exist for a very long time. ENSO teleconnections are an example of geographically disconnected regions affecting each other through physical processes. These climatological relationships between two disconnected regions, typically at large distances, are named teleconnections. This project is motivated by these phenomena. The aim is to improve the understanding of one such teleconnection. I investigate climate phenomena in the central and eastern tropical Pacific regions and their relationship with the climate in western Antarctica. I focus on the Amundsen Sea Low (ASL) which is the dominant low pressure system in the south Pacific sector of the southern Ocean. The ASL is important to the climate in the whole of western Antarctica (Hosking et al., 2013; Küttel et al., 2012; Turner et al., 2013) and may play a part in solving the puzzle of increasing Antarctic sea ice in today’s warming climate (Turner et al., 2009, 2016). Therefore, it is important to understand the ASL and any phenomena that may affect it.

El Niño Southern Oscillation events have global implications both climatologically and socio-economically. The ENSO cycle is the strongest inter-annual signal in the coupled ocean-atmosphere system (Sun et al., 2013) and has global climate implications. For example, during strong El Niño events, there are typically droughts in Indonesia, southern Africa and Australia while there are heavy rains and flooding in Ecuador and Peru (Ahrens, 2009). Storms are directed into California and there is heavy rain in the Gulf Coast states due to storm tracks shifting under El Niño conditions. Some of the more direct economical losses are due to flooding, winds and drought (Ahrens, 2009). While the ENSO teleconnection to the Antarctica may not directly affect humans, indirect effects such as sea level changes resulting from melting ice/glacial in the western Antarctic region may affect human populations globally.

¹It is unknown if this quote actually originated from him.

Historically, there has been more research on northern hemisphere climate phenomena than on the southern hemisphere. One of main reasons is the larger population and thus greater economical activity in the northern hemisphere. This may have led to an imbalance in climate interest between the two hemispheres. The Amundsen Sea Low is a highly important feature climatologically for the western Antarctic climate. Its depth and location can affect the conditions in the whole of western Antarctica (Ding et al., 2011). This includes changing temperatures, winds and sea ice. The area has undergone significant changes in the past decades (Schneider et al., 2011), and therefore it is important to study the region in detail to improve the understanding of western Antarctica climate and the southern hemisphere in general.

In this project, I attempt to investigate the mechanism behind the ENSO teleconnection to the ASL. In particular, I am interested in the seasonality of the teleconnection. This is because the seasonality seems at first counter-intuitive. ENSO events peak in austral summer while the teleconnection peaks in austral winter. Furthermore, I investigate the linearity of the teleconnections. This allows greater understanding of the differences in the ASL response within different magnitudes of El Niños. The content of the chapters is summarised below:

Chapter 1 presents a basic overview of the tropical and southern hemisphere circulation and dynamics. In particular, I summarise previous understanding on ENSO, general circulation of the southern hemisphere and the ASL.

Chapter 2 discusses the models and datasets used in this thesis. These include the ERA-interim, UPSCALE and the Unified Model. I also present the experimental setup and model evaluation in this chapter.

Chapter 3 examines the seasonality of the ENSO teleconnection to the ASL. It shows results from the perpetual El Niño time-slice model runs. In particular, I try to construct a mechanistic flowchart in order to understand the difference in the teleconnection between the seasons.

Chapter 4 examines the the transient response of the teleconnection. In this chapter, I focus on results from the transient runs where I ‘switch on’ El Niño in austral summer and winter. In particular, I study the difference in the transient response between the two seasons.

Chapter 5 focuses on the linearity of the teleconnection. I investigate linearity of the ENSO–Amundsen Sea region teleconnection across different magnitudes El Niños in austral summer and winter.

Chapter 6 examines the model resolution dependence on the climatology and teleconnection to the ASL.

Chapter 7 summarises the overall findings and is the conclusion to the thesis. I also present possible future work in this chapter.

Chapter 1

Introduction

This chapter will introduce previous studies that the work in this thesis builds upon. Background information on the Amundsen Sea Low (ASL) and its role in the Antarctic climate will be presented in Section 1.1. Section 1.2 provides an overview of the El Niño Southern Oscillation. Previous works on the circulation of the atmosphere, particularly the Hadley cell and the tropospheric jets, will be discussed in Section 1.3. The following Section 1.4 presents previous works on the ENSO teleconnection to the Amundsen sea region. Finally, the scientific aims of the thesis are summarised in Section 1.5.

1.1 Amundsen Sea Low

This thesis mainly investigates the ENSO teleconnection to the Amundsen sea region. The dominant feature affected by this teleconnection is the ASL. Therefore it is important to understand the basics of the ASL. This section presents the climatology of the ASL (Section 1.1.1) and its role on the Antarctic climate (Section 1.1.2).

1.1.1 Climatology, annual cycle and recent trends

The Amundsen sea low (ASL) lies approximately between the Antarctic Peninsula and the Ross Sea, see Figure 1.1 and is sometimes called the Amundsen–Bellingshausen Sea low (Hosking et al., 2013). It is a quasi–stationary climatological low pressure centre found in the south Pacific sector of the southern Ocean (Hosking et al., 2013), see Figure 1.2. The ASL is part of three climatological low pressure centers located near 30°E, 120°E and 200°E longitude along the circumpolar trough (Turner et al., 2013). The circumpolar trough is a ‘ring’ of low pressure that extends around Antarctica at a mean latitude of around 66°S (King and Turner, 2007). There is no direct counterpart in the northern hemisphere due to the largely

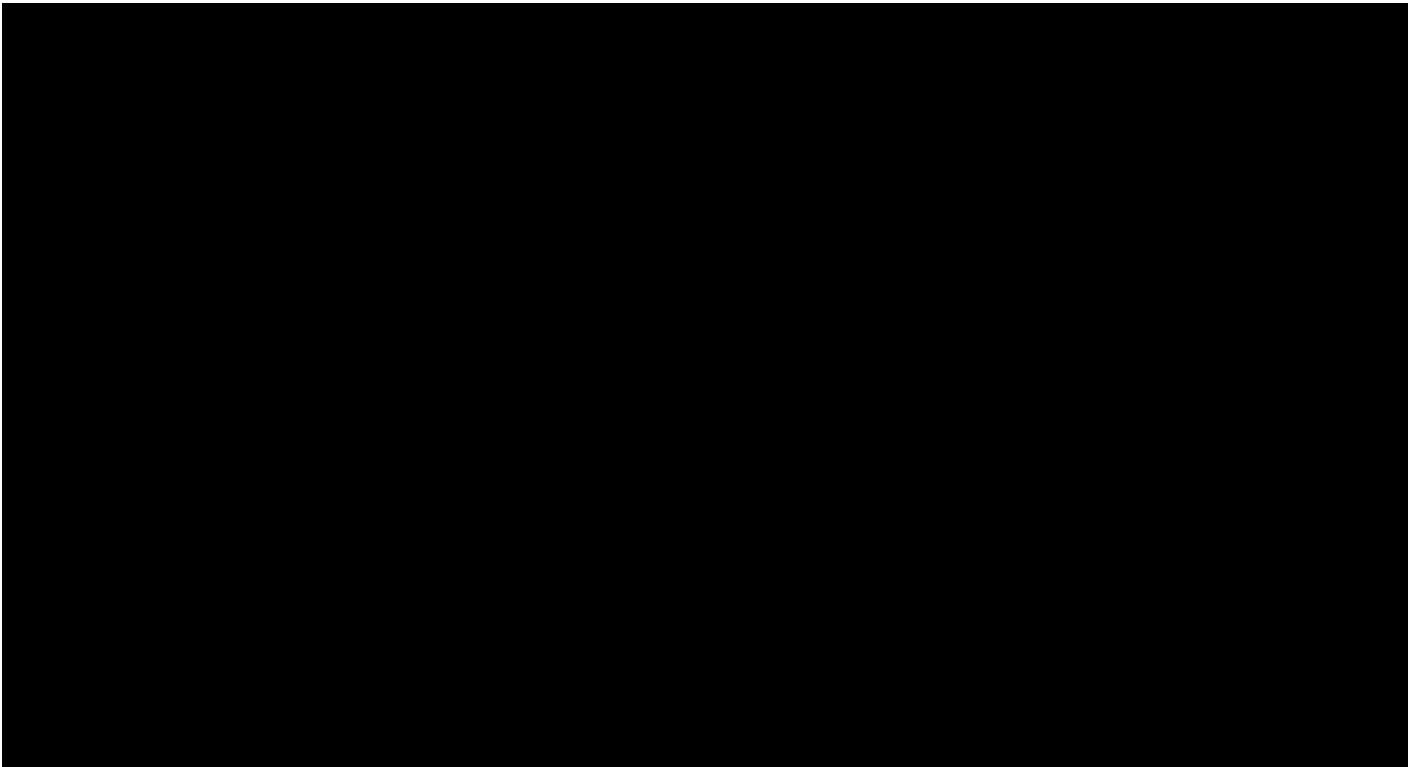


Fig. 1.1 The location of the Bellingshausen Sea, Amundsen Sea and Ross Sea are shown. These seas show the regions where the ASL resides. Figure taken from Hosking et al. (2013).

uninterrupted ocean in the southern hemisphere where there are virtually no landmasses blocking circulation.

The ASL is the can be seen from the time averaging over the large number of synoptic and subsynoptic scale low pressure systems propagating through this area (Fogt et al., 2012). Riffenburgh (2007) described two points of origin for these synoptic and subsynoptic low pressure systems: firstly, there are low pressure systems that form in the mid-latitudes and spiral in towards the circumpolar trough. Secondly, there are low pressure systems that are created in the circumpolar trough itself. Both types of events happen with approximately the same frequency. Note that the unique topography and geography of Antarctica plays a significant role in contributing to the enhanced baroclinicity needed for the formation of these low pressure systems in the circumpolar trough (Hosking et al., 2013; Lachlan-Cope et al., 2001; Walsh et al., 2000). In fact, the ASL would not exist as it does if it were not for the unique orography of Antarctica. Lachlan-Cope et al. (2001) showed that the asymmetrical orography in Antarctica is necessary for the presence of the maximum synoptic variability in the Amundsen–Bellingshausen Sea. In their model experiment, they used a displaced axi-symmetric Antarctic orography and found that the maximum variability no longer lay on the Amundsen–Bellingshausen Sea region. Walsh et al. (2000) found that any reduction

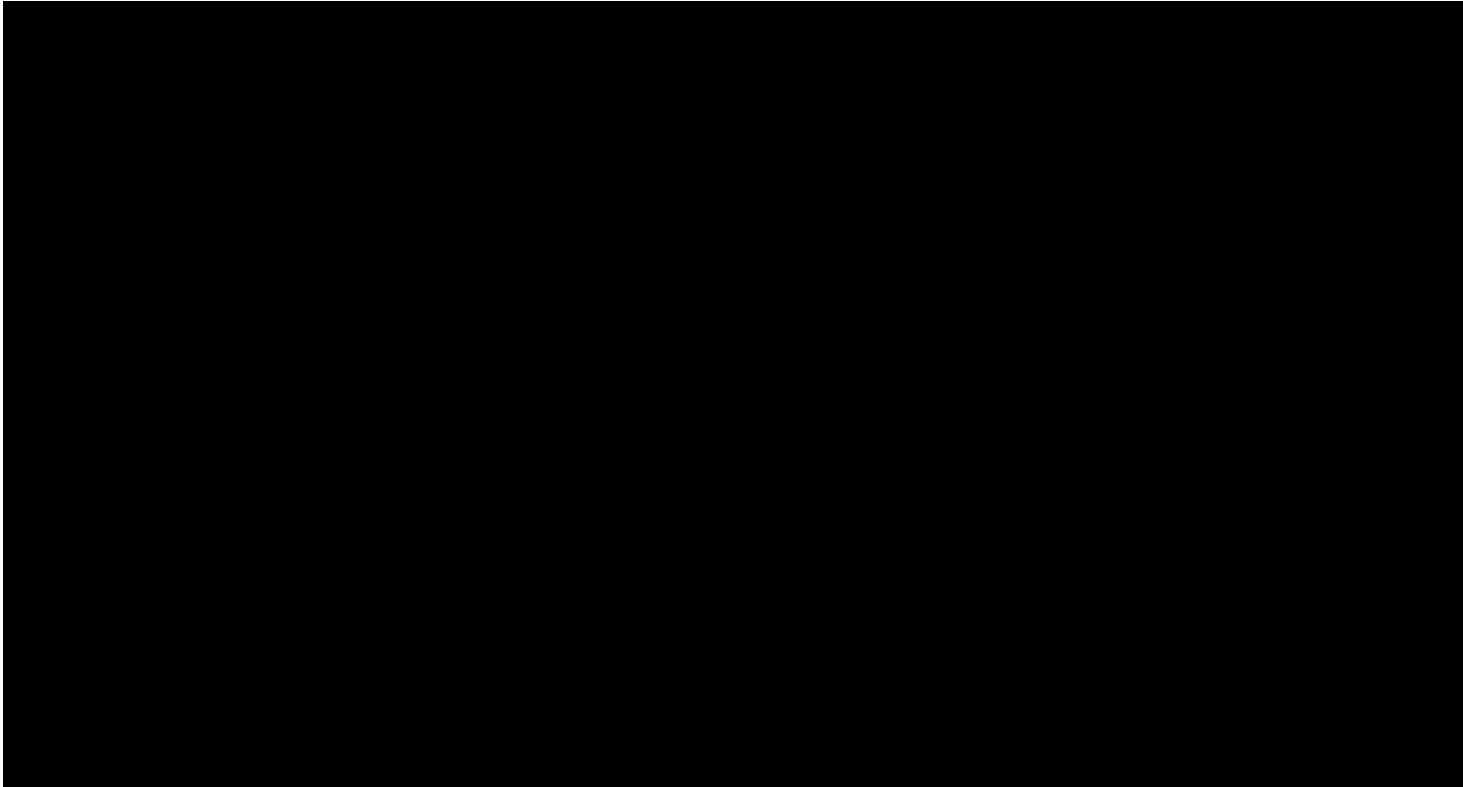


Fig. 1.2 The location of the ASL is marked with a white cross. Blue regions indicate low pressure while red regions indicate high pressure. Region contained within the black ‘box’ is the location where the ASL can be found. The two other low pressure systems ($\sim 20^\circ\text{E}$ and $\sim 120^\circ\text{E}$) are part of the three low pressure systems located along the circumpolar trough. Figure taken from <https://climatedataguide.ucar.edu/climate-data/amundsen-sea-low-indices>.

in the height of Antarctica caused the circumpolar trough to broaden and move towards the Antarctic coastline. This has the effect of changing the location and strength of the low pressure systems that are formed in the circumpolar trough. The Amundsen sea region (ASR) circulation variability is highest throughout the southern hemisphere (Lachlan-Cope et al., 2001). This is due to the shape of the Antarctic ice sheet and the high orography near it.

The above paragraph described the ASL in an statistical sense (time averaging of the low pressure systems). Dynamically, the ASL is caused by the tropical sea surface temperature (SST) asymmetry (Inatsu and Hoskins, 2004) which, similar to the Icelandic and Aleutian low which Rossby (1939b), generate Rossby waves that form the ASL. Previous work by Inatsu and Hoskins (2004) found that zonally symmetric tropical SSTs expand the southern hemisphere storm tracks polewards and eastwards and cause its spiral structure to be lost. The southern hemisphere storm tracks are important for the existence of the ASL. Furthermore, they found that the zonal asymmetry in the tropical SST excited stationary waves. This in turn explains most of the zonal asymmetry of the southern hemisphere storm

tracks. These dynamical effect can be seen to drive the statistics found in the synoptic and subsynoptic low pressure systems as described before.

Note that the ASR is defined differently in different studies. Fogt et al. (2012) defined it as the region within 45° – 75° S, 180° – 60° W. Turner et al. (2013) selected a smaller area of 60° – 75° S, 50° – 180° W. Their reasoning was that they just needed to capture the central location and depth within the region to provide an usable metric. Hosking et al. (2013) defined it as the region within 60° – 75° S, 190° – 70° W. This thesis will follow the definition of Hosking et al. (2013).

Turning to seasonality of the ASL, there is a large seasonal variability in both location and the central pressure of the ASL (Fogt et al., 2012; Hosking et al., 2013; Turner et al., 2013). As seen from Figure 1.3, the ASL depth is greatest during austral winter. During austral winter, Hosking et al. (2013) showed that the ASL reached a maximum relative depth of -11 hPa. The ASL showed a minimum relative depth in austral summer of -6 hPa. Note that the relative central pressure is defined as the central pressure of the ASL subtracted from its nearby surroundings (the ASR). This is also named the ABL index in Hosking et al. (2013). The inter-annual variability of the sea level pressure (SLP) in the ASR is also the greatest during austral winter and lowest during austral summer. The longitude of the ASL tends to maximise (minimise) during austral summer (winter) while the latitude of the low pressure centre is further southwards (northwards) in austral winter (summer) (Fogt et al., 2012; Hosking et al., 2013; Turner et al., 2013).

Moving on to trends of the ASL, following Turner et al. (2013), Figure 1.4 shows that between 1979–2008, the ASL has exhibited complex and non-uniformed changes across the seasons. Turner et al. (2013) found only three months (January, March and September) when the trends in the ASL depth were significant at the 10% level. In January, the ASL has deepened by 1.7 hPa per decade. In September, there has been a large downwards trend in the ASL pressure. However, this is mainly due to one anomalous year in 2008 where the ASL had a pressure of 958 hPa. This was the lowest pressure in the 30 year record. If this year is removed, the long-term trend is no longer significant at the 10% level. March shows an increase in ASL pressure, due to the weakening of the circumpolar trough. In general, reanalysis data indicates the ASL has deepened during austral winter and autumn (Turner et al., 2009, 2013), albeit with high uncertainty, and this may have played a role in historic increases in Antarctic sea ice (Raphael et al., 2016), see Section 1.1.2.

1.1.2 Role of the Amundsen Sea Low for Antarctic climate

The following provides a short overview on the role of the ASL on Antarctic climate which is important for this thesis. This is because the ENSO–ASR teleconnection will predominantly

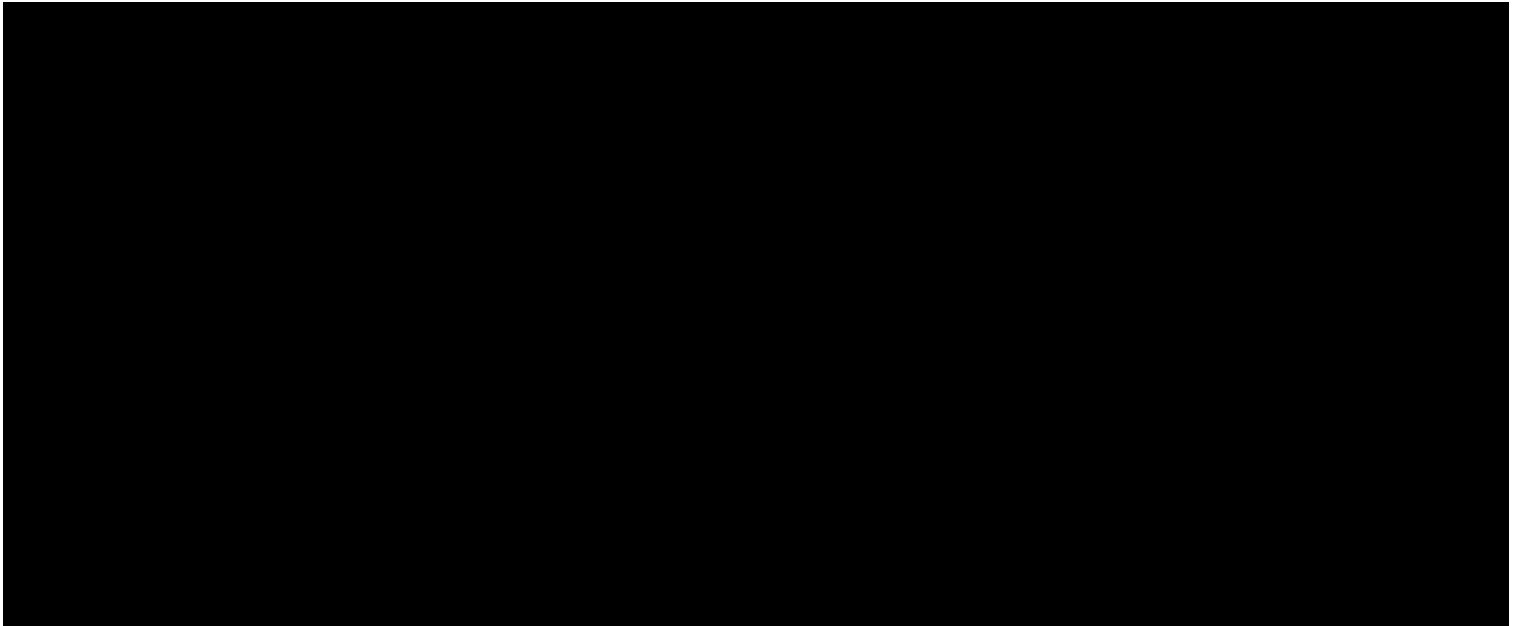


Fig. 1.3 Seasonal mean SLP for (a) December–January–February, (b) March–April–May, (c) June–July–August and (d) September–October–November. (e)–(h) show the relative pressure with respect to the ASR (black lined region). Data used is ERA-Interim 1979–2011. Figure taken from Hosking et al. (2013).

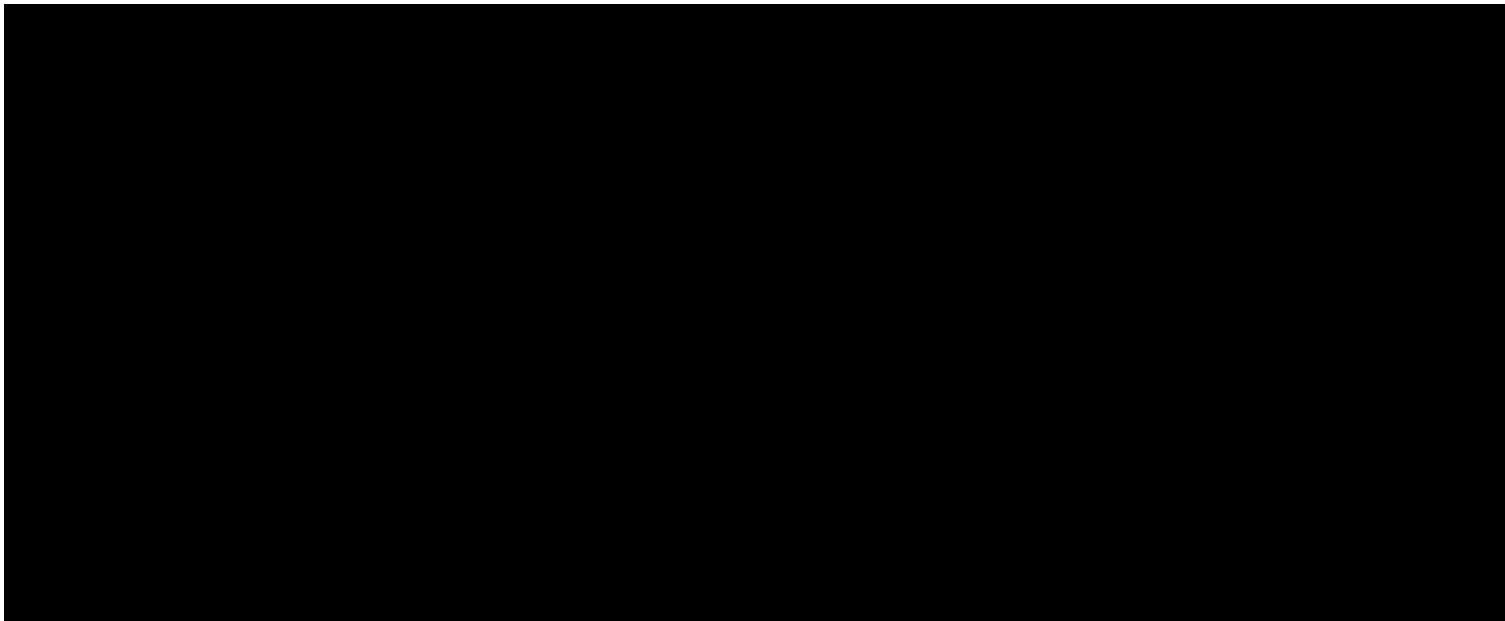


Fig. 1.4 The trend in depth of the ASL over 1979–2008. The units is in hPa decade^{-1} . Trends significant at the 10% level are marked with stars. Adapted from Turner et al. (2013).

affect the ASL which will affect these surface variables. Furthermore, the increasing Antarctic sea ice in today's warming climate is still a major open question. Understanding the ASL may play a role in answering this question.

The climate in western Antarctica is greatly affected by the ASL (Hosking et al., 2013; Küttel et al., 2012; Turner et al., 2013). Hosking et al. (2013) found that both the longitude and strength of the ASL may play a role in determining surface wind conditions, surface air temperature, precipitation and sea ice content near West Antarctica. However, this relationship is complex and may be seasonally and geographically dependent. In order to investigate the effect ASL variability has on meridional wind at 10 metres, surface air temperature, precipitation and sea ice content, Hosking et al. (2013) split the ERA–Interim dataset by separating the ASL longitude and pressure into four quartiles. They performed composite analysis of the lower quartile minus the upper quartile. The dataset spanned 1979–2011 so that each quartile had 8 years of data. The composite of ASL longitude is shown in Figure 1.5. Summarising the results, the longitude of the ASL had the largest significant effect on the 10 metre meridional wind in austral autumn (MAM) and winter (JJA). During these times there is a strengthening of the northerly flow over the Amundsen sea and the eastern Ross sea. Conversely, there is a strengthening of the southerly flow over the western Ross sea. The surface air temperature and precipitation show warmer and moister (colder and drier) conditions in the Amundsen sea (western Ross sea) (see Figure 1.5 (f,g,j,k)). There is a dipole of anomalies in the sea ice content during austral winter: the sea ice content is around 20% greater (30% smaller) over the Ross sea (Amundsen sea) (see Figure 1.5 (n,o)). The anomalies are weaker and more constrained during austral spring and are even geographically different in austral summer.

Figure 1.6 shows the composite of the ASL relative central pressure. In summary, only austral winter and spring seasons shows significant differences for 10 metre meridional wind in western Antarctica and its surrounding oceans. The northerly wind is strengthened when the ASL is deeper. This results in increased precipitation over the coastal western Antarctica as the northerly winds bring warm moist marine air into the region. The warm air also increases surface air temperatures over Ellsworth land. There are also regions with decreased surface air temperatures, but these are not statistically significant based on the thresholds applied in the study. The changes in sea ice content are also not statistically significant, but do show an increase over the Amundsen sea. This is unexpected and still an open question as the increased northerly flow should push the ice towards the coast thus reducing ice coverage.

Although Hosking et al. (2013) did not find a statistically significant relationship between ASL depth and the sea ice content in the ERA–Interim dataset, the ASL has been linked to sea ice changes in recent warming climates in other studies (Turner et al., 2009, 2016). Under recent warming, Arctic sea ice extent has been decreasing (Parkinson and Cavalieri, 1989) with accelerating trends since the 1980s (Cavalieri et al., 2012; Comiso et al., 2008; Johannessen et al., 1995; Meier et al., 2007; Parkinson et al., 1999). However, Parkinson

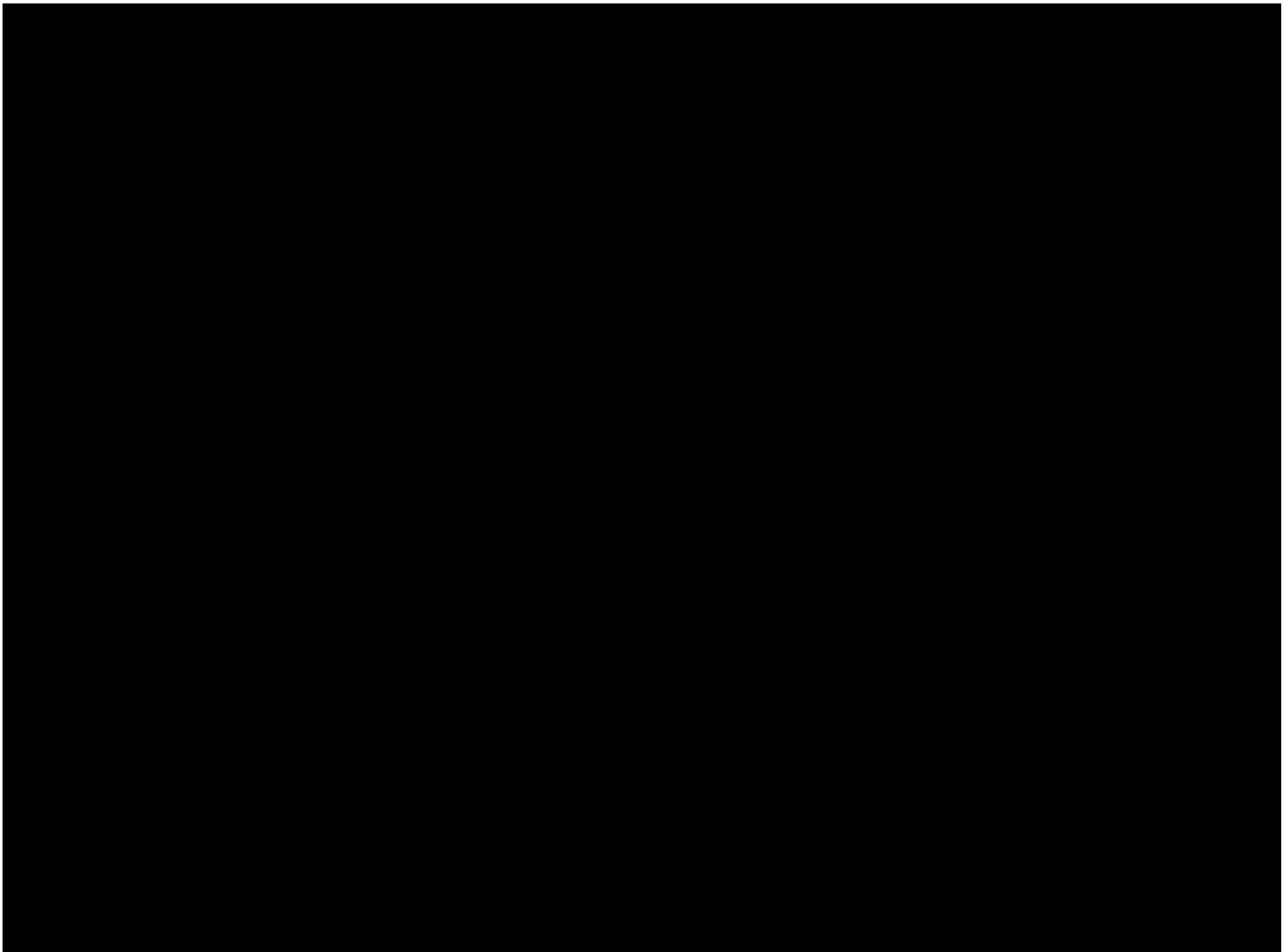


Fig. 1.5 Seasonal difference of surface variables in western Antarctica according to seasonal ASL longitude. The data used is ERA–Interim for the period 1979–2011. The dataset is split into four quartiles according to the ASL longitude and the graphs are composites of the lower and upper quartiles. The columns consists of the four austral seasons: December–January–February (DJF), March–April–May (MAM), June–July–August (JJA) and September–October–November (SON). The rows consists of the different surface variables: V10 (meridional wind at 10 metres), SAT (surface air temperature), PPN (precipitation) and SIC (sea ice content). The crosses are the locations of the ASL for each year. The statistical significance (at 5% using a Student’s t–test is denoted by the thick black line. Figure taken from Hosking et al. (2013).

and Cavalieri (2012) found that Antarctic sea ice has increased on average since the late 1970s in sharp contrast to the Arctic, see Figure 1.7. This may seem puzzling given the warming climate since the 1970s. Parkinson and Cavalieri (2012) found that Antarctic sea ice increased at an extent of $17100 \pm 2300 \text{ km}^2 \text{ yr}^{-1}$ with much of the increase located in the Ross

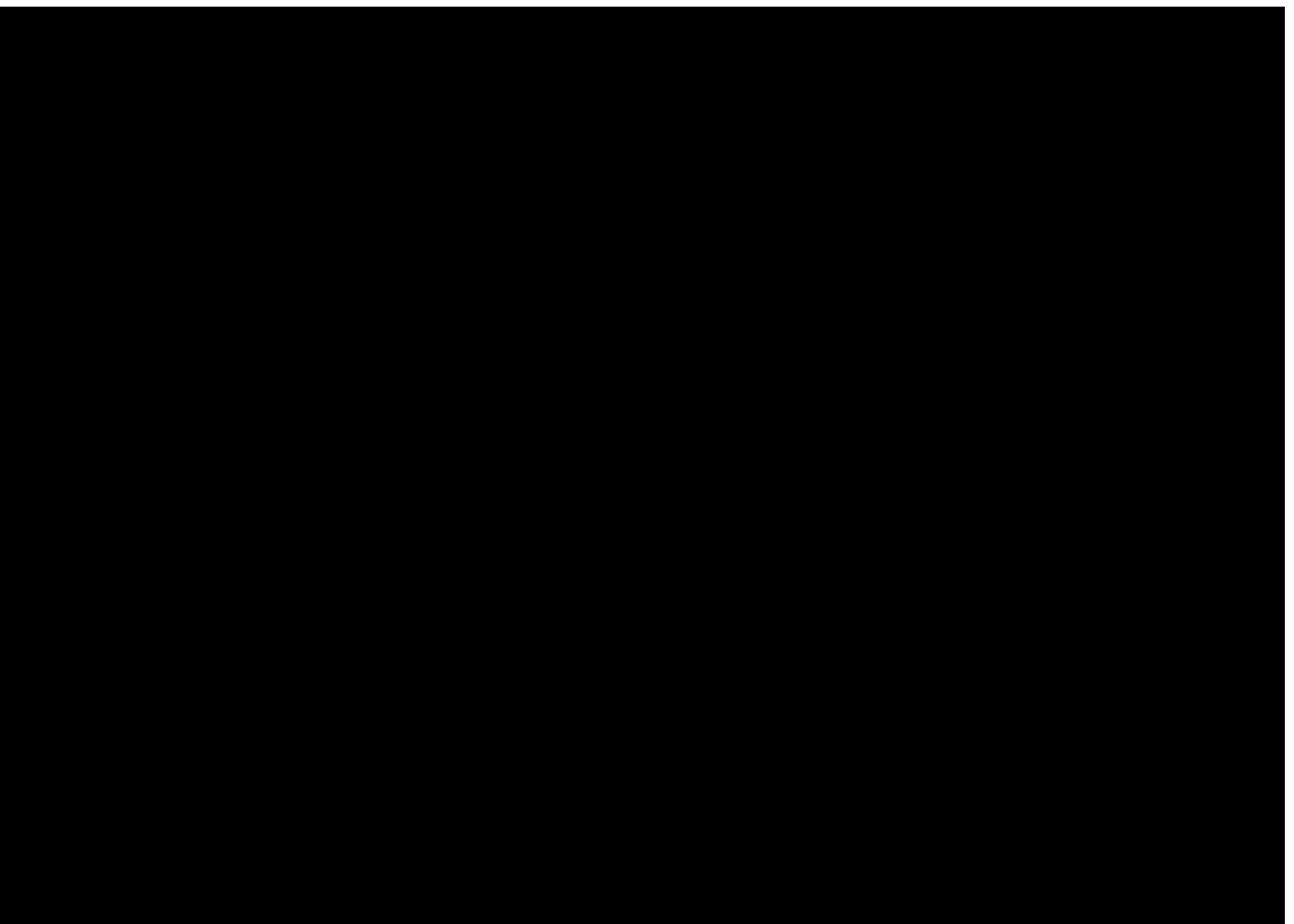


Fig. 1.6 Same as Figure 1.5 but categorised by ASL depth. Figure taken from Hosking et al. (2013).

sea ($13700 \pm 1500 \text{ km}^2 \text{ yr}^{-1}$) while the ASR experienced the most significant sea ice decrease in Antarctica ($-8200 \pm 1500 \text{ km}^2 \text{ yr}^{-1}$). Turner et al. (2009) also found a sea ice increase in the Ross sea and decrease in the ASR in all four seasons from 1979–2000 (although the changes in sea ice extent were only significant in both sectors in autumn). These patterns may be linked to the deepening of the ASL resulting in greater meridional flow off the Ross ice shelf (Turner et al., 2009, 2016) and lower meridional flow off the Amundsen Sea.

However, in 2016–2017, Antarctic sea ice extent broke with the previous trend and dropped significantly (Viñas, 2017), see Figure 1.7. The drop is larger than the accumulated increase from 1979 to present day. Currently, it is not clear if this is part of internal variability or if this is a shift in behavior of the Antarctic sea ice.

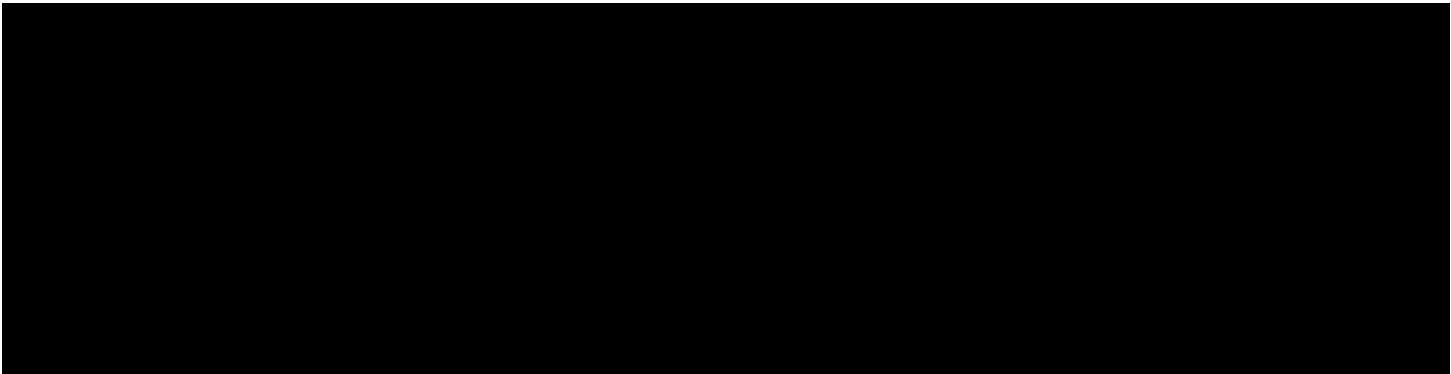


Fig. 1.7 Anomalies in sea ice extent in the Antarctic between 1979–2017. Figure taken from Viñas (2017).

Summary

This section summarised the basics of the Amundsen sea low (ASL). There are three key messages. Firstly, the ASL is formed from low pressure systems propagating through the Amundsen sea region (ASR) and the unique orography of Antarctica. Secondly, there is a seasonality associated with the ASL climatology. This mainly affects the pressure and longitude of the ASL. Thirdly, the ASL is important for Antarctic climate. Surface variables in Antarctic are often affected by the ASL. One crucial example is that the Antarctic sea ice changes have been associated with the trends in the pressure of the ASL.

1.2 El Niño Southern Oscillation

This section presents basic information on the El Niño Southern Oscillation (ENSO). It presents the overview of ENSO (Section 1.2.1), its indices (Section 1.2.2), the types of ENSO (Section 1.2.3) and their teleconnections (Section 1.2.4). Understanding the basics of ENSO is crucial to understanding the ENSO–ASR teleconnection which will be presented later in the thesis.

1.2.1 What is the El Niño Southern Oscillation?

ENSO is a large scale mode of climate variability associated with the fluctuations in sea surface temperature (SST) across the central and eastern Pacific in the tropics (Ahrens, 2009; Philander, 1990; Sun et al., 2013). This is a quasi periodic cycle with a period of approximately two to seven years (Philander, 1990; Rasmusson and Carpenter, 1982). The ENSO cycle has global climate implications as it is the strongest inter–annual signal in the coupled ocean–atmosphere system (Karoly, 1989a; Sun et al., 2013; Wolter, 1989).

Figure 1.8 shows the structure of the ocean and tropical circulation during El Niño and neutral conditions (i.e non–El Niño conditions).

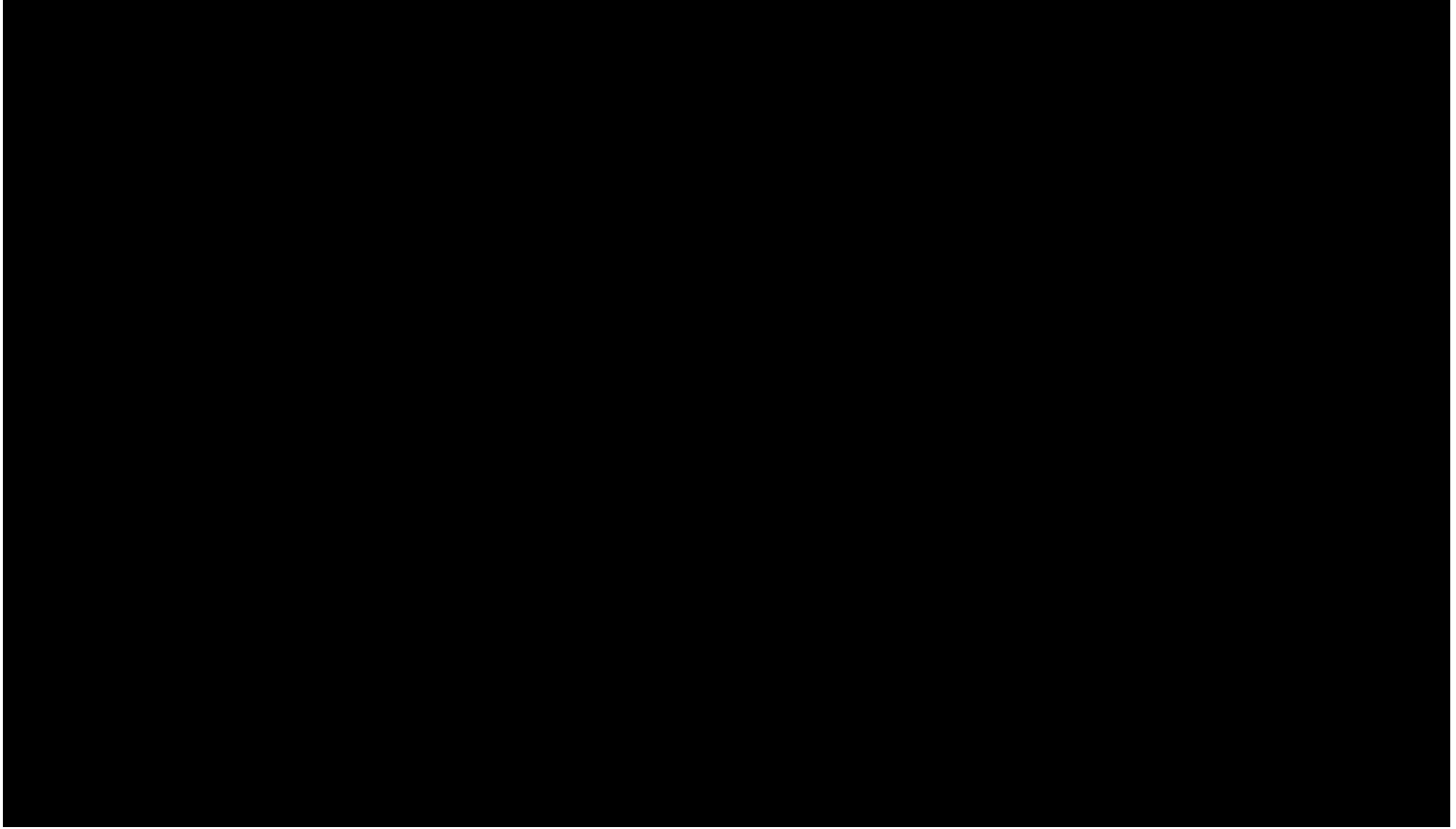


Fig. 1.8 The ocean and tropical circulation under neutral and El Niño conditions. Top: neutral condition. Bottom: El Niño conditions. Figure taken from Ahrens (2009).

During the ENSO neutral conditions, the trade winds are observed to be strong (Ahrens, 2009). Trade winds are winds that blow westwards and equatorwards in both the northern and southern hemispheres (Ahrens, 2009). The winds push the surface water from east to west. As the cold surface water is advected towards the west, it is heated by solar radiation, creating a warm pool of water in the west Pacific. As the surface water advects westwards, deeper cooler water is upwelled in the eastern Pacific. As a result of this, the thermocline is higher than in the east compared to the west. The thermocline is the separation of warm surface water and cooler deep water. This advection of water is reflected on the surface as a cold surface pool of water in the eastern Pacific.

The surface winds are part of the Walker circulation (Ahrens, 2009) which is a convective cell that extends from the eastern Pacific to the western Pacific, see Figure 1.8. In the western Pacific, the warm vertical advection of the high humidity surface waters drive convective instability and rapid vertical motion which forms clouds. Some of the air is advected

westwards and cooled in the process. The cool dry air sinks in the eastern Pacific. This 'completes' the Walker circulation.

During El Niño conditions, the pressure difference between eastern and western Pacific weakens/reverses, see Ahrens (2009). This weakens the trade winds and the Walker circulation weakens or even reverses. Without the easterly surface wind, the 'warm tongue' of water in the west Pacific will be much further to the east. This leads to anomalously warm water in the Central and eastern Pacific thereby reducing the upwelling in the east and reducing and deepening the thermocline. Note that the thermocline deepens at the equator, but rises in regions just outside of the equator.

La Niña conditions can be seen as an intensification of the normal conditions, which includes anomalously strong Walker circulation and stronger upwelling of cold ocean waters in the eastern Pacific. The net effect is that the eastern and Central Pacific has colder than normal sea surface temperature (SST).

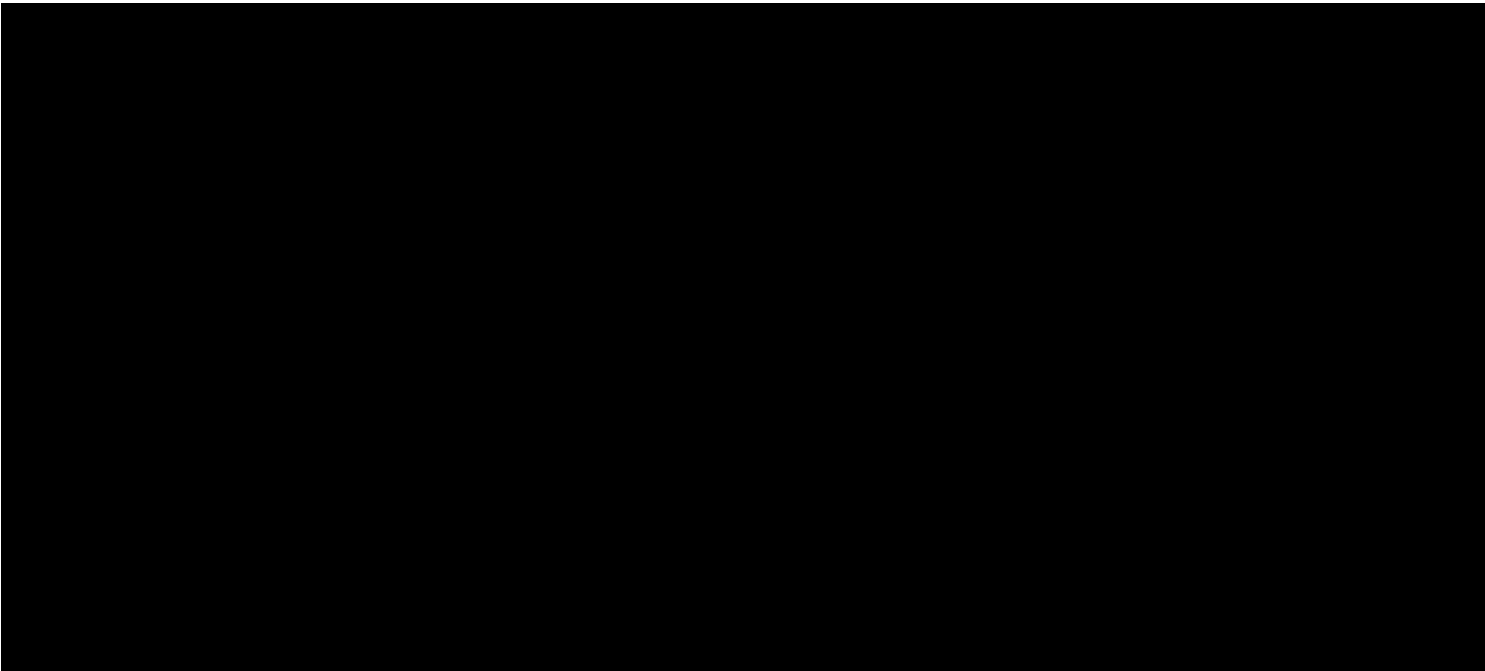


Fig. 1.9 Monthly Niño3.4 temperature for strong historic El Niños. This figure was taken from <https://www.climate.gov/news-features/blogs/enso>

Note that there is a seasonality associated with ENSO events. ENSO events tend to peak at the end of the year in austral (boreal) summer (winter), see Ahrens (2009) for details. Figure 1.9 shows the monthly Niño3.4 temperature for strong historic El Niños. As seen from the figure, El Niño events tend to peak in austral summer. Further details on the evolution of strong historic El Niños can be found in Appendix B.

1.2.2 ENSO indices

It is important to have metrics or indices to quantify the magnitude of the El Niño or La Niña events. However, as the processes and regions involving ENSO are complex and large, it is difficult to identify an universal index. This thesis uses the Niño3.4 index to examine ENSO events, but others such as the Oceanic Niño Index (ONI) and the Southern Oscillation Index (SOI) are also used in the literature.

The Niño3.4 index measures the (usually monthly) SST anomaly relative to climatology region between the Central Pacific and the eastern Pacific at 5°S–5°N and 170–120°W, see Figure 1.10. If the Niño3.4 index is greater or less than a certain threshold (usually ± 0.45 K or ± 0.5 K), it is classified as an El Niño or La Niña event. The climate is considered to be in ENSO neutral conditions if the index is between the upper and lower thresholds. The Niño3.4 region captures ENSO anomalies in the eastern Pacific and Central Pacific. The Niño3 region can be used as a eastern Pacific preferred index while the Niño4 can be used as a Central Pacific preferred index. The Niño3.4 index is a very common index due to its simplicity and is used by many studies (e.g. Trenberth and Stepaniak (2001), Sun et al. (2013) and McPhaden (2015)). Another advantage of this index is that the sea surface temperature measurements in the tropics are plentiful in recent history. However, as with most metrics, the Niño3.4 index is not perfect. One disadvantage is that a threshold is used to determine the presence of El Niño or La Niña events. In reality, SST anomalies in the Niño3.4 region are fairly continuous (see Figure 1.11).

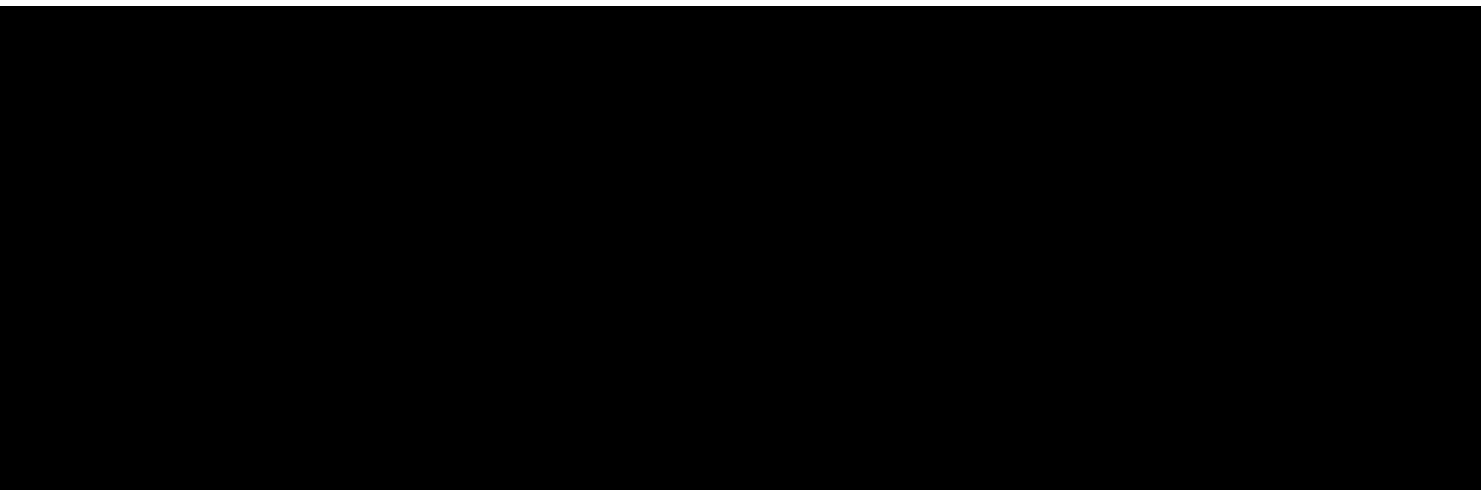


Fig. 1.10 The locations of the Niño regions. The Niño1+2 region lies on 0–10°S, 90–80°W, the Niño3 region is located on 5°N–5°S, 150–90°W, the Niño4 is in 5°N–5°S, 160°E–150°W and the Niño3.4 region is situated in 5°N–5°S, 170–120°W. This figure was taken from <https://www.ncdc.noaa.gov/teleconnections/enso/indicators/sst.php>

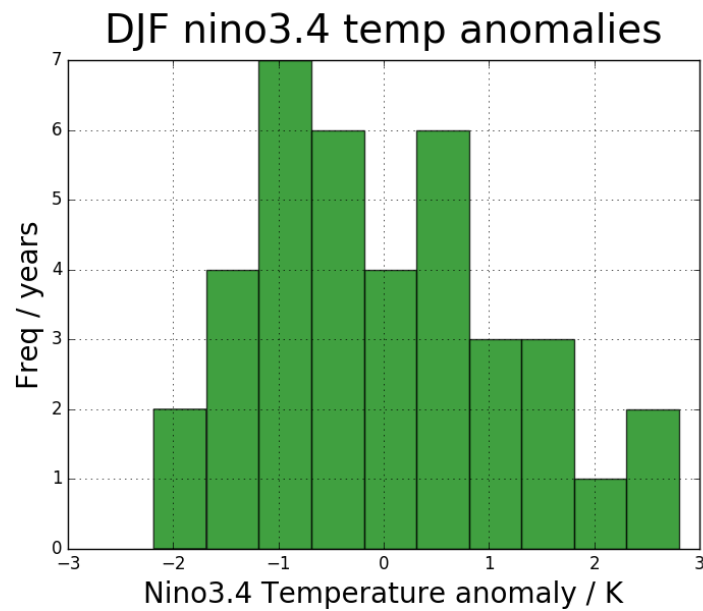


Fig. 1.11 Histogram of the Niño3.4 index from 1979–2016. Dataset used is the ERA–Interim.

Figure 1.12 shows the evolution of the Niño3.4 index from 1982–2016. The figure shows that the Niño3.4 index has been approximately between -2.5 K to $+3$ K in recent history. El Niños and La Niñas with a magnitude of Niño3.4 anomaly over 2 K can be considered as extreme events as these happen very rarely. For example, only the strongest three El Niños in this time period reached over 2 K in the Niño3.4 region. These are the 1982–1983 event, the 2015–2016 event and the 1997–1998 El Niño, in descending order of strength. For further details regarding extreme ENSO events, see Appendix B.

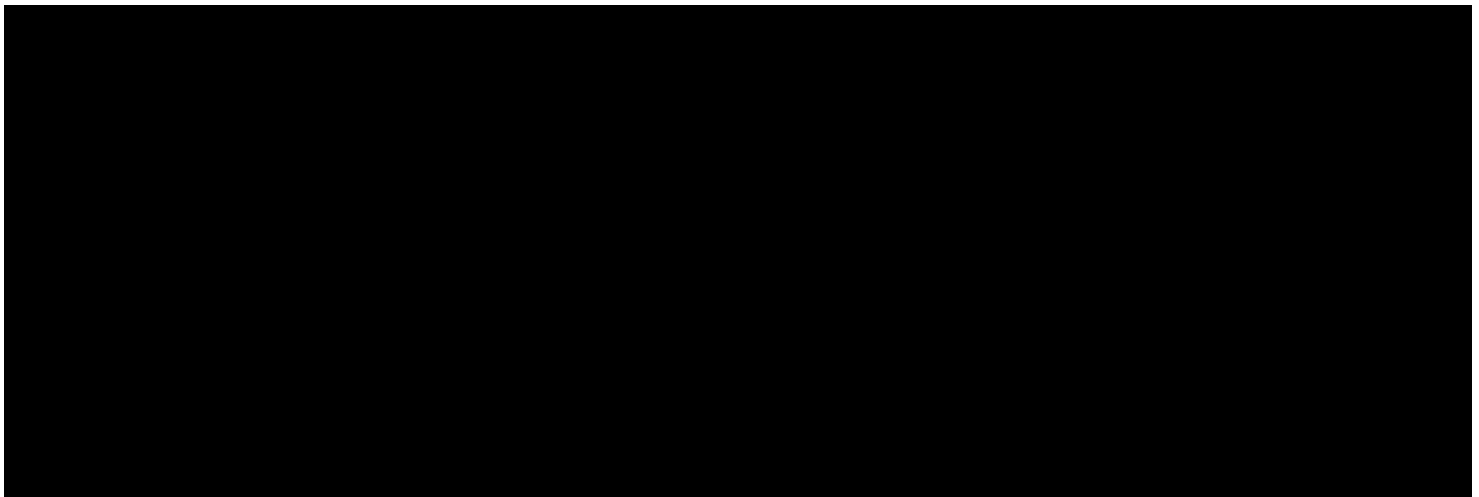


Fig. 1.12 The evolution of the Niño3.4 index from 1982–2016. Figure was taken from <https://iri.columbia.edu/wp-content/uploads/2016/07/figure2.gif>

The ONI is an index based on the Niño3.4 temperature. It consists of looking at five consecutive three month periods of the Niño3.4 SST anomaly. It is considered to be in El Niño (La Niña) conditions if the ONI is higher (lower) than 0.5 K (−0.5 K).

The Southern Oscillation Index (SOI) is the observed SLP difference between Tahiti in French Polynesia and Darwin, Australia. The SOI is a measure of the large scale pressure difference between the eastern and western Pacific – in effect, it measures the strength of the Walker circulation. During El Niño (La Niña), the SLP is lower (higher) in Tahiti¹ than Darwin². In short, the SOI is negative during El Niño and positive during La Niña.

While this thesis uses the Niño3.4 index (based on seasonal data), the analysis could have been done using any of the other indices and the overall results would be similar.

1.2.3 El Niño Southern Oscillation types

The different types of ENSO will be explored below. It is important to understand the differences between ENSO types as the ENSO–ASR teleconnection changes according to the specific ENSO. Further details of the teleconnection will be given in Section 1.4.

El Niño events can be divided into two main types: eastern Pacific (EP) El Niño and Central Pacific (CP) El Niño (Sun et al., 2013; Trenberth and Stepaniak, 2001), see Figure 1.13. The EP El Niño is the classic ‘textbook’ El Niño that consists of maximum warming in the eastern equatorial Pacific (Hu et al., 2016) in the Niño3 region (Kug et al., 2009). It is sometimes referred as the cold–tongue El Niño, see again Kug et al. (2009). Conversely, the CP El Niño has maximum warming in the Central equatorial Pacific in the Niño4 region. The CP El Niño has also been referred to in previous works as the warm–pool El Niño or El Niño Modoki (Ashok et al., 2007; Karumuri and Toshio, 2009). The Trans–Niño index can be used to determine whether an ENSO event is classified as a EP or a CP event. It is the difference between normalized mean SST anomalies for the Niño1+2 regions and the Niño4 region (Trenberth and Stepaniak, 2001), see again Figure 1.10.

There are several major differences in the tropical surface variables and teleconnections between the EP El Niño and the CP El Niño (Kug et al., 2009). The structure of the winds and the Walker circulation are different between the EP and CP El Niños (Karumuri and Toshio, 2009; Kug et al., 2009). Additionally, Kug et al. (2009) found that the precipitation, atmospheric vertical circulation, surface zonal wind anomalies are shifted to the west in a CP El Niño compared to an EP El Niño. Furthermore, the zonal scales of the circulations tend to be smaller for CP El Niños. According to Kug et al. (2009), the CP El Niño has stronger atmospheric response to the same level of SST anomaly and thus may indicate stronger

¹eastern Pacific

²western Pacific

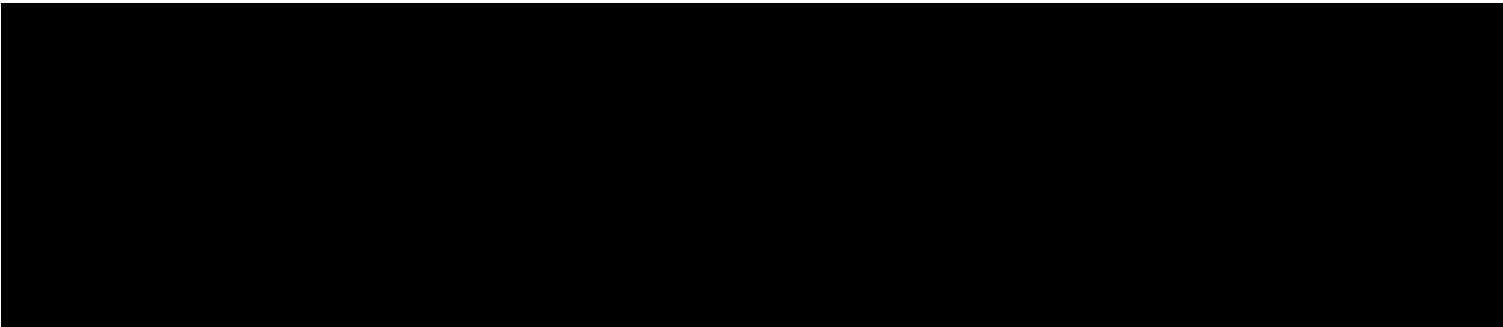


Fig. 1.13 Location and structure of SST anomalies of EP El Niño and CP El Niño in ERA–Interim. See Section 2.1 for details on ERA–Interim. The figure is taken from Hu et al. (2016)

teleconnections in general. However, the actual situation with each specific teleconnection is complex and cannot be so easily generalised. For example, the teleconnection to the high latitude southern hemisphere (in particular, the ASR) response to eastern Pacific SSTs is significantly more than western Pacific SSTs, see Li et al. (2015b)³. Moreover, Sun et al. (2013) has found that EP El Niño excites the Pacific–South–America (PSA) pattern differently compared to the CP El Niño and the SLP anomalies in the high latitude southern hemisphere are more evident in EP El Niño compared to CP El Niño. Additionally, Ashok et al. (2007) found that some teleconnections over areas such as Japan, New Zealand, western coast of United States may have the opposite impact to convective (EP) El Niño.

In conclusion, the two different El Niño types have significant differences between their locations and structures. This leads to differences in the surface variables and teleconnections associated with El Niño. However, it is difficult to estimate the differences in the ENSO–ASR teleconnection without further analysis. Note that in reality, there is not a clear cut between the EP and CP El Niño. Rather, there is a spectrum of El Niños with most being hybrids between EP and CP.

1.2.4 Global teleconnection impacts

ENSO events have both global climatological and socio–economic implications. The ENSO cycle is the strongest inter–annual signal in the coupled ocean–atmosphere system thus leading to its global climate implications (Sun et al., 2013). The following presents some examples of the teleconnections globally.

There are regions in the world that have significant climate responses arising from El Niño or La Niña events, see Figure 1.14. These global teleconnections often involve local changes in precipitation, temperature and surface pressure. For example, during strong El

³Note that this study contained a cooling in the EP but a heating in the CP. Furthermore, the cooling has a different magnitude compared to the heating. Moreover, the imposed SSTs are not El Niños but rather general temperature changes trends. Therefore, this is not a ‘clean’ comparison.

Niño events, there are typically droughts in India (Loveday, 1985; Rasmusson and Carpenter, 1983; Whetton and Rutherford, 1994), Indonesia (Amien et al., 1996; Harger, 1995; Naylor et al., 2001), southern Africa and Australia (Ahrens, 2009) while there are heavy rains and flooding in Ecuador and Peru (Ahrens, 2009). Storm tracks are also moved: storms are directed into California and there is heavy rain in the Gulf Coast states (Ahrens, 2009). These changes often are not only important climatologically but also social–economically. El Niño events has known to cause famines in India (Loveday, 1985), Indonesia (Amien et al., 1996; Harger, 1995; Naylor et al., 2001), south America (Ropelewski and Halpert, 1987) and cause crop production changes in Sri Lanka (Zubair, 2002) and China (Ropelewski and Halpert, 1987).

Note that the topic of El Niño teleconnections is extremely vast and this is only meant to be a brief overview of the global teleconnections and their impacts on society.

Summary

Section 1.2 has summarised previous literature on the El Niño Southern Oscillation. In particular, there are several crucial points to note. Firstly, El Niño Southern Oscillation (ENSO) refers to the quasi periodic cycle of SST anomalies across the tropical Pacific. There are three possible states of ENSO: El Niño, neutral and La Niña. ENSO events tend to peak in austral summer. Secondly, there are multiple ENSO indices that are commonly used



Fig. 1.14 Map of the commonly known global teleconnections found during El Niño and La Niña in summer and winter. Figure taken from <https://www.pmel.noaa.gov/elnino/impacts-of-el-nino>

including the Niño3.4 temperature, Oceanic Niño index and the Southern Oscillation index. Thirdly, ENSO can be separated in the eastern Pacific El Niños and the central Pacific El Niños. These have different structures, tropical variables and teleconnections. Lastly, ENSO events have strong climatological and social–economical impacts globally. The next section moves on to the circulation of the atmosphere.

1.3 Circulation of the atmosphere

This section presents background information on the circulation of the atmosphere. The general circulation and its seasonality is of particular importance to the ENSO–ASR teleconnection, details will be discussed in Section 1.4 and Chapter 3. Previous works on the intertropical convergence zone and Hadley cell (Section 1.3.1), tropospheric jets (Section 1.3.2) and the circulation in the high latitude southern hemisphere (Section 1.3.3) will be discussed.

1.3.1 The Hadley cell and the ITCZ

In a rotating Earth model, there are three major circulation cells (Ahrens, 2009). These are the Hadley cell, Ferrel cell and the Polar cell. This work on this thesis is mainly associated with the Hadley cell⁴. The Hadley cell exists from the tropics to around 30°. At the equator, the warm moist air rises and forms clouds within deep convective systems. This is the intertropical convergence zone (ITCZ). As the rising air reaches the tropopause, the air moves laterally towards the poles. The air cools as it moves towards the poles. As it reaches approximately 30°, the cool dry air sinks. A portion of the surface air then undergoes a reverse flow towards the equator which, under the influence of the Coriolis force, results in a north-easterly flow in the northern hemisphere. This ‘completes’ the Hadley cell. The Ferrel cell approximately exists between 30° and 60°. It is a thermally indirect cell (Ahrens, 2009). This means that cool air rises and warm air sinks. The weak polar cell is located between 60° and the pole.

The Hadley cell is often visualised by meridional mass flux streamfunction (zonal mean), see Figure 1.15. The positive gradient of mass flux streamfunction indicates movement of mass northwards while the negative gradient indicates southwards movement. The Hadley cell undergoes a continuous seasonal migration (Kang and Lu, 2012) and is stronger in the winter hemisphere (Cook, 2003; Dima and Wallace, 2003).

⁴And the Ferrel cell to a less extent. The polar cell is not of interest to the work in this thesis.

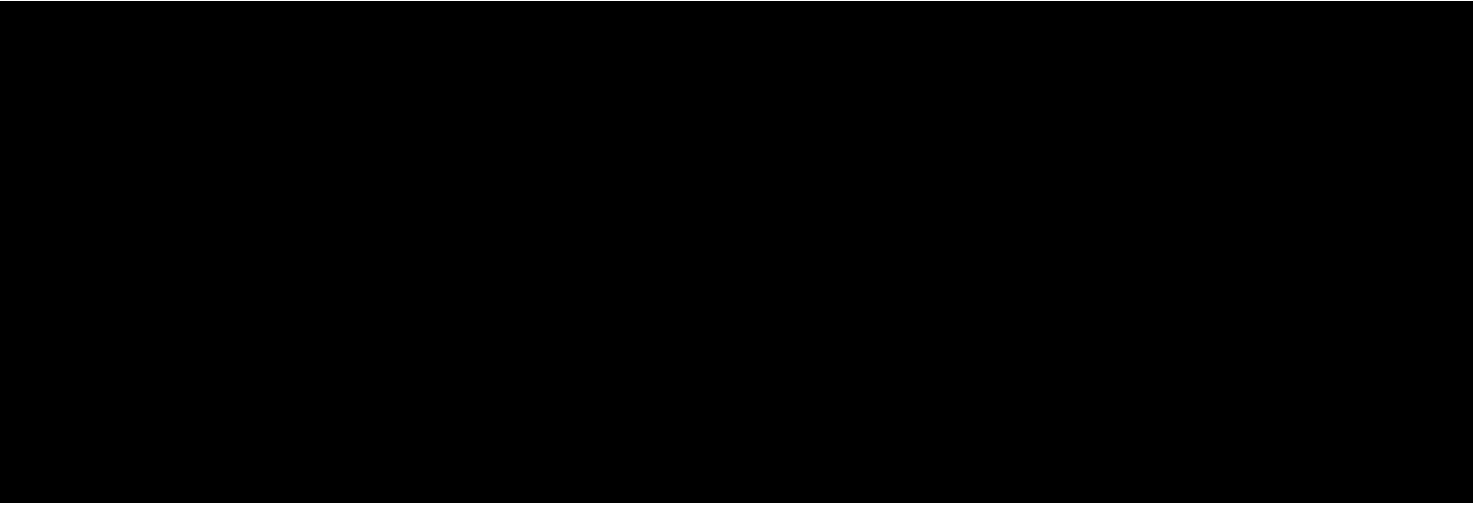


Fig. 1.15 Zonal mass streamfunction and momentum in the atmosphere. Mass streamfunction is in magenta while the angular momentum is in blue. Solid magenta contour shows positive mass streamfunction while dashed contours show negative values. Contour intervals are $20 \times 10^9 \text{ kg s}^{-1}$. Figure taken from Schneider (2006).

The Hadley cell strength is also affected by ENSO events. Oort and Yienger (1996) showed that during El Niño, two strengthened direct Hadley cells were superimposed on top of the winter Hadley cell. Conversely, in La Niña, two weakened direct Hadley cells were superimposed. The difference in Hadley cell strength between El Niño and La Niña is around $3\text{--}4 \times 10^{10} \text{ kg s}^{-1}$. However, the Hadley cells do not change uniformly. During El Niño, the Atlantic and western Pacific Hadley circulation seems to weaken while the eastern Pacific Hadley circulation is strengthened.

Turning to the ITCZ, it is the ascending branch of the Hadley circulation and can be identified as a tropical band of convective clouds. It can also be identified as the maximum in time–mean precipitation (Philander et al., 1996; Schneider et al., 2014). The location and structure of the ITCZ is especially important for the atmosphere. This is because fluxes of heat, moisture, momentum and radiation differ significantly depending whether a region is inside or outside the ITCZ, see again Waliser and Gautier (1993).

The ITCZ usually lies just slightly north of the equator. It migrates towards the seasonally warmer hemisphere and lies approximately between 9°N in boreal summer and 2°N in boreal winter (Schneider et al., 2014). The northern hemisphere tends to be $\sim 1.2\text{--}1.5 \text{ K}$ warmer than the southern hemisphere due to the Atlantic meridional overturning circulation (AMOC) transporting energy northwards (Schneider et al., 2014). The AMOC is a large scale ocean circulation responsible for around one third of the global northward heat transport (Trenberth and Caron, 2001; Zickfeld et al., 2007). This temperature difference explains why the ITCZ is located north of the equator, see Appendix A for details. During El Niño (La Niña), the

ITCZ shifts southwards (northwards). This is because of the strong energy uptake (release) by the ocean (Schneider et al., 2014). The ITCZ can shift up to around 5° under extreme El Niño conditions.

1.3.2 Jets

As will be discussed in Chapter 3, the seasonality of the ENSO–ASR teleconnection is found to be linked to the seasonality of the jets. Therefore, the jets are critical to the work in this thesis. Background information and previous studies on the tropospheric jets are given below.

Tropospheric zonal flow has two dynamically distinct jets: the subtropical jet (STJ) and the polar front jet (PFJ) (also called the mid–latitude jet or eddy–driven jet) (Eichelberger and Hartmann, 2007), see Figure 1.16. The Hadley cells redistribute heat from the equator to 30° , leading to a discontinuity in the temperature of the troposphere close to 30° . This discontinuity generates a thermal wind whose strength is proportional to the temperature difference between the tropical and extra–tropical air (Galvin, 2007). The temperature discontinuity creates the STJ which lies close to the top of the troposphere at the poleward boundary of the Hadley circulation (Eichelberger and Hartmann, 2007), see Figure 1.16 and Figure 1.17. Essentially the STJ is the westerly acceleration created from local vorticity balance due to the poleward moving air in the upper branch of the Hadley circulation (Eichelberger and Hartmann, 2007; Held and Hou, 1980; Woollings et al., 2010). The core of the STJ lies approximately at 200 hPa height (12–15 km) which is approximately 1–4 km below the tropical tropopause. The STJ does not extend far into the stratosphere but can extend far (7 km or more) below the core (Galvin, 2007).

The PFJ is located in the mid–latitudes of both hemispheres (Barnes and Polvani, 2013). The PFJ is caused by momentum and heat forcings arising from the transient mid–latitude eddies (Eichelberger and Hartmann, 2007; Held, 1975; Woollings et al., 2010); it is an eddy driven jet, see again Figure 1.16 and Figure 1.17. While the deviations in the STJ flow are small (it usually remains within 10° of its mean latitude), the PFJ can have large variations in its meridional position (Galvin, 2007). Note that the STJ and the PFJ may be very close together or even indistinguishable spatially from each other at times (Galvin, 2007; Woollings et al., 2010). The PFJ is usually much narrower than the STJ and thus affects less of the atmosphere compared to the STJ, see again Galvin (2007).

Moving on to the seasonality of the jets, both the magnitude and location of the jet streams are affected by season (Gallego et al., 2005; Galvin, 2007; Nakamura and Shimpo, 2004). The STJ and PFJ are stronger in winter and weaker in the summer (Galvin, 2007). This is due to the reduced Hadley circulation and the lower temperature gradient in summer. The following discussion on the southern hemisphere jet streams mainly follows Gallego et al.

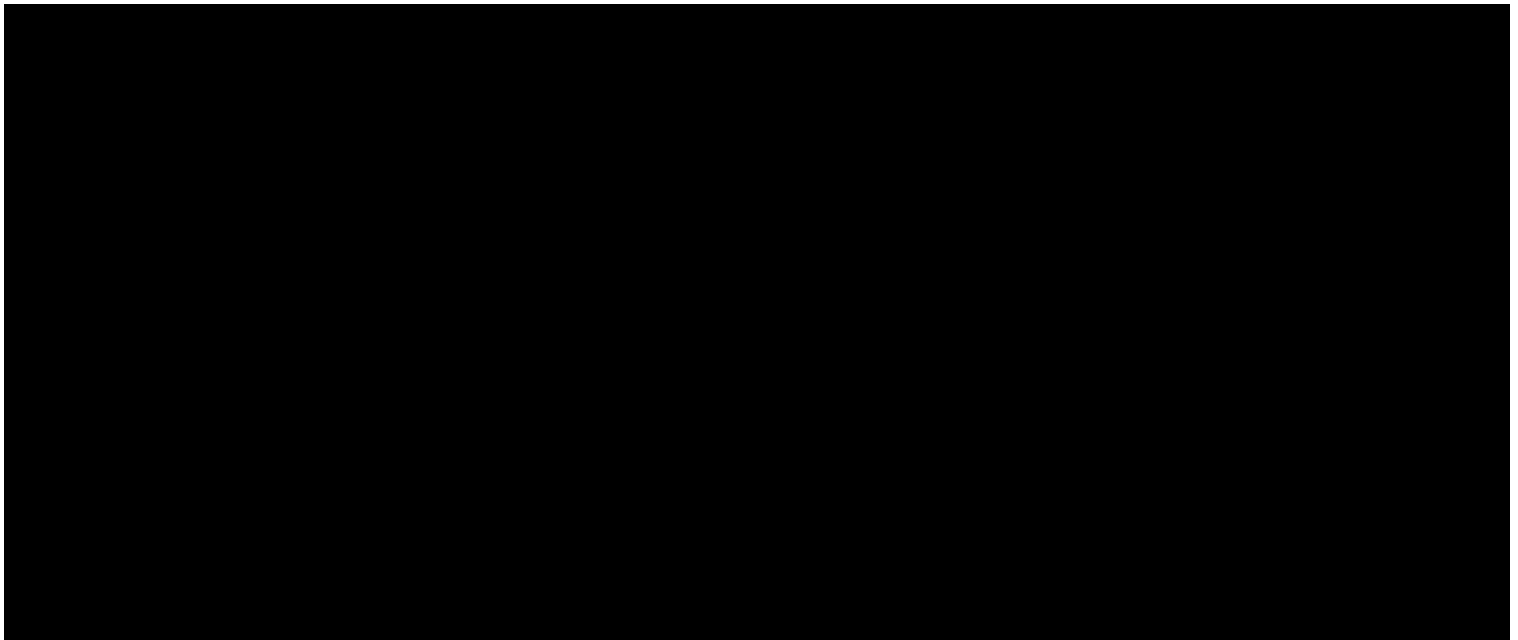


Fig. 1.16 Idealised diagram of the location of the STJ and PFJ and their relations with the circulation cells. The STJ lies on the poleward edge of the Hadley cell ($\sim 30^\circ$) while the PFJ is on the poleward edge of the Ferrel cell ($\sim 60^\circ$). In reality, jets vary with latitude and strength and are not always spatially distinct. Figure taken from Schneider (2006).

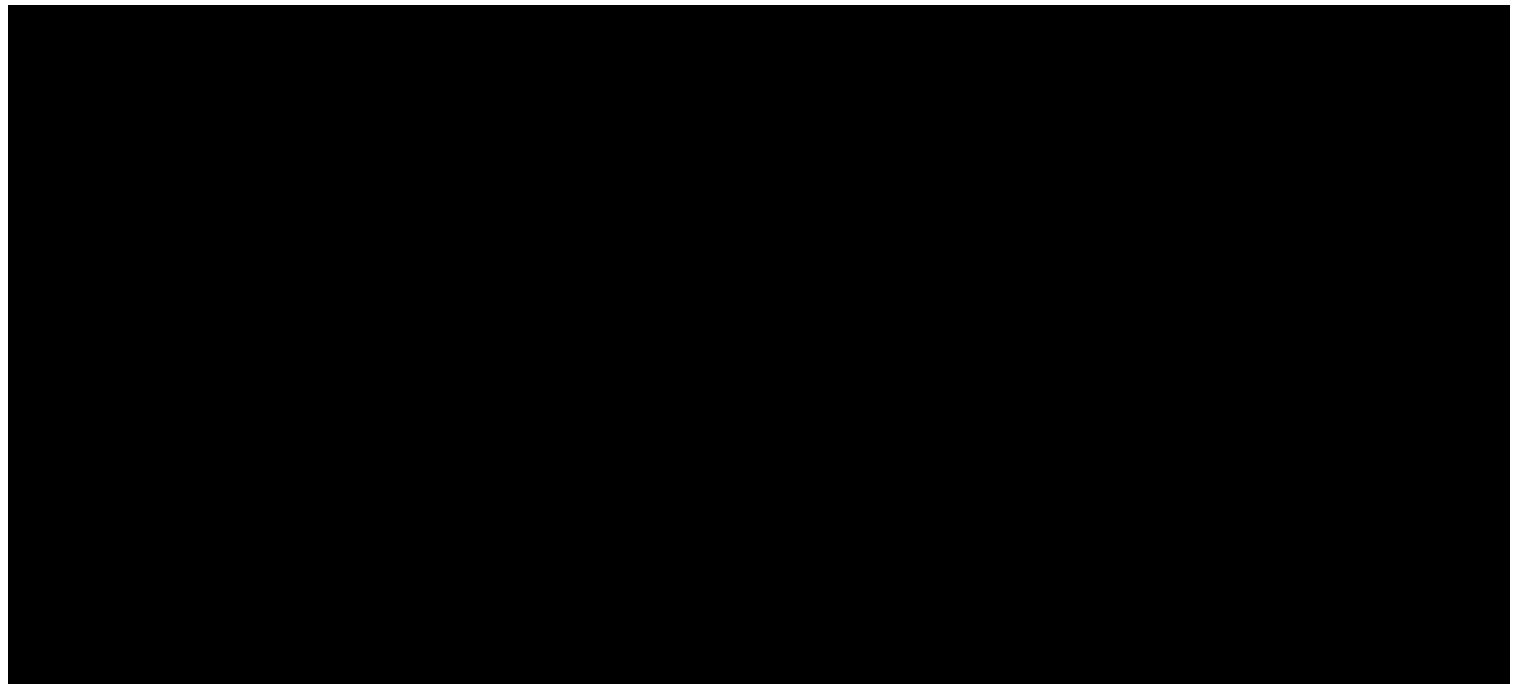


Fig. 1.17 The zonal wind speed with height is shown. The maximum wind speeds (westerly) are the STJ and the PFJ. Both jets lie just below the tropopause and the wind speeds extend far below the core. Figure taken from Schneider (2006).

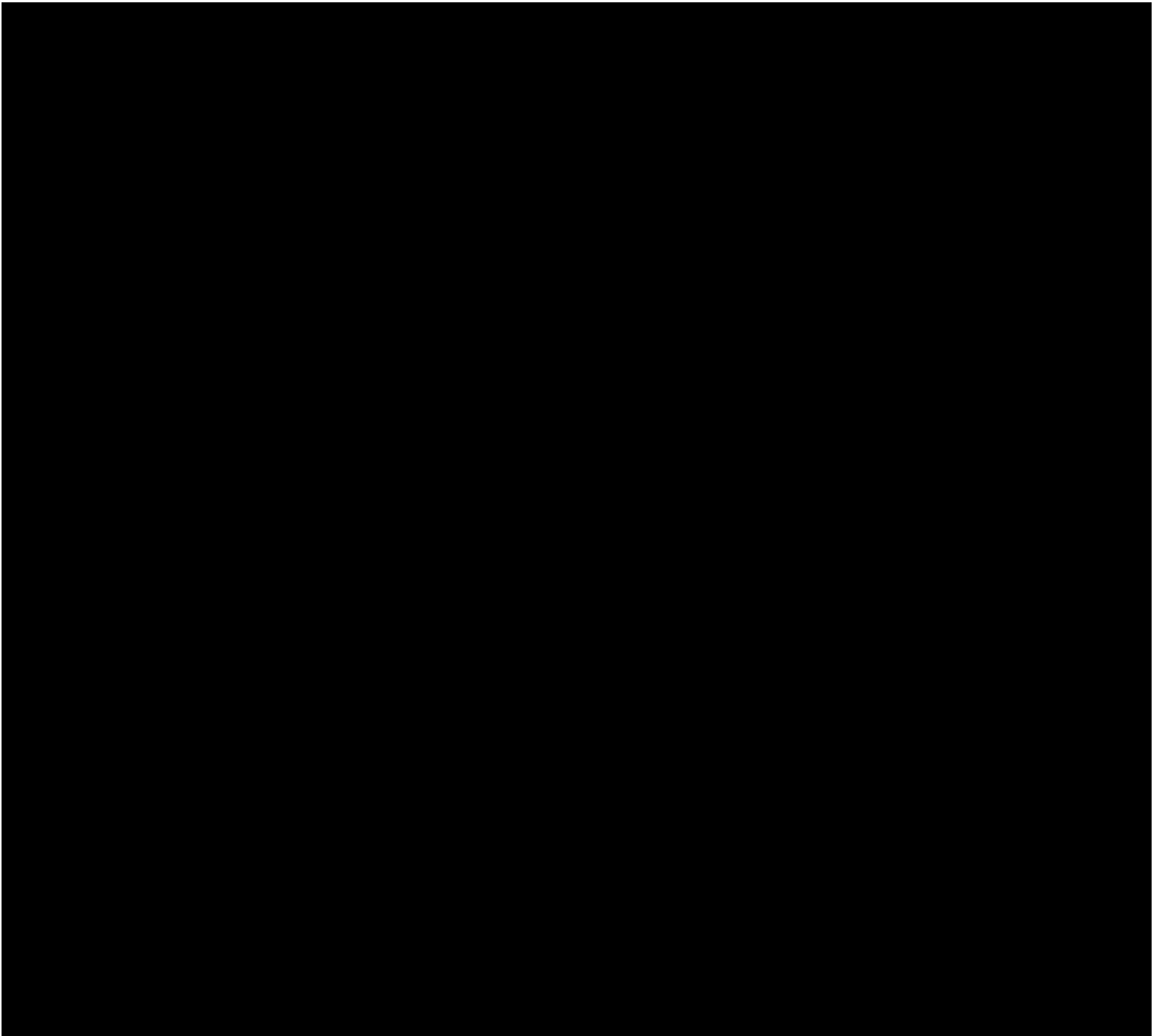


Fig. 1.18 The monthly detection frequency and location of the STJ and PFJ. Black lines show the mean jet centre latitude with the grey shades as the ± 1 standard deviation. The jet is only drawn if the detection frequency is greater than 25%. The detection frequency for each month is shown on top of each figure. Figure taken from Gallego et al. (2005).

(2005). During winter, the STJ maximum velocity is around $50\text{--}60\text{ m s}^{-1}$ in the Pacific sector. The minimum strength of the STJ is found over the Atlantic. They found that the STJ reached detection frequencies above 50% between April and November (approximately austral spring,

winter and autumn) while the frequency is very low during austral summer, see Figure 1.18 and Figure 1.19. The jet frequency is defined as the percentage of years between 1958–2002 where Gallego et al. (2005) detected the presence of the jet (given certain conditions, for details see Gallego et al. (2005)). The PFJ has the opposite phase in seasonality regarding detection frequencies: it is found maximally (98.3% of all days) in February and minimally (53.8% of all days) in June, see again Figure 1.18 and Figure 1.19. It is known as the double jet or dual jet when both jets are present and spatially distinct. Note that the seasonal detection frequency changes are much larger for the STJ compared with the PFJ. The main seasonality of the PFJ is in its latitude (unlike the STJ which has less meridional movement). During January and February (approximately austral summer), the PFJ is located around 40°S while shifting southwards to 55–60°S towards the end of the austral winter. In summary, Gallego et al. (2005) agreed with previous works (such as Bals-Elsholz et al. (2001), Van Heerden and Taljaard (1998), Vincent (1998) and Kidson and Sinclair (1995)) and found that the austral summer was characterized by a single circulation maximum around 35 m s⁻¹ at 42°–45°S. Austral winter was characterized by a dual jet structure with a strong STJ at around 30°S and the higher latitude PFJ. Note that there is a longitudinal structure to the jet: the split jet is most commonly seen in the Pacific (Codron, 2007; Williams et al., 2007).

ENSO events affect different portions of the jets differently. ENSO mainly impacts the STJ in the Pacific sector and, to a lesser extent, the PFJ in the Pacific Ocean (Gallego et al., 2005). The Pacific Ocean STJ location is displaced northwards during El Niño. Furthermore, the STJ speed is up to 50% greater in the Pacific region during El Niño compared with La Niña. During La Niña, the STJ frequency is reduced and has the impact of reducing the average speed of the STJ. The PFJ tends to displace southwards and has a 20% lower speed during El Niño years. Chen et al. (1996) also found similar results for the jet speeds during the 1986–89 ENSO cycle.

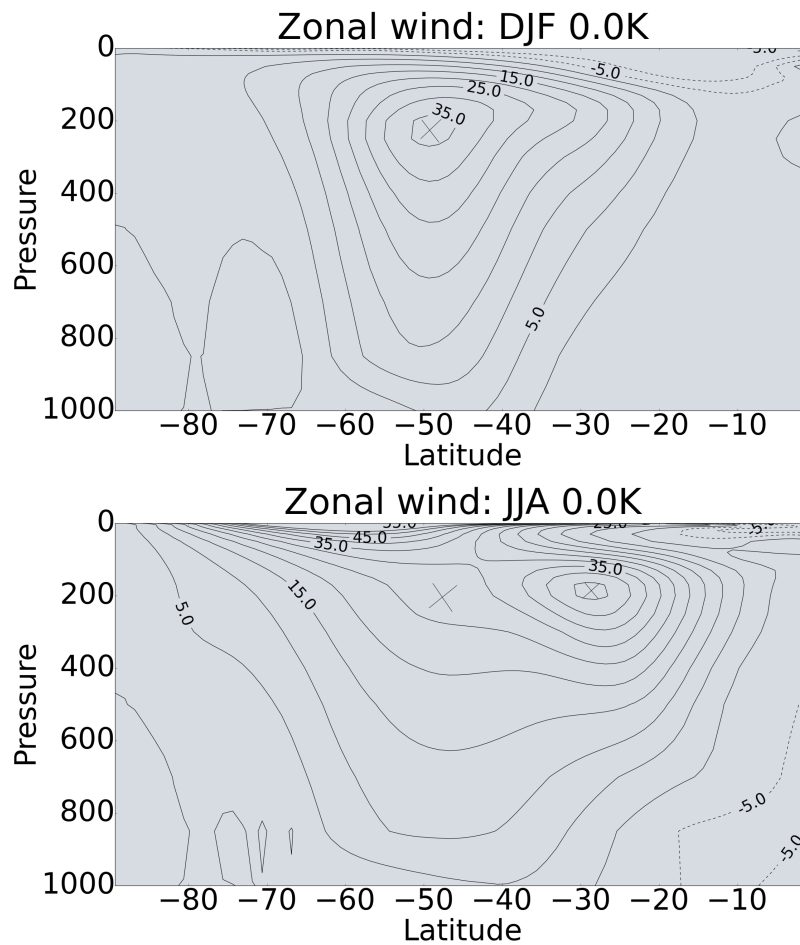


Fig. 1.19 Zonal wind speeds in austral summer (DJF) and austral winter (JJA). There is a split jet (dominant STJ + PFJ) in winter compared to the single jet (PFJ) in summer. The crosses approximately show the core of the jets (maximum local speed). The dataset used is from the baseline timeslice year 2000 SST run, see Section 2.3 for details.

1.3.3 Circulation and patterns in the southern hemisphere

The following will present background material on the circulation and patterns in the southern hemisphere. In particular, the two principal modes of variability in the southern hemisphere will be discussed. These are the southern annular mode and the Pacific–South America pattern. These patterns turn out to be key for the ENSO–ASR teleconnection. Varying seasons showing different structures in anomalies which map onto these modes of variability. Further details will be given in Chapter 3.

Southern annular mode

The southern annular mode (SAM) is the principal mode of large scale atmospheric variability in the southern hemisphere extra-tropics and high latitudes (Abram et al., 2014; Marshall, 2003; Thompson et al., 2011). It has also been called the Antarctic Oscillation (Gong and Wang, 1999) and the high latitude mode (Rogers and van Loon, 1982) and is often diagnosed as the leading empirical orthogonal function (EOF) of the SLP or low level geopotential height. Limpasuvan and Hartmann (1999) found that the SAM explained 36% of the total variance in the southern hemisphere. It is a zonally symmetric annular structure with a zonal wavenumber three pattern superimposed (Marshall, 2003; Trenberth et al., 2007), see Figure 1.20 top panel. The SAM is associated with meridional excursions of the PFJ (Hartmann and Lo, 1998; Lorenz and Hartmann, 2001; Thompson and Wallace, 2000; Yang and Chang, 2007). The SAM is characterised by synchronous pressure or geopotential height anomalies of opposite signs in the mid-latitudes and high latitudes (Hartmann and Lo, 1998; Limpasuvan and Hartmann, 1999; Thompson and Wallace, 1998; Trenberth et al., 2007). During positive SAM, the mid latitude westerly wind maximum shifts towards the high latitudes and the meridional pressure gradient increases and vice versa. The SAM impacts locations over the mid and high latitudes of the southern hemisphere including New Zealand (Kidston et al., 2009), Australia (Ho et al., 2012), southern south America (Silvestri and Vera, 2003) and Antarctica (Genthon et al., 2003; Kwok and Comiso, 2002; Marshall et al., 2006).

Figure 1.21 shows the first, second and third EOFs calculated for the 500hPa geopotential height (following studies such as Thompson and Solomon (2002a)) using monthly averaged data south of 20°S. The SAM shows as a pressure difference between the high latitudes and the mid latitudes in the southern hemisphere. The superimposed wavenumber 3 is much weaker compared to ERA-interim. In this thesis, the SAM will be treated as this general zonally symmetric pressure differential between the high and mid latitudes in the southern hemisphere⁵. Many studies (Gong and Wang, 1999; Ho et al., 2012; Marshall, 2003) who uses the Antarctic oscillation index assume this general zonal structure. The Antarctic oscillation index is commonly used as an index for the SAM. The index is given as the normalized zonally meaned SLP of 40°S minus 65°S for each month (Gong and Wang, 1999). Unsurprisingly, the Antarctic oscillation index shows high correlation with the first EOF (Gong and Wang, 1999). Brief remarks on the seasonality of the SAM can be found in Appendix C.

El Niño Southern Oscillation events have strong impacts on the southern annular mode (SAM). L'Heureux and Thompson (2006) found that variations in ENSO are strongly corre-

⁵The SAM is *defined* as the first EOF of low level geopotential height.

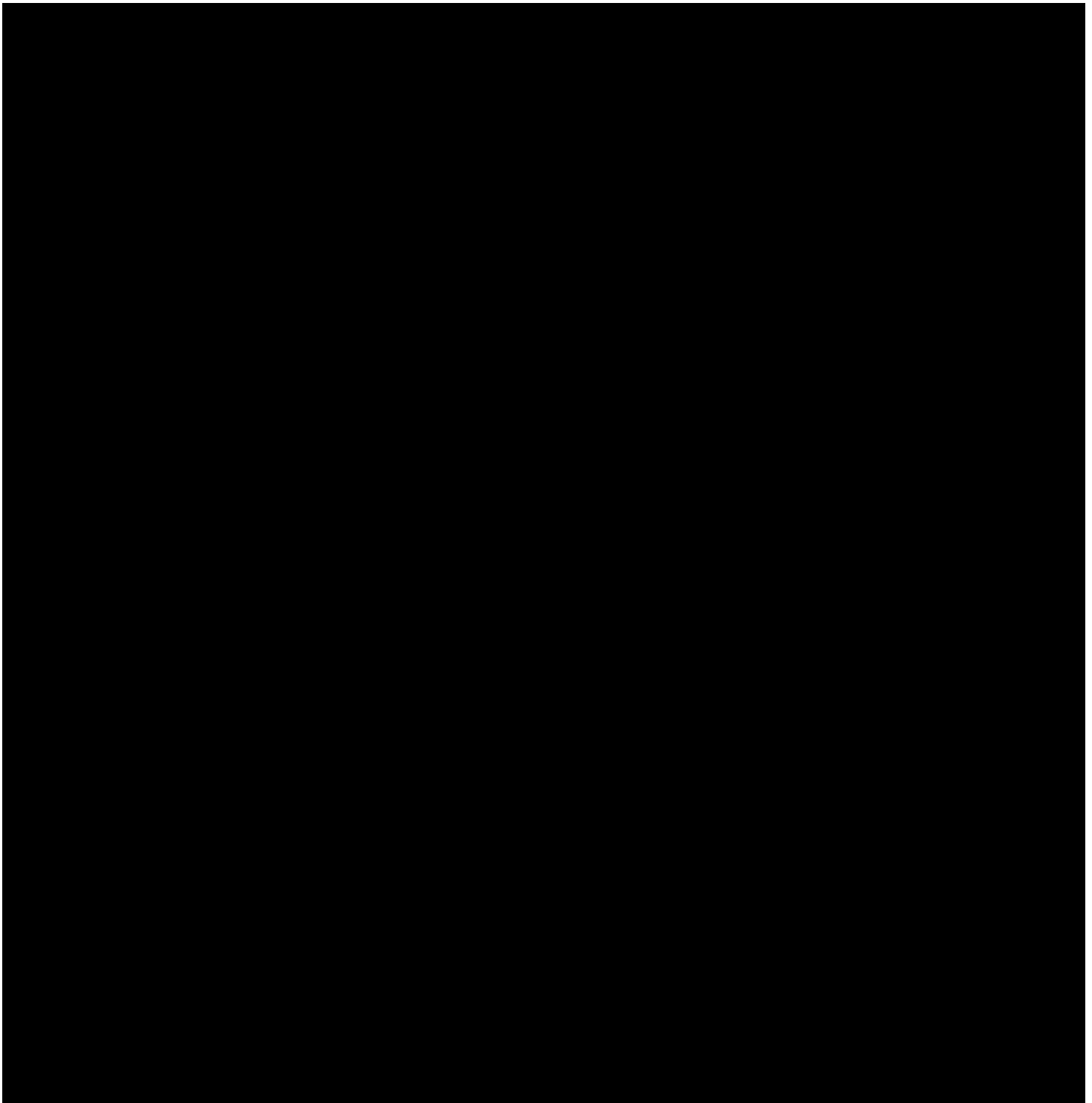


Fig. 1.20 Examples of EOFs for the 500 hPa seasonal mean height anomalies. Data was from ECMWF reanalysis. Top panel shows the EOF1 pattern (SAM). Middle panel shows the EOF2 pattern (PSA1). Bottom panel shows the EOF3 pattern (PSA2). Note that these are examples of EOFs, exact EOF structures may not always match this schematic. Figure taken from Mo (2000).

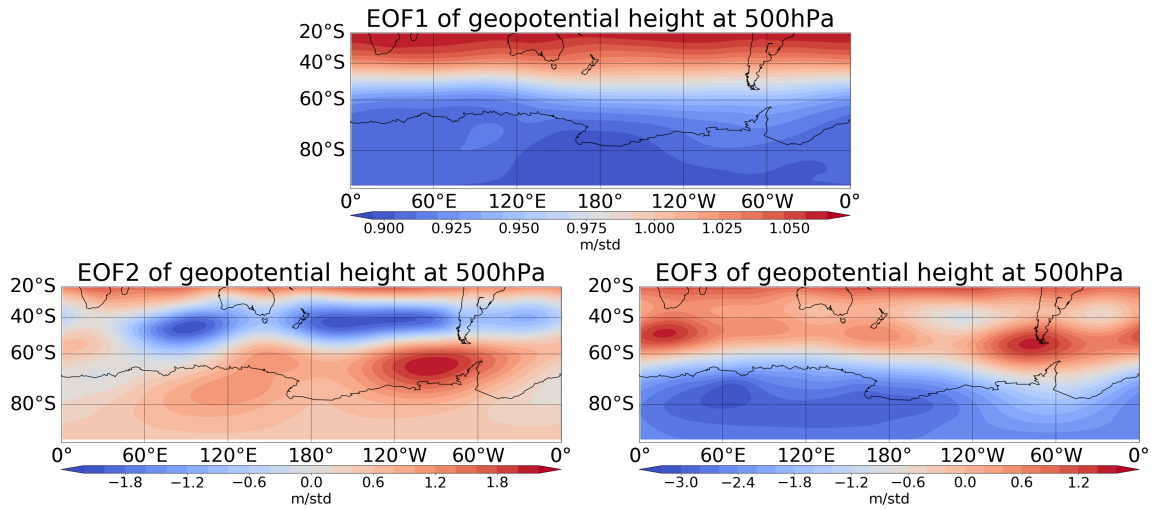


Fig. 1.21 First, second and third EOF in HadGEM3 (the model used for the experiments in this thesis) using the 500 hPa seasonal mean height anomalies. Units are in metres per standard deviation in the principal component time series.

lated with the SAM. They found that during austral summer, around 25% of the year-to-year variability of SAM is linearly related to ENSO. Fogt and Bromwich (2006) found that the SAM is only connected to ENSO during the austral spring and summer when ENSO is the strongest. They also suggested that the SAM is positively correlated with the SOI during these times.

Turning to the Amundsen sea low, Turner et al. (2013) also investigated the impact of SAM on the ASL. They found that the average ASL central pressure anomaly was negative, (-2.87 ± 8.7) hPa, when the SAM was positive and the ASL was positive, (3.43 ± 10.5) hPa, when the SAM is negative. The meridional location of the ASL also seems to be strongly influenced by the SAM. During positive SAM years, the ASL mean annual position is anomalously southwards, while the position was anomalous northward, during negative SAM conditions.

Pacific–South American pattern

While the SAM is the EOF1, the Pacific–South America pattern (PSA) can be seen as the second (EOF2) and third (EOF3) EOFs. They are two wavenumber 3 patterns in quadrature and appear as wave trains of alternating positive and negative geopotential height anomalies between the tropics and high latitudes (Fogt et al., 2011). These wave trains are the Pacific–South American (PSA) patterns, see Figure 1.20. PSA1 (EOF2) is related to SST anomalies over the Central and eastern Pacific and has been identified as the ENSO response in the southern hemisphere (Karoly, 1989b), see Section 1.4 for details. The PSA1 has a wave

train pattern stretching from the central Pacific to Argentina (Mo and Paegle, 2001). PSA2 patterns have a 90° zonal phase difference, see Figure 1.20. Note that these PSA patterns have been associated with polewards propagating Rossby waves (Hoskins and Karoly, 1981).

In this thesis, the focus will be on the PSA1. Therefore, further mention of the PSA in this thesis will only mean the PSA1.

Figure 1.21 also shows the EOF2 (PSA1) and EOF3 (PSA2) for the southern hemisphere (20° – 90° S) 850hPa geopotential height field. The EOF2 shows as a wavetrain of positive–negative–positive geopotential from the Pacific midlatitudes to the Amundsen sea region (ASR). The EOF3 shows a wavetrain that has a approximately phase difference of 90° .

Summary

This section presented background information on the general circulation of the atmosphere. In particular, the focus is on the southern hemisphere. There are several key messages. Firstly, the Hadley cell is a circulation cell that stretches from the equator to 30° . Its ascending branch in the tropics is the intertropical convergence zone (ITCZ). During El Niño, the ITCZ shifts southwards. Secondly, there are two tropospheric jets. These are the subtropical jet (STJ) and the polar front jet (PFJ). During austral winter, the dominant jet is the STJ while the higher latitude PFJ is dominant in austral summer. Thirdly, two main empirical orthogonal functions (EOFs) are identified in the southern hemisphere. These compare to the southern annular mode (SAM) and the Pacific–South–America pattern (PSA), respectively.

1.4 Teleconnections involving the Amundsen Sea Low

El Niño Southern Oscillation signals are associated with many large scale changes in the high latitude southern hemisphere. Some examples include changes to high latitude atmospheric circulation (Ding et al., 2012; Fogt et al., 2011; Karoly, 1989b; L’Heureux and Thompson, 2006), southern Ocean SSTs anomalies (Ciaasto and England, 2011; Ciaasto and Thompson, 2008), precipitation (Bromwich et al., 2000; Cullather et al., 1996), near surface temperature (Bertler et al., 2004; Ding et al., 2011) and Antarctic sea ice (Simpkins et al., 2012; Stammerjohn et al., 2008). It is important to understand the ENSO teleconnection to the southern hemisphere high latitudes.

This section presents background information on teleconnections involving the ASL. In particular, the focus is on ENSO–ASR teleconnections. Previous studies on the basics of the ENSO–ASR teleconnection will be presented in Section 1.4.1. The proposed mechanisms in

previous studies are covered in Section 1.4.2. Finally, Section 1.4.3 will cover some other previous work on Rossby waves and teleconnections.

1.4.1 ASR teleconnections

The teleconnection between ENSO and the ASL is well known (Chen et al., 1996; Hoskins and Karoly, 1981; Lachlan-Cope and Connolley, 2006; Liu et al., 2002; Turner, 2004). According to Turner et al. (2013), both the SAM and ENSO heavily affect climate in the region between the Antarctic Peninsula and the Ross sea and alter the depth and location of the ASL. Turner et al. (2013) investigated this using reanalysis⁶ data for the period 1979–2001 and using European Centre for Medium-Range Weather Forecasts (ECMWF) operational analyses data for 2002–2008. The dataset was separated into El Niño and La Niña conditions based on whether the SST anomaly was greater or less than +0.5 K or –0.5 K. Turner et al. (2013) found that during El Niño, the mean ASL pressure anomaly was positive ($+0.83 \pm 9.94$) hPa on average. Conversely, the pressure anomaly was negative (-2.55 ± 9.40) hPa on average during La Niña. The ASL was also found to be slightly further southeast during El Niño conditions⁷. These findings are mostly consistent with previous studies by Bertler et al. (2004) but in disagreement with Kreutz et al. (2000) who found a deepening of the ASL during El Niño.

Fogt et al. (2011) also investigated the combined effects of ENSO and SAM on west Antarctica. They found that strong teleconnections only occur during (El Niño & SAM–) and (La Niña & SAM+) when the two effects constructively interfere. In the (El Niño & SAM+) and (La Niña & SAM–) cases, the ENSO teleconnections are reduced as the effects destructively interfere.

Moving on to seasonality, Turner et al. (2013) found that the ASL pressure anomaly from ENSO was minimum during austral autumn (0.35 hPa) and maximum during austral winter (3.7 hPa). This is perhaps surprising as ENSO tends to peak in austral summer. In a different study, Jin and Kirtman (2009) found that the southern hemisphere ENSO response tends to lead ENSO by approximately two months (i.e. peak in SON). Moreover, the ASR temperature correlation with tropical ENSO indices was found to be highest in austral winter and autumn and lowest (or even reversed) in austral spring and summer (Bertler et al., 2004).

⁶ERA-40

⁷Although these results were not statistically significant.

1.4.2 Mechanisms of ENSO–southern hemisphere teleconnection

There are several proposed mechanisms regarding ENSO teleconnections to southern high latitudes (including the ASR). One such mechanism is teleconnection via the PSA. Schneider et al. (2011) showed that the first PSA pattern can be seen directly through regressions of southern hemisphere atmospheric circulation on tropical ENSO indices. They argued that PSA1 can be interpreted as an Rossby wave train propagating from the tropics to the high latitudes (Karoly, 1989b). Furthermore, Li et al. (2015a) showed that changes in the tropical eastern Pacific SSTs can cause circulation changes which will in turn create a Rossby wave source (RWS) anomaly. The RWS can be understood as an divergence in the wave flux (for details on wave flux, see Plumb (1985)). The Rossby waves then propagate towards the high latitude southern hemisphere. There is a seasonality associated with the PSA: it is strongest in austral spring (Jin and Kirtman, 2009; Schneider et al., 2011). Jin and Kirtman (2009) argued that this was because the RWS is strongest one season before (after) the peak of the ENSO in the southern (northern) hemisphere, due to anomalous divergence/convergence that was dependent on local seasonality.

Another proposed teleconnection mechanism is the projection of ENSO variability onto the SAM (Fogt and Bromwich, 2006; Fogt et al., 2011; L’Heureux and Thompson, 2006; Schneider et al., 2011), see Section 1.3.3. According to Schneider et al. (2011), there is also a distinct seasonality for this mechanism: it is strongest in austral summer. The reasons for this have not been fully explored but could be due to the increased amplitude of ENSO tropical heating during austral summer (L’Heureux and Thompson, 2006). However, it could also be due to seasonal characteristics of the large–scale hemispheric circulation (Jin and Kirtman, 2009; Schneider et al., 2011).

Liu et al. (2002), Chen et al. (1996) and Yuan (2004) suggested a teleconnection mechanism in terms of the Hadley and Ferrel cells. The El Niño would intensify the Hadley cell which increases the speed of the subtropical jet (STJ). The STJ will then also move equatorwards. This will in turn alter the Ferrel circulation which results in an increased frequency of storm tracks moving equatorwards. This reduces the number of synoptic and subsynoptic low pressure systems that pass through the ASR, which therefore leads to the ASL weakening under El Niño conditions.

1.4.3 Rossby waves and teleconnections

Rossby waves

Rossby waves are crucial to much of the work in this thesis. In particular, various Rossby wave techniques such as the computation of Rossby wave sources (RWS) and Rossby wave

ray tracing are used in this thesis. The following paragraphs aim to provide a brief overview on Rossby waves.

Key research on atmospheric Rossby waves can be traced back to a series of papers written by Rossby (Rossby, 1939a,b, 1945). His original aim was to ‘interpret, from a single point of view, several at first sight independent phenomena’ (Rossby, 1939b). Examples of these phenomena included understanding eddies (that seemed very stationary) in the monthly (and daily) isentropic charts over the United States of America over boreal summer; various larger dimensions low and high pressure systems (e.g. Icelandic and Aleutian lows; Asiatic and Pacific highs) that appear in weather maps over the northern hemisphere after performing weakly averages; low pressure troughs that seem stationary over the USA in five day mean pressure and isentropic charts in the upper troposphere (Rossby, 1939b). These phenomena all turned out to be related to atmospheric Rossby waves.

Practically all forms of wave motion in the atmosphere and ocean are dispersive (Rossby, 1945) meaning that the phase velocity differs from the group velocity. One such type of dispersive wave are atmospheric Rossby waves. Rossby waves exist due to the latitudinal variation of the vertical component of the Earth’s vorticity (Dickinson, 1978). In essence, Rossby waves are inertial waves that exists due to the Earth’s rotation (Coriolis restoring force). As a parcel of air moves towards the equator (poles), it will deviate towards the west (east) due to the Coriolis force. However, potential vorticity (PV) must be conserved in an atmosphere with no diabatic heating or friction. Potential vorticity is defined as

$$\text{PV} = \frac{\zeta \cdot \nabla \theta}{\rho}, \quad (1.1)$$

where ζ is the absolute vorticity, ρ is the density of the air parcel and

$$\theta = T \left(\frac{p_0}{p} \right)^{\frac{R}{c_p}}, \quad (1.2)$$

where θ is the potential temperature, p is the pressure of the air parcel, p_0 is the standard reference pressure (usually taken as surface pressure), R is the gas constant of air (approximately $8.31 \text{ J K}^{-1} \text{ mol}^{-1}$) and c_p is the specific heat capacity of air. One of the unique property of PV is that it must be conserved when there is no diabatic heating or friction in the atmosphere. Therefore, as the absolute vorticity is

$$\zeta = \zeta_r + f, \quad (1.3)$$

where ζ_r is the relative vorticity and f is the planetary vorticity. The relative vorticity must change when an air parcel moves in latitude to conserve PV. The conservation of the absolute vorticity as parcels of air move northwards or southwards is in essence the Rossby wave.

By neglecting divergence and nonlinear effects while considering an incompressible and homogeneous atmosphere on a plane Earth with horizontal motion only, Rossby (1939b) arrived at the Rossby wave formula

$$c = U - \frac{\beta L_x^2}{4\pi^2}, \quad \text{or} \quad c = U - \frac{\beta}{k^2}, \quad (1.4)$$

where c is the phase speed of the wave in the x direction, U is the zonal wind, β is the meridional gradient of the Coriolis parameter⁸, L_x is the wavelength in the x direction and k is the zonal wavenumber. Equation (1.4) contains several essential consequences. Firstly, it provides a relationship between U and β for stationary waves ($c = 0$). Secondly, as $\beta L_x^2/(4\pi^2)$ is always positive (there cannot be negative wavelengths), $U - c$ is always positive. This means that crests and troughs always moves westwards with respect to the background flow.

Rossby waves are not only limited to the x direction. More generally, equation (1.4) can be written as (Andrews, 2010)

$$c = U - \frac{\beta}{k^2 + l^2 + f_0^2 m^2 / N_b^2}, \quad (1.5)$$

where k is the zonal wavenumber, l is the meridional wavenumber, m is the vertical wavenumber, f_0 is the Coriolis parameter and N_b^2 is

$$N_b^2 = -\frac{g}{\rho_0} \frac{d\bar{\rho}}{dz}, \quad (1.6)$$

where g is the gravitational acceleration, ρ_0 is the reference value of background density, $d\bar{\rho}/dz$ is the background density gradient. Given real values of horizontal wavenumbers, real and non zero vertical wavenumber, the following condition arises

$$U - c = \frac{\beta}{k^2 + l^2 + f_0^2 m^2 / N_b^2} < U_c \equiv \frac{\beta}{k^2 + l^2}, \quad (1.7)$$

where U_c is the critical velocity. Therefore, vertical propagation is only possible in stationary waves ($c = 0$) if U is between zero and U_c .

⁸This is a simplification as it assumes vorticity is only dependent on latitude. In this thesis, β^* will be used instead of β . Where β^* is the meridional gradient of absolute vorticity.

Further information on the Rossby wave source (RWS) and Rossby wave ray tracing can be found in Section 2.5.

Teleconnections

In the following paragraphs, recent works on the Atlantic–ASR teleconnection will be presented. Li et al. (2015a) studied the effects of warming SSTs in the tropical Atlantic during recent decades on west Antarctica. They mainly investigated the Rossby wave bridge between these locations to explain the Atlantic–west Antarctic teleconnection. Li et al. (2015a) imposed a idealized heating perturbation over the tropical Atlantic in different seasons to compute the Rossby wave responses. The focus of their methodology is to treat the generation and propagation of the Rossby waves separately. This is because any physical phenomena linking two geographically distinct locations must have both a source term and a propagation term. If either term is missing, the teleconnection will not exist.

The RWS is mainly given by the absolute vorticity and divergence of the winds (Li et al., 2015a; Sardeshmukh and Hoskins, 1987). Further details of the RWS will be given in Section 2.5. Li et al. (2015a) calculated the anomalous RWS in the different seasons. They found that it is stronger in June–July–August (JJA) compared to December–January–February (DJF). Furthermore, the RWS in DJF does not penetrate as far polewards and appears more localised compared to JJA. This seasonal variance arises from the differences in the climatological flow between DJF and JJA rather than the differences in the vorticity and divergences generated by the heating itself (Li et al., 2015a).

Turning to the Rossby wave propagation, a commonly used (Hoskins and Karoly, 1981; Karoly and Hoskins, 1982; Li et al., 2015a,b; Scaife et al., 2017) method is Rossby wave ray tracing developed by Hoskins and Karoly (1981) and Karoly and Hoskins (1982). This method allows visualisation of the path taken by the stationary Rossby wave train. The rays are set off at the peak of the RWS and are allowed to propagate southwards. At any point in the propagation, the rays can either propagate (in various directions), reflect or terminate. Further details on the Rossby wave ray tracing can be found in Section 2.5.

Li et al. (2015a) applied ray tracing analysis and found that the Rossby waves could not propagate to the high latitude southern hemisphere in December–January–February (DJF) while they could do so in March–April–May (MAM), June–July–August (JJA) and September–October–November (SON) (even though the propagation seems maximal in JJA), see Figure 1.22. The rays in DJF are reflected before reaching the high latitudes. Note that Li et al. (2015a) cautioned against interpreting the literal path of the waves from the ray tracing due to the fine scale structure in the ‘waveguide’ which stretches the WKBJ assumption.

Additionally, Simpkins et al. (2014) have also done research on the role of Atlantic SST trends on the extratropical southern hemisphere and have created a schematic diagram outlining the mechanism of the teleconnection of the tropical Atlantic SST to the high latitude southern hemisphere, see Figure 1.23. This diagram shows the process of the teleconnection from the tropics to the high latitude southern hemisphere. One of the scientific aims of Chapter 3 is to create a similar diagram for the Pacific ENSO teleconnection to the ASL.

Turning to the Pacific and other oceans, Li et al. (2015b) performed a follow up study expanding the scope of the works of Li et al. (2015a). Li et al. (2015b) investigates the effects of SST anomalies (due to climate change) in the tropical Oceans on western Antarctica in austral winter. These included the tropical Atlantic, the tropical west Pacific, the tropical east Pacific⁹, the tropical west Indian Ocean and the tropical east Indian Ocean. Li et al. (2015a) found that the RWS over the Atlantic and eastern Pacific is weak while the RWS over the Indian and western Pacific Oceans is strong.

As discussed before, strong RWS anomalies alone does not necessarily mean strong teleconnections. In order to get the complete picture, the Rossby wave ray tracing should be taken into account. Figure 1.24 shows the Rossby wave ray tracing from the five different oceans. As seen before in Li et al. (2015a), in the tropical Atlantic, the Rossby waves propagates towards the high latitude southern hemisphere via the waveguide formed by the subtropical and polar front jet. In contrast to the Atlantic Ocean, the other basins are weakened by the STJ (Li et al., 2015b). This is especially true in the Indian Ocean basins where some of the trajectories are reflected back towards the Equator. The trajectories north of the subtropical jet are reflected while the trajectories south of the STJ reaches the

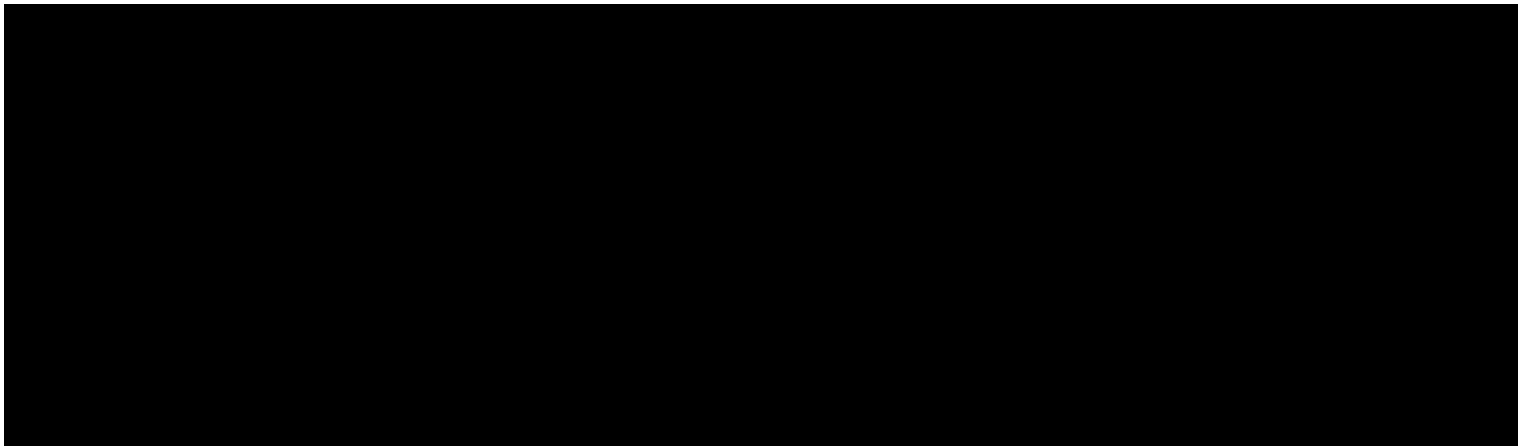


Fig. 1.22 Rossby wave ray tracing in different seasons starting from the southern Atlantic for zonal wavenumber $k = 3$. The ray tracing is performed with background states of every five year period from 1979 to 2012. The background shading indicates the zonal wind which is crucial for the wave tracing. Figure taken from Li et al. (2015a).

⁹Unlike the other ocean basins, a cooling is imposed in the eastern Pacific.

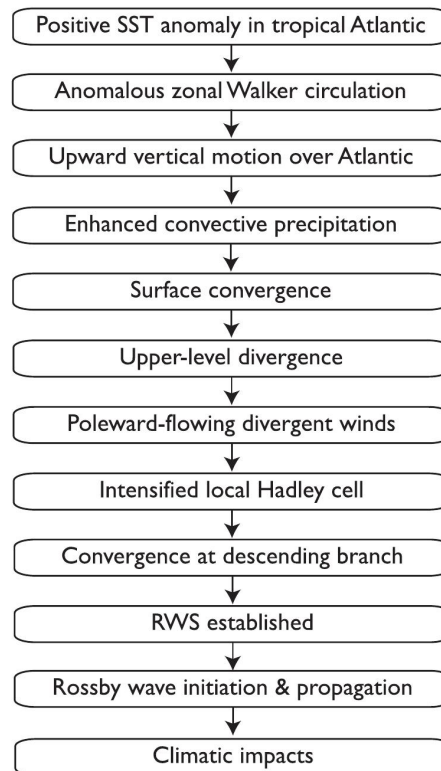


Fig. 1.23 Atlantic–high latitude teleconnection mechanistic flowchart. Figure taken from Simpkins et al. (2014).

high latitude southern hemisphere. The propagation of Rossby waves in the western Pacific shows a more complicated behaviour: all the trajectories are reflected back towards the tropics. This is because the zonal wind shear is too high between the subtropical and subpolar jet which creates a reflection zone (like a double-sided mirror) just below Australia, see Figure 1.25. In contrast, the eastern Pacific does not see this strong reflection zone and thus most of the waves pass through to western Antarctica, see again Li et al. (2015b). In conclusion, they found that SSTs anomalies (austral winter) in the tropical Atlantic, Indian and eastern Pacific created a weaker low pressure system off the western Antarctic coast while the western Pacific warming (austral winter) induced an increase in pressure on the Ross sea, see Figure 1.26. These conclusions seem to agree well those of with Ding et al. (2011).

However, it is important to note the difference between the aims of Li et al. (2015a,b) and the scientific aims of this project. As it is not the intent of Li et al. (2015a,b) to investigate El Niño in general, their experiment contains positive SSTs in the western Pacific, Atlantic and the Indian Ocean but contains negative SSTs in the eastern Pacific. While it is possible to assume that positive SSTs (El Niños) will create the opposite effect (i.e. positive pressure



Fig. 1.24 Rossby wave ray tracing from each of the different ocean sectors for wavenumber $k=3$. The ray tracing is performed with background states of every five year period from 1979 to 2012. The background shading indicates the zonal wind which is crucial for the wave tracing. Figure taken from Li et al. (2015b).

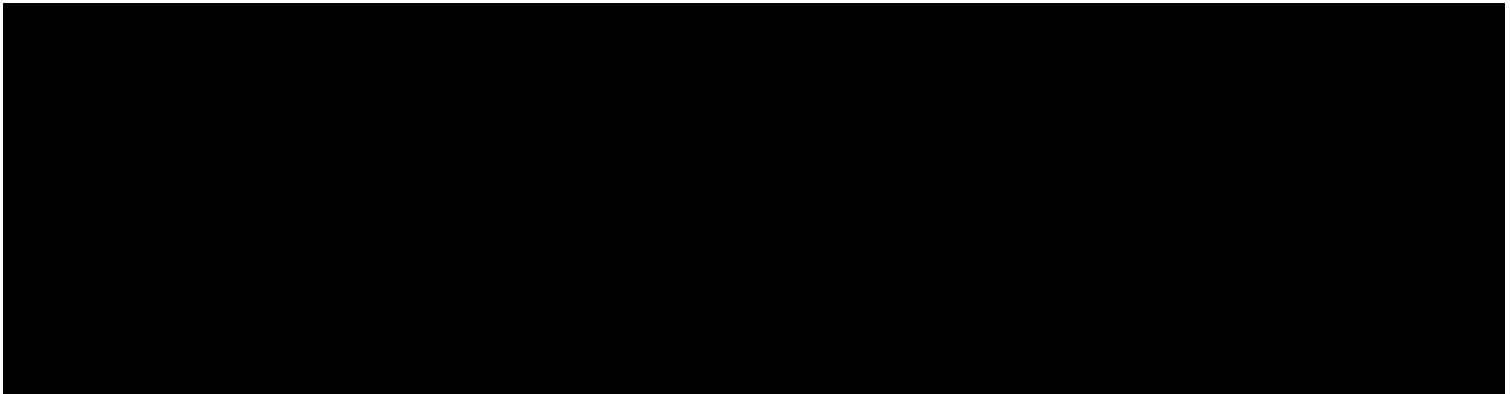


Fig. 1.25 Total Rossby wave number is shown. The units are in m^{-1} . The white areas are regions of the reflection zones while the grey areas are the termination zones. Figure taken from Li et al. (2015b).

off the western Antarctic coast, including the ASR), neither the structure nor magnitudes will necessarily be simply reversed. As discussed before, there are significant differences in magnitudes of the ENSO–ASR teleconnection between El Niño and La Niña, see Fogt et al. (2011) for details and the imposed SSTs are not structurally similar to El Niños or La Niñas. Furthermore, the SST magnitudes are different between the Ocean sectors. Therefore, caution must be exercised when applying these results to ENSO–ASR teleconnections.

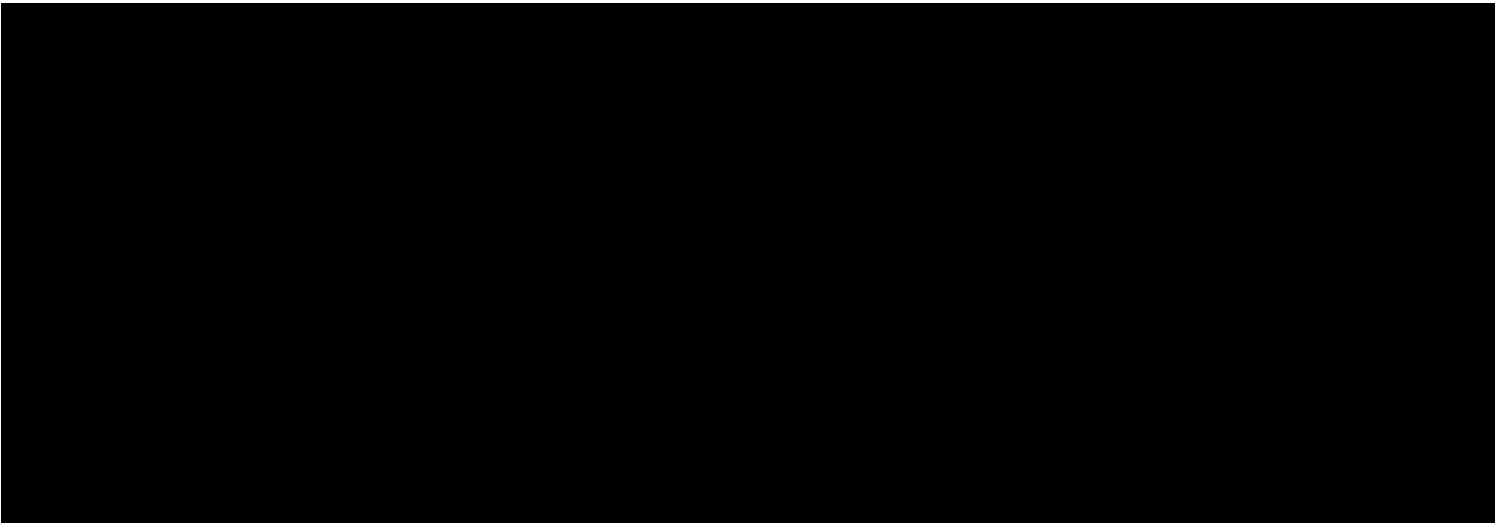


Fig. 1.26 Simulated sea level pressure response to the four tropical SST anomalies. Units are in hPa. Figure taken from Li et al. (2015b).

Summary

Section 1.4 summarised some of the previous studies on the teleconnection to the ASR. There are several key conclusions. Firstly, ENSO generates positive anomalies in the ASR during El Niño and negative anomalies during La Niña. Secondly, there is a clear seasonality associated with the ENSO–ASR teleconnection. It is strong in austral winter and autumn and weak in austral summer and spring¹⁰. Thirdly, there are three proposed mechanisms regarding the ENSO–ASR teleconnection: teleconnection via the PSA, the SAM and the circulation cells. Fourthly, previous studies such as Li et al. (2015a,b) have studied the teleconnection of tropical SSTs to western Antarctica using Rossby wave methods. These analysis methods allow the separation of the source and the propagation. The Rossby wave methods of Hoskins and Ambrizzi (1993); Hoskins and Karoly (1981); Karoly and Hoskins (1982); Sardeshmukh and Hoskins (1987) can be applied to investigate the ENSO–ASR teleconnection and its seasonality. Finally, the exact mechanism of the ENSO–ASR teleconnection and its seasonality is still an open question. This thesis will try to answer these questions.

¹⁰Exact seasonality depends on study.

1.5 Scientific aims

Seasonality of teleconnections

The aim of Chapter 3 is to understand better the seasonality of the ENSO–ASR teleconnection. As seen from Section 1.4, perhaps counter-intuitively, the observed teleconnection appears to be weak in the season when the ENSO is strong (DJF). It is strongest when ENSO events are weaker (JJA, SON). Several methods and experimental designs in Chapter 3 are influenced by the works of Hoskins and Karoly (1981); Li et al. (2015a,b); Simpkins et al. (2014); Turner et al. (2013). Particularly, Rossby wave methods (RWS and ray tracing) will be used to look at the difference in the teleconnection between austral winter and summer. Wave flux methods following Plumb (1985) will also be used in order to gain a deeper understanding of the seasonal difference in the Rossby wave propagation.

The transient nature of the teleconnection will be further explored in Chapter 4. In particular, the focus is on how the reaction timespan changes between various critical variables in the ENSO–ASR teleconnection mechanism.

Linearity of teleconnections

Investigating the linearity of the ENSO teleconnection to the ASL is one of the main scientific aims of Chapter 5. The difference between the teleconnection of El Niño and La Niña has been studied in previous literature, see for example Hoerling et al. (1997) and Turner et al. (2013). Turner et al. (2013) found that the ASL had different response rates to El Niño and La Niña events. Not only is the sign of the response rate opposite (as expected) but the magnitude is also different. However, there are very few studies which have investigated the linearity within different magnitudes of El Niño itself. Many previous studies either quote a single value for El Niño teleconnections (Trenberth, 1997; Turner et al., 2013) or group all El Niño years together without taking magnitude into account (Liu et al., 2002; Turner, 2004). While this is a perfectly valid way of analysis and provides a good general overview for the teleconnection under El Niño conditions, the actual teleconnection under El Niño may not be linear over a wider range of perturbations. As seen in works such as Li et al. (2015a) and Simpkins et al. (2014), the teleconnection is complex and it is unlikely that all the processes are linear.

Resolution and model dependence

The representation of the ENSO–ASR teleconnection may vary depending on the resolution of the model. It is often not practical to use only observations or reanalysis in climate science

as there is often not enough data (ERA–Interim starts in 1979) for investigating regions with large internal variability. Furthermore, it may be difficult to design a specific experiment without model runs. Therefore, it is important to understand whether the teleconnection and its mechanism remains robust under different model resolutions. As the ASL is created from synoptic and sub–synoptic low pressure systems, resolution may change the representation of these low pressure systems. This is because the scales of some key processes may be too small to be simulated properly in coarse climate models. Chapter 6 tackles the representation of the ASL and the ENSO–ASR teleconnection for model configurations with different horizontal resolutions.

Chapter 2

Model, setup and methods

This chapter introduces the model and methods used for the experiments in this thesis. In Section 2.1, details on the existing reanalysis and datasets are presented. These include the ERA–Interim reanalysis and the UPSCALE dataset. Section 2.2 presents a basic description of the model used. The experimental setup is explored in Section 2.3. This presents information on the experiments used in Chapters 3, 4 and 5. Model evaluation is carried out in Section 2.4 where the model simulation of the ENSO–ASR teleconnection is compared with reanalysis data. In particular, critical variables such as the SSTs, zonal wind and SLP are shown. Finally, in Section 2.5, details on the tools employed to analyse Rossby wave methods will be discussed. These include the Rossby wave source (RWS) calculations, Rossby wave ray tracing and the calculation of the wave flux.

2.1 Existing datasets

This section will introduce some of the existing datasets used in this thesis. ERA–interim is mainly used as a proxy for observations while UPSCALE is used to explain the impacts of horizontal resolution on climate simulations.

ERA Interim

ERA–Interim is a global atmospheric reanalysis produced by the European Centre for Medium–Range Weather Forecasts (ECMWF) (Dee et al., 2011). Reanalysis uses data assimilation of historical observations. Typically, it uses a fixed assimilation scheme throughout the historic period. The discussion of the ERA–Interim reanalysis will mainly follow the documentation by Dee et al. (2011). The ERA–Interim project is a new atmospheric reanalysis aimed to replace the outdated ERA–40 reanalysis and covers the period from 1

January 1979 to present day. The spatial resolution of the dataset is approximately 80 km (T255 spectral). The vertical resolution is 60 vertical levels from the surface to 0.1 hPa. The analysis in Chapters 3 and 5 will mainly use seasonal means for ERA–Interim for analysis.

ERA–Interim is used as a proxy for atmospheric observations. Reanalysis can be useful for evaluating models as it is spatially and temporally continuous and has high temporal resolution as opposed to relatively sparse observations, especially in the southern hemisphere. However, it is important to be aware of the limitations of reanalysis datasets in general. They are not observations, but rather are based on observations that have been fed through a model. Therefore, it is important not to treat them as absolute ‘truth’. Furthermore, reanalysis datasets tends to perform worse at locations with fewer observations as there is less information to constrain the model state. An example of this is Antarctica in the pre–satellite era when there were few station and surface observations compared to other regions.

UPSCALE

UPSCALE is short for UK on PRACE: weather–resolving Simulations of Climate for globAL Environmental risk (Mizielinski et al., 2014). It is a project that ran ensembles of HadGEM3 (GA3.0 configuration) atmosphere only global climate simulations at varying resolutions over the period 1985–2011. There are five N96 (130 km) ($1.875^\circ \times 1.25^\circ$) ensembles, three N216 (60 km) ($0.83^\circ \times 0.56^\circ$) ensembles and five N512 (25 km) ($0.35^\circ \times 0.23^\circ$) ensembles. Figure 2.1 shows the landmass resolution for N96, N216 and N512. Mizielinski et al. (2014) chose these resolutions for UPSCALE as, at the time the simulations were performed, these were the common resolutions used for climate modeling (N96), seasonal prediction (N216) and global weather forecasting (N512).

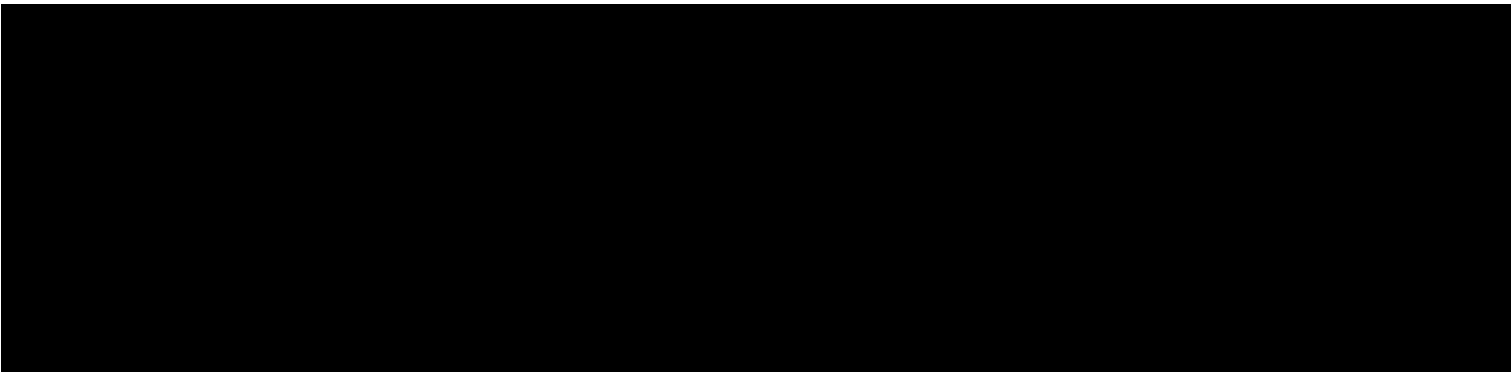


Fig. 2.1 Maps of varying horizontal resolutions. Left panel shows the N96 (130 km) resolution, middle panel shows the N216 (60 km) resolution and right panel shows the N512 (25 km) resolution. Topographical height in metres. Regions with less than 50% landmasses is shown as ocean (blue) colour. Figures taken from <http://proj.badc.rl.ac.uk/upscale>.

UPSCALE is mainly used in this thesis for testing the resolution dependence of the representation of the Amundsen sea low (ASL) and its teleconnection to the tropical Pacific. The role of resolution is important in modeling many different physical and dynamical processes (Demory et al., 2014; Roberts et al., 2009, 2015; Schiemann et al., 2014; Shaffrey et al., 2009). UPSCALE was chosen as the dataset for resolution dependence as their runs attempt to keep as many parameters identical as possible across the different resolutions. This allows the impact of resolution to be investigated cleanly (Mizielinski et al., 2014). For details, see Chapter 6.

2.2 Model description

This section presents information on the Hadley Centre Global Environment Model version 3 (HadGEM3) version of the Unified Model (UM) used in the experimental runs of this thesis. The UM is a numerical model of the atmosphere used for both weather and climate research. Different configurations of the UM can be used to make weather forecasts for the coming days up to climate projections over the next centuries. The version used in these experiments was the UM version 8.4 (HadGEM3) at N96 horizontal resolution and with 85 vertical levels up to an altitude of ~ 85 km (UM8.4 N96L85) Global Atmosphere (GA) 4.0. N96 corresponds to a global latitude–longitude grid of 144 by 192 points ($1.875^\circ \times 1.25^\circ$) (Mizielinski et al., 2014). The model is run here in an atmosphere–only configuration with prescribed observed SSTs and sea ice from the HadISST dataset (Rayner et al., 2003). Details on the HadGEM3 GA4.0 can be found in Walters et al. (2014). This model is used in Chapters 3, 4 and 5.

2.3 Experimental setup

This section presents a description of the experimental setup for the HadGEM3 model experiments in Chapters 3, 4 and 5. In particular, the experimental setup was designed to tackle the scientific aims of these three chapters. Time–slice experiments are setup to investigate the seasonality (Chapter 3) and the linearity (Chapter 5) of the ENSO–ASR teleconnection. These time–slice experiments have imposed tropical SST anomalies that are an empirical representation of the ENSO pattern. These artificial SSTs consists of a simple analytical function added to the observed climatological SSTs. In the longitudinal direction, a $\tanh()$ function was used originating at 0°N , 180°W and propagating towards the east. In the latitudinal direction, a two sided exponential decay function originating at 0°N and extending uniformly into both hemispheres was used. The exponential decay was

set so that the imposed anomaly is negligible near at 10°N and 10°S . The result of this is a ‘textbook’ eastern Pacific (EP) El Niño that is symmetric in the latitudinal direction. Note that the imposed La Niña anomalies are simply a reverse of the El Niño anomaly.

In order to investigate the ENSO–ASR teleconnection linearity, nine of these time–slice experiments were performed with varying El Niño/La Niña strengths, these are: -3.0 K , -2.25 K , -1.5 K , -0.75 K , 0.0 K (baseline), 0.75 K , 1.5 K , 2.25 K , 3.0 K anomalies in the Niño3.4 region. Each experiment was run for 54 years. The patterns of SST anomalies in the experiments are shown in Figure 2.2 for comparison with panel (a) of Figure 1.13. The baseline SSTs used is for year 2000 climatological conditions (1995 – 2005) as shown in Figure 2.3, along with the 1.5 K and 3.0 K El Niño cases. Note that these are intended to be idealised ENSO–like SST perturbations that capture the broad large–scale pattern of a classical EP ENSO event, rather than being designed to mimic a specific real world event. The use of a wide range of amplitudes allows investigation of the behaviour of the ENSO–ASR teleconnection over a wide range of states. These experiments therefore implicitly neglect details, such as that SST anomalies during La Niña events tend to be located more towards the CP compared with El Niños.

Turning to the investigation of the transient ASR response in Chapter 4, two additional sets of HadGEM3 model experiments consisting of 106 ensembles of seven months integrations were run. In these experiments, the model was initialised from particular dates in the control and the $+1.5\text{ K}$ El Niño anomaly was then ‘switched’ on, one month into the run. The runs are then continued for another six months with the SST anomalies held fixed throughout. This experimental approach allows a better understanding of the transient evolution for the ENSO–ASR teleconnection. The El Niño that is imposed in the transient runs has an amplitude of $+1.5\text{ K}$. As these experiments are used to explore the seasonality of the ENSO–ASR teleconnections, one set of runs is initialised from start dates on the 1st May (to investigate JJA) and the other set on the 1st November (to investigate DJF). Both sets include an identical El Niño perturbation. This means that the imposed El Niño starts on the 1st June and 1st December and reaches 1.5 K on the 10th June and 10th December, respectively, see Figure 2.4. 106 ensemble members in total (53 DJF ensembles and 53 JJA ensembles) were run. Each ensemble member was initialised using atmospheric initial conditions taken from a different year of the control experiment.

Note that the SST is not ‘switched’ on instantaneously but rather ramped up over ten days. This is to reduce any spurious (non–physical) model artifacts. However, even a ramp up over ten days introduces some artifacts. Figure 2.5 shows the mean precipitation anomaly (10N – 10S , 180E – 90W) in the transient runs. The top figure shows the anomaly for the November to May experiments while the bottom figure shows the May to November experiments. There

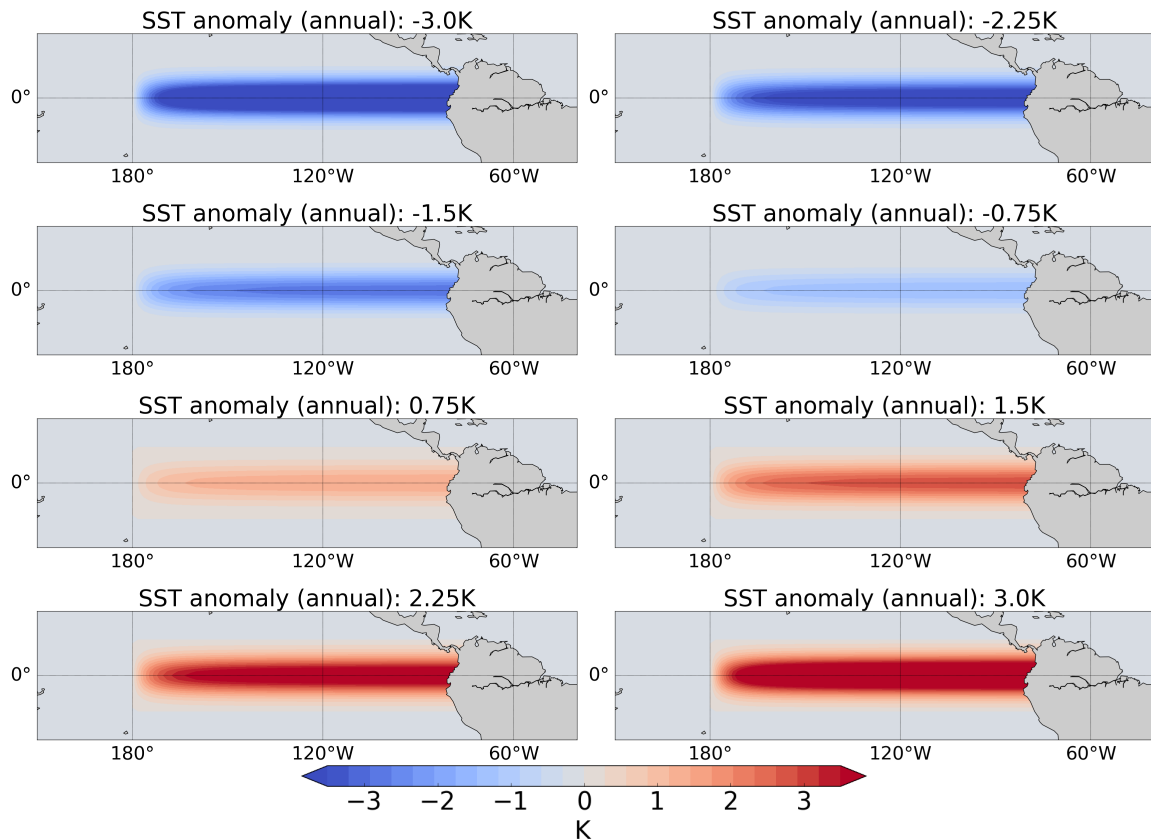


Fig. 2.2 Idealised SST anomaly in the Pacific. Top row (in order from left to right): -3.0 K, -2.25 K, -1.5 K and -0.75 K. Bottom row (in order from left to right): 0.75 K, 1.5 K, 2.25 K and 3.0 K

are two possible issues evident from these graphs. Firstly, the precipitation is expected to show an increase on a short timescale before reaching an equilibrium. This is because the mean tropical precipitation magnitude does not vary much between seasons. The intertropical convergence zone (which coincides with most of the tropical precipitation) mainly moves equatorwards or polewards between seasons. As seen in the bottom panel of Figure 2.5, there seems to be an ‘overshooting’ behaviour in JJA. The precipitation overshoots before slowly reducing to a fixed level. Furthermore, there is a difference in magnitude in the equilibrated precipitation response between DJF and JJA (in the ‘equilibrium’, after the overshooting problem). The precipitation anomaly approximately reaches 3 mm / day in DJF while it is approximately 2 mm / day in JJA. While some of this difference may be due to physical factors that induce a seasonal dependence in the response, some *may* be due to model artifacts. However, as these transient runs are only used in Chapter 4, where the focus is on timescales rather than magnitudes, this does not pose a serious problem.

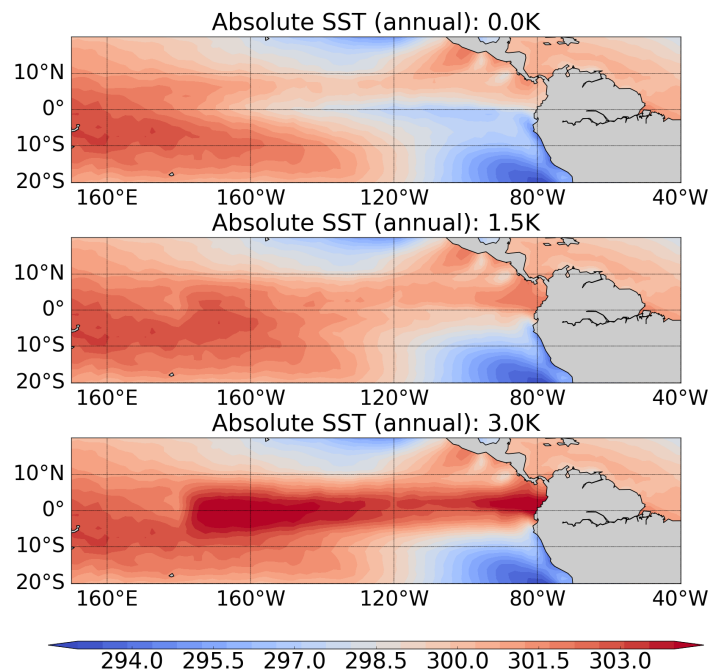


Fig. 2.3 Absolute SST in the Pacific for the HadGEM3 model experiments. Top panel shows baseline, middle panel shows 1.5 K El Niño run and the bottom panel shows the 3.0 K El Niño run.

Summary

This section has provided a description of the experimental setup. There are two key points to note. Firstly, time–slice runs with varying amplitudes of Niño3.4 temperature anomalies in the Niño3.4 region were run for the analysis in Chapter 3 and 5. Idealised perpetual ENSO conditions are imposed in these runs. Each experiment is 54 years long. Secondly, two sets of transient ‘switch on’ experiments are performed for Chapter 4. Each experiment has 53 seven month long ensemble members. One set initialises the 1.5 K El Niño ‘switch on’ in November and another in May.

2.4 Model evaluation

Overview

It is important to evaluate the fidelity of the model simulation of both the atmospheric climatology and the ENSO–ASR teleconnection before use. This section will present a comparison of the climatology and the ENSO–ASR teleconnection between HadGEM3 and the ERA–Interim reanalysis dataset. For the climatology, the comparison will be between ERA–Interim over 1995–2005 and the baseline year 2000 HadGEM3 run. The year 2000

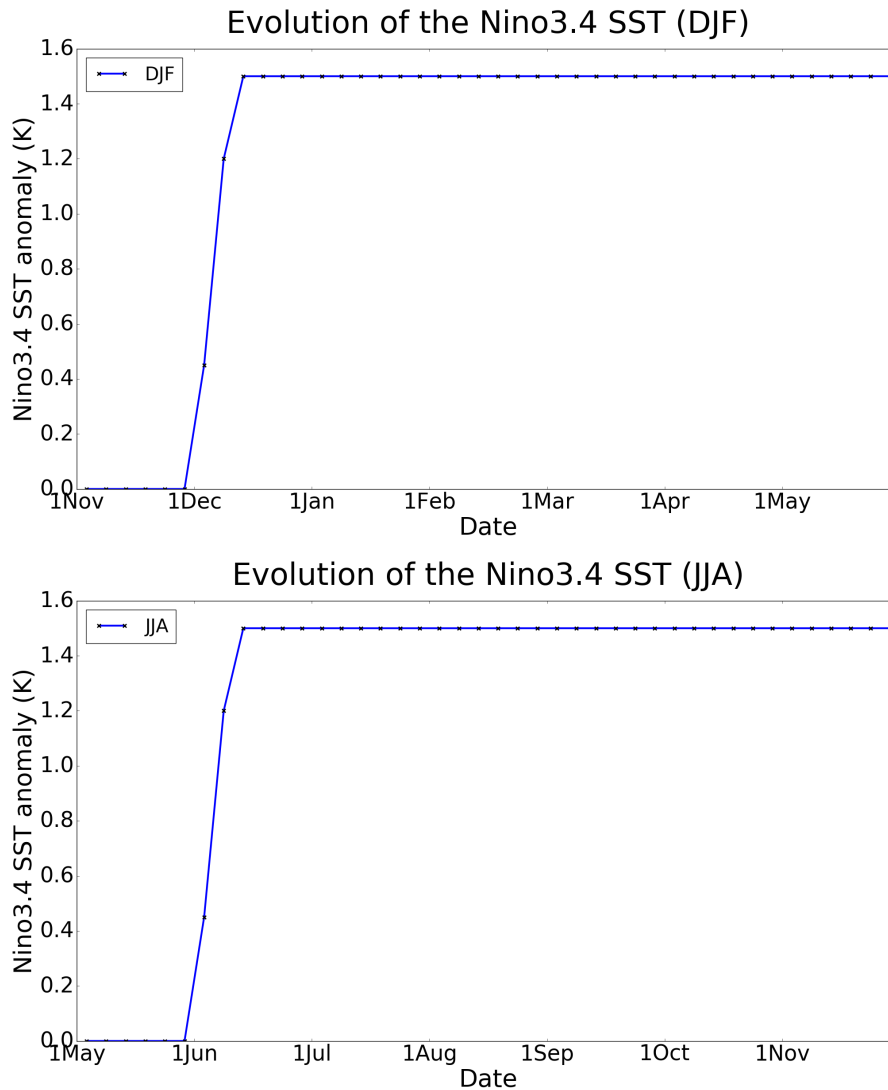


Fig. 2.4 Evolution of Niño3.4 temperature anomaly in the transient runs. Points represent five-day-means.

averages are climatological conditions from 1995–2005. The variables included in this evaluation include tropical Pacific SSTs under El Niño and La Niña conditions, the southern hemisphere zonal wind and the SLP in the ASR. These variables have been selected as they are important for in the ENSO–ASR teleconnection (details in Chapter 3).

Turning to the ENSO–ASR teleconnection evaluation, the comparison will be between a composite of ENSO events in ERA–interim and the 1.5 K HadGEM3 run. This is not a direct like for like comparison because the HadGEM3 experiments have a perpetual El Niño of a fixed amplitude throughout the year while there is a marked seasonality and variation in amplitude to observed ENSO events in ERA–Interim data (Chiodi and Harrison, 2017; Hu

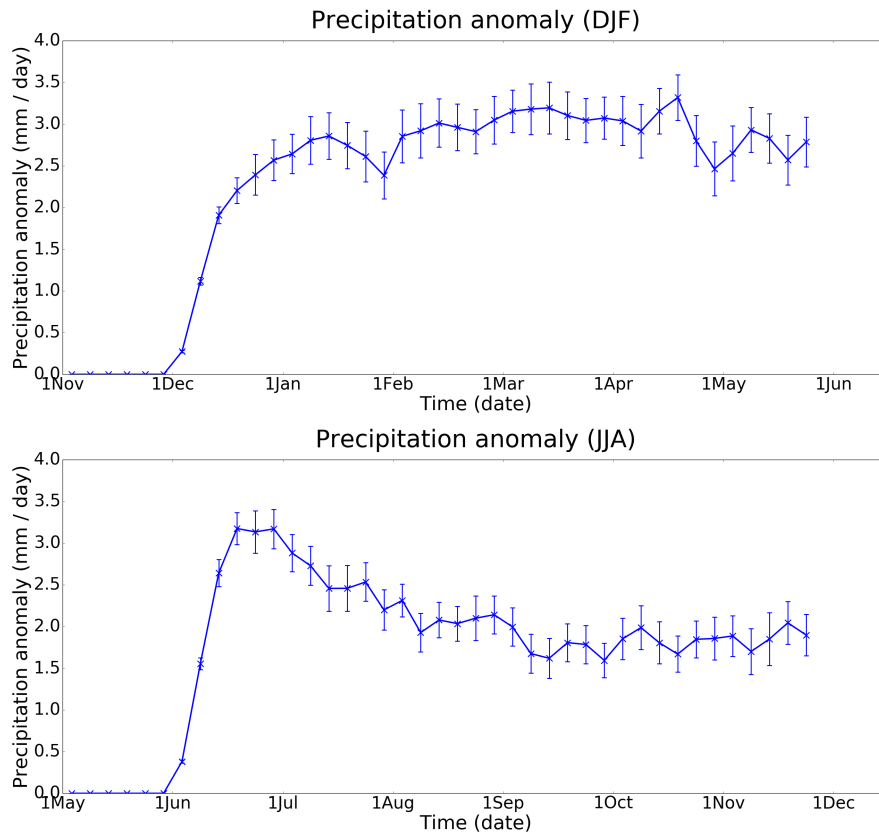


Fig. 2.5 Evolution of mean precipitation (10°N – 10°S , 180°E – 90°W) in transient runs.

and Fedorov, 2016; McPhaden, 1999). For example, while the strongest El Niños can reach a Niño3.4 anomaly of approximately 3.0 K in DJF, El Niños at the strength of 3.0 K and 2.25 K in JJA are unheard of historically. Therefore, it is important to treat these comparisons and evaluation as a qualitative rather than a quantitative assessment of the model performance.

ERA–Interim was used to produce composites of El Niño and La Niña conditions. Years with higher (lower) than 1.0 K (–1.0 K) ONI are used for the El Niño (La Niña) composites. All other years are considered to be ENSO neutral conditions. The El Niño (La Niña) composites had a Niño3.4 temperature of ~ 1.8 K (~ -1.5 K) in DJF and ~ 1.0 K (~ -0.9 K) in JJA. To try and provide a closer quantitative comparison with the 1.5 K HadGEM3 experiment, all ERA–Interim composites of meteorological fields have been linearly scaled to simulate a 1.5 K Niño3.4 temperature anomaly.

SST

This section presents a discussion of the SSTs evaluation under year 2000 conditions, El Niño and La Niña conditions. Figure 2.6 shows the absolute SST of ERA–Interim (left panels) and

the HadISST dataset used in the HadGEM3 model runs (right panels). The top row shows the comparison between the ERA–Interim dataset (left) and the HadGEM3 baseline year 2000 run (right). The ERA–Interim reanalysis uses an SST dataset comprised of NCEP 2D–Var SSTs, NOAA Optimum Interpolation Sea Surface temperature v2, the NCEP Real–Time Global sea surface temperature (NCEP RTG) and Operational Sea Surface temperature and Sea–Ice analysis (OSTIA) (Dee et al., 2011).

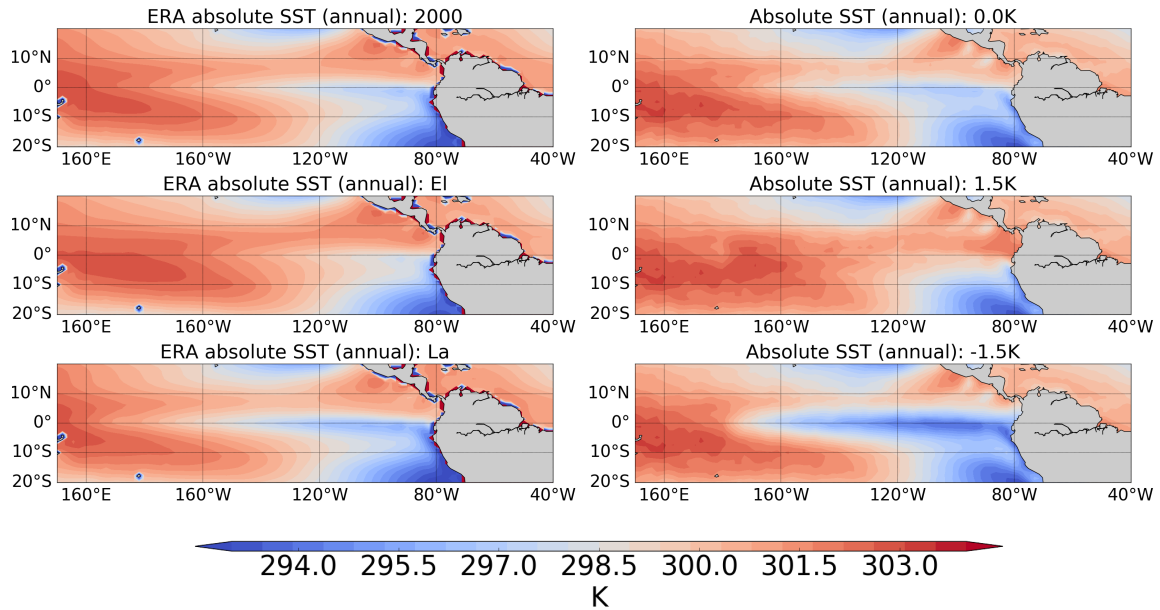


Fig. 2.6 Comparison of the SST in ERA–Interim with HadGEM3. Left panels show plots of ERA–Interim data. Right panels show HadGEM3. Top row show the baseline SST (1995–2005), middle row show the SST under El Niño conditions and the bottom row shows the SST under La Niña conditions.

As expected, the pattern of climatological SSTs between ERA–Interim and the model are similar. There is a ‘cold tongue’ stretching from the tropical eastern Pacific to the tropical central Pacific. As seen from Figure 2.6, there is a cool spot towards Chile in both cases. There seems to be a difference in resolution and smoothness between ERA–Interim and HadISST. However, this is likely due to the regridding in post–processing rather than any actual difference. In the middle row, the comparison of the ERA–Interim composite of El Niño minus neutral conditions with the 1.5 K El Niño HadGEM3 run is shown. Both panels show a weakening of the ‘cold tongue’ and the macro–structure changes are similar. In the bottom row, the comparison of the ERA–Interim composite of La Niña minus neutral conditions with the –1.5 K La Niña HadGEM3 run are presented. Both panels show a strengthening and extension of the ‘cold tongue’ and the macro–structure changes also seem to be similar.

Zonal wind

Moving on to the zonal wind, it is important to evaluate the simulation of the zonal wind structure in the HadGEM3 model. This is because the subtropical (STJ) and polar front jets (PFJ) play a crucial role in the ENSO–ASR teleconnection, see Chapter 3 for details. Figure 2.7 shows the comparison of the structure of the zonal mean zonal wind in the southern hemisphere in the ERA–Interim dataset (top row), scaled ERA–Interim (middle row) and HadGEM3 experiments (bottom row). Austral summer (DJF) is shown on the left column, while austral winter (JJA) is shown on the right column. The ERA figures show the composite of El Niño minus neutral years. The solid contours show the baseline zonal wind speeds and the coloured contours show the anomalies due to El Niño conditions.

Structurally, the baseline is very similar in ERA–Interim and the HadGEM3 experiment. In DJF, there is a maximum wind speed located at the polar front jet (PFJ) around 200 hPa 50°S. The maximum PFJ strength is slightly higher in the model; it is around 30 m s^{-1} in ERA and $\sim 35 \text{ m s}^{-1}$ in the baseline experiment. Structurally, the zonal wind changes under El Niño are similar between the model and ERA–Interim. They are mostly positive northwards of the PFJ and mostly negative southwards of the PFJ. This means that on average the PFJ shifts equatorwards during El Niño in DJF, consistent with earlier works (Lu et al., 2008). The magnitude of the change is similar between ERA and the HadGEM3¹. In JJA, the baseline zonal wind is also structurally similar between ERA and the HadGEM3 runs. The dominant feature is the the strong subtropical jet (STJ) located around 200 hPa 30°S. The maximum speed of the STJ is around 40 m s^{-1} in both HadGEM3 and ERA–Interim. The changes in the zonal mean wind due to El Niño in JJA are structurally similar, but have a weaker magnitude in ERA (even the scaled version) compared to the HadGEM3 model.

Figure 2.8 shows the equivalent comparison to Figure 2.7 but for the La Niña composites and -1.5 K HadGEM3 experiment. In DJF, there is an increase in wind speed on the poleward side of the PFJ and decreased wind speeds on the equatorward side of the PFJ in both ERA and the HadGEM3 model, indicating a polewards shift that is opposite to the El Niño response in Figure 2.7. While the structure of the wind anomalies due to La Niña are similar between the reanalysis and model in DJF, these are greater in JJA. In ERA, there is a general increase in wind speeds centred approximately around 50°S in JJA during La Niña conditions. In HadGEM3, the increase seems to be very close to the jet at around 35°S. The magnitude of changes seems to be weaker in both seasons in HadGEM3 compared to ERA.

In conclusion, the climatological structure of the zonal winds between the model and ERA–Interim are broadly in good agreement with each other. The structural changes under

¹Discounting the upper level (stratosphere) winds near the tropics. These heights are not within area of interest of this thesis.

ENSO events are also broadly captured. However, zonal wind anomalies are slightly smaller under La Niña conditions in the model compared to ERA–Interim.

The main focus of this thesis is the ENSO–ASR teleconnection. Both ENSO and the ASR are located in the Pacific sector. Therefore, model evaluation on the Pacific zonal wind is also performed. Figures 2.9 and 2.10 show the model evaluation of the zonal wind in the Pacific (120E–60W) for the El Niño and La Niña runs, respectively. As seen from Figure 2.9, the general seasonality of the climatology is captured in the model. In DJF (JJA), the maximum zonal wind is located at approximately 50°S (30°S) in both ERA–interim and HadGEM3. The speed of the jet across the two seasons are also generally captured well

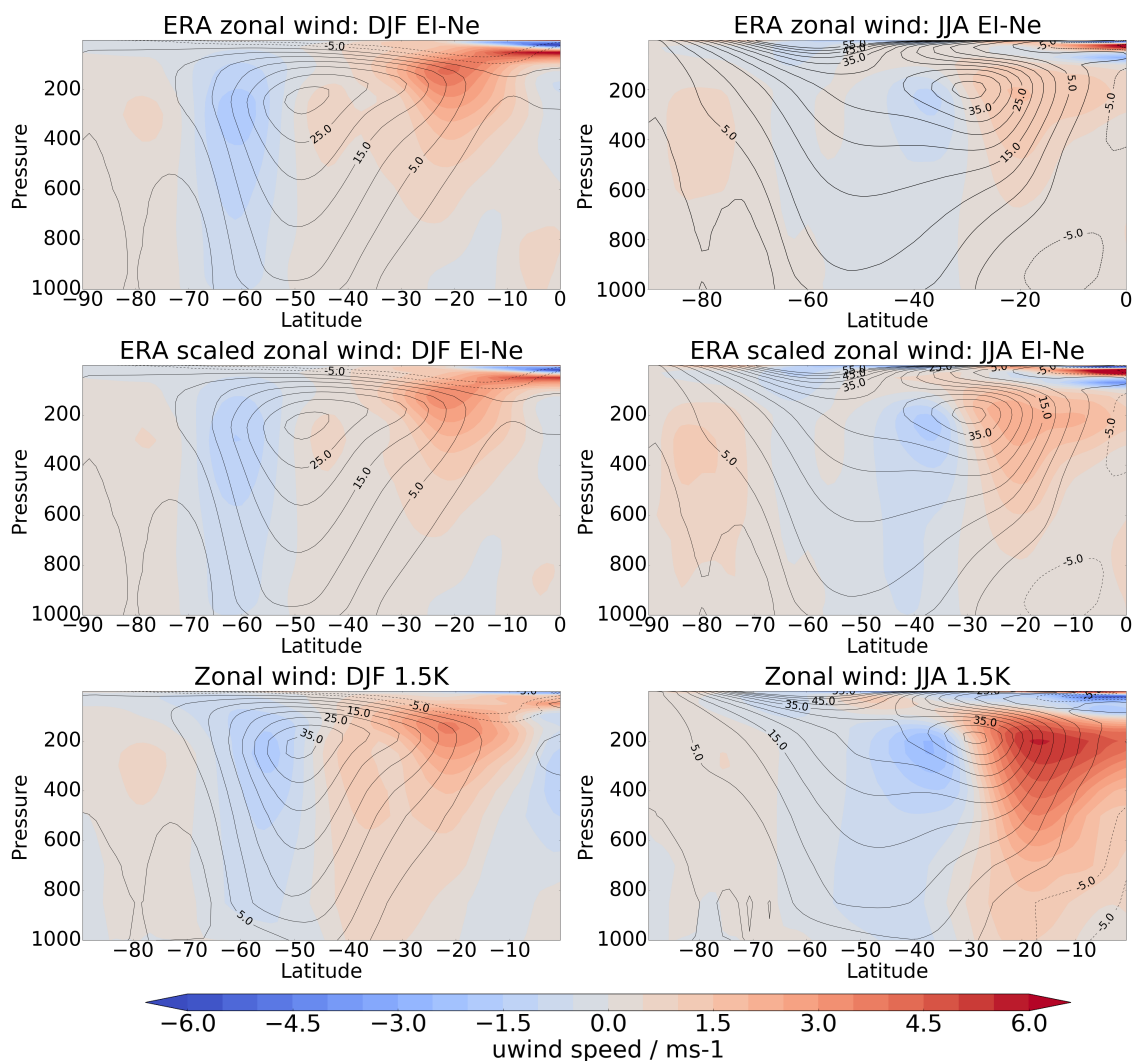


Fig. 2.7 Zonal mean zonal wind between ERA–Interim (top), ERA–Interim scaled (middle) and HadGEM3 runs (bottom) for the baseline and El Niño conditions. Solid contours show baseline zonal wind speeds while the coloured contour shows the anomaly.

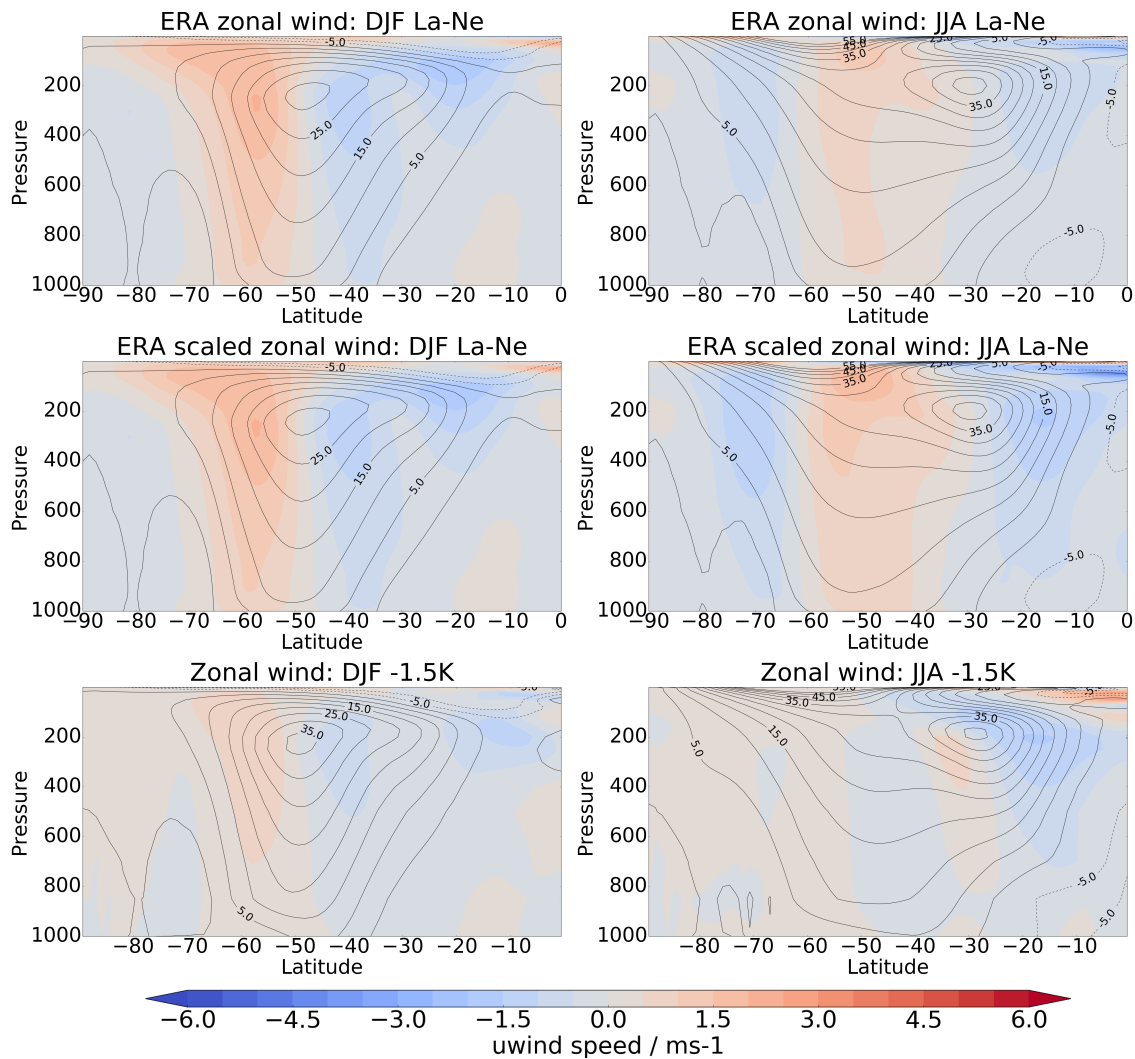


Fig. 2.8 Same as Figure 2.7 but for La Niña conditions.

in the HadGEM3 model (albeit slightly higher in the model). In DJF, the maximum zonal wind speed is approximately 30 m s^{-1} in HadGEM3 and 25 m s^{-1} in ERA–interim. In JJA, the maximum zonal wind speed is approximately 50 m s^{-1} in HadGEM3 and 40 m s^{-1} in ERA–interim.

The structure of the anomalies under El Niño is also captured reasonably well in the model: in JJA, there is a positive anomaly just equatorwards of the jet core and a negative anomaly further polewards of the jet core. In DJF, there is a positive anomaly at around $20\text{--}25^\circ\text{S}$ and a negative anomaly $50\text{--}60^\circ\text{S}$. The magnitudes of these anomalies tend to be slightly weaker in HadGEM3 compared to ERA–interim.

Figure 2.10 shows the Pacific zonal wind climatology and anomaly under La Niña conditions. While the structure of the anomalies are somewhat captured (approximately

inverse of El Niño conditions), the magnitude of the changes are much lower in HadGEM3 compared to ERA–interim. This could explain the poor representation of the SLP anomalies in HadGEM3 under La Niña conditions in the following.

In conclusion, HadGEM3 seems to capture the structure and speed of the climatological Pacific zonal wind reasonably well. The anomalies under El Niño conditions are also generally captured. However, the zonal wind anomalies under La Niña conditions are overly weak compared to ERA–interim.

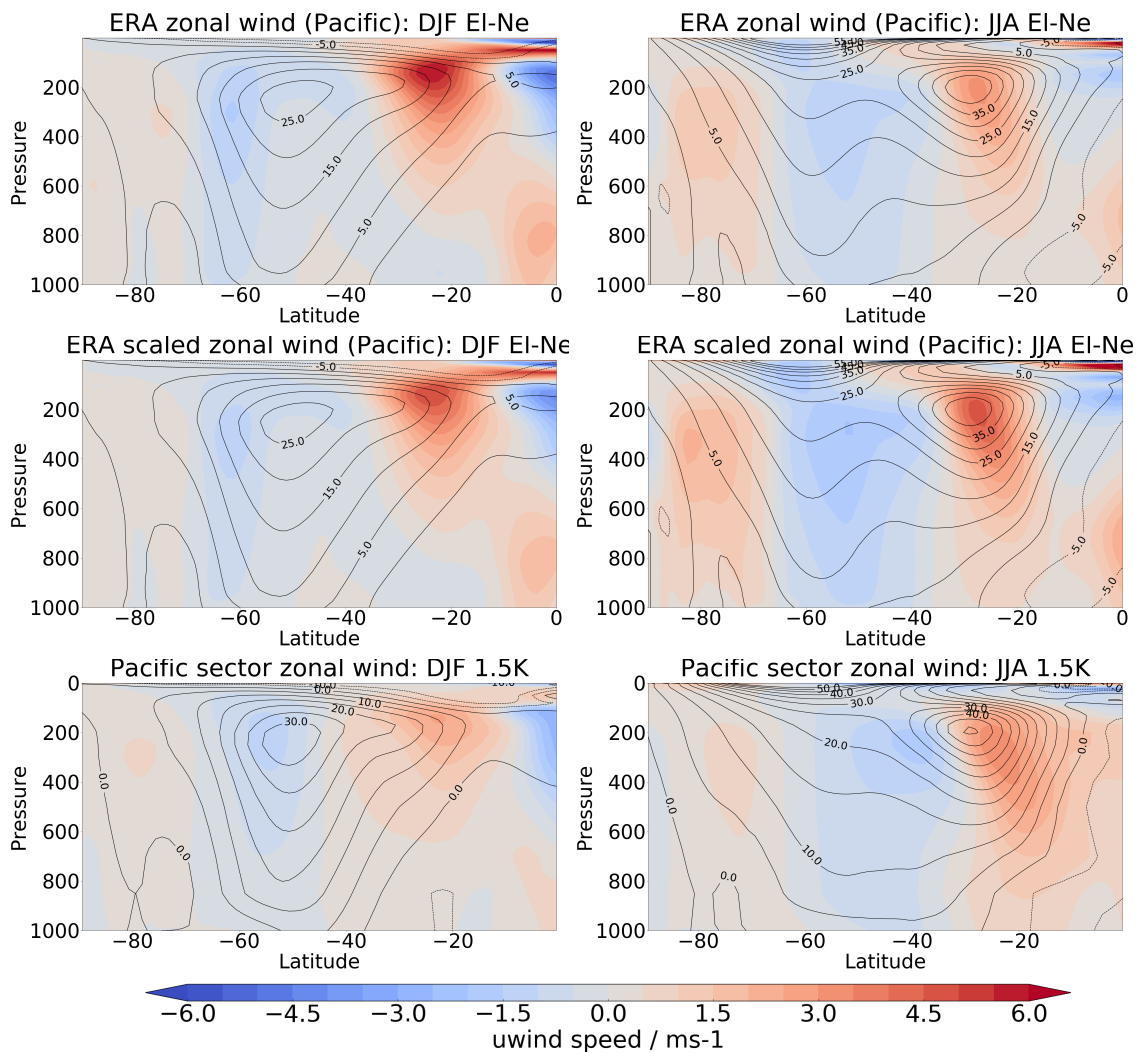


Fig. 2.9 Same as Figure 2.7 but for the Pacific sector.

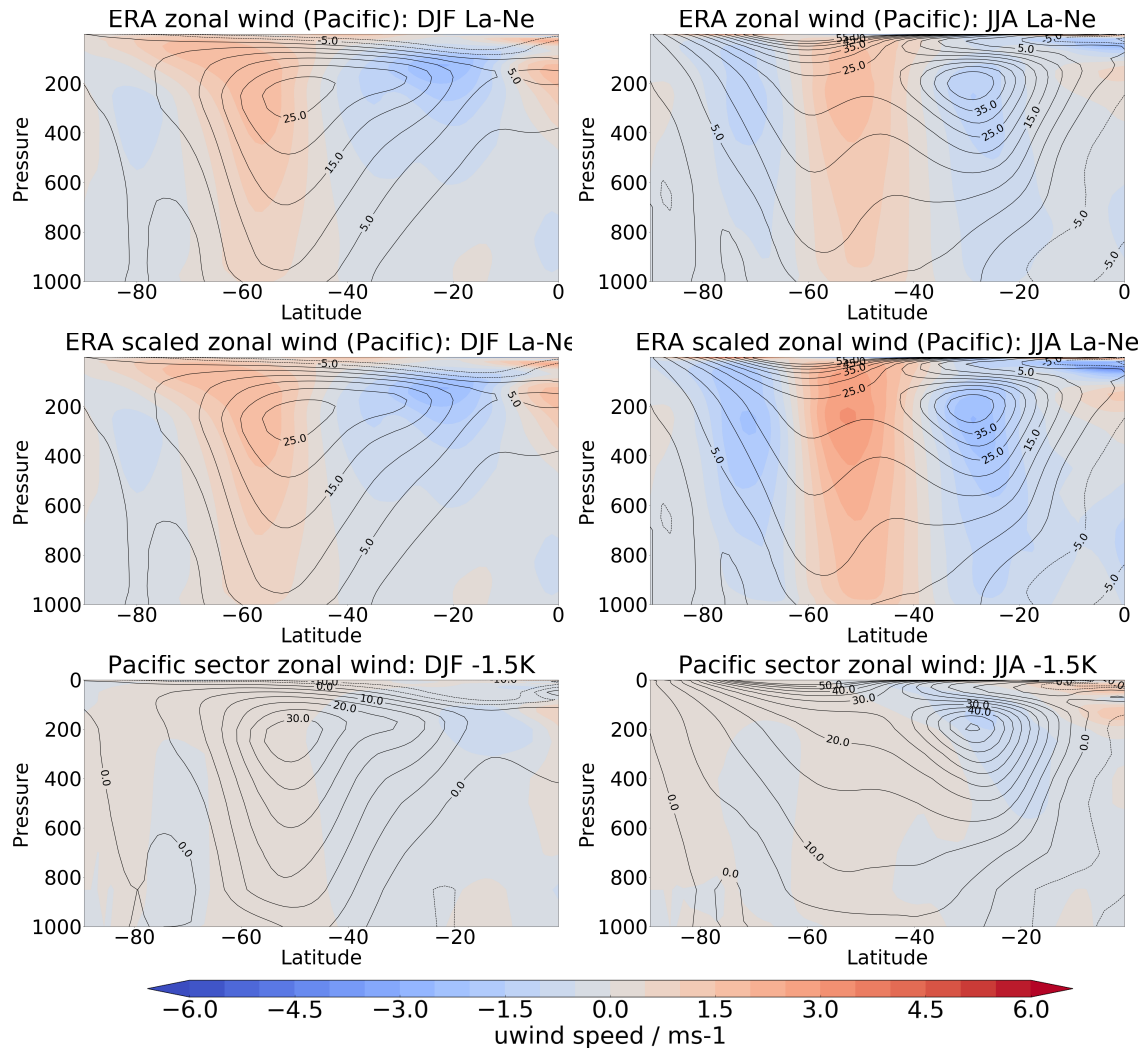


Fig. 2.10 Same as Figure 2.8 but for Pacific sector.

Sea Level Pressure (SLP)

Since this project relates to teleconnection to the Amundsen sea low (ASL), the next analysis assesses the representation of the ASL in the HadGEM3 model. Figure 2.11 shows the climatological SLP in the high southern latitudes for ERA–Interim over 1995–2005 (left panels) and the baseline year 2000 HadGEM3 run (right panels). The top row shows the austral summer (DJF) while the bottom row shows austral winter (JJA). There is seasonality in the structure and strength of the ASL in both ERA–Interim and HadGEM3. In DJF, the ASL is located further eastwards compared to in JJA. Furthermore, the low pressure system is more localised in JJA compared to DJF in both the model and reanalysis. This agrees with previous literature (Hosking et al., 2013). The ASL is slightly weaker in the model compared to ERA–Interim in both seasons. In general, the model representation of the

ASL climatologically does not seem to have any major deficiencies. Note that the larger differences in SLP climatology inland features are less important for this thesis as the inland over Antarctica are likely to be related to the representation and resolution of orography.

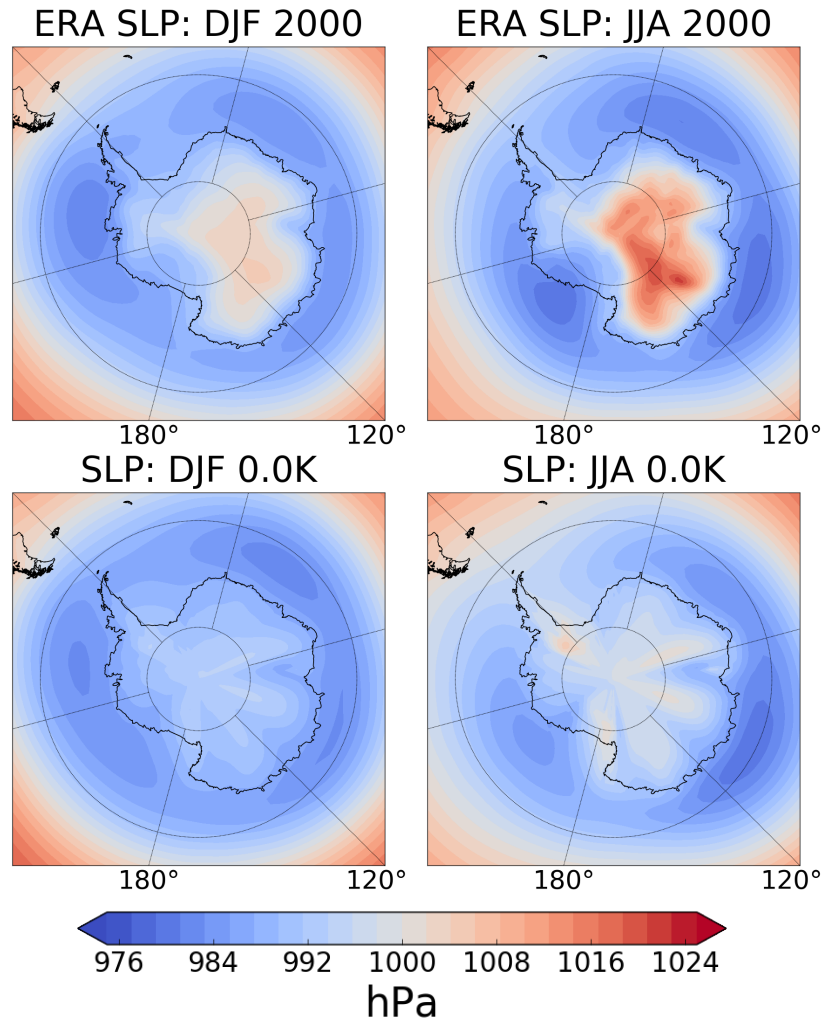


Fig. 2.11 SLP in the high latitudes (55S–90S) between ERA–Interim (left) and HadGEM3 (right).

Figure 2.12 shows the SLP anomalies for the ERA–Interim El Niño composite (left) and the +1.5 K El Niño HadGEM3 (right). The left column shows austral summer (DJF) and the right column shows austral winter (JJA). Both ERA and HadGEM3 show that DJF has a weaker SLP anomaly over the ASR during El Niño compared with JJA. Furthermore, the structure seems to be captured well in the HadGEM3 model. In DJF, the positive SLP anomaly at high latitudes stretches across the whole of Antarctica while in JJA the anomalies are more localised and have a wavetrain structure extending from the tropics. However, there are some differences between the ERA composites (scaled) and the model. In JJA, the magnitude of the SLP anomaly over the ASL in HadGEM3 seems to be 30% weaker

than in the scaled ERA–Interim composite (HadGEM3: 6.1 hPa, ERA scaled: 8.7 hPa). Furthermore, the resemblance to the EOF2 pattern seems stronger in HadGEM3 compared to ERA. In particular, the negative anomalies of the wavetrain in the HadGEM3 model seem to be stronger compared to ERA scaled (HadGEM3: -6.7 hPa, ERA scaled: -3.8 hPa). In DJF, the anomaly is further eastwards in HadGEM3 compared with ERA.

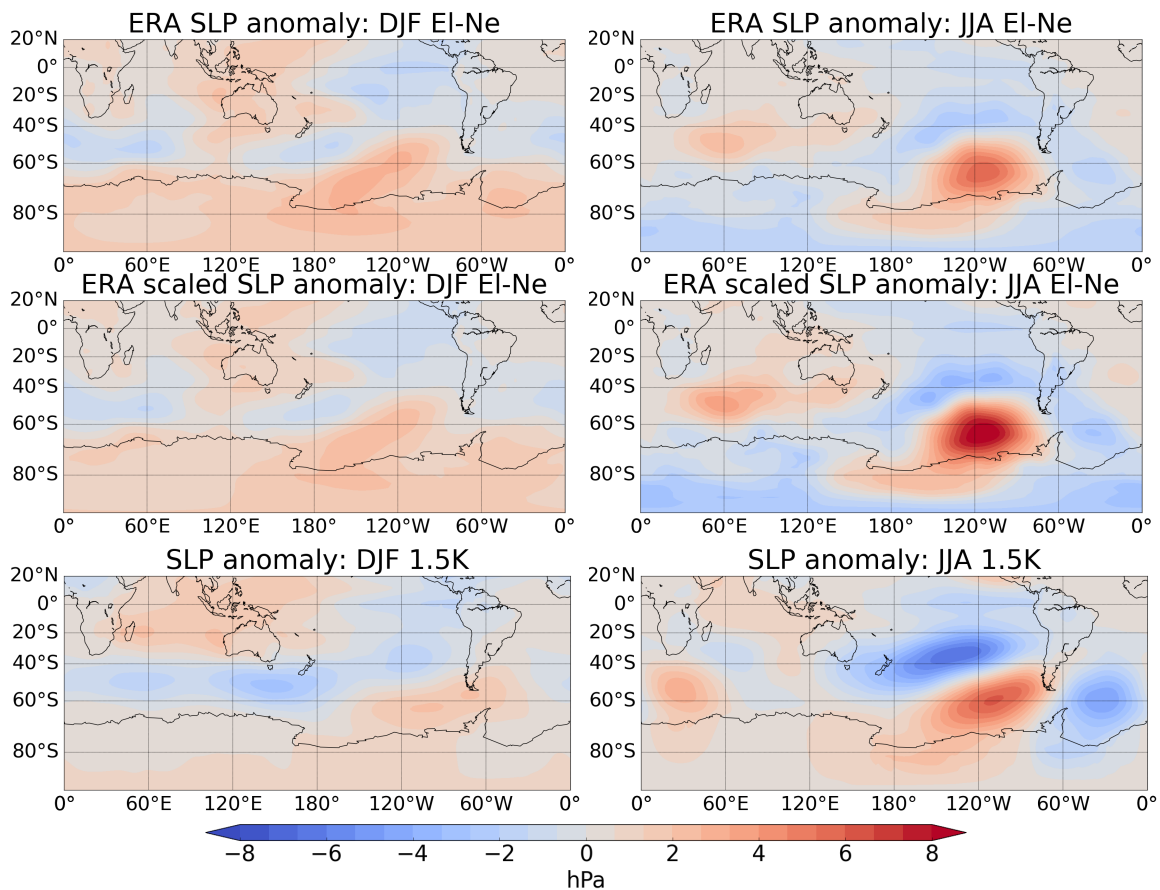


Fig. 2.12 SLP anomalies under El Niño conditions in ERA–Interim (top), ERA–Interim scaled (middle) and HadGEM3 (bottom).

Note that the Amundsen sea low (ASL) is highly variable (see again Chapter 1). Therefore, one would expect a high standard deviation to be associated with the SLP anomaly in the ASR. Figure 2.13 shows the difference in the SLP anomaly between the 1.5 K El Niño HadGEM3 model run and the scaled ERA–Interim data. The hatched areas show the regions where HadGEM3 SLP response differs significantly (two standard errors). Note that although both seasons show some differences in the ASR (maximum 3.6 hPa in JJA, 4.1 hPa in DJF), these differences in the ASR are not highly statistically significant. However, as seen from the right panel of Figure 2.13, one of the negative anomalies (Pacific mid latitudes) associated with the wavetrain emanating from the tropical Pacific is hashed. This indicates that the

Pacific mid latitude negative SLP anomaly is stronger in the HadGEM3 model compared ERA–Interim in JJA.

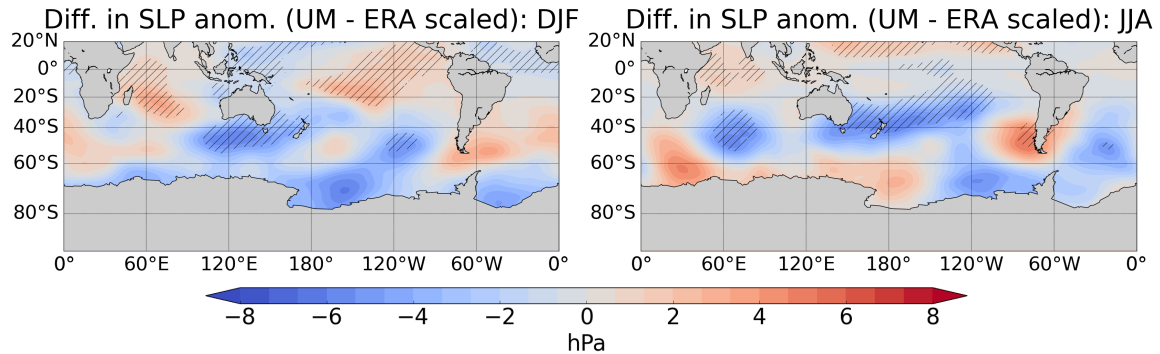


Fig. 2.13 Difference in SLP anomaly between the HadGEM3 and ERA scaled under El Niño conditions in DJF (left) and JJA (right). Hashed regions approximately indicate 95% significance (two standard errors).

Figure 2.14 shows the ERA–Interim La Niña composites and the -1.5 K La Niña HadGEM3 run. While the pattern of the negative SLP anomaly in the ASR is similar between ERA and HadGEM3 (in both DJF and JJA), the location of the positive anomaly in JJA is too far southeast in HadGEM3. More importantly, the magnitude of the anomalies are much lower in HadGEM3 compared with ERA–Interim (in both seasons). For example, in JJA, the central (peak) ASR anomaly in ERA is approximately -8.5 hPa while the HadGEM3 model produces a -2.0 hPa changes. While the comparison is not like for like, this difference is likely due to the HadGEM3 model not producing the teleconnection to the ASR under La Niña conditions. One possible explanation is the unrealistic nature of the idealised La Niña SST pattern imposed in the model. The La Niña is merely imposed as the inverse of El Niño. However, real world La Niñas are not structurally similar to El Niños. One possible method to diagnose this further is to perform a model experimental with a ‘realistic’ La Niña, see Section 7.6.2 for details.

Figure 2.15 shows the differences in SLP response to La Niña between the HadGEM3 model and ERA–Interim. However, unlike under El Niño conditions, there are large areas with hatched differences in the ASR in both seasons. This indicates that the teleconnection, or its lack, in the model is statistically significantly weaker than in ERA–Interim.

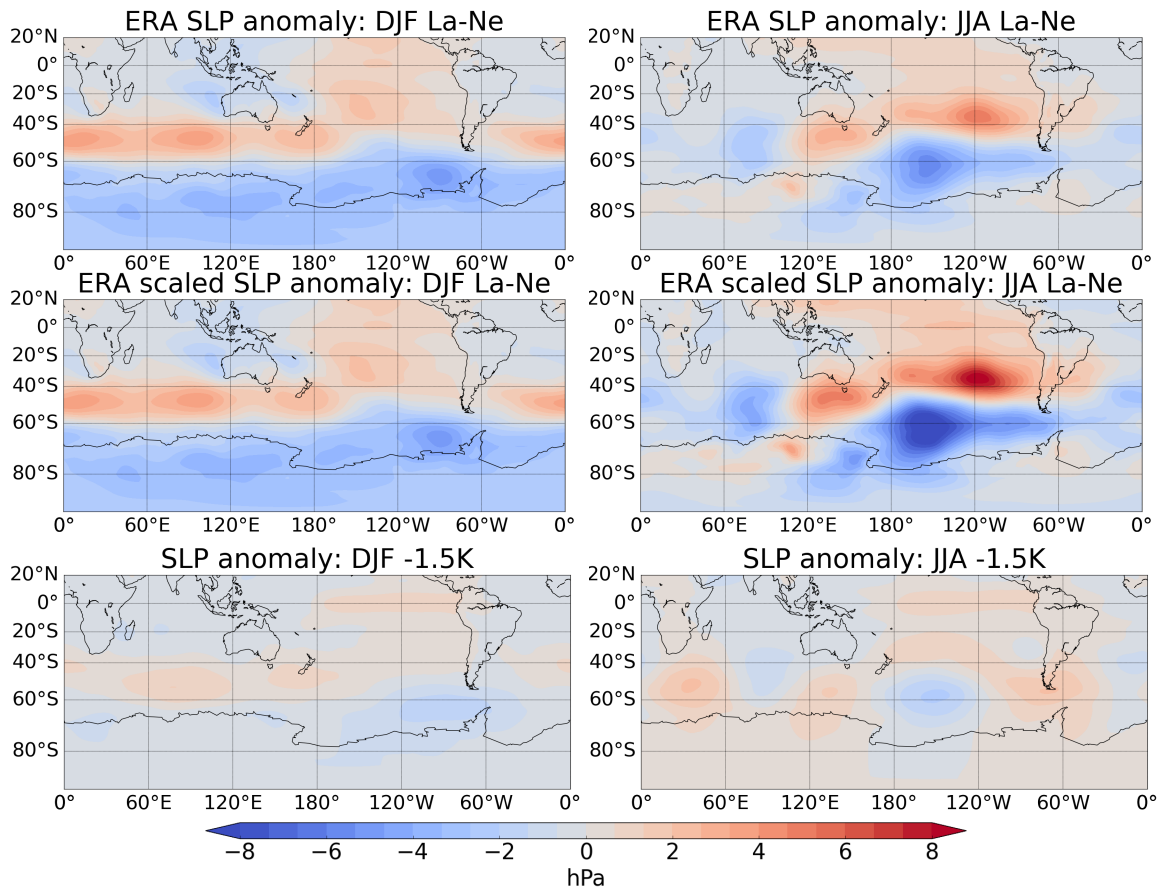


Fig. 2.14 Same as Figure 2.12 but for La Niña conditions.

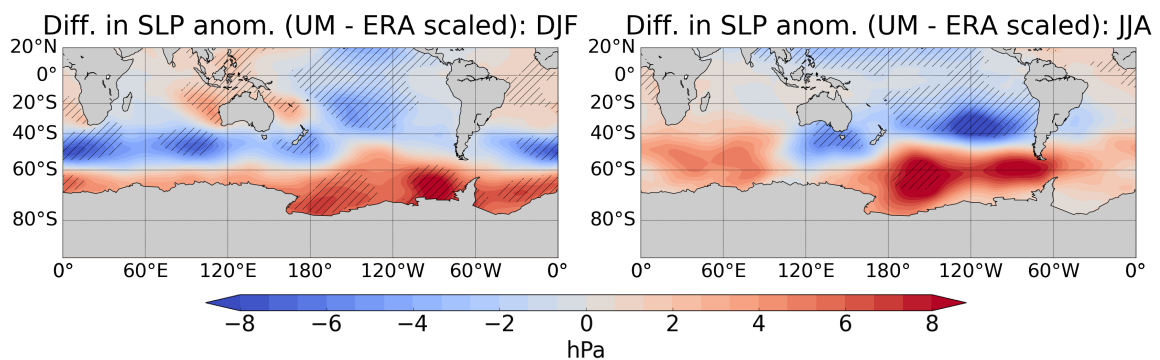


Fig. 2.15 Same as Figure 2.13 but for La Niña conditions.

Summary

This section has compared the SST (tropical Pacific) and southern hemisphere zonal wind and SLP patterns in HadGEM3 against ERA–Interim data for both the climatology and the ENSO–ASR teleconnection. The climatologies seem to be well represented by the model and are broadly consistent with ERA–Interim.

Turning to the ENSO–ASR teleconnection, the model seems to perform better under El Niño conditions compared to La Niña. Although there are some differences in the magnitude of the anomalies between ERA–Interim and HadGEM3 under El Niño conditions, the overall pattern of response appears to be captured in the HadGEM3 model. Furthermore, there does not seem to be any statistically significant difference in the ASR SLP anomaly. However, the model does not perform as well in representing the SLP anomalies for La Niña conditions. In La Niña, while the structure of the SLP anomaly tends to stay somewhat similar, the magnitude of change is statistically significantly smaller in the model compared with ERA. As a result, the La Niña runs are not used in any of the following chapters due to this modeling problem.

2.5 Methods

The analysis in this thesis uses a variety of Rossby wave analysis methods. Methods include: Rossby wave source calculation, Rossby wave ray tracing and analysis of wave activity fluxes. These methods allow the visualisation of the source and propagation of the standing waves and are described below.

Rossby wave source

We mainly follow (Sardeshmukh and Hoskins, 1987) for our discussion on the Rossby wave source (RWS). Their research presented a one–level vorticity equation model and considered the Rossby wave source at an upper tropospheric level. They started with the non–linear vorticity equation following Sardeshmukh and Hoskins (1985)

$$\left(\frac{\partial}{\partial t} + \mathbf{v} \cdot \nabla\right)\zeta = -\zeta D + F, \quad (2.1)$$

where \mathbf{v} is the horizontal velocity, ζ is the absolute vorticity, D is the divergence and F is the frictional term. Following Sardeshmukh and Hoskins (1987), the generation of Rossby

waves is possible by rewriting equation (2.1) into

$$\left(\frac{\partial}{\partial t} + \mathbf{v}_\psi \cdot \nabla\right)\zeta = S + F, \quad (2.2)$$

where v_ψ is the rotational wind associated with ζ and S is the Rossby wave source. \mathbf{v} can also be rewritten in terms of its rotational and divergent components

$$\mathbf{v} = \mathbf{v}_\psi + \mathbf{v}_\chi, \quad (2.3)$$

where \mathbf{v}_ψ is the rotational wind, \mathbf{v}_χ is the divergent wind and $\nabla \cdot \mathbf{v}_\chi \approx D$. Equation (2.1) can be rewritten into

$$\left(\frac{\partial}{\partial t} + \mathbf{v}_\psi \cdot \nabla\right)\zeta = -\zeta D - \mathbf{v}_\chi \cdot \nabla\zeta + F. \quad (2.4)$$

Therefore,

$$S = -\zeta D - \mathbf{v}_\chi \cdot \nabla\zeta, \quad (2.5)$$

which can be rewritten as

$$S = -\zeta D - v_{\chi_x} \nabla\zeta_x - v_{\chi_y} \nabla\zeta_y. \quad (2.6)$$

where S is the Rossby wave source, ζ is the absolute vorticity, D is the divergence of the wind, v_{χ_x} is the x component of the divergent velocity and v_{χ_y} is the y component of the divergent velocity. Equation (2.6) is the equation that is used in our thesis for RWS calculations. In the following description, ζD is referred to as the first term, $v_{\chi_x} \nabla\zeta_x$ as the second term and $v_{\chi_y} \nabla\zeta_y$ as the third term in the equation. Note that the RWS anomaly, which is used frequently in this thesis, is taken as the RWS of the perturbed run minus the baseline run.

The rationale behind the RWS is that even though the divergent flow is only a small part of total horizontal flow, the vorticity associated with it is extremely important for understanding tropical–extratropical interactions on longer than synoptic timescales (Sardeshmukh and Hoskins, 1987). They found that a heating in the equator may cause a non–local ‘effective Rossby wave source’ to appear in the subtropical westerly jets. This may play a role in explaining strong tropical–extratropical teleconnections (Sardeshmukh and Hoskins, 1987).

The main assumption used in this RWS calculation is that the upper–level divergence and convergence associated with a tropical heating can be specified. For example, if there is a large horizontal convective outflow at one height level, there has to be changes in the levels below in order to not break the thermal wind balance. This will imply spreading the divergence over approximately 2 km. However, the assumption is that such adjustments have already occurred in the divergence field in the model.

Note that it is not straightforward to divide the different terms in equation (2.6) into those associated with the unforced wave dynamics and those that represent a wave forcing. This point will be addressed in Section 3.5.2 as this is important for the interpretation of the results.

Ray tracing

In order to understand the dispersion of Rossby waves in the atmosphere, one of the methods used is Rossby wave ray tracing. Ray tracing was developed by Hoskins and Karoly (1981), Karoly and Hoskins (1982). It allows the user to understand how the background climatological state impacts the propagation of a linear barotropic Rossby wave (Hoskins and Karoly, 1981; Li et al., 2015a). In essence, with ray tracing techniques, a hypothetical Rossby wave can be initialised from its chosen starting location (usually a region with a strong RWS anomaly) and its theoretical propagation under certain simplifying assumptions can be traced.

The theory for ray tracing shown below follows Hoskins and Karoly (1981), Karoly and Hoskins (1982) and Hoskins and Ambrizzi (1993). For simplicity, the ray tracing will be presented in Cartesian coordinates. The derivation starts with the dispersion relation for Rossby waves

$$\omega = Uk - \frac{\beta^* k}{K^2}, \quad (2.7)$$

where ω is the frequency, U is the zonal wind, K is the total wavenumber ($K = \sqrt{l^2 + k^2}$), k is the zonal wavenumber, l is the meridional wavenumber and β^* is the meridional gradient of absolute vorticity. Note that the meridional gradient of absolute vorticity can be expressed as $\beta^* = \beta - U_{yy}$ where β is the planetary vorticity gradient and U_{yy} is the second derivative of the zonal wind with respect to latitude. For the case of stationary waves, the frequency is zero. Therefore, equation (2.7) can be rewritten as

$$K^2 = \frac{\beta^*}{U}. \quad (2.8)$$

Note that the wave train evolves according to the propagation of wave energy (given by the group velocity) even though it is a stationary wave. The group velocities of the waves are

$$c_{gx} = \frac{\partial \omega}{\partial k} = \frac{2\beta^* k^2}{K^4}, \quad (2.9)$$

$$c_{gy} = \frac{\partial \omega}{\partial l} = \frac{2\beta^* kl}{K^4}, \quad (2.10)$$

where c_{gx} is the group velocity in the x direction and c_{gy} is the group velocity in the y direction. Thus the direction of propagation of the wave front can be found by dividing equation (2.9) by equation (2.10) to get

$$\frac{dx}{dy} = \frac{c_{gx}}{c_{gy}} = \frac{k}{l}. \quad (2.11)$$

$K = \sqrt{l^2 + k^2}$ and equation (2.8) can be used to rewrite equation (2.11) to give

$$\frac{dx}{dy} = \frac{k}{\sqrt{\frac{\beta^*}{U} - k^2}}. \quad (2.12)$$

Equation (2.12) is the equation that will be used for ray tracing. The angle (angle = $\tan^{-1}(dy/dx)$) of the Rossby wave ray can be computed for any given k . Equation (2.12) can be used to trace the theoretical path of the wave train. It is the same equation found in Hoskins and Karoly (1981, Eq. (5.26)) and Li et al. (2015a, Eq. (5))². One is able to convert between Hoskins and Karoly (1981, Eq. (5.26)) and Li et al. (2015a, Eq. (5)). Importantly, the paths of the ray tracing using are identical between the two equations. Note that l controls the meridional direction of the rays. It is set to -1 (southwards propagating) initially as this thesis is mainly concerned with the southern hemisphere. It is important to note that the calculation above is shown in Cartesian coordinates. Calculations are converted to polar coordinates numerically in all our calculations.

There are several assumptions used for this derivation. Firstly, the Wentzel, Kramers, Brillouin and Jeffreys approximation (WKBJ) (see Hoskins and Karoly (1981) for details) is used. This approximation assumes that variations are slow relative to the scale of the wave. As discussed in Li et al. (2015a) and Hoskins and Karoly (1981), this assumption holds well for small-scale waves but may be questionable in planetary scale waves. Secondly, equation (2.7) is valid for zonally symmetric flow only. However, there are meridional flows in the climate system (both in the HadGEM3 model and the real world). Nevertheless, this equation can be used as an approximation if the zonal gradients of the absolute vorticity are small relative to the meridional gradients of the absolute vorticity. As the background flow is organised into jets, the zonal gradients are usually small compared to the meridional gradients. While Li et al. (2015a) suggested that one such exception may be located in the eastern Pacific (our area of interest), our analysis of the El Niño HadGEM3 runs shows that the meridional gradient in this area still dominates the zonal gradients. The meridional gradients are shown in Chapters 3, Figures 3.13 and 3.14. Additionally, ray tracing is limited to two

²In different coordinate systems.

dimensions in our work. This is because, as seen from equation (1.7), there exist a maximum U wind for vertical propagation of Rossby waves. This critical velocity is approximately 10 m s^{-1} for stationary wave number 3 Rossby waves. As our region of interest is in the STJ, the U speeds will most likely greatly exceed this critical velocity. Note that there are also several limitations in the implementation of ray tracing. Further details can be found in Appendix D.

Figure 2.16 shows an example of the Rossby ray tracing using data from the 1.5 K El Niño HadGEM3 run. A Rossby ray is first initialised at a starting location in the RWS anomaly. Equation (2.12) was used to calculate the initial wave trajectory. The ray is then stepped forward to a new point – the step size used was equivalent to approximately a hundredth of a grid point³. Note that the final trajectory of the wave does not seem to be very sensitive to the step size. Using the variables taken from the closest grid point to the ray's new location, equation (2.10) is used to propagate it forwards again. This process is continued and repeated until a fixed number of propagation steps are carried out or if the wave is terminated. As the focus of this thesis is in the southern hemisphere, signals north of the equator add no value to the analysis. Therefore rays are terminated if they hit the equator to save computational resources. Note that waves are set off from multiple starting locations within the RWS anomaly region. A Rossby ray is initialised every two degrees latitude and four degrees longitude within the RWS region. In each experiment, a total of 50 rays are released with 5 at each longitude and 10 at each latitude. The central coordinates are based on the location of the maximum RWS anomaly.

There are three possibilities for the ray trace on any timestep during the propagation. It could either propagate, reflect or terminate. The wave can reflect when it hits the reflecting surface of $\beta^*/U < k^2$, see blue regions in Figure 2.16. This can happen when β^* is large or U is small. When this happens, the sign of l is reversed and the wave is reflected. Note that the wave will become evanescent on the other side of the reflection as the square root becomes imaginary. Termination happens when the zonal wind becomes negative, see red regions in Figure 2.16. This is because Rossby waves cannot propagate in easterly winds and thus the wave is terminated. As the wave approaches a termination zone, wave number approaches infinite (see Equation (2.8)). For a stationary wave with constant wave number, one can view this as a slow down in the group velocity (see Equations (2.9 and (2.10)). This means that the wave can never approach the termination zone and can be viewed as being

³Note that the ray tracing is calculated in arbitrary units (both length and time) as my main interest is on the path of the Rossby wave and not the time taken for each intermediate step. This is because the wavetrain only takes approximately 18 days to reach the high latitude southern hemisphere from tropical heatings (see Li et al. (2015b) and Li et al. (2015a)), which is much shorter than the seasonal timescales that are used in Chapters 3 and 5.

absorbed. If the wave is neither in a reflection zone nor termination zone, it will propagate in a direction according to equation (2.12), see white regions in Figure 2.16. Note that during any time step, the winds and background fields from the closest grid point is used.

Following Li et al. (2015a), ray tracing is performed using zonal wavenumber 3 in this thesis. However, to explore the sensitivity to the choice of wavenumber, analysis using wavenumbers 1, 2, 4 and 5 are also carried out. These different wavenumbers shows only small differences in the path of the rays into the ASR and the overall picture is unchanged. Details on the comparison between wavenumbers can be found in Appendix E. Additionally, following Li et al. (2015a), a 2-D Gaussian filter is used on the β^* and U fields. This is because the Rossby waves (at wavenumber 3) are large and hence their propagation will not be overly affected by small scale features in the climatology. The Gaussian filter is set to have a radius of 15 degrees – this filters out much of the ‘noise’ in the background fields. If the filter is switched off, there may be situations where the waves would either terminate or reflect on one individual grid point of the wind. This is unrealistic as the waves will unlikely ‘see’ these small scale structures. The overall results are not highly sensitive to the exact size of the filter. Examples of ray tracing performed with different sizes of filters can be found in Appendix F.

Note that, while seasonal climatological fields are used for ray tracing, a test was conducted in which ray tracing was also performed for every individual season before summation.

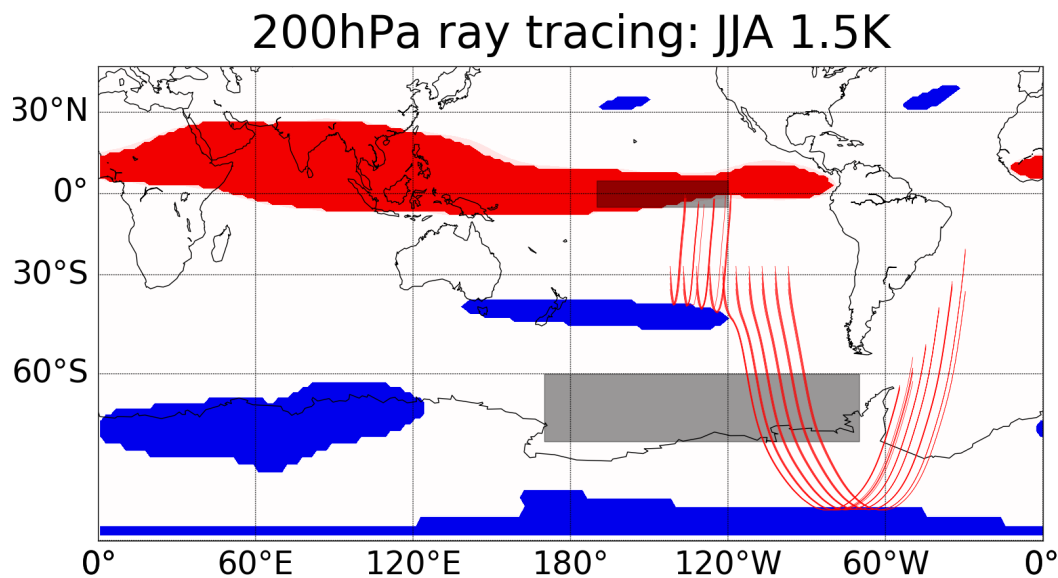


Fig. 2.16 Example of the Rossby wave ray tracing. Performed on 1.5 K El Niño run at 200 hPa in JJA. Red regions indicates termination zones, the blue regions indicates reflection zones and the white regions indicates propagation zones. Red lines indicate path of hypothetical Rossby waves. The shaded regions are the Niño3.4 region and the ASR.

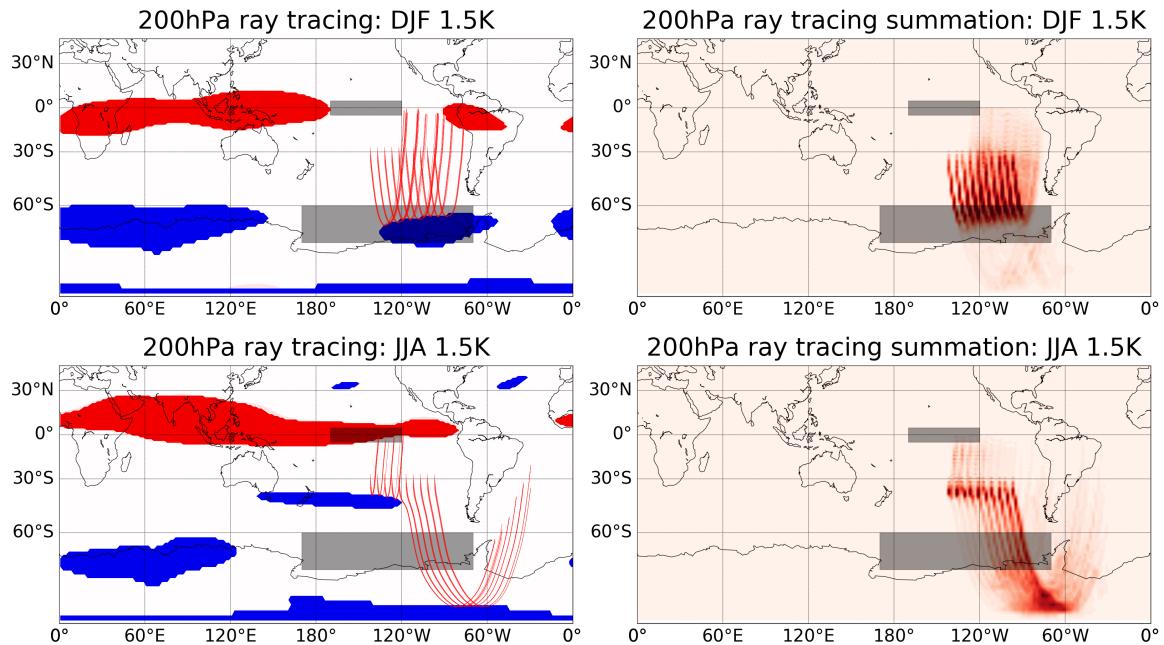


Fig. 2.17 Comparison of ray tracing performed on 54 year climatologically or individual seasons. Left: Performed using the 54 years climatology. Right: Performed on individual seasons before summation. The top panels show 1.5 K El Niño run in DJF and the bottom panels show 1.5 K El Niño run in JJA. These were chosen to represent reflection and propagation, respectively.

The results turned out to be similar between these methods, see Figure 2.17. The left panels on Figure 2.17 shows the Rossby wave tracing performed on the seasonal climatology, while the right panels shows ray tracing performed for every season before summation. The top row shows the 1.5 K El Niño experiment in DJF while the bottom row shows the JJA season. As seen from the figure, the paths of the hypothetical wave trains between the left and right panels are very similar. Since the results are largely independent of these particular methodological choices, the 54 years climatologies from the timeslice experiments were used for this thesis to save computational resources.

It is not clear whether the baseline or the perturbed climatologies should be used for calculating the Rossby wave ray tracing. For example, in order to calculate the 1.5K ray tracing, should the 1.5K climatological be used or should the baseline climatology with 1.5K RWS be used. The main argument for using the baseline climatology is because the climatology itself is affected by the wavetrain. Therefore it is potentially possible to form a circular argument (climatology changes wavetrain which changes climatology) if the baseline climatology is not used. However, there are also arguments against using the baseline climatology. One such argument is that the STJ (which causes the reflection zones) is not only affected by the wavetrain but also the intensification of the Hadley cell and other non-linearities. It is difficult to decouple the former and latter. In this thesis, the calculations

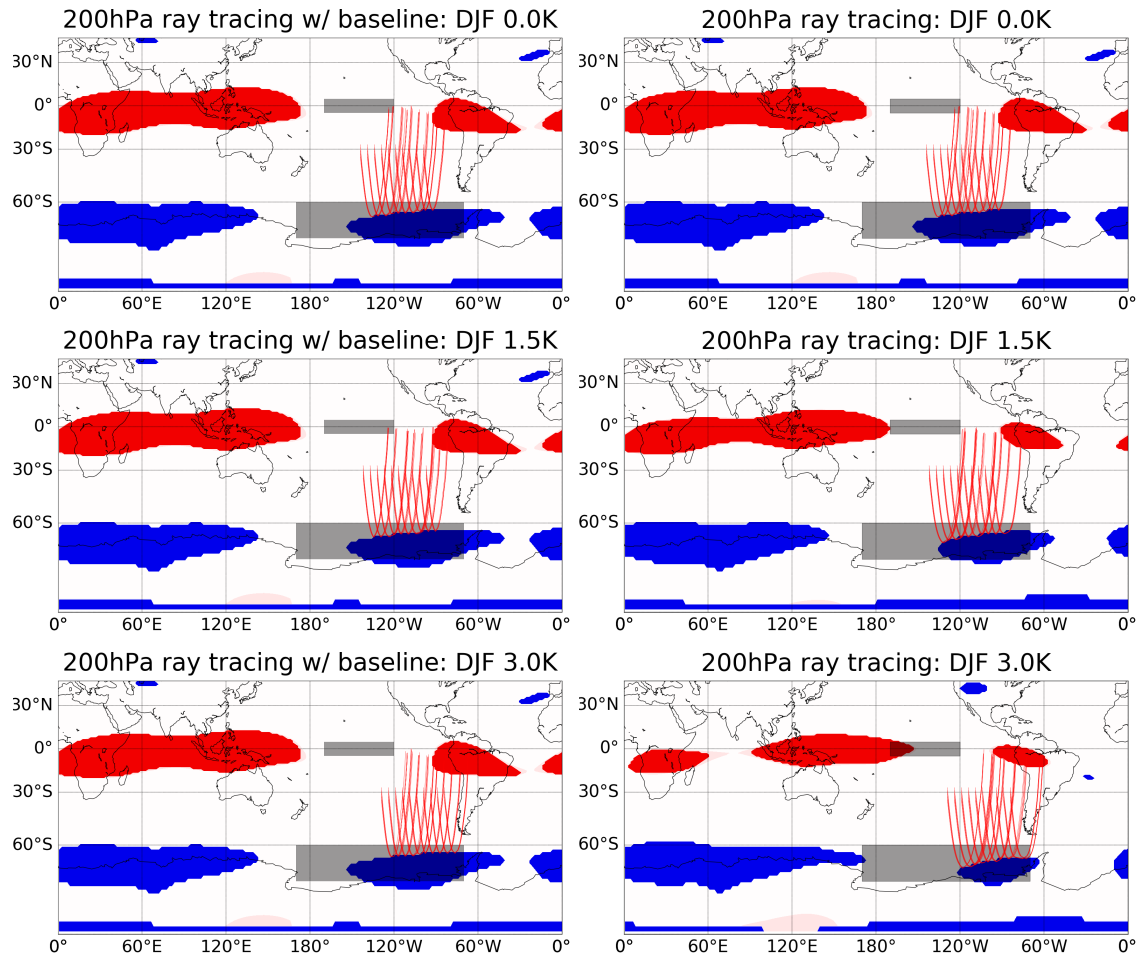


Fig. 2.18 Rossby wave ray tracing performed on the 0.0 K (top), 1.5 K (middle) and 3.0 K (bottom) El Niño runs for austral summer (DJF) with baseline (left) and perturbed (right) climatologies.

will use the perturbed climatology with the perturbed RWS. However, Figures 2.18 and 2.19 shows the ray tracing using the baseline climatology versus the perturbed climatology under DJF and JJA, respectively. As seen from Figure 2.18, there is little change in the path of the rays in DJF. The rays are reflected at approximately 60° S in both cases. In JJA, under the perturbed climatology, the amount of rays reaching the ASR decreases as El Niño conditions increase. This is due to the eastwards movement of the reflection zone. However, under baseline climatology, the reflections do not (cannot) move. Therefore, the same amount of rays reach the ASR under the different El Niño conditions. However, most importantly, the seasonality between the seasons is not lost. Regardless of the climatology used, there is propagation in JJA but reflection in DJF.

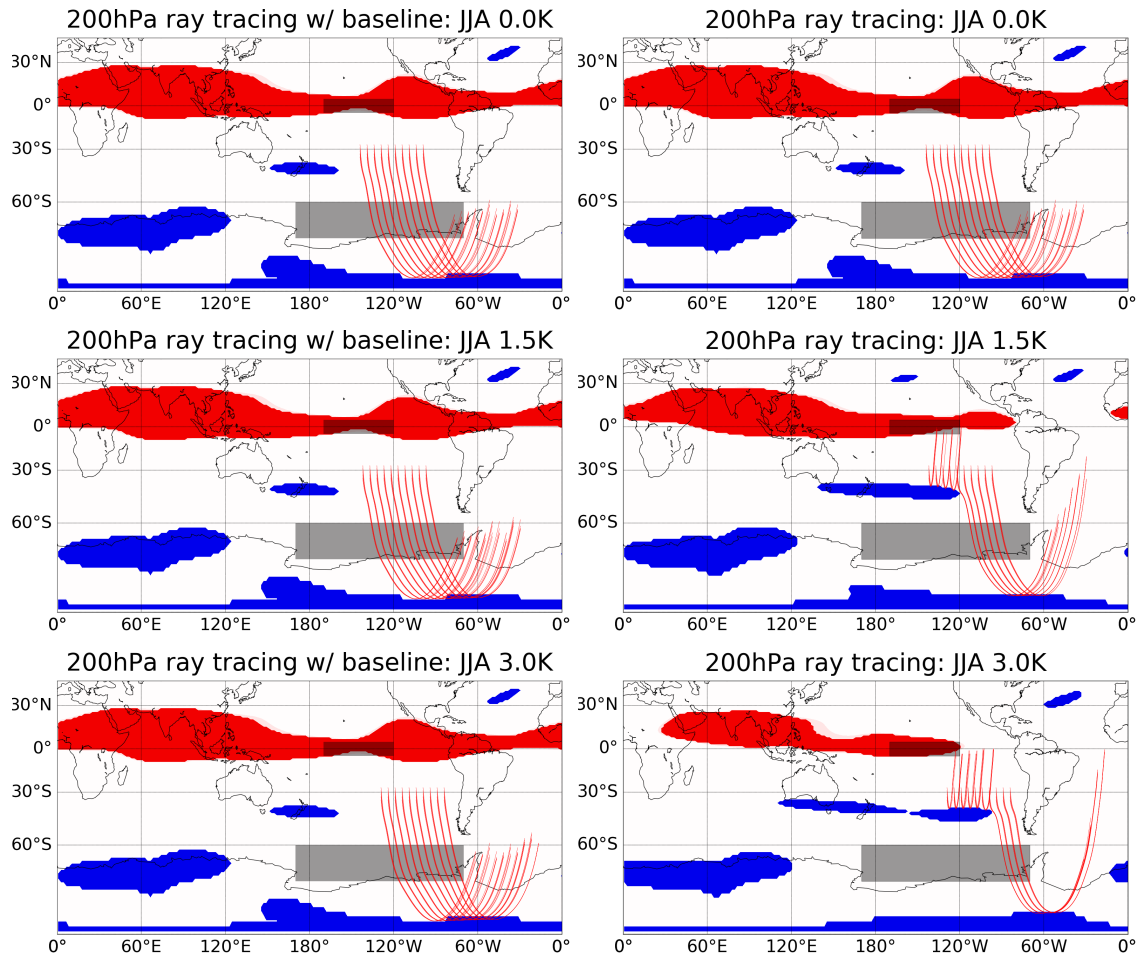


Fig. 2.19 Same as Figure 2.18 but for JJA.

In conclusion, while ray tracing uses several assumptions and has certain limitations, it is still a valuable method used to understand the propagation path of the hypothetical Rossby waves from source regions.

Wave activity flux

In addition to the RWS and ray tracing calculations, the wave activity flux in the experiments is derived following Plumb (1985). This combines information about the wave sources and wave propagation to give an overall quantitative picture of wave energy fluxes. Both the ray tracing and wave flux analysis provide useful information to understand and interpret teleconnection responses and thus both techniques are employed in this thesis. This thesis will only deal with the 2D wave flux (latitudinal and longitudinal directions). This is because the flux in the vertical direction is usually much smaller compared with that in the horizontal directions, see again Plumb (1985). The 2-D wave flux analysis is applied in the upper

troposphere, since this is the region of strong upper level divergence from convective motions which acts as a RWS. The model output fields in the upper troposphere are available on 170 hPa, 200 hPa and 250 hPa levels. The analysis here focuses on the 200 hPa level only. Following Plumb (1985), the 2D wave activity flux is given by

$$F_s = p \cos(\phi) \left(\begin{array}{c} v'^2 - \frac{1}{2\Omega a \sin 2\phi} \frac{\partial(v'\Phi')}{\partial\lambda} \\ -u'v' + \frac{1}{2\Omega a \sin 2\phi} \frac{\partial(u'\Phi')}{\partial\lambda} \end{array} \right), \quad (2.13)$$

where the prime denotes the remainder after removing the zonal averages at each latitude and height, p is pressure divided by 1000 hPa, u is the zonal wind, v is the meridional wind, Ω is the Earth's rotation rate, a is the radius of the Earth, ϕ is the latitude, Φ is the geopotential and λ is the longitude. Note that Plumb (1985) used the time-averaged flow for the calculation of the wave flux. It was defined as the time-averaged flow over 10 winters, for which data was available. Therefore, the 54 years climatologies from the timeslice experiments will be used for the wave flux calculation in my work.

2.6 Concluding remarks

In this chapter, background information about the global atmospheric model, existing model datasets and experimental setup have been presented. The experiments in this thesis used the HadGEM3 model. There are two sets of experiments: the time slice experiments and the 'switch on' transient experiments. The time slice experiments have various magnitudes of idealised perpetual ENSO SST anomalies imposed in the tropical Pacific and will be used in Chapters 3 and 5. The two sets of 'switch on' experiments have 53 ensemble members each and are initialised in May and November. These will be used in Chapter 4 to investigate the transient response of the ENSO-ASR teleconnection.

Model evaluation of the climatology and the ENSO-ASR teleconnection has also been carried out in this chapter. The model performs well in simulating the climatological large-scale features of the southern hemisphere circulation. Turning to the teleconnection, the model generally captures the teleconnections under El Niño conditions compared to the reanalysis dataset. It captures most of the structural changes with some magnitude differences when compared with reanalysis. Importantly, none of the differences in the SLP anomalies are statistically significant. However, the model does not perform as well in simulating the ENSO-ASR teleconnection under La Niña conditions. Critically, the SLP anomalies are statistically significantly different from ERA-Interim. Therefore, the La Niña experiments will not be used in any further analysis.

Rossby wave methods have also been discussed in this chapter. These include the Rossby wave source calculation, Rossby wave ray tracing and the wave flux calculation. The limitations and disadvantages of these methods have been described.

Chapter 3

The seasonality of El Niño teleconnections to the Amundsen Sea region

This chapter will investigate the seasonality of the ENSO–ASR teleconnection. Section 3.1 presents an overview of the scientific aim and the hypothesised mechanistic flowchart. The effects of the ENSO–ASR teleconnection will be presented in Section 3.2. Tropical circulation and their changes under El Niño will be discussed in Section 3.3. Section 3.4 focuses on the tropospheric jets under ENSO conditions. The Rossby wave source (RWS) will be investigated in Section 3.5. In particular, the focus is quantifying and explaining its changes under El Niño. Section 3.6 will discuss the propagation of Rossby waves. This section will mainly use ray tracing analysis and wave flux calculations. Section 3.7 presents some information on the ENSO–ASR teleconnection in austral summer (DJF). Lastly, the conclusions will be presented in Section 3.8.

3.1 Overview

The seasonality of the ENSO teleconnection to the ASL has always been a curiosity. As seen in Section 1.4, the observed teleconnection peaks in austral winter (JJA)/austral spring (SON) even though ENSO tends to peak in austral summer (DJF). While the teleconnection has been documented in the past (Chen et al., 1996; Lachlan-Cope and Connolley, 2006; Li et al., 2015b; Turner, 2004; Turner et al., 2013), the exact mechanism that causes these seasonal differences is still not fully understood. The main aim in this chapter is to investigate the seasonality of the teleconnection with a focus on comparing austral winter and summer

seasons. The chapter will largely use the El Niño timeslice HadGEM3 model runs. The transient response of the teleconnection will be covered in Chapter 4. A specific objective of this chapter is to understand the teleconnection mechanism ‘step-by-step’ and visualise it as a flowchart, which is conceptually similar to the Atlantic teleconnection flowchart produced by Simpkins et al. (2014).

3.2 Effect of the teleconnection

This section discusses the SLP changes in the Amundsen Sea region (ASR) under El Niño conditions in the HadGEM3 runs. Figure 3.1 shows the annual mean SLP anomaly for the 1.5 K and 3.0 K El Niño runs. Note that all figures shown in this chapter are time averaged over the 54 years of the HadGEM3 runs unless specified otherwise. During El Niño events, the ASL weakens (positive SLP anomalies in the ASR) in agreement with previous literature. Moreover, the SLP anomalies strengthen under stronger El Niño conditions (Figure 3.1). Details regarding the linearity of this change are discussed in Chapter 5. The SLP anomalies show wavetrain-like structure emanating from the tropical Pacific. This is similar to the Pacific–South–America (PSA) wave train and may suggest that the mechanism of the teleconnection is related to modulating the PSA wavetrain. Note that the anomaly does not necessarily coincide exactly with the ASL. In fact, the position of the ASL (and the anomaly) is highly variable and changes every year. However, in general, a positive (negative) anomaly in the ASR would mean a weaker (stronger) ASL.

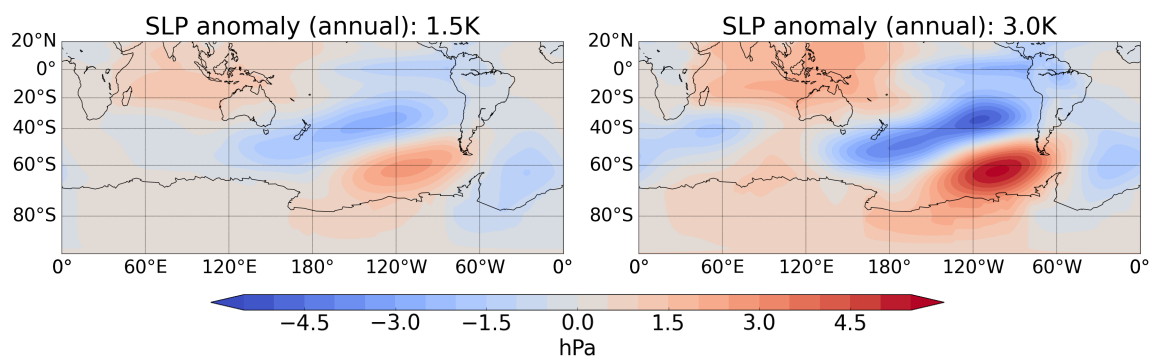


Fig. 3.1 Anomalous annual time-means (over 54 years climatology) SLP under 1.5 K and 3.0 K (Niño3.4 temperature) El Niño conditions. Units are in hPa.

As discussed in Section 1.4, there are different teleconnection responses in different seasons (e.g. Jin and Kirtman (2009); Turner et al. (2013)). Figure 3.2 shows the SLP anomaly for the 1.5 K El Niño run in the four seasons. Previous studies have found that the El Niño teleconnection to the ASL is maximal during austral winter (and autumn) and minimal during

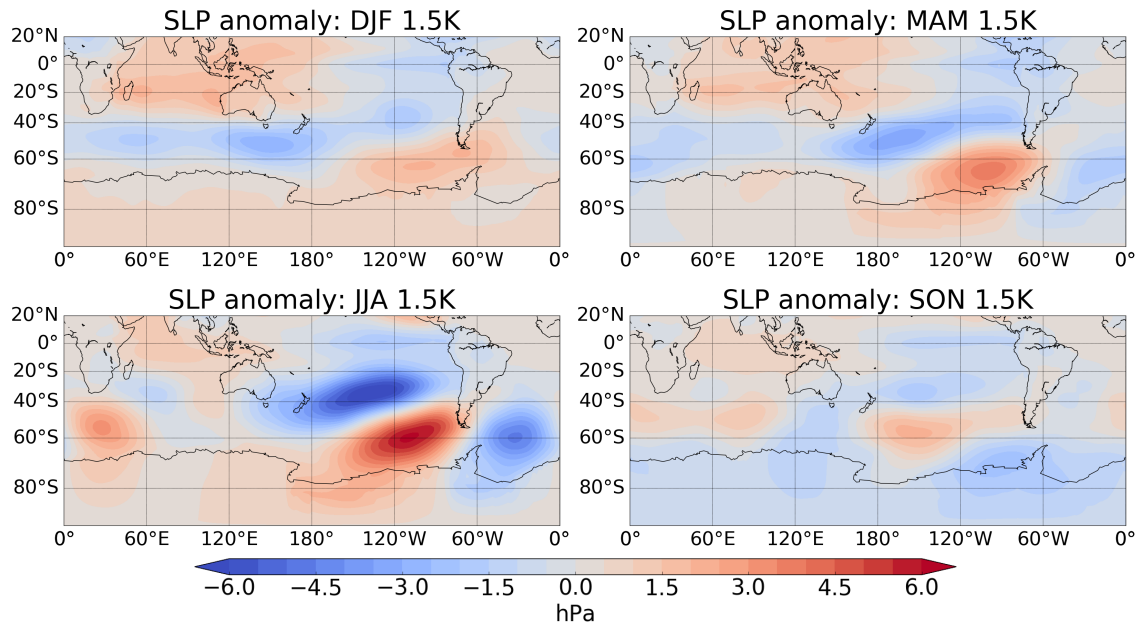


Fig. 3.2 Seasonal time-measured (over 54 years climatology) SLP anomalies under 1.5 K (Niño3.4 temperature) El Niño conditions. Units are in hPa.

austral summer (and, depending on the study, also weak in spring) in both observations and reanalysis. Figure 3.2 also shows a maximum teleconnection response in austral winter in HadGEM3. Note that, as will be discussed later in Chapter 4, the seasonal response of the teleconnection may be approximated to reanalysis even though the imposed SST forcing is perpetual in the HadGEM3 experiments.

In addition to the 1.5 K El Niño runs, the *peak* SLP anomalies of various El Niño magnitudes in all four seasons are shown in Figure 3.3. The SLP anomaly is strongest in JJA in runs with tropical anomalies between 0.75–2.25 K¹ and in MAM for 3.0 K. The SLP anomaly is weakest in SON for the El Niño magnitudes between 0.75–1.5 K and weakest in DJF for amplitude between 2.25–3.0 K. However, note that the SLP anomalies between SON and DJF are not statistically significantly different. However, Figure 3.3 only shows the *peak* SLP anomaly and contains no information regarding its areal size or structure. This information is found in the maps of Figure 3.2, where structural differences in the SLP anomaly between DJF and SON are evident. While SON contains a slightly stronger, but not statistically significantly stronger, SLP anomaly, the anomaly has a smaller spatial extent compared to DJF. Furthermore, the structure of the SLP anomaly in SON is closer to an EOF2 pattern (like in JJA) in comparison to the EOF1-like structure in DJF. As this may indicate different mechanisms (for details, see Section 3.7), this chapter will focus on DJF

¹3.0 K JJA seem to have a lower SLP anomaly than 2.25 K. This will explore this in Chapter 5.

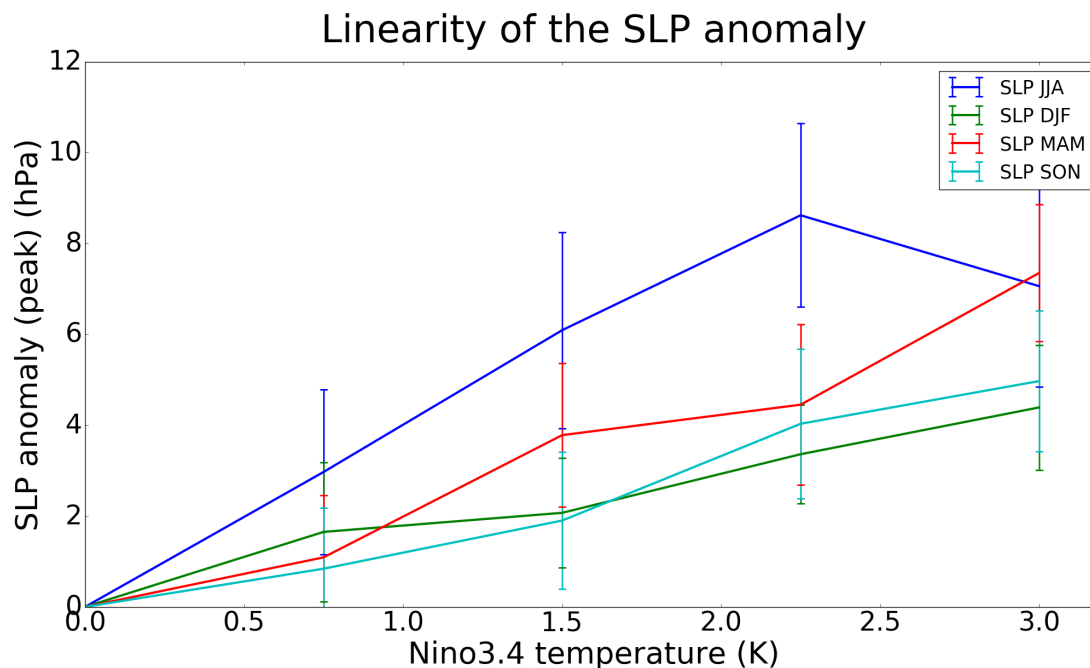


Fig. 3.3 SLP in the four seasons under four different El Niño (0.75 K, 1.5 K, 2.25 K, 3.0 K) conditions.

and JJA only. These seasons represent the minimum and maximum SLP changes under El Niño, respectively.

The left panels of Figure 3.2 show the anomalous time–meaned SLP for austral summer (DJF) and austral winter (JJA), respectively. The magnitude and the structure are both very different between the two seasons. Similar to previous literature, the maximum magnitude of the SLP change in HadGEM3 is significantly stronger in JJA compared with DJF². Furthermore, the structure of the SLP anomalies in JJA are wavetrain-like. They seem to have a similar structure to the PSA (EOF2). The alternating negative–positive–negative SLP changes can be seen extending from around approximately 30°S, 110°W towards the ASR and then towards the Weddell sea. Note that the origin has slight variation in longitude as the strength of the El Niño event changes. Conversely, the anomaly in DJF is spread more zonally. It envelops the whole of Antarctica with a weak maximum located around the ASR. DJF seems to reflect a SAM–like (EOF1) signal due to its zonal symmetry. This may hint at different teleconnection mechanisms between the two different seasons.

The standard error of the SLP in DJF and JJA in the baseline model run is shown in Figure 3.4. In DJF, the error peaks at around 0.5 hPa while it peaks at around 0.8 hPa in JJA

²Again, at this point in the text, it has not been established if perpetual El Niño experiments may even be approximated to reanalysis. However, Chapter 4 demonstrates that perpetual El Niños should not provide an additional effect on seasonal timescales as the ENSO–ASR teleconnection timescale is significantly lower than one season.

in the ASR. This means that most of the ASR SLP changes in Figure 3.2 are statistically significant. It is important to note that the value quoted is the standard error, not the standard deviation. Since there are 54 years of data per experiment, the standard deviation would be around 4 hPa and 6 hPa, respectively.

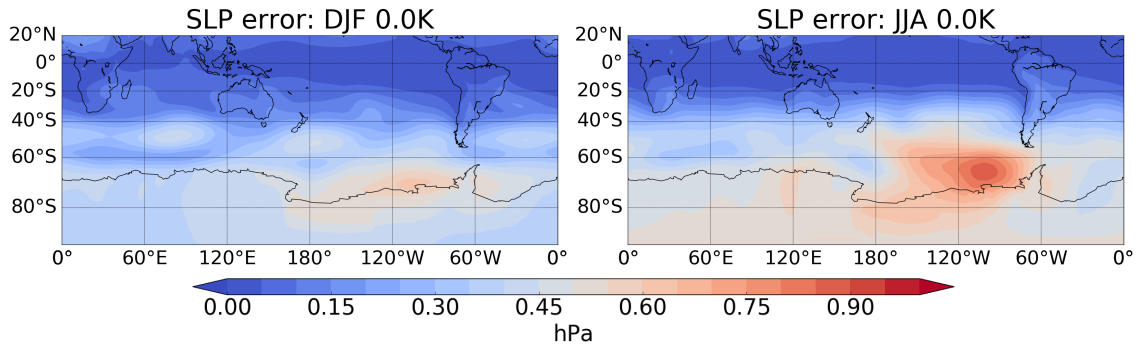


Fig. 3.4 Seasonal standard error of the SLP in the baseline (0.0 K) run.

Summary

This discussion has focused on the SLP anomalies in connection with the ENSO–ASR teleconnection. There are two key results. Firstly, the SLP anomaly due to El Niño in the ASR is mostly strongest in JJA and weakest in DJF. Secondly, the structure of the SLP anomalies are different between seasons. It is a PSA–like pattern in JJA and EOF–like in DJF.

3.3 ENSO and tropical circulation

Moving on to the tropical circulation, one parameter that can be used as a proxy for tropical circulation is the precipitation rate because increased tropical circulation causes more warm moist air to rise from the surface, leading to increased precipitation. Figure 3.5 shows the precipitation rate (annual climatologically, time–meaned) for the HadGEM3 model runs under baseline and El Niño (1.5 K and 3.0 K) conditions. In the baseline run, there are two branches of the intertropical convergence zone (ITCZ): one in the northern hemisphere and another in the southern hemisphere (easily seen between 0–20°S, 120–180°E). This double ITCZ is a known issue in models and usually does not reflect reality. For example, Hubert et al. (1969) found that a double ITCZ rarely exist in satellite observations. HadGEM1 (the predecessor to HadGEM3) is known to show a climatological double ITCZ structure (Lin, 2007). In Atmospheric Model Intercomparison Project (AMIP) runs, the southern branch is

commonly seen because of excess precipitation in the tropics, see again Lin (2007). This is associated with overly strong trade winds, excessive surface latent heat flux and not enough surface shortwave flux which causes the southern branch to appear. The northern branch of the ITCZ reflects reality more than the southern branch.

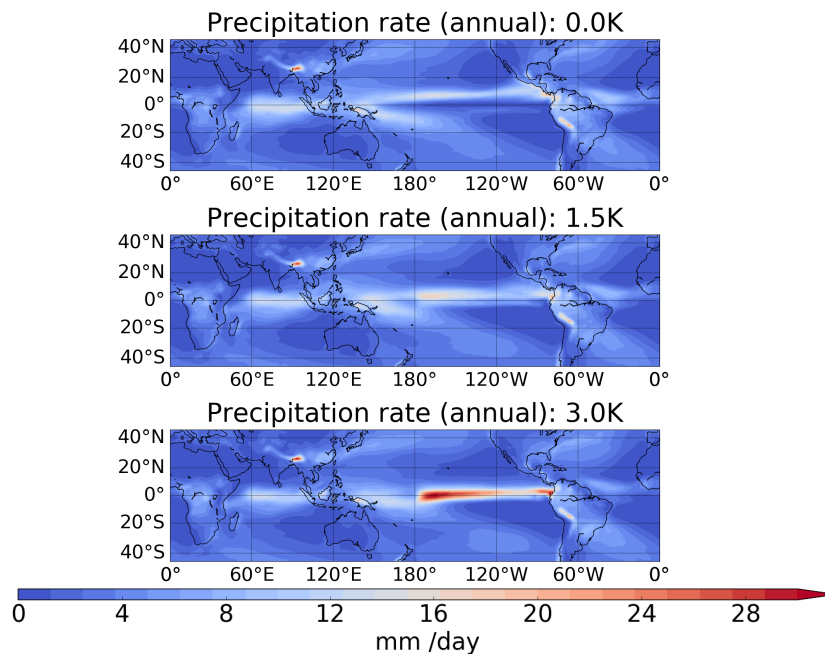


Fig. 3.5 Absolute time-meaned (over 54 years climatologies) annual precipitation rate under baseline (0.0 K) and (1.5 K and 3.0 K) El Niño conditions. Units are in mm / day.

In the baseline model run (top panel, Figure 3.5), the ITCZ lies at around 0°N–10°N. This agrees with previous literature. As the El Niño strength increases, the ITCZ shifts towards the south and increases in strength, as found by Schneider et al. (2014). Note that under extremely strong El Niño conditions (3.0 K), the model shows that the ITCZ has shifted enough to almost reach the equator (bottom panel, Figure 3.5). This is because the warmer SSTs in the tropics drive increased vertical uplift and thus an intensified Hadley circulation. However, while it is obvious that the ITCZ has strengthened, caution must be exercised when interpreting the magnitude of change in the precipitation. This is because the southern branch of the ITCZ, which is a model artifact, seems to shift northwards as the El Niño increases in magnitude. During strong El Niños, the northern and southern branches overlap at the equator. It is unclear how much of the change comes from the strengthening of the Hadley cell (and thus the ‘real’ ITCZ) and how much is from the summation of the two branches overlapping.

I have also looked at the seasonal precipitation anomalies in austral summer (DJF) and austral winter (JJA) (not shown). The starting latitude and strength of the ITCZ differs

between the two seasons, but they show a structurally similar change under El Niño: the ITCZ shifts southwards and strengthens.

Turning to another tropical circulation proxy, Figure 3.6 shows the anomalous outwards longwave radiation (OLR) at the top of the atmosphere (TOA) in the 1.5 K El Niño run during austral summer (DJF) and austral winter (JJA). Note that under El Niño conditions, the OLR decreases at the equator and increases off-equator to the north and south which suggests an increase in cloud fraction and cloud height at the equator but slight decrease off-equator. Similar to the changes in the precipitation, the difference between the seasons under El Niño are minimal.

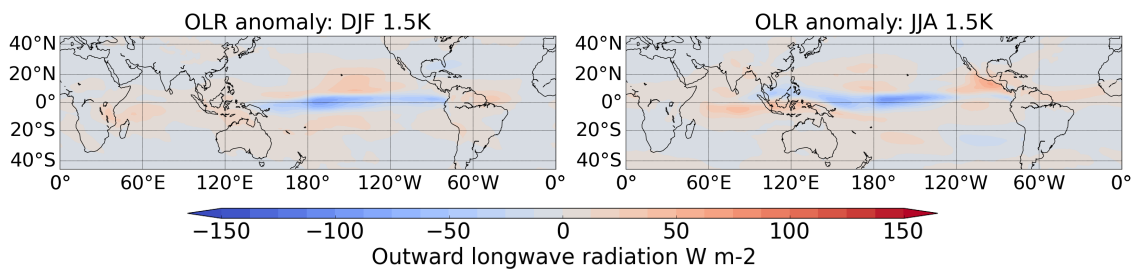


Fig. 3.6 Seasonal time-measured (over 54 years climatologies) OLR (TOA) *anomaly* under (1.5 K) El Niño conditions under austral summer (DJF) and austral winter (JJA). Units are in W m^{-2} .

Other proxies such as cloud top height and cloud bottom height show a similar story (details in Appendix G): the tropical circulation strengthens under El Niño.

Having established that El Niño affects the position of the ITCZ and precipitation rates, the following will explore its effect on the strength of the mass streamfunction as a measure of the Hadley cell. Understanding the changes in the Hadley cell can provide further insights into the changes of the tropospheric jets.

Figure 3.7 shows the zonal mean mass streamfunction in austral summer (DJF) and austral winter (JJA) for the 1.5 K El Niño run. This can be compared to Lu et al. (2008) who studied the response of the zonal mean atmospheric circulation under El Niño compared to global warming. They found that under El Niño conditions, the Hadley cells tend to intensify and contract equatorwards. The Ferrel cells (in particular in the southern hemisphere) also move equatorwards. The solid contours in Figure 3.7, showing results from HadGEM3, represent the baseline mass streamfunction while the coloured contours represents the changes under El Niño conditions. In DJF (JJA), there is an increase (decrease) in the streamfunction close to the centre of the cell and decreases (increase) on the edges. This will intensify and contract the Hadley cell in both seasons as the cell is positive in DJF but negative in JJA. These changes are consistent with Lu et al. (2008).

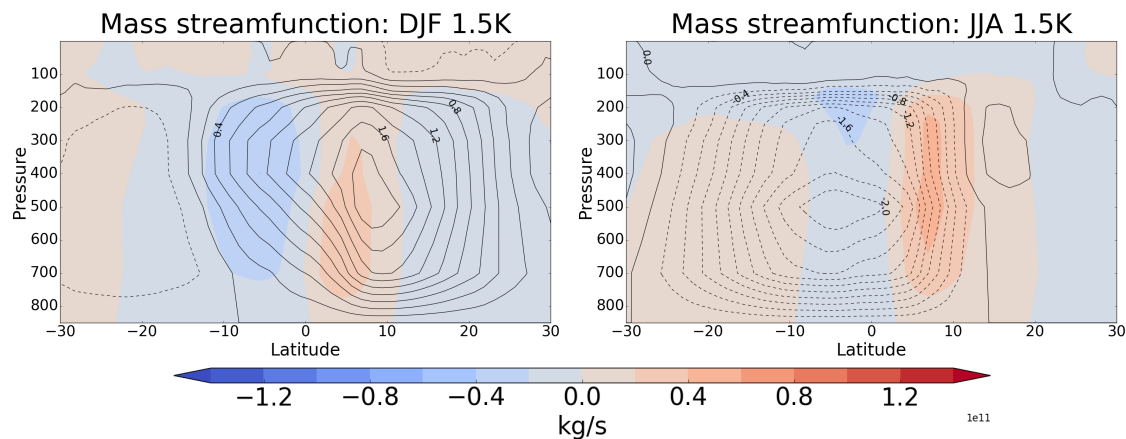


Fig. 3.7 Seasonal time-measured (over 54 years climatologies) mass streamfunction in austral summer (DJF) and austral winter (JJA). The solid contours show the mass streamfunction during neutral (baseline) conditions. The coloured contours show the mass streamfunction anomalies under the 1.5 K El Niño condition. Units are in $10^{11} \text{ kg s}^{-1}$.

Summary

The above results show that the tropical circulation strengthens under El Niño conditions. Proxies such as precipitation, outwards longwave radiation, cloud top height and cloud bottom height has been used as proxies for the tropical circulation. All these proxies show the same strengthening.

Additionally, the results shows that the tropical circulation cells strengthen and contract under El Niño conditions. This is consistent with Lu et al. (2008).

3.4 Jet movement

As it will be discussed later in Section 3.5, the jets are crucial to Rossby wave source (RWS) generation. This section discusses changes in the tropospheric jets under El Niño in HadGEM3. In particular, it is important to understand the effect El Niño has on the structure of the zonal winds.

As seen in Section 3.3, the circulation cell contracts under El Niño conditions (Gallego et al., 2005; Lu et al., 2008). This is expected to cause the subtropical jet (STJ) to also shift equatorwards (Gallego et al., 2005). Furthermore, as the Ferrel cell shifts equatorwards (Lu et al., 2008), the polar front jet (PFJ) is also expected to be further equatorwards during El Niño. Additionally, in the winter hemisphere, the circulation cell is expected to strengthen (Gallego et al., 2005; Lu et al., 2008). This will be associated with a stronger STJ.

Figure 3.8 shows the latitude–pressure profiles of the zonal averaged zonal wind in DJF and JJA for the 1.5 K and 3.0 K El Niño model runs. The solid contours show the wind speed for the baseline model run while the coloured contours show the wind speed anomaly under El Niño conditions. The climatological wind structure is different between the two seasons. In DJF, there is a maximum in wind speed of approximately 32 m s^{-1} at around 50°S , 200 hPa; this is the PFJ while the STJ is weak in the summer. Its latitude matches with previous literature such as Gallego et al. (2005). In JJA, the maximum wind speed of approximately 50 m s^{-1} is found at around $25\text{--}30^\circ\text{S}$, 200 hPa; this is the STJ. Its latitude matches with previous studies such as Van Heerden and Taljaard (1998), Vincent (1998) and Gallego et al. (2005). Note that there is also a weaker zonal wind maximum at around 45°S , 200 hPa. As seen in previous studies (Barnes and Polvani, 2013; Galvin, 2007), this is the PFJ as JJA is characterised by two distinct jets in the southern hemisphere.

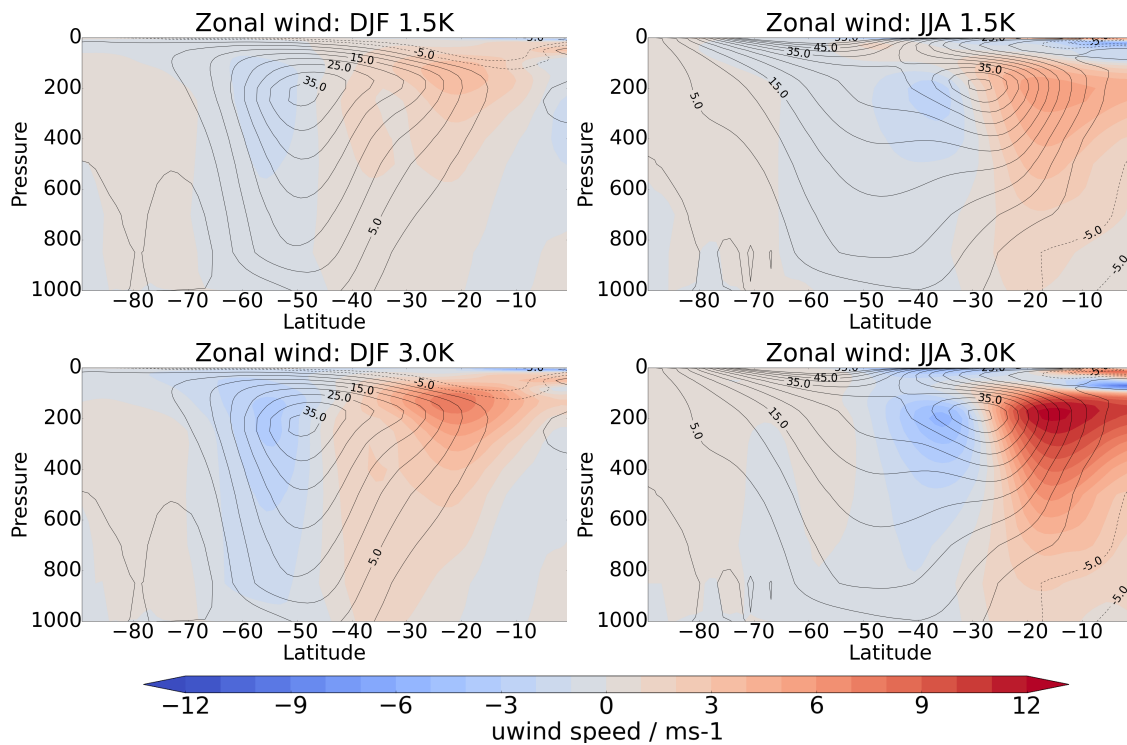


Fig. 3.8 Seasonal time-measured (over 54 years climatologies) zonal-mean zonal wind in austral summer (DJF) and austral winter (JJA). The solid contours show baseline zonal winds while the coloured contours show the anomalies under El Niño conditions (1.5 K and 3.0 K). Units are in m s^{-1} .

Under El Niño conditions in austral summer (DJF), there are positive zonal wind anomalies north of the PFJ and negative wind anomalies south of the PFJ. The maximum of the positive anomaly is located at around $\sim 25^\circ\text{S}$, $\sim 150 \text{ hPa}$ while the negative anomaly max-

imises at $\sim 55^\circ\text{S}$, ~ 200 hPa. Note that the centre of the positive anomaly is far from the PFJ³ and thus has little effect on it. However, the negative anomaly lies closer to the PFJ and thus will reduce its intensity. This weakening matches with previous literature (Gallego et al., 2005).

The anomalous zonal mean zonal wind under El Niño conditions in austral winter (JJA) have different magnitude and structure compared to austral summer (DJF). There are positive anomalous zonal wind speeds northwards of the STJ and negative anomalies southwards of the STJ. However, the positive anomaly (peak) is located around $\sim 20\text{--}25^\circ\text{S}$, $\sim 200\text{--}400$ hPa while the negative anomaly is approximately at $\sim 35^\circ\text{S}$, ~ 200 hPa. The positive anomaly is much stronger in JJA compared with DJF. For example, in the 3.0 K El Niño run, the peak strength of the positive anomaly in JJA is $>12\text{ m s}^{-1}$ while it is only $\sim 7\text{ m s}^{-1}$ in DJF. Furthermore, due to the different location of the jets in the different seasons, the positive anomaly centre lies very close to the northwards side of the STJ core. The weaker negative anomaly (compared to the positive anomaly in JJA) is also very close to the southwards side of the STJ core. The net effect of this is that the STJ shifts equatorwards and strengthens. This strengthening agrees with previous literature (Gallego et al., 2005).

Figure 3.9 shows the zonal wind anomaly for the 1.5 K El Niño model run during austral summer (DJF) and austral winter (JJA) at 200 hPa. Again, the solid contours show the baseline zonal wind speeds and the coloured contours show the changes under El Niño conditions. In JJA, the strongest zonal wind speeds are located around 30°S , $90^\circ\text{E}\text{--}150^\circ\text{W}$. Under El Niño conditions, there is a strong positive anomaly approximately located at 30°S , 130°W and a negative anomaly at approximately 40°S , 120°W . This dipole shifts the maximum winds towards the east. In DJF (200 hPa), the climatological maximum wind speed is located around 50°S , $50^\circ\text{W}\text{--}150^\circ\text{E}$. Under El Niño conditions, the zonal wind speed anomalies in DJF are weaker in strength and more zonally symmetric compared with JJA. The zonal wind speeds in Figure 3.8 and 3.9 will be important in explaining the RWS in Section 3.5.

Summary

This section shows results concerning the changes in zonal wind structure in the southern hemisphere under El Niño and their relation to changes in the subtropical and polar front jet. During JJA, the STJ is strongest while the PFJ is strongest during DJF.

As seen in Section 3.3, the Hadley cell strengthens and contracts. In JJA, this is associated with an acceleration and equatorwards shift in the STJ under El Niño conditions. This is

³This anomaly does lie near the weak STJ in DJF. However, as the STJ is weak, this has little effect.

consistent with previous works (Gallego et al., 2005). In DJF, the PFJ weakens (slightly) and shifts equatorwards (slightly) under El Niño conditions.

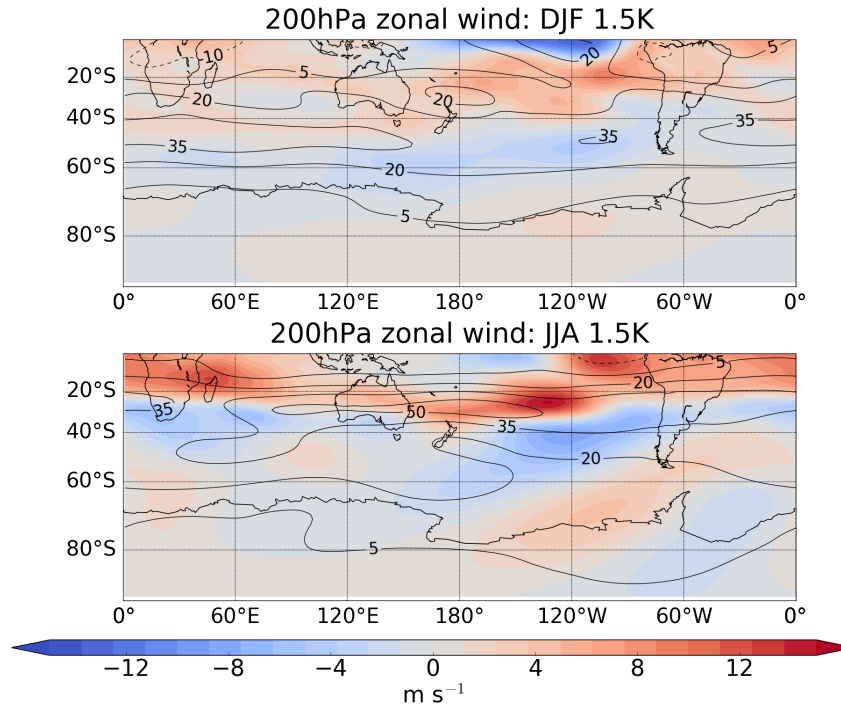


Fig. 3.9 Seasonal time-measured (over 54 years climatologies) 200 hPa zonal wind in austral summer (DJF) and austral winter (JJA) under (1.5 K) El Niño conditions. Units are in m s^{-1} .

3.5 Rossby Wave Source

With any physical phenomenon that connects two geographically separate locations, there must be a source and a method of propagation. Without either a source or propagation mechanism, there cannot be a transmission between the two locations. This applies equally to the ENSO teleconnection to the ASR. In order to understand the seasonal difference in the teleconnection mechanism, it is necessary to investigate the seasonal changes of the source and propagation terms. This section will focus on the Rossby wave source under El Niño conditions.

3.5.1 Quantifying the changes in the Rossby wave source

Rossby wave propagation via modulation of the PSA has been hypothesized as a possible ENSO teleconnection mechanism to the high latitudes (Jin and Kirtman, 2009; Schneider

et al., 2011). However, Rossby waves can propagate only in westerly wind flows and terminate if they hit the $U = 0$ (zonal wind) line, see equation (2.12). At first sight, this may seem to present a problem as the tropics have easterly flow, see Figure 3.10. However, it is important to note that the RWS generated from a tropical heating source may not be located at the same location as the heating, see for example Li et al. (2015a). Similarly, Sardeshmukh and Hoskins (1987) found that ‘for heating embedded in the equatorial easterlies, the major part of this “effective Rossby wave source” is then not in the easterlies at all, but lies nearer the subtropical westerly jets and its intensity depends upon the strength and sharpness of those jets.’

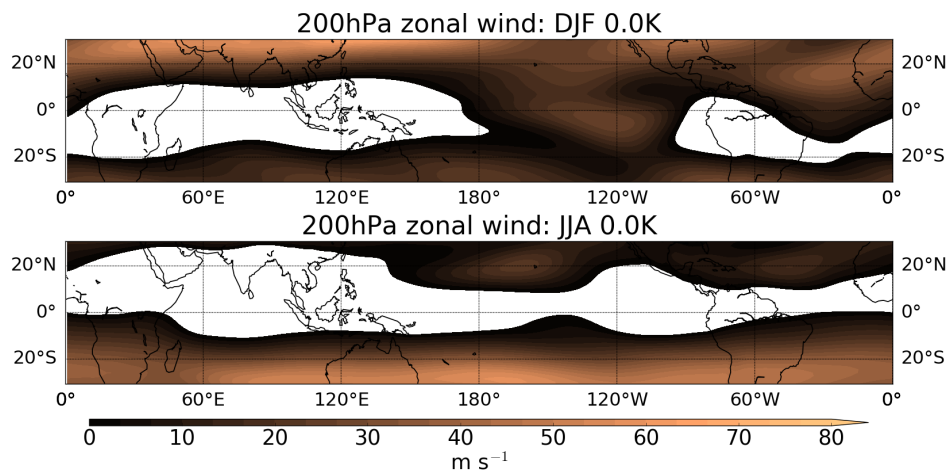


Fig. 3.10 Seasonal tropical time-measured (over 54 years climatologies) 200 hPa zonal wind in austral summer (DJF) and austral winter (JJA) under (1.5 K) El Niño conditions. Areas with zonal wind of 0 m s^{-1} or below are whited out. Units are in m s^{-1} .

The RWS was calculated following equation (2.6) and the methods shown in Section 2.5. Figure 3.11 shows the RWS at 200 hPa for the model runs. The top row shows the *absolute* RWS for the baseline run. The middle and bottom row shows the RWS *anomaly* for the 1.5 K and 3.0 K El Niño runs, respectively. The coloured contours show the RWS while the arrows show the *absolute* wind speed and direction. As seen from Figure 3.11 (left panels, middle and bottom row), there is little changes to the RWS (close to zero RWS anomaly) under El Niño conditions in austral summer (DJF). Note that in DJF, the majority of the RWS is located in the northern hemisphere (not shown). There are stronger RWS anomalies in austral winter (JJA) under El Niño conditions (right panels, middle and bottom row). In JJA, there is a strong positive RWS anomaly located at approximately 30°S , $100\text{--}120^\circ\text{W}$. The peak magnitude of this anomaly is approximately $5.5 \times 10^{-10} \text{ s}^{-1}$ in the 1.5 K El Niño run and over $7.5 \times 10^{-10} \text{ s}^{-1}$ in the 3.0 K El Niño run. There is also a weaker negative RWS anomaly located at around 30°S , $150\text{--}180^\circ\text{W}$. These changes are of a comparable magnitude

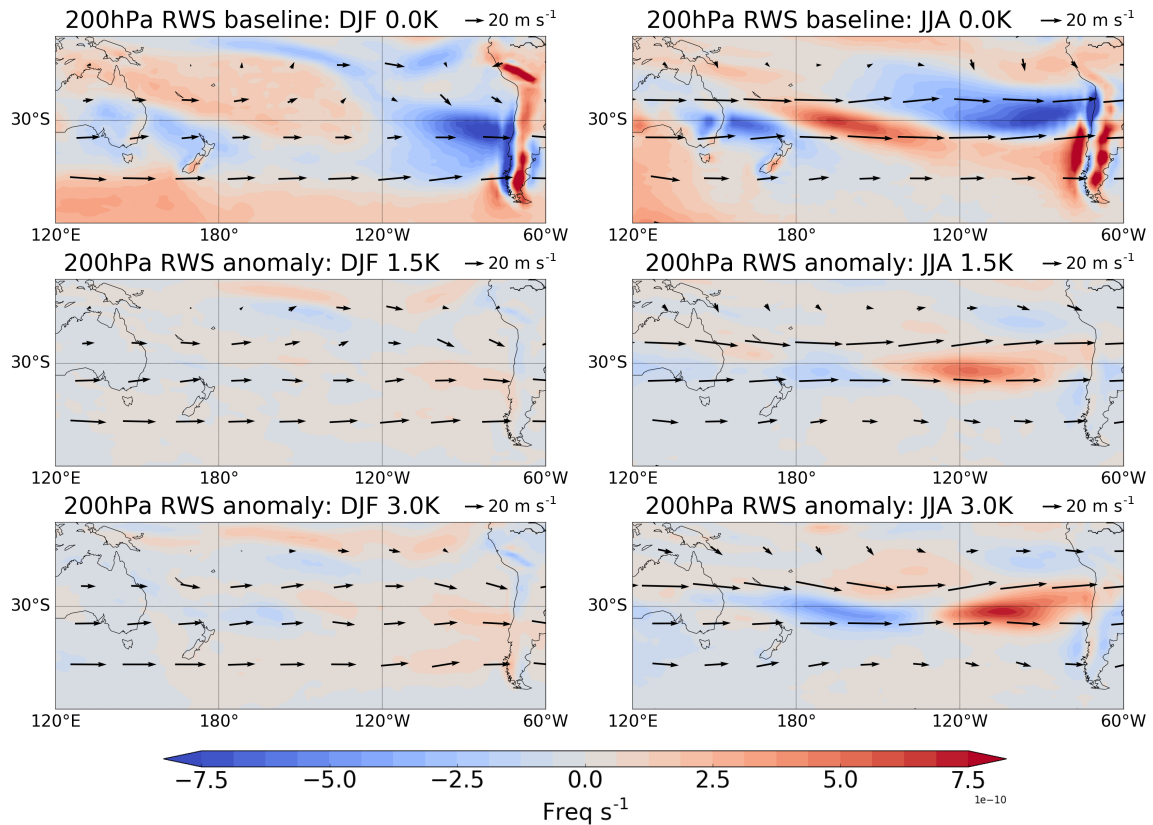


Fig. 3.11 Seasonal RWS in austral summer (DJF) and austral winter (JJA). The RWS is calculated from the 54 years climatology of each experiment. Arrows show the wind direction and speed. Top row: baseline, middle row: 1.5 K, bottom row: 3.0 K. Left column: DJF, right column: JJA. Units are in s^{-1} .

to the *absolute* RWS in the baseline run. Note that the strong Rossby wave sources near the Chilean coast may be due to the orography found in this area.

There are three terms in the RWS equation: ζD , $v_{\chi_x} \nabla \zeta_x$ and $v_{\chi_y} \nabla \zeta_y$, see again equation (2.6). Figure 3.12 shows the contributions from each term for the 1.5 K El Niño run. The top left panel shows the total RWS anomaly, the top right panel shows the contribution from the first term (ζD), the bottom left panel shows contributions from the second term ($v_{\chi_x} \nabla \zeta_x$) and the bottom right panel shows contributions from the third term ($v_{\chi_y} \nabla \zeta_y$). Most of the change in RWS in JJA can be explained by the ζD term, where ζ is the absolute vorticity and D is the divergence of the wind.

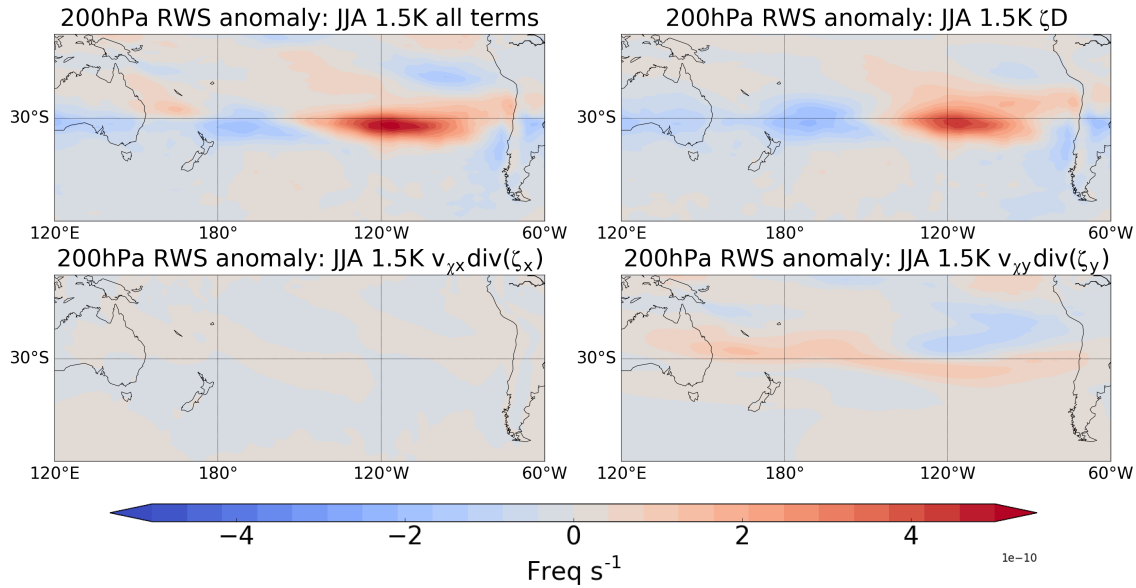


Fig. 3.12 Contributions of each RWS terms to the overall RWS anomaly in austral winter (JJA) under (1.5 K) El Niño conditions. Top left panel shows the total RWS anomaly, top right panel shows the first RWS term (ζD), bottom left panel shows the second RWS term ($v_{\chi_x} \nabla \zeta_x$), bottom right panel shows the third RWS term ($v_{\chi_y} \nabla \zeta_y$). Units are in s^{-1} .

3.5.2 Explaining the changes in the Rossby wave source

Figure 3.13 shows the *absolute* values of the zonal wind U , meridional wind V , horizontal divergence D , absolute vorticity ζ and ζD in the baseline (0.0 K), 1.5 K El Niño and 3.0 K El Niño runs during austral winter (JJA) and austral summer (DJF), respectively.

In austral winter (JJA), there is a strong STJ over the Pacific sector in the baseline run (top row of Figure 3.13). The jet becomes stronger as the El Niño increases in magnitude. The maximum zonal wind speed location (MZWL) also shifts towards the east during El Niño conditions. The meridional wind (second row) is positive on the northeast side and negative on the southeast side of the MZWL in the baseline model run. This is associated with divergence to the east side of the MZWL, see Figure 3.13 third row. There is also negative meridional wind on the northwest side and a positive meridional wind on the southwest side of the MZWL. This creates a convergence on the west side of MZWL. As the Niño3.4 temperature increases, the quadrupole structure of meridional wind intensifies and tracks the maximum zonal wind location (MZWL) towards the east. This is associated with the regions of divergence and convergence to strengthen and shift eastwards as well.

Turning to vorticity (fourth row), it increases at 30°S and extends eastwards as the El Niño strength increases. While the percentage increase of the peak vorticity at 30°S does not seem large, it is essential for the RWS to be established. As an example, in the 3.0 K El Niño

run, the RWS could not have been established as strongly if the model had the divergence field from the 3.0 K run but the vorticity field from the baseline.

In austral summer (DJF), the STJ is weak compared to in JJA. Additionally, the changes in the zonal wind under El Niño conditions in the Pacific region at $\sim 30^\circ\text{S}$ are also small

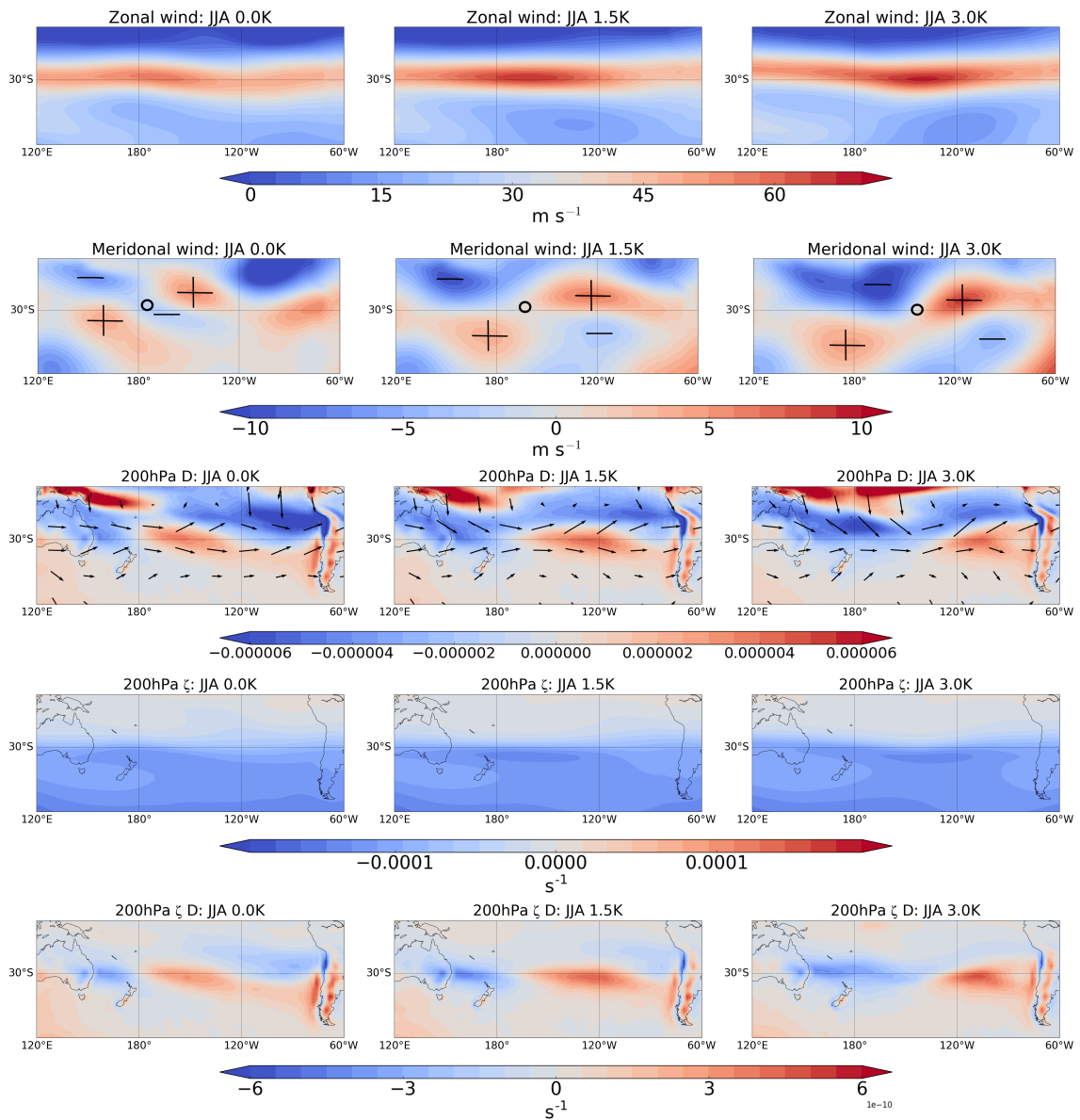


Fig. 3.13 Absolute zonal wind, meridional wind, divergence, absolute vorticity and ζD in austral winter (JJA) under baseline (0.0 K) and El Niño (1.5 K and 3.0 K) conditions. The top row shows the zonal wind. The second row shows the meridional wind. The third row shows the divergence in coloured contours. The arrow vectors show the wind speed and direction. Note that the meridional wind has been enhanced by a factor of five in these vectors to aid visualisation. The fourth row shows the absolute vorticity. The bottom row shows ζD .

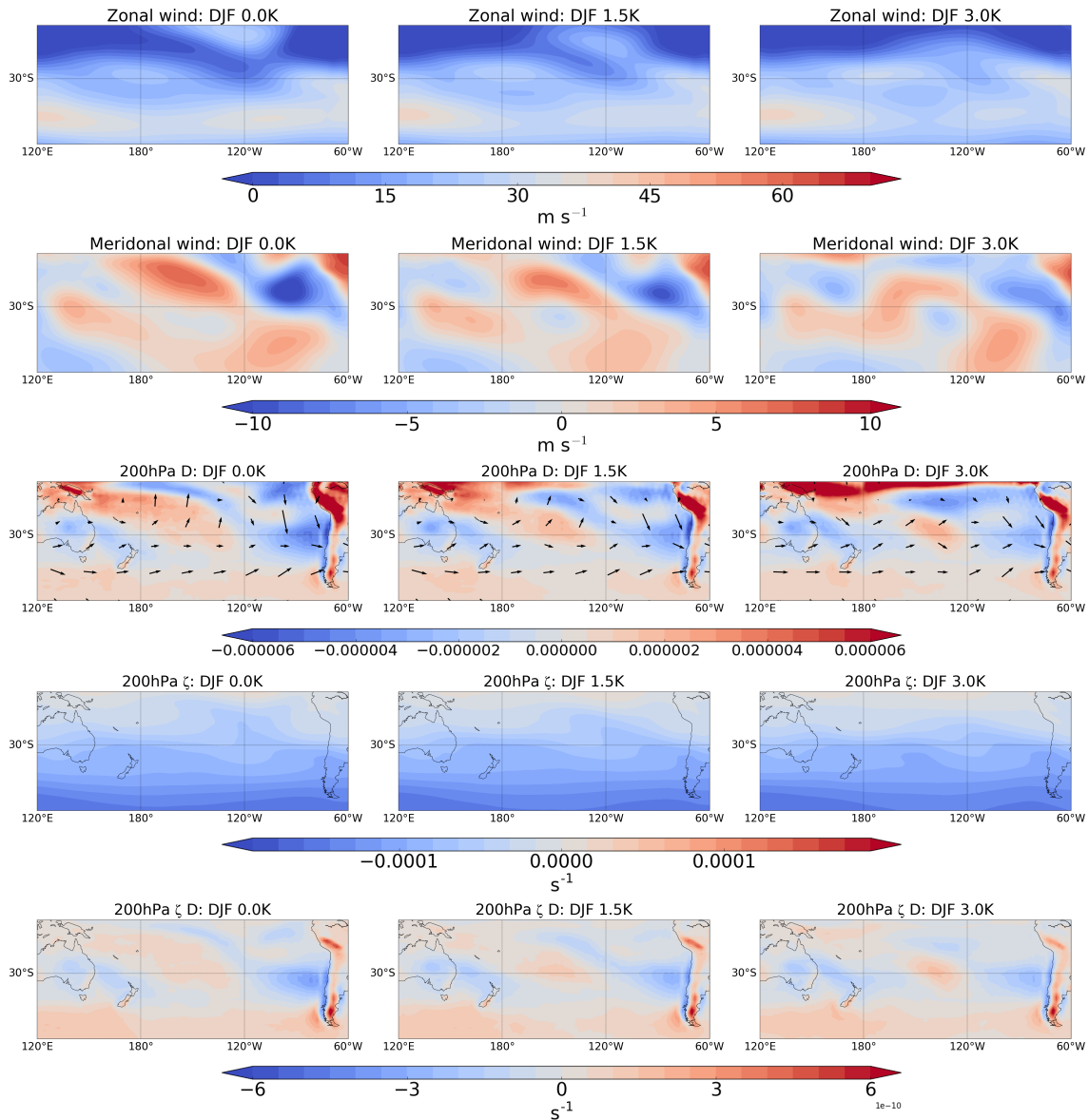


Fig. 3.14 Same as Figure 3.13 in DJF

compared to in JJA. Therefore, the changes in the divergence (third row of Figure 3.14) and absolute vorticity (fourth row of Figure 3.14) under El Niño are small compared to JJA. The *absolute* RWS (fifth row of Figure 3.14) changes very little and there is minimal RWS anomaly in this season. Note that there is little *absolute* RWS in the southern hemisphere (ignoring the sources near the coast and inland) in DJF.

Li et al. (2015a) reported that the RWS anomalies from their Atlantic SST depended primarily on differences in the climatological flow between austral summer and austral winter. This is also the case for the Pacific heating applied in these experiments. This is because the

high zonal wind speed of the jet is needed to create the large *absolute* RWS in the baseline. The El Niño conditions only change the location and the magnitude of the existing RWS to create these anomalies.

As mentioned in Section 3.5.1, the RWS changes are mainly determined by the product of absolute vorticity and divergence changes. As the three terms in the RWS add linearly, it is easy to decouple them and find the contribution from each term (Figure 3.12). However, it is harder to show quantitatively if the contribution from the ζD term is due to changes in the vorticity or divergence as the effects are multiplicative. One method is to separate the term into components linear in anomalous vorticity, linear in anomalous divergence and nonlinear in both vorticity and divergence. This means

$$(\zeta D)_{\text{anom}} = \zeta_1 D_1 - \zeta_0 D_0, \quad (3.1)$$

where the label (anom) indicates the composite and subscripts 1 and 0 indicate El Niño and neutral conditions, respectively. It is then possible to split the El Niño variables into linear and nonlinear terms

$$(\zeta D)_{\text{anom}} = (\zeta_0 + \zeta')(D_0 + D') - \zeta_0 D_0. \quad (3.2)$$

Multiplying out equation (3.2) obtains

$$(\zeta D)_{\text{anom}} = \zeta_0 D' + \zeta' D_0 + \zeta' D', \quad (3.3)$$

where the first term ($\zeta_0 D'$) contains changes linear in the anomalous divergence and the second term ($\zeta' D_0$) is linear in the anomalous vorticity. Finally, the third term ($\zeta' D'$) is nonlinear in the anomalous quantities. It is important to note that it is non-trivial to decompose the effects that cause the wavetrain and changes in the climatology due to the wavetrain itself. Changes in the STJ are likely to be associated with anomalous divergences while the anomalous vorticity is likely to be associated with the presence of the wavetrain. The top panel of Figure 3.15 shows the relative contribution of $\zeta_0 D'$, $\zeta' D_0$ and $\zeta' D'$ to $(\zeta D)_{\text{anom}}$ for all four El Niño experiments. The bottom panels of Figure 3.15 shows maps of the $\zeta_0 D'$, $\zeta' D_0$ and $\zeta' D'$ for the 1.5 K and 3.0 K El Niños.

As seen from maps in Figure 3.15, the greatest contribution comes from the $\zeta_0 D'$ term in both the 1.5 K and 3.0 K El Niño cases. This is perhaps expected from the middle panels of Figure 3.13 where the divergence of the zonal winds strengthens and shifts eastwards following the MZWL. The strong RWS is strongly associated with both the strength and location of the changing divergence as El Niño magnitude increases. There is a smaller but

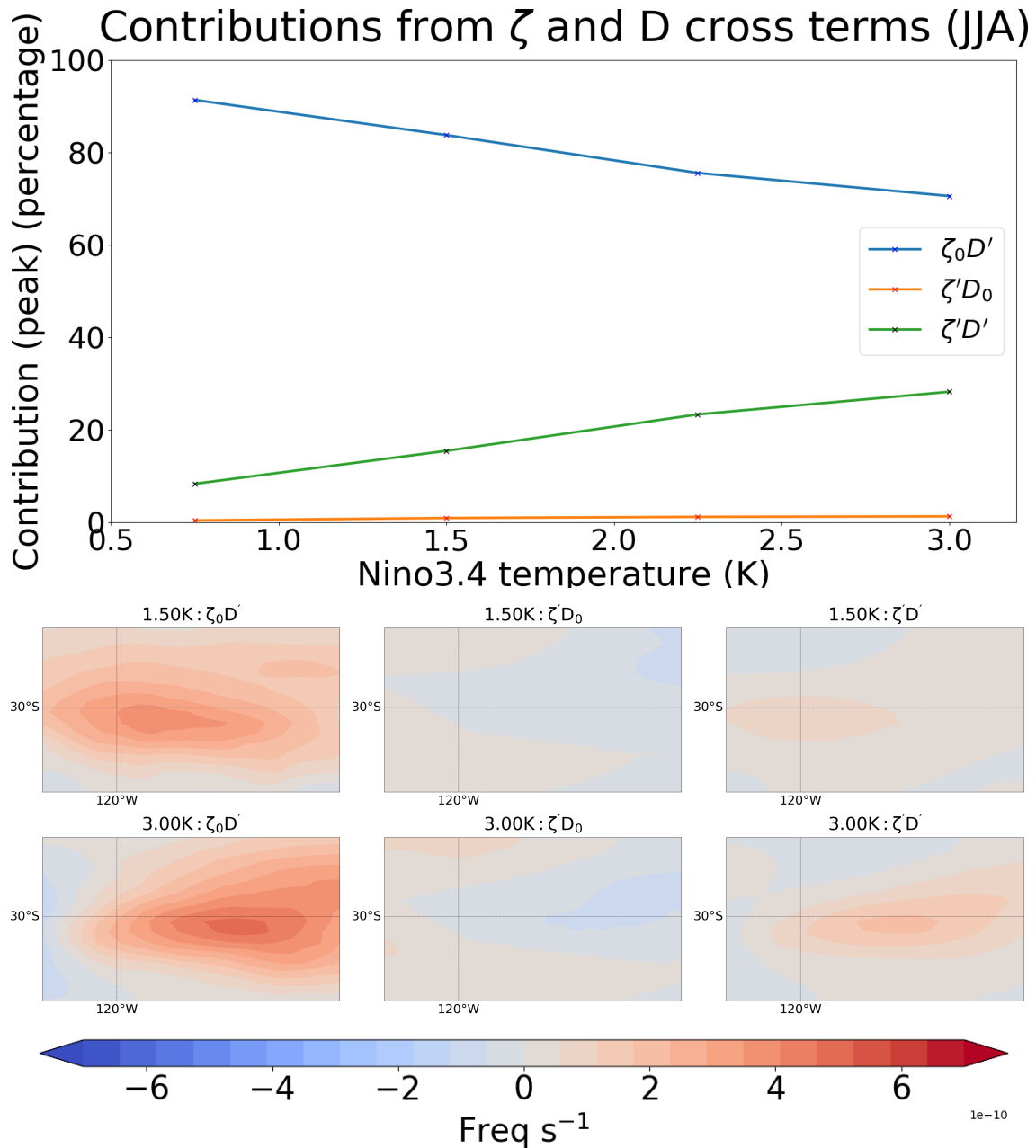


Fig. 3.15 Contributions of $\zeta_0 D'$ (top), $\zeta' D_0$ (middle) and $\zeta' D'$ (bottom) to the ζD anomaly in austral winter (JJA) under (1.5 K and 3.0 K) El Niño conditions. Region is 25–35 S, 250–270 E. Units are in s^{-1} .

still significant contribution from the non-linear term ($\zeta' D'$). $\zeta' D_0$ has little contribution in both cases.

As seen from the top panel of Figure 3.15, the proportion of contribution from the non-linear term ($\zeta' D'$) increases as El Niño magnitude increases. It accounts for approximately

8.3%, 15.4%, 23.3% and 28.2% of the total anomalous ζD in the 0.75K, 1.5K, 2.25K and 3.0K El Niño experiments, respectively. Conversely, the proportion of contribution from $\zeta_0 D'$ term decreases as El Niño temperature increases. It accounts for around 91.4%, 83.8%, 75.6% and 70.6% in the 0.75K, 1.5K, 2.25K and 3.0K El Niño experiments, respectively. This suggests that the contribution to the RWS is not easily decomposed into linear terms. Furthermore, the greater the El Niño, the more important the non-linear terms become.

Summary

This section discussed the effects of El Niño on the Rossby wave source (RWS). In JJA, under El Niño conditions, a strong positive RWS anomaly appears at approximately 30°S, 100–120°W and a weaker negative anomaly appears at around 30°S, 150–180°W. These anomalies are formed as the location of the maximum zonal wind (MZWL) intensifies and shifts eastwards. This is associated with the anomalous divergence and absolute vorticity which plays the major role in determining the RWS.

In DJF, there are lower wind speeds in the subtropics associated with the weak STJ (Section 3.4). Consequently, the MZWL is missing. This means that the RWS anomalies are unable to be generated in austral summer under El Niño conditions.

3.6 Propagation of the teleconnection

The previous section established that the anomalous RWS induced by El Niño conditions only appears in austral winter (JJA) and not in austral summer (DJF). In this section, results on the subsequent propagation of the Rossby waves will be presented. Specifically, the focus of this section is to investigate the differences in the propagation characteristics for waves under the hypothetical situation where both seasons generated RWS anomalies. Rossby wave ray tracing, as well as the wave flux following Plumb (1985), will be used to diagnose the propagation.

Figure 3.16 shows examples of Rossby wave propagation using ray tracing techniques for the baseline and El Niño (1.5 K and 3.0 K) model runs. The two shaded boxes show the location of the Niño3.4 region (in the tropics) and the ASR (in the southern hemisphere). The blue areas show the reflective zones ($\beta^*/U < k^2$), the red areas are the termination zones ($U < 0$) and the white areas are the propagation zones. The red lines are example paths taken by using Rossby waves using ray tracing. The Rossby waves are initialised approximately at the location of the strong positive RWS *anomaly* in austral winter (JJA). Note that the location of the RWS *anomaly* approximately coincides with the location of the *absolute*

RWS. The rays were also initialised from the same location in austral summer (DJF) even though there is no RWS anomaly present, in order to examine the effects of the different background conditions between seasons on the potential propagation of Rossby waves. In JJA, the rays are able to propagate from the RWS location to the ASR. The path taken by the rays approximately follows the PSA wavetrain. Note that for the 0 K case, all of the initiated rays propagate into the ASR. However, for the 3 K case, only approximately half the rays get through and the other half is reflected in mid latitudes. This has implications regarding saturation of the teleconnection as the El Niño increases in intensity; the potential for saturation effects will be further explored in Chapter 5. In DJF, the initiated Rossby wave rays are all reflected at around 60°S before reaching deep into the ASR.

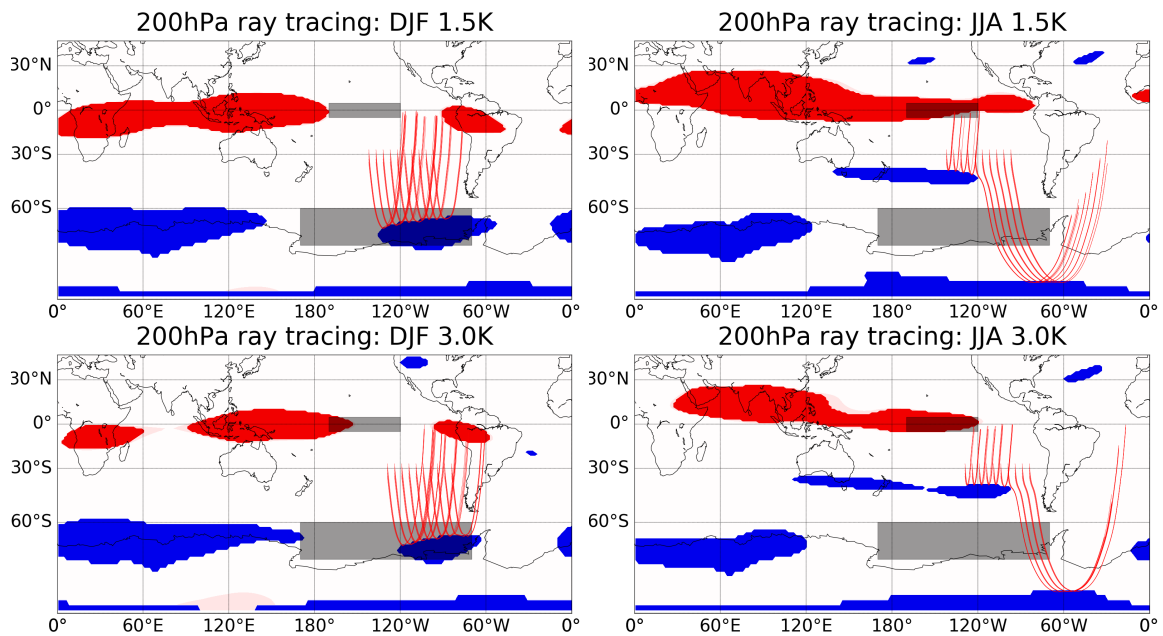


Fig. 3.16 Rossby wave ray tracing performed on the 1.5 K and 3.0 K El Niño runs for austral summer (DJF) and austral winter (JJA). The rays were initialised approximately at the location of the positive RWS anomaly found in JJA. The red regions indicate termination, the blue regions indicate reflection while the white region indicate propagation regions. The red lines are the paths taken by the rays.

Note that there are two main reasons for not propagating the Rossby waves from the negative RWS anomaly. Firstly, the negative RWS anomaly is much weaker in magnitude compared to the positive anomaly, see again Section 3.5.1. Secondly, all propagation in JJA is reflected if Rossby wave ray tracing is initiated at the negative RWS anomaly. For details on the Rossby wave propagation from the weaker negative RWS anomaly, see Appendix J.

In order to understand what causes the formation of the stationary wave reflection zone at $\sim 60^{\circ}\text{S}$, 60°W – 120°W in austral summer (DJF) and the reflection zone at $\sim 40^{\circ}\text{S}$, 150°E – 120°W in austral winter (JJA), it is important to understand the condition for reflection. Reflection

occurs when $\beta^*/U < k^2$, where β^* is the meridional gradient of absolute vorticity, U is the zonal wind and k is the wavenumber. As k is fixed in the examples of Figure 3.16, reflection will occur when β^* is small or if U is large. The U and β^* are shown in Figure 3.9 and the top row of Figure 3.17, respectively. While U is also related to β^* , it is difficult to determine the reflection zones by looking at the U field directly. The β^* field provides more insight as it maps very closely to the propagation and reflection zones. Note that the wave termination zones have been whited out in Figure 3.17. In DJF (Figure 3.17, top left panel), there are regions where β^* is negative at $\sim 60^\circ\text{S}$, $0\text{--}120^\circ\text{E}$ and $\sim 60^\circ\text{S}$, $60\text{--}120^\circ\text{W}$ matching the two reflection zones in DJF in Figure 3.16. In JJA (Figure 3.17, top right panel), there is a region of negative β^* at $\sim 60^\circ\text{S}$, $0\text{--}120^\circ\text{E}$ and $\sim 40^\circ\text{S}$, $150^\circ\text{E}\text{--}120^\circ\text{W}$. These match the reflections zones as seen in Figure 3.16. This close match suggests that β^* plays a key role in determining the location of the reflection zones. In the bottom row of Figure 3.17, the absolute vorticity is presented with a carefully selected colourbar to highlight the local changes seen in the β^* . In DJF, the rays pass from high absolute vorticity ($> -0.0012 \text{ s}^{-1}$) towards lower absolute vorticity as it moves polewards. However, at around 60°S , the absolute vorticity increases with latitude as there is a local maximum in the ASR. This means the rays experience a negative gradient of absolute vorticity in this area (which means negative β^*) which causes the reflection zone. In JJA, the rays only pass through regions with decreasing absolute vorticity with latitude and there is no sign change in the gradient of the absolute vorticity. This is because the local maximum of absolute vorticity is missing in the ASR as opposed to DJF. Note that there is also a local maximum in absolute vorticity at around 40°S , $150^\circ\text{E}\text{--}120^\circ\text{W}$ in JJA as expected.

The meridional gradient of absolute vorticity can be expressed as $\beta^* = \beta - U_{yy}$ where β is the planetary vorticity and U_{yy} is the curvature of the zonal wind with respect to latitude. Figure 3.18 shows the U_{yy} in the 1.5 K El Niño run for austral summer (DJF) and austral winter (JJA). Note that the data was been filtered using triangular truncation at wavenumber 20 to minimise artifacts from differentiation.

In JJA, there is a region of strong positive U_{yy} at the equatorwards and polewards side of the STJ (approximately 20°S and 40°) while there is strong negative U_{yy} at the location of jet (approximately 30°S). This is likely caused by the STJ: the zonal wind increases approaching the STJ from the north and decreases with latitude on the poleward side of the STJ core. The location of the regions of strong U_{yy} coincides with the approximate location of the MZWL as seen in the top row of Figure 3.13. In DJF, there is a weak positive U_{yy} at $\sim 60^\circ\text{S}$, $60\text{--}120^\circ\text{W}$ that did not exist in JJA. This weak U_{yy} , along with the weakening β , is enough to create a reflection zone. This is likely generated from the zonal wind maximum at 50°S , 100°W , see again Figure 3.9.

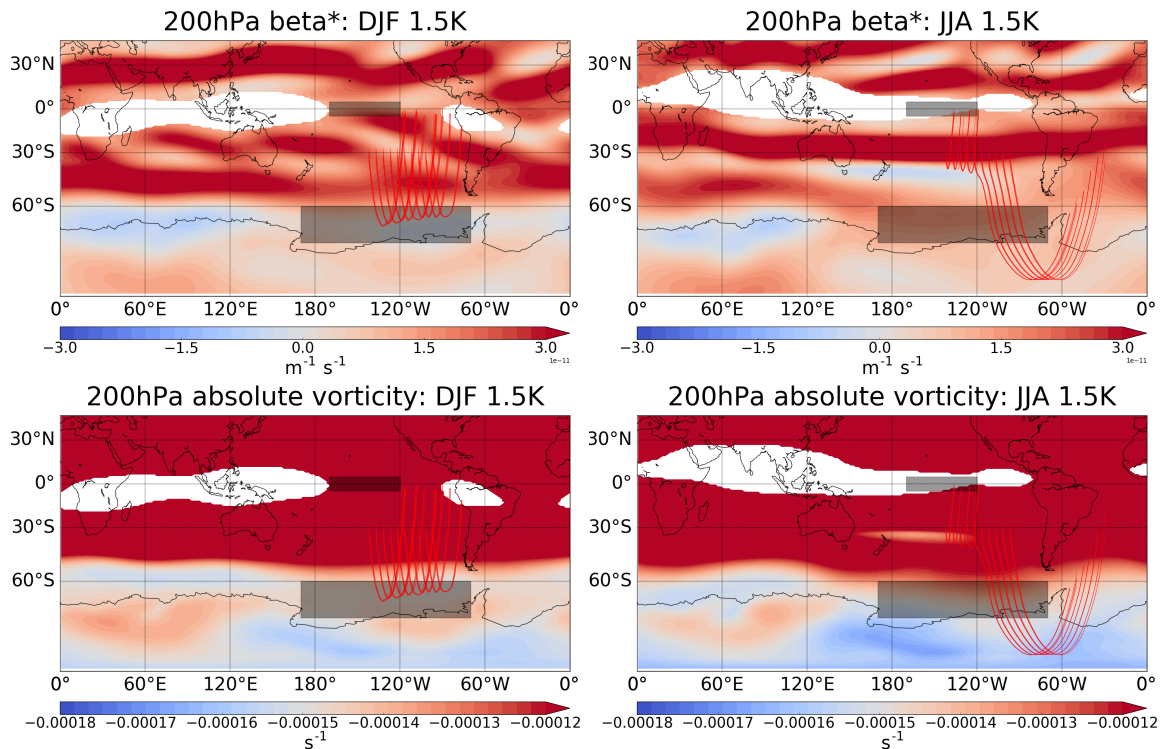


Fig. 3.17 Meridional gradient of absolute vorticity (β^*) and absolute vorticity under El Niño (1.5 K) conditions in austral summer (DJF) and austral winter (JJA). The termination zones are whited out for reference. Units are $\text{m}^{-1} \text{s}^{-1}$ for the meridional gradient of absolute vorticity and s^{-1} for absolute vorticity.

To complement the ray tracing analysis, Figure 3.19 shows the wave activity flux calculated following Plumb (1985) in the 1.5 K and 3.0 K El Niño runs for austral summer (DJF) and austral winter (JJA). In JJA, the wave flux can be seen to travel towards the ASR and then towards the Weddell sea. The path taken is PSA-like and approximately matches with the Rossby wave ray tracing analysis shown previously (right panels of Figure 3.16). In DJF, there is a lack of any significant wave flux at latitudes southwards of approximately 50–60°S. Additionally, the wave flux under 3.0 K El Niño in JJA shows a greater wave propagation into the ASR compared to the 1.5 K case. These results broadly matches with the previous ray tracing analysis. Note that, caution must be exercised when interpreting the wave flux at lower latitudes as the geostrophic winds and height analysis are unreliable (see Karoly et al. (1989) for details). Figures showing absolute wave flux can be found in Appendix H. Additionally, figures showing the reproduction of Karoly et al. (1989, Fig. 2) using the ERA-40 dataset can be found in Appendix I.

It is important to note that the positive and negative regions of the RWS do not necessarily correspond to a divergence and convergence in the wave flux, respectively. However,

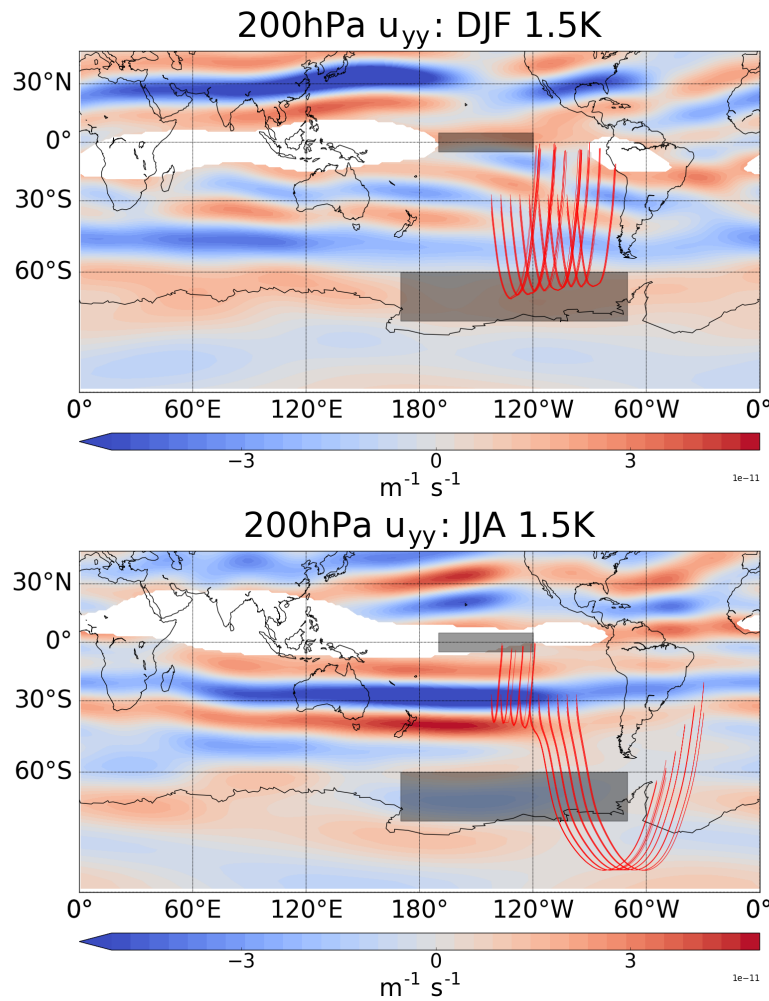


Fig. 3.18 Curvature of zonal wind with respect to latitude (U_{yy}) under El Niño (1.5 K) conditions in austral summer (DJF) and austral winter (JJA). The termination zones are whited out for reference. Units are $\text{m}^{-1} \text{s}^{-1}$.

propagation from the negative RWS anomaly is not shown in this section as the RWS is much weaker and all propagation from the weaker negative RWS anomaly is reflected in JJA. For details on the Rossby wave propagation from the weaker negative RWS anomaly, see Appendix J.

Summary

The propagation of the Rossby waves from the Rossby wave source (RWS) anomaly to the Amundsen Sea region (ASR) is discussed in this section. There are several key conclusions. Firstly, Rossby wave propagation was diagnosed with ray tracing analysis and wave flux calculations. The results from both methods showed that wave propagation is present in

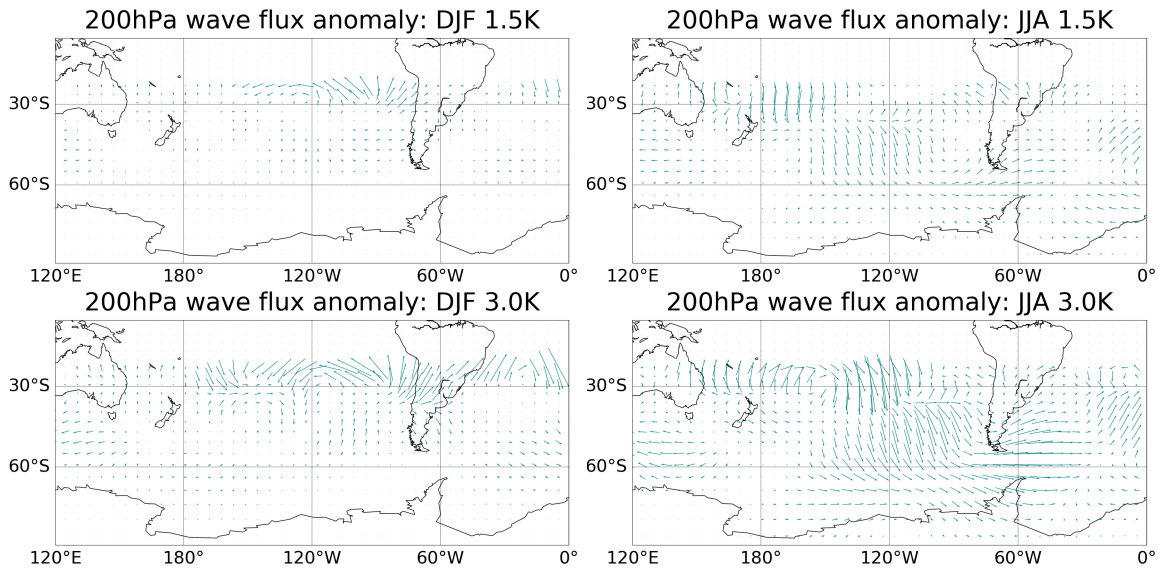


Fig. 3.19 Wave flux anomaly following Plumb (1985) under El Niño (1.5 K and 3.0 K) conditions in austral summer (DJF) and austral winter (JJA).

austral winter (JJA) but not in austral summer (DJF). Secondly, the propagation of the waves in ray tracing is mainly determined by the presence (or lack) of wave reflection zones. This reflection zone is determined by β^* which is further determined by the meridional curvature of the zonal winds, U_{yy} . Thirdly, due to the fast moving jets, U_{yy} is strongly negative equatorwards of the jets. Conversely, U_{yy} is strongly positive polewards of the jets. In DJF, the poleward side of the polar front jet (PFJ) reflects the majority of the rays that are entering the ASR. In JJA, due to the position of the MZWL, only some of the waves are reflected and the others propagate to the ASR.

3.7 Sea level pressure anomaly in austral summer (DJF)

In the sections above, the mechanistic differences in the teleconnection between austral summer (DJF) and austral winter (JJA) have been investigated. However, the weaker EOF1-like signal in DJF remains an open question. There are still SLP anomalies in the ASR, albeit weaker than in JJA, even though Rossby wave generation and propagation is not favourable in the summer season. One likely explanation for these weak SLP anomalies is the direct modulation of the SAM. As seen in Figure 3.7, the Hadley and Ferrel cells contract under El Niño conditions. This causes the STJ and the PFJ to contact equatorwards, see Figure 3.8. As the SAM is related to the meridional movement of the PFJ (Hartmann and Lo, 1998; Lorenz and Hartmann, 2001; Thompson and Wallace, 2000; Yang and Chang, 2007) and associated changes in synoptic wave fluxes, this will favour a more negative phase of the SAM event. A

more negative SAM event would cause anomalously high pressure over Antarctica in general. This fits the EOF1-like SLP anomaly pattern seen in DJF.

3.8 Concluding remarks

This chapter has focuses on understanding of the mechanism behind the seasonality of the ENSO-ASR teleconnection. The mechanistic development of the ENSO-ASR teleconnection has been discussed, step by step, and is shown as a flowchart in Figure 3.20.

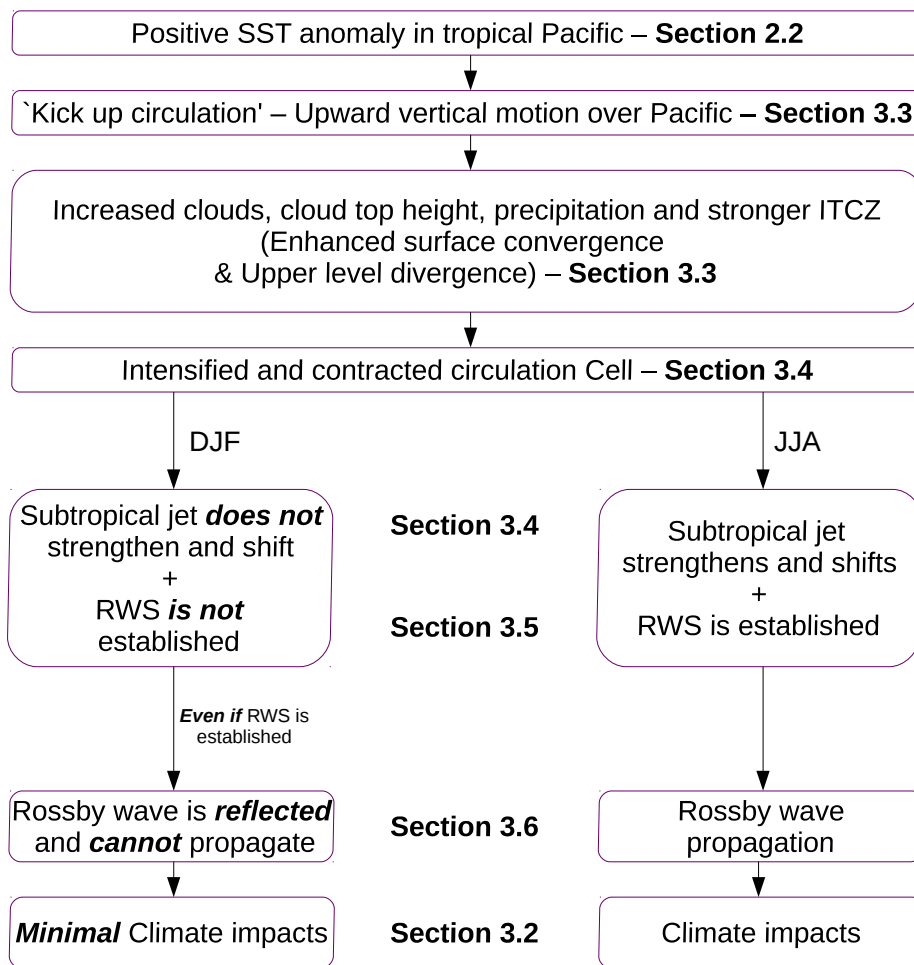


Fig. 3.20 Flowchart showing the ENSO teleconnection mechanism to the ASL. The flowchart starts with combined boxes for both seasons, this shows that there are minimal differences between the seasons. However, the response between the seasons splits at the subtropical jets. Therefore, there is a set of textboxes for austral summer (DJF) and austral winter (JJA), respectively.

The tropical response in both summer and winter seasons is similar. A positive SST anomaly in the tropical Pacific strengthens the Hadley circulation in both seasons. This can be seen as increased tropical precipitation and decreased outgoing longwave radiation.

The locations and strengths of the jets (STJ and PFJ) are different in the two seasons. In austral winter (JJA), there are two distinct jets in the southern hemisphere. These are the dominant STJ and higher latitude PFJ. The STJ is strong, even in neutral ENSO conditions, and there is divergence and vorticity associated with it. Under El Niño conditions, the STJ is strengthened by the zonal wind anomalies associated with the strengthened Hadley cell. In particular, the maximum speed of the STJ is found in the Pacific sector and the wind anomalies strengthens and shifts the maximum speed eastwards. This causes the already strong divergence and the absolute vorticity to strengthen further and shift eastwards. As the RWS depend mainly on the divergence and absolute vorticity, the strengthening and shifting of these fields is associated with the strong positive RWS anomaly (and a weaker negative anomaly) at 30°S, 100–120°W (and 30°S, 150–180°W). However, in austral summer (DJF), there is only a PFJ at around 40–50°S; the anomalous RWS at around 30°S is absent. The summer anomalies generated are also weaker as the Hadley cell is always stronger in the winter hemisphere. In consequence, minimal RWS anomalies are generated.

Using Rossby wave ray tracing, the propagation of Rossby waves to the high southern latitudes is found only to be possible in JJA but not in DJF. In JJA, the Rossby waves propagate from the RWS anomaly at 30°S, 100–120°W towards the ASR and then to the Weddell Sea. This path is approximately the path taken by the PSA pattern. However, in DJF, the Rossby waves are reflected at around 60°S and do not reach deep into the ASR. This reflection zone is attributed to the PFJ in DJF. The jet in this location creates a maximum zonal wind barrier which causes the U_{yy} to become positive on the polewards side of the jet. This is enough to overcome the planetary vorticity to create a wave reflection zone.

The results from ray tracing are supported by wave flux calculations following Plumb (1985). In JJA, there are wave fluxes traveling from the Pacific mid latitudes towards the ASR while there is minimum wave fluxes in the high latitudes in DJF.

In conclusion, the strong ENSO teleconnection to the ASR in JJA is caused by the strong RWS anomaly from the jet and the absence of termination or reflection zones between the Rossby wave source anomaly and the Amundsen sea region.

Monthly changes in the teleconnection

While the majority of this chapter has presented seasonal analyses, Figure 3.21 shows the *peak* monthly anomalies of the RWS, wave flux and SLP in the 0.75 K (black line), 1.5 K

(red), 2.25 K (blue) and 3.0 K (yellow) El Niño experiments. Figure 3.21 also shows the longitude of the *peak* zonal mean zonal wind (southern hemisphere only) in the baseline run.

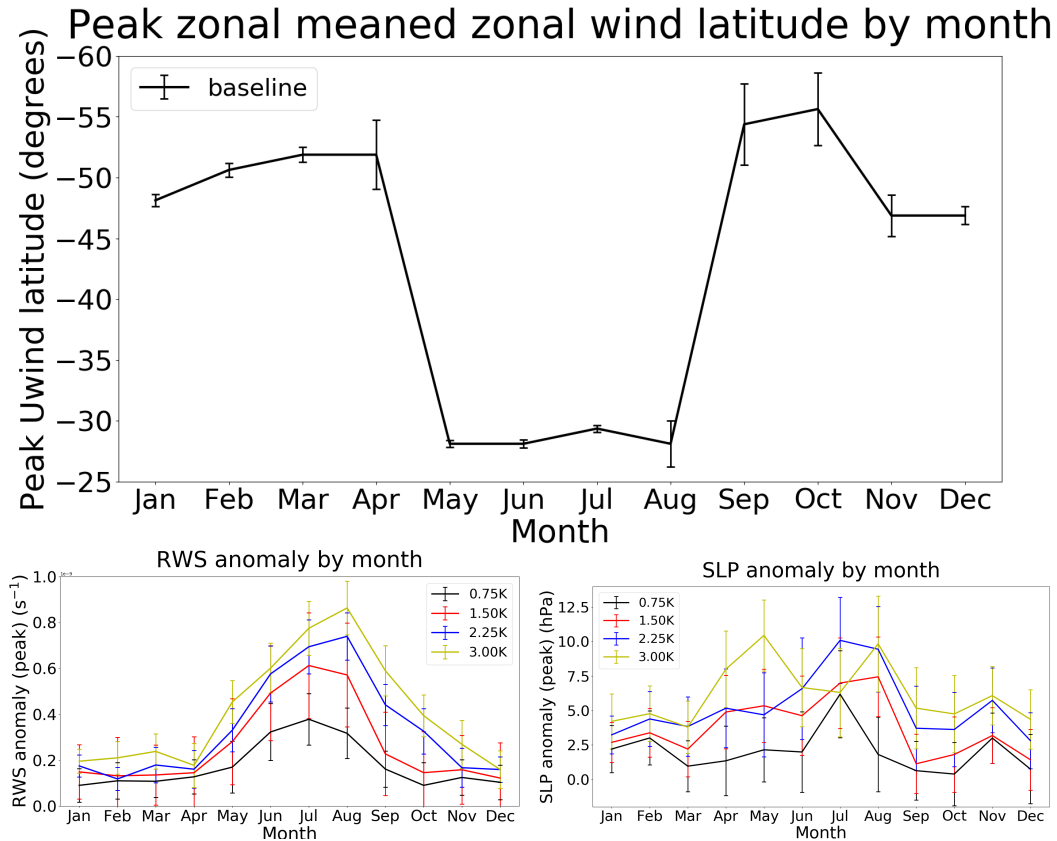


Fig. 3.21 RWS anomaly, SLP anomaly and longitude of peak zonal mean zonal wind by month under four different El Niño (0.75 K, 1.5 K, 2.25 K, 3.0 K) conditions.

As discussed in Section 3.5, the RWS anomaly is related to the strength of the STJ. The bottom left panel of Figure 3.21 shows a bimodal distribution in the longitude of the peak zonal mean zonal wind. In September to April, the longitude of the peak is at approximately 50°S while the longitude is at approximately 30°S between May to August. This shows the presence of the high latitude PFJ and the lower latitude STJ, respectively. As expected, the RWS anomaly seems to be strong within May to August period compared to the September to April period. This leads to a stronger SLP anomaly during May to August. The peak month of the RWS and SLP anomaly are in July to August in the 0.75–2.25 K cases. However, the 3.0 K case presents a different picture. The SLP anomaly is small compared to 2.25 K. This will be further explored in Chapter 5.

Linking back to reality

It is important to treat these studies as an idealised investigation into the teleconnection mechanisms rather than as a definitive study of real world ENSO–ASL teleconnection magnitudes. I have neglected several aspects of observed ENSO characteristics, for example its seasonal evolution. However, the controlled nature of the model experiments had enabled a detailed assessment of the mechanism involved in ENSO–ASR teleconnections and their dependence on season.

Chapter 4

The seasonality of El Niño teleconnections to the Amundsen Sea region – transient response

This chapter focuses on the transient response of the ENSO–ASR teleconnection. Section 4.1 provides an overview to this chapter. The transient response in austral winter is given in Section 4.2 while the transient response in austral summer is discussed in Section 4.3. Conclusions for this chapter can be found in Section 4.4.

4.1 Overview

This chapter analyses the transient model experiments introduced in Chapter 2. The main scientific aim is to understand the time scale for each step in the mechanistic flowchart, shown in Figure 3.20. There are several motivations for this. Firstly, the order of the events in the proposed mechanism from Chapter 3 can be verified using the transient model runs. As the mechanistic flowchart is causal, those variables associated with processes nearer to the tropics can be expected to react more quickly than variables nearer to the pole. Secondly, by understanding the timescale for the teleconnection to propagate from the tropics to the ASR, the validity of the seasonal mean analysis in Chapter 3 can be verified. The analysis in Chapter 3, which uses seasonal means, implicitly assumes that the teleconnection take less than one season to connect the tropics to the ASR. If the propagation of the teleconnection is on similar or greater timescale than one season, the results in Chapter 3 may be invalid. For example, if the teleconnections operate on greater than seasonal timescales, the background fields, which control the propagation, will have changed. Thirdly, further understanding

of the individual steps in the teleconnection can be gained by knowing their characteristic reaction timescale.

The analysis shown here would be difficult, if not impossible, to perform using observations or reanalysis data. This is because, obviously, El Niño events do not ‘switch on’ instantaneously (or over a ten day period) in nature. Therefore, model experiments are required to perform this analysis. Previous literature (Li et al., 2015a,b), has looked at the transient Rossby wave dynamics in a dry primitive equation model, investigating warming in the Atlantic, western Pacific and Indian Ocean and a cooling in the eastern Pacific. They found that the 200 hPa geopotential height anomaly, as a proxy for a Rossby wavetrain, took approximately 18 days to reach the ASR.

The transient response of the teleconnection in austral winter (JJA) and austral summer (DJF) will be explored in Section 4.2 and 4.3, respectively. In this chapter, the data will be analysed using five–day–means. This time averaging was chosen as a balance to provide a relatively short timescale in order to capture rapid changes in variables while still producing lower standard deviations than for daily data.

This chapter will quantify the response time of variables by looking at both the time taken for the responses of variables to reach 25% of their peak value (T25) and the time taken for the variable to reach its peak value (T100). In order to emphasise the transient response of the circulation, more emphasis will be placed on the T25. However, both metrics will be shown as T100 provides insight into the timescale required to reach a new equilibrium. Note that we chose to use the T25 and T100 instead of values from the timeslice runs due to the overshooting problem as discussed in Section 2.3. There are several problems with using the T100 only. Firstly, the T100 may not only contain the reaction time but also the seasonality. For example, if the SSTs were switched on during the 1st of May and the reaction time was one month, the variable still may not peak on the 1st of June. This is because the climatology may favor teleconnection at a earlier or later time. Therefore, as an example, if the teleconnection was favoured in August, the T100 may appear larger than a month. However, this problem is mostly avoided in the T25 as transient value is much lower than the equilibrium value and thus the change due to the transient nature is more dominant than the seasonality. Secondly, the errors (as seen in Figures below) tend to be greater as one approaches the ‘peak’ value. This can cause difficulties in determining a ‘peak’ date if values are close together but their variance are high. Additionally, the peak value is used in many of the plots found in this chapter. while this has the disadvantage of being determined by one space point, there are also disadvantages with using a averaged value across a region. Many of the phenomena in this chapter (e.g. RWS anomaly) have both positive and negative changes (i.e. there is a positive and negative RWS anomaly in the

El Niño runs). As there are often reasons (e.g. for the RWS anomaly, this thesis does not propagate from the negative source) to ignore one of these changes, the average is not suitable under these circumstances. Additionally, many of the anomalies are not geographically fixed but rather changes in longitude or latitude as El Niño magnitude increases. This means that the region of interest will often be large compared to the signal. These large regions of interest may worsen the signal to noise ratio in regions that often already have high internal variability. Therefore, for the purposes of this chapter, the peak value will be used in much of the analysis.

Note that, in this chapter, all points in figures show the date of the midpoint of the five-day-mean. All error bars denotes two standard errors unless specified otherwise. The horizontal dotted lines always show the peak value (upper line) and 25% of peak value (lower line). *For simplicity, only the start dates will be given in the text (i.e. 1–6 July will be written as 1 July or day 31 for the experiment initialised on 1 June).*

4.2 Transient response of the teleconnection in JJA

This section will discuss results on the transient response of the ENSO–ASR teleconnection in JJA. In particular, analyses will focus on variables critical for the teleconnection. These include the precipitation, zonal wind, Rossby wave source, wave flux and sea level pressure (ASR). These variables are chosen as they represent the tropical circulation, reaction of the subtropical jet, Rossby waves reaction and the magnitude of the ENSO–ASR teleconnection, respectively.

Tropical precipitation

As the El Niño heating in the tropical Pacific is switched on in the model on the 1st June (ramped up over ten days until the 10th June, for details see Section 2.3), variables associated with the tropical circulation are expected to be the first to respond. The top graph of Figure 4.1 shows the average precipitation anomaly between 10°N – 10°S , 180°E – 90°W . This region was chosen to cover the ITCZ and its movement due to changing seasons, El Niño conditions and internal variability. As seen in Figure 4.1, there is minimal delay in the reaction of tropical precipitation to the imposed SSTs. T25 is on the 6 June and lags the ramping up of the SSTs by only around 5 days. T100 for the precipitation in the Pacific is on the 16 June and is also approximately 5 days behind the SSTs (which peak on 11 June due to the averaging), see again Figure 2.4 for the SST ramp up.

The maps in Figure 4.1 (bottom row) show the precipitation anomaly for three snapshots of five-day-means at 1 June, 11 June and 21 June. As expected, there are minimal precipitation anomalies on 1 June as the SST anomalies are only just beginning to ramp up. There are precipitation anomalies forming over the tropical Pacific by 11 June and reaching a peak by 21 June. The structure of the precipitation anomalies is similar to the annual averages shown in Section 3.3 with the majority of the precipitation between 0°N – 5°N , 180°E – 90°W .

Figure 4.1 indicates a decrease in the precipitation after late June/early July. This is the ‘overshooting’ that was described in Section 2.3 and is likely to be a model artifact. While it may affect the magnitude of these variables, it should not affect the initial time needed for the variables to respond.

Zonal wind

Figure 4.2, top, shows the peak zonal wind anomaly at 200 hPa found in the region 15°S – 40°S , 180°E – 300°E . This region and height was selected to capture the greatest change in the zonal wind of the STJ in this season (JJA). The reaction time for the zonal wind anomaly is longer than for the precipitation. This can be seen in both the ramp up stage (T25) and the peak/equilibrium stage (T100). For example, while the precipitation on June 6 has exceeded 25% of the peak value, the zonal wind has only reacted minimally by this point. The T25 for zonal wind is on day 11 and is approximately 5 days later than for the precipitation. T100 for zonal wind is on 1 July (31 days after SST ramp up). This delay between the zonal wind and precipitation is expected as zonal wind changes are coupled to the Hadley cell changes which includes the tropical circulation.

The maps in Figure 4.2 (bottom) show snapshots of the zonal wind anomalies at 200 hPa on June 1, June 16 and July 1. In the left panel, there are minimal zonal wind anomalies as expected. In the middle panel, the zonal wind anomalies are forming with a structure which approximately matches the equilibrium response shown in Section 3.3. There is a positive and negative zonal wind anomaly dipole at around 30°S , west of 120°W and 30°S , east of 120°W which grows and peaks by early July as seen in the right panel.

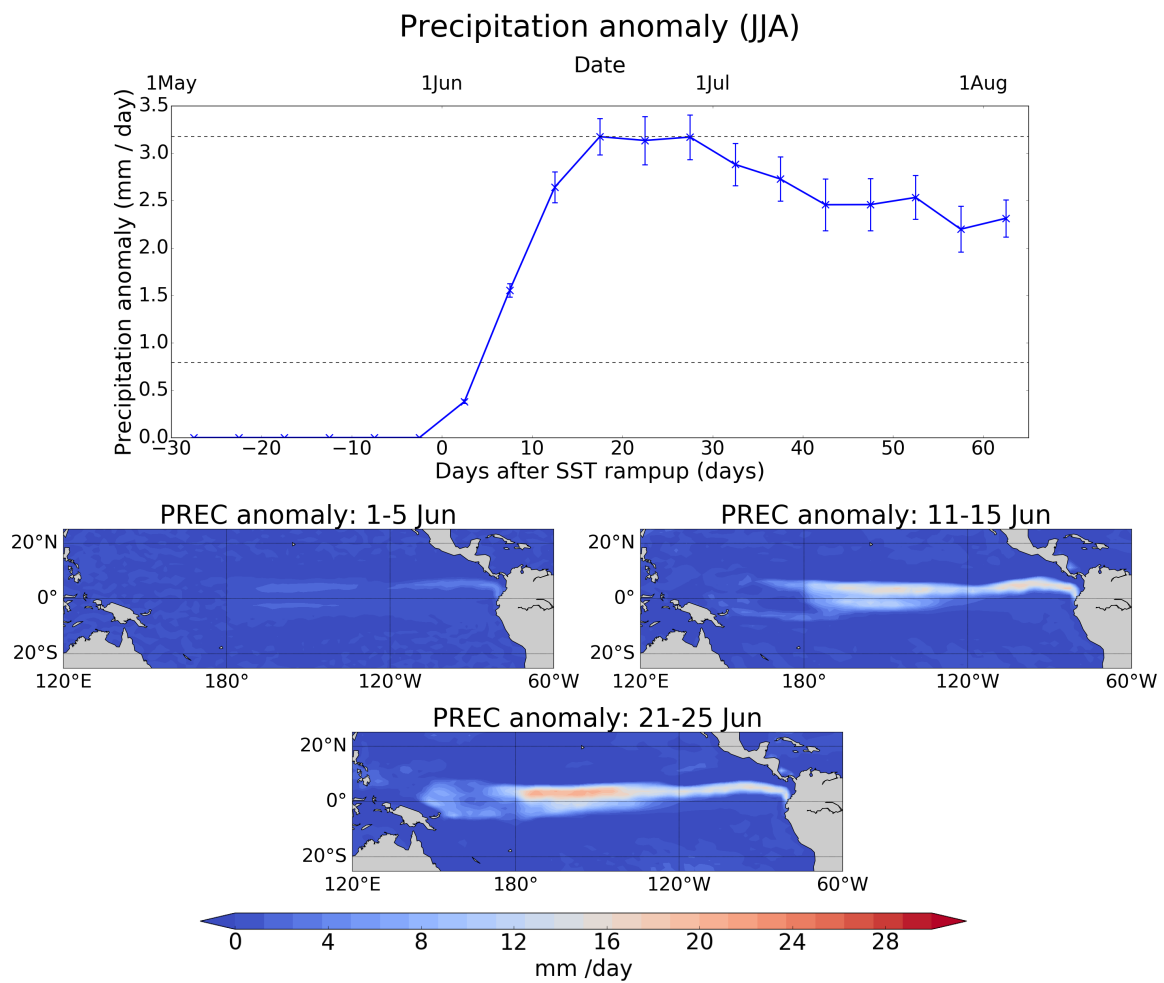


Fig. 4.1 Precipitation anomaly in JJA. Top: the mean precipitation anomaly (10°N – 10°S , 180°E – 90°W) in every five-day-mean from 1 May to 5 August. All error bars are two standard errors unless otherwise specified. Middle and bottom: ‘snapshots’ of the precipitation anomaly on the 1–5 June (middle left), 11–15 June (middle right) and 21–25 June (bottom).

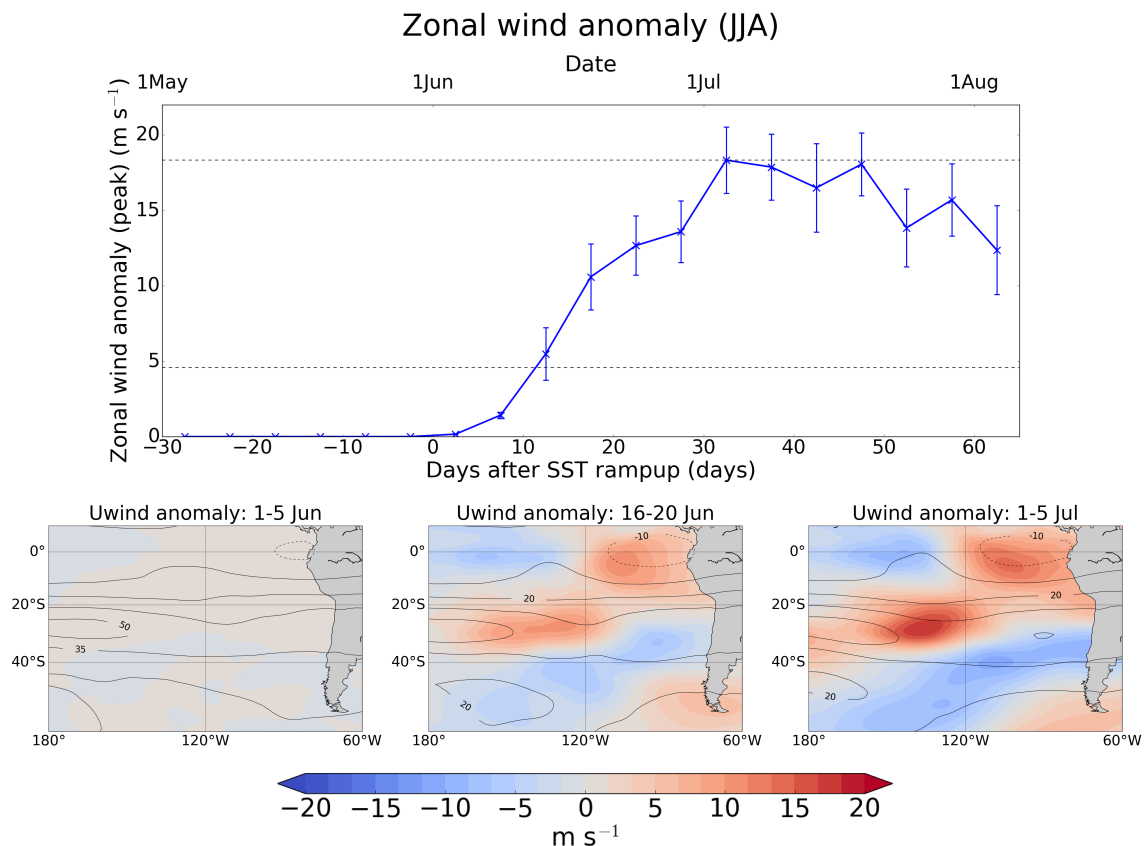


Fig. 4.2 200 hPa zonal wind anomaly in JJA. Top: *peak* anomaly (15°S–40°S, 180°E–300°E) from 1 May to 5 August. Bottom: ‘snapshots’ of the anomaly on the 1–5 June (left), 16–20 June (middle) and 1–5 July (bottom).

RWS

As seen in Section 3.5, the anomalous RWS under El Niño conditions is mainly caused by absolute vorticity and divergence changes. These are mainly determined by the zonal wind anomaly and the location of the climatological STJ. As the location of the STJ is relatively unchanged over short timespans of days to weeks, the baseline STJ is effectively immobile over this one month period. Therefore, the RWS anomaly would be expected to have high correlation with the strength and location of the zonal wind anomaly only. Similar to the zonal wind, the RWS anomaly reaches T25 by the 11 June (Figure 4.3, top). The peak numeric value (T100) is on the 26 July.

The bottom row of Figure 4.3 shows the snapshots of the RWS anomaly at 200 hPa on June 1, June 21 and July 16. In the left panel, there are minimal RWS anomalies. In the middle panel, there is a positive anomaly forming at around 110°W–100°W and a negative anomaly at approximately 160°E–180°E. Both of these anomalies grow stronger as seen in

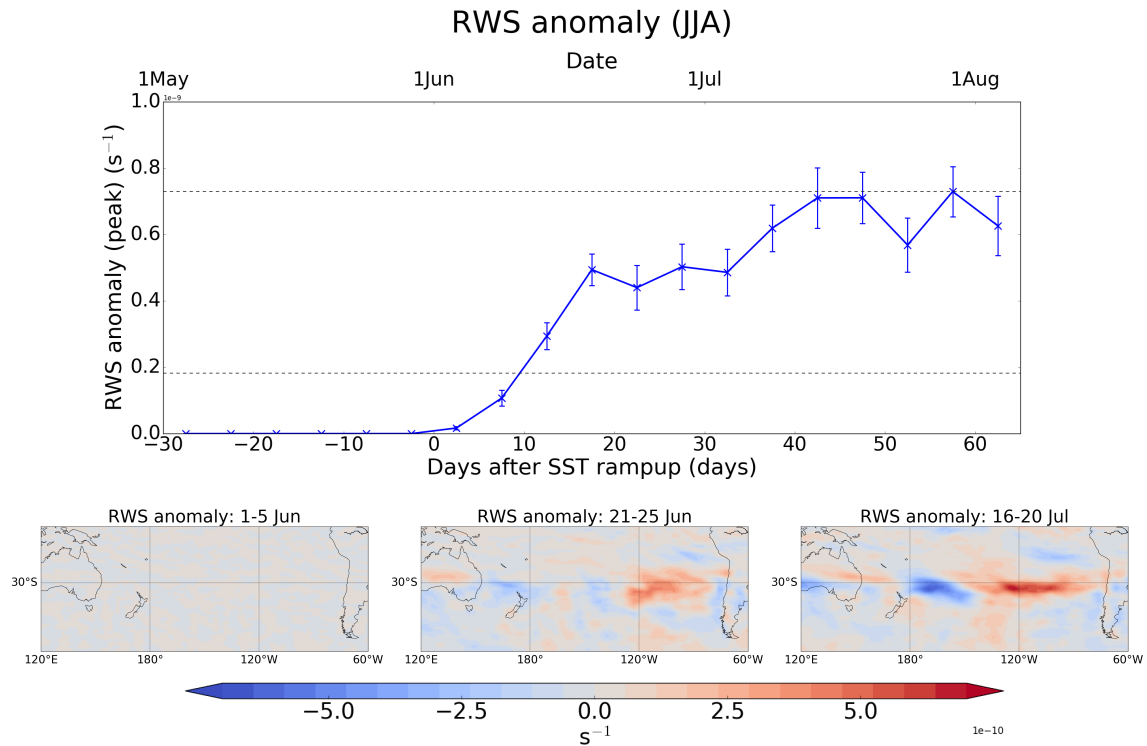


Fig. 4.3 200 hPa RWS anomaly in JJA. Top: *peak* anomaly (ASR) from 1 May to 5 August. Bottom: ‘snapshots’ of the anomaly on the 1–5 June (left), 21–25 June (middle) and 16–20 July (bottom).

the right panel. In the right panel, the strong positive anomaly is located around 120°W and the weaker (comparatively) negative anomaly is located at approximately 160°W, similar to the seasonal RWS anomaly in Figure 3.11.

Wave activity flux

Figure 4.4 shows the mean wave flux anomaly in the ASR as a function of time after the SST anomaly is imposed. The T25 and T100 can only serve as a guide due to the statistically indistinguishable values both before and after T25 and T100. Furthermore, unlike the other variables in this chapter, the wave flux is not a scalar but a vector quantity. Therefore, Figure 4.4 provides an oversimplification by only showing the magnitude of the vector. For example, a wave flux pointing northwards in the ASR would show a positive magnitude but is not showing a wave train propagating into the ASR. Nevertheless, the T25 is on the 11 June. The T100 is on the 16 July.

As mentioned above, the information provided by Figure 4.4 may be misleading. Therefore, the successive five-day-means of wave flux in June are shown in Figure 4.5, which shows the growth of the PSA-like wave train towards the ASR. There is minimal wave

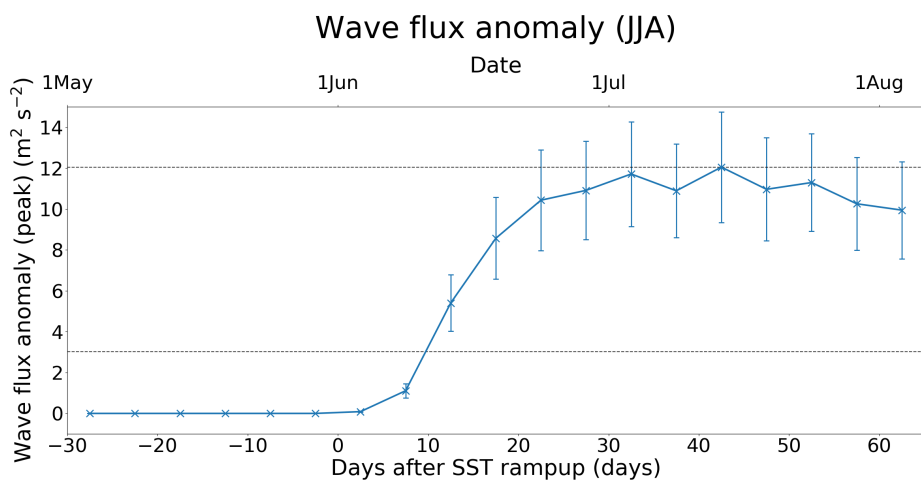


Fig. 4.4 Peak transient 200 hPa wave flux anomaly in JJA (ASR) from 1 May to 5 August.

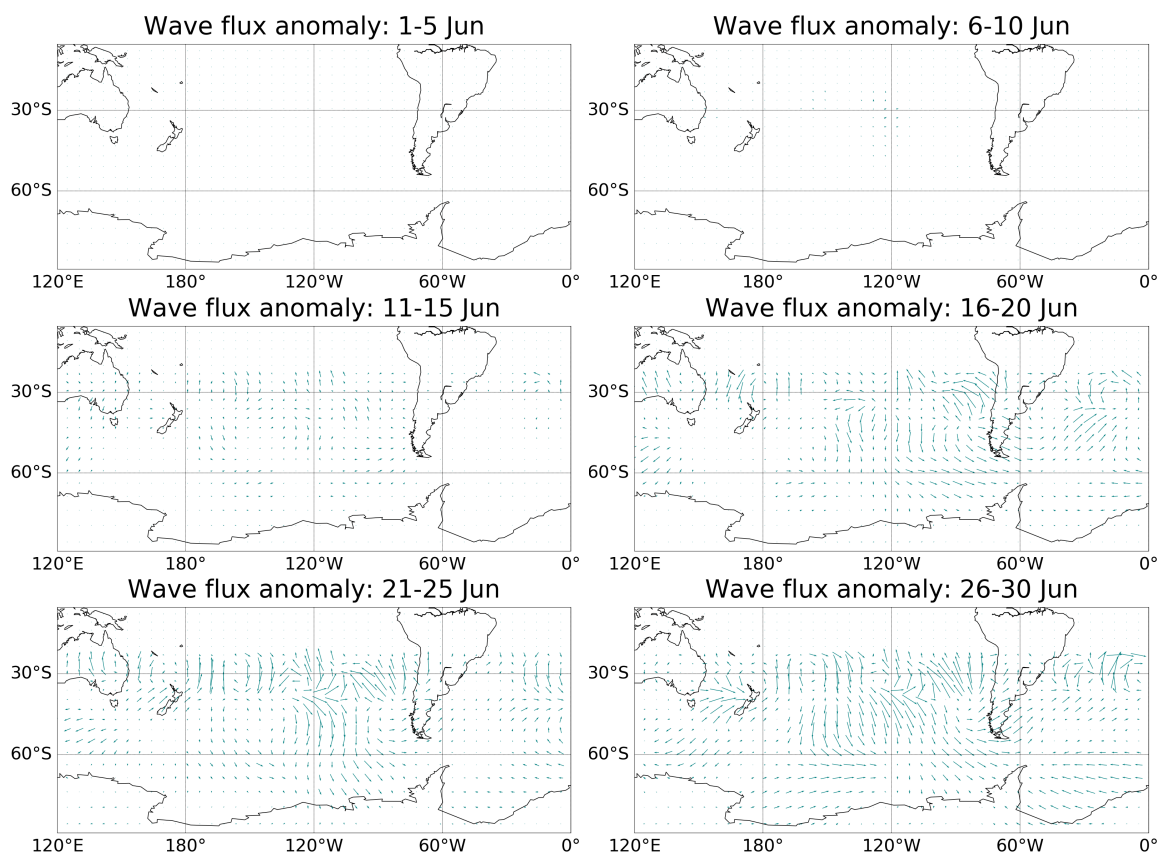


Fig. 4.5 Five-day-mean of the 200 hPa wave flux anomaly from 1 June to 10 July. Arrows indicate the direction and size of the wave flux.

flux response between 1–10 June. Anomalous wavefluxes start to appear in the tropics and midlatitude on the 11 June. This is coincidental with the zonal winds and the RWS

anomaly. Figures 4.2 and 4.3 show that both the zonal wind and RWS anomalies do not react much in the first ten days (1–10 June). At 11 June, the zonal wind and RWS anomalies reach approximately 40% and 30% of peak value, respectively. This is associated with the anomalous wavefluxes in the tropics and midlatitudes. As time progresses, the wavefluxes then grow in strength and start to change in the high latitudes. Anomalous wave flux appears in the ASR on the 16 June and grows as time progresses.

SLP

The basic teleconnection of interest is the changes in the sea level pressure in the Amundsen Sea region, which depends directly on the wave flux anomaly in the ASR. Accordingly, it would be expected to peak at the same time as the wave flux anomaly. The top panel in Figure 4.6 shows the *peak* SLP anomaly in the ASR during the transient austral winter experiments. T25 is on 16 June and while this is earlier than expected (as the SLP is expected to be on similar timescales to the wave flux), the errors are larger and still overlap between the two variables, see Section 4.4 for details. The SLP reaches T100 on the 11 July. While this matches with the peak wave flux date, the dates before and after show very similar anomalies. Therefore, it is important to note that this match is not statistically significant, see Section 4.4 for details.

The bottom row of Figure 4.6 shows the SLP anomaly maps on 1 June, 26 June and 6 July. In the left panel, there is a minimal response in SLP in the ASR. In the middle panel, a positive SLP anomaly has formed over the ASR. Furthermore, negative SLP anomalies are situated in the mid latitudes and the Weddell Sea. These are the beginnings of the characteristic PSA (EOF2) pattern. These patterns become stronger as time passes until reaching the ‘peak’ as seen in the right panel, where they become similar to the equilibrium JJA response shown in Figure 3.2.

Summary

This section has discussed the transient response of the ENSO–ASR teleconnection in austral winter following a rapid switch on of an El Niño SST anomaly (JJA). In particular, the timescales of different processes were investigated. Two basic metrics (T25 and T100) have been used. These are the time taken for the anomalous response of a variable to reach 25% and 100% of its peak value, respectively. The results in this chapter found that precipitation, zonal wind, RWS, wave flux and SLP begins to react (T25) approximately 5, 10, 10, 15 and 15 days after SST ramp up.

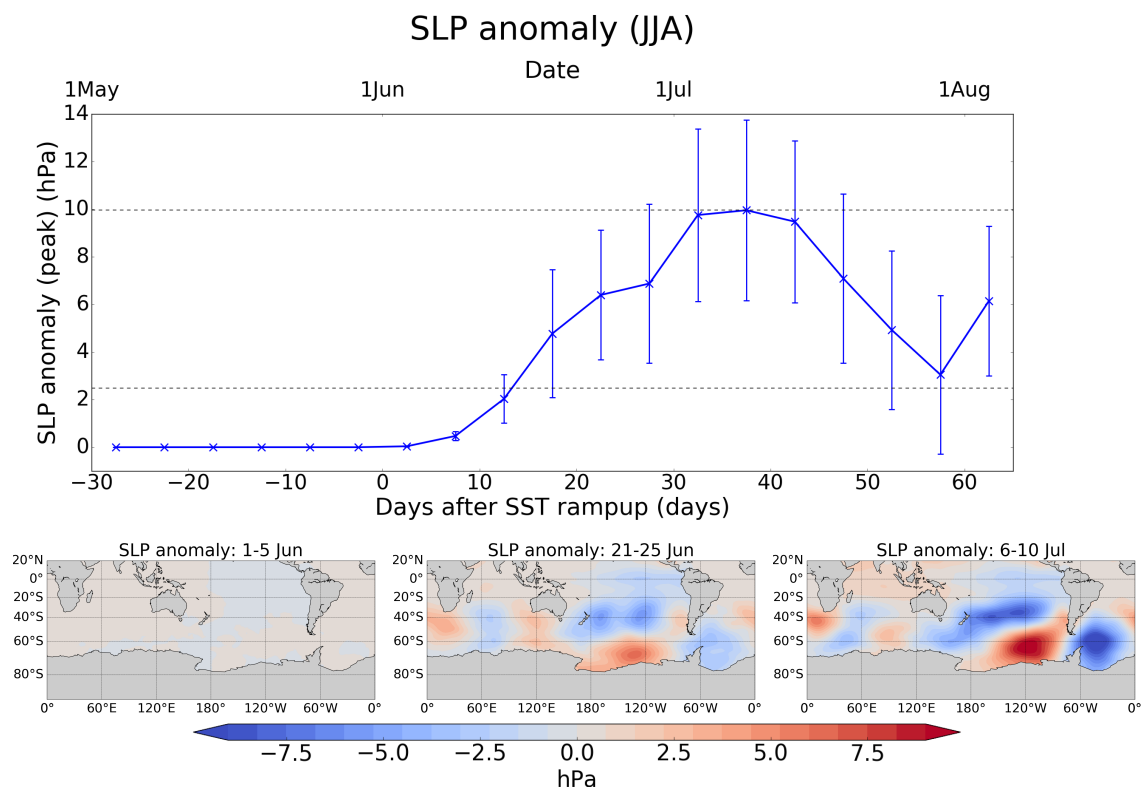


Fig. 4.6 SLP anomaly in JJA. Top: *peak* anomaly (ASR) from 1 May to 5 August. Bottom: ‘snapshots’ of the anomaly on the 1–5 June (left), 26–30 June (middle) and 6–10 July (bottom).

4.3 Transient response of the teleconnection in DJF

This section will describe equivalent results to Section 4.2 for the transient 1.5 K El Niño experiments initialised on 1 November. Rossby wave methods will also be used to verify that this mechanism does not play a strong role in the austral summer ENSO–ASR teleconnection. Variables including the sea level pressure and wave flux will be discussed.

SLP

Figure 4.7 shows the temporal evolution of the five-day-mean *peak* SLP anomaly in the ASR during DJF. While it is possible to approximately identify a peak (T100) in the SLP anomaly for JJA (Figure 4.6), there is no clear peak during DJF. The teleconnection is weaker in DJF compared to JJA. The SLP anomaly only increases in strength as DJF transitions into MAM and JJA (not shown). It is therefore much more difficult to determine when the SLP has reached an ‘equilibrium’ state. This is especially true due to the lower signal (and consequently signal to noise) in DJF compared to JJA. Therefore, any determination made

will not be statistically significant. Furthermore, the T25 is exceeding difficult to determine, again due to the low signal to noise ratio.

Wave flux

As discussed in Chapter 3, unlike JJA, the main teleconnection mechanism in DJF is due to the changes in the location and strength of the PFJ. Figure 4.8 shows the *peak* wave flux anomaly in the ASR. The graph has the same scale as the JJA wave flux anomaly graph (Figure 4.4) for ease of comparison. As seen from Figure 4.8, as expected, the strength of the wave flux is much weaker in DJF. Furthermore, it is important to note that no wavetrain can be seen propagating through the ASR from the midlatitudes in DJF.

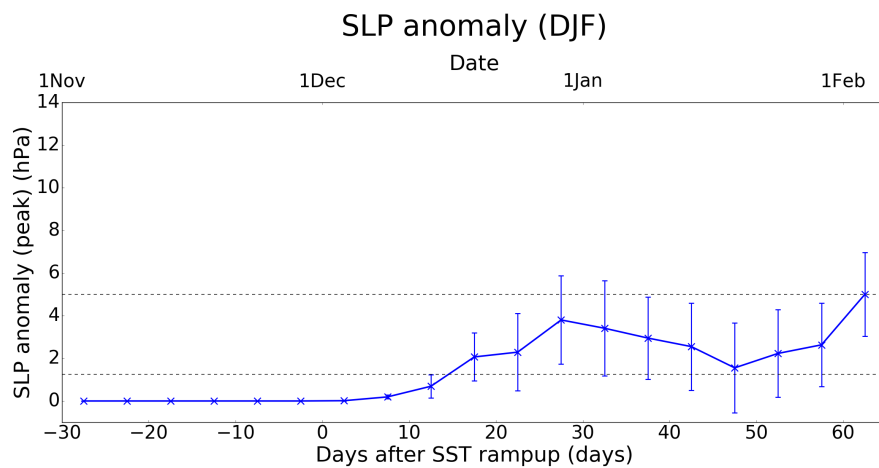


Fig. 4.7 Peak SLP anomaly (ASR) from 1 November to 5 February.

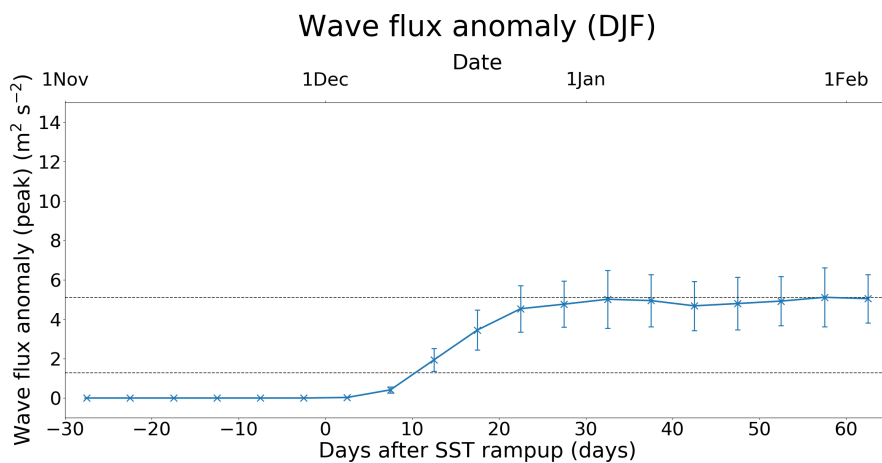


Fig. 4.8 Peak wave flux anomaly (ASR) from 1 November to 5 February.

Summary

It is very difficult to analyse the transient response in the DJF ensemble due to the low signal to noise of the response. However, the lack of wave fluxes may at least suggest that the ENSO–ASR teleconnection under DJF do not operate under the Rossby wave mechanism.

4.4 Concluding remarks

The main scientific aim of this chapter is to understand the timescales of various variables within the proposed teleconnection mechanism. As the proposed mechanistic flowchart is causal, the transient reaction times will allow, to a certain degree, confirmation of the flowchart. Furthermore, the timespans can be used to verify that the transient teleconnection response are quicker than one season.

The estimated response times of key climate variables for the JJA transient ensemble are summarised in Figure 4.9. The red crosses show the T25 while the blue dots show the T100 timespans. The reaction times are measured in days from 1 June when the SST anomalies start to ramp up. The lower end of the T100 error bars are defined as the first date that contains a value that is statistically indistinguishable to the peak value at two standard errors. Conversely, the upper end of the T100 error bars is the date of the last (temporally) point which has a value that is statistically indistinguishable to the peak value at two standard errors. Therefore, the T100 error bars uncertainties represent the range of statistically indistinguishable dates to the peak value. The error bars for the T25 dates are calculated differently. The lower end of the T25 error bar in Figure 4.9 show the first five–day–mean whose error bar crosses the 25% peak value threshold. The upper end of the T25 error bar shows the last five–day–mean whose error bar crosses the 25% peak value. Therefore, the T25 error bars in Figure 4.9 show the first and last possible points to cross the 25% peak value accounting for the statistical uncertainties in the responses. The wave flux T25 and T100 is not included due to potential problems with using the magnitude of the wave flux vector.

In austral winter (JJA), the teleconnection mechanism starts from the ramp up of the SST anomalies in the tropics. This starts at day 1–5 (T25), ramps up over ten days, and reaches equilibrium at day 11–15 (T100). Due to the averaging, the first five–day–mean to reach equilibrium will be day 11–15. The SSTs will in turn modify tropical circulation (variables such as precipitation) which starts five days later at day 5–10 (T25) and reaches equilibrium at around day 16–20 (T100). The increased circulation will alter the STJ by increasing its strength and shifting the MZWL towards the east, changing the zonal wind in this region. The zonal wind reaches T25 five days later at day 11–15 and T100 at day

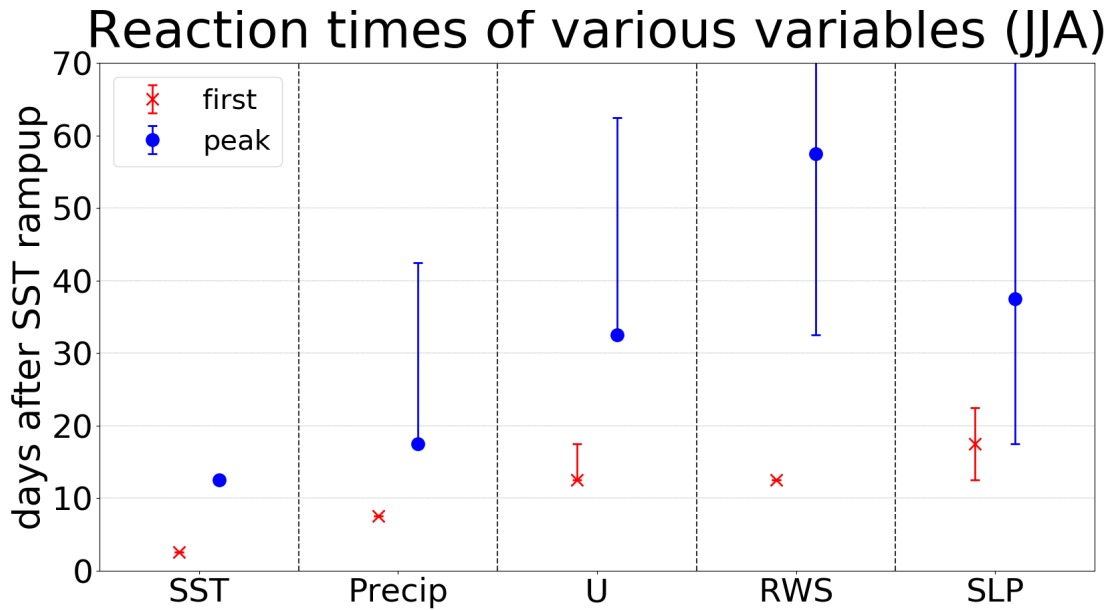


Fig. 4.9 Reaction times of critical variables (SST, precipitation, zonal wind, RWS, wave flux and SLP) in JJA. Red crosses show T25 timings while blue circles show T100 timings. All timings calculated from previous graphs (Figures 4.1, 4.2, 4.3, 4.4, 4.6).

31–35. The divergence and absolute vorticity fields will also shift towards the east as they are associated with the MZWL. The RWS is mainly associated with the changes in divergence and absolute vorticity. The RWS T25 happens on the same five-day-mean as the zonal wind on day 11–15 and the T100 is on day 56–60.

After the RWS forms, the wave train then propagates to the southern high latitudes. This takes approximately 5–15 days. The SLP T25 is on day 16–20 while the T100 is on day 36–40. This suggests that the ENSO–ASR teleconnection process is on timescales that are much smaller than one season (90 days).

Chapter 5

The linearity of El Niño teleconnections to the Amundsen Sea region

This chapter will investigate the linearity of the ENSO–ASR teleconnection. Section 5.1 presents an overview for this chapter. The linearity of the ENSO–ASR teleconnection in austral winter is discussed in Section 5.2 while the linearity in austral summer is found in Section 5.3. The conclusions of this chapter is presented in Section 5.4.

5.1 Overview

The linearity between the strength of the Pacific ENSO SST anomaly and the amplitude of the teleconnection in the ASR is not fully known. If the Niño3.4 temperature changes, it is unclear if the SLP in the Amundsen Sea region will also change linearly. One of the main reasons for this is due to the relatively low number of observed ENSO events and the relatively high internal atmospheric variability in the ASR. Furthermore, individual ENSO events differ greatly in their amplitude and structure making it difficult to draw robust conclusions about the sensitivity of the mechanisms involved in the teleconnections to varying amplitudes of SST change. Most previous studies (Bertler et al., 2004; Kreutz et al., 2000; Turner et al., 2013) use reanalysis data such as ERA–Interim or ERA–40 to study the ENSO–ASR teleconnection. There are only 37–38¹ and 44 years of data in ERA–Interim and ERA–40, respectively, this limits the number of ENSO events available for analysis. While there are reanalysis datasets that stretch further into the past (such as ERA-20 which covers years 1900–2010), the constraining data in the high latitudes, including data on the ASR, are sparse in the pre–satellite era.

¹these numbers are still changing as ERA–Interim is still being updated

Due to the high variability in the ASR, many previous studies do not distinguish between the strengths of El Niños and La Niña events in their analysis (Fogt et al., 2011; Turner et al., 2013). These studies tend to perform composite analysis of ‘El Niño minus neutral’ or ‘El Niño minus La Niña’ conditions. While this is a valid method of understanding the overall effects of El Niño or La Niña on the teleconnection, it does not take into account that different ENSO magnitudes may cause different responses. Even studies such as Hoerling et al. (1997) which investigates the nonlinearity of teleconnections to the northern hemisphere in Boreal winter, focus on the difference between El Niño and La Niña rather than different magnitudes of El Niño or La Niña events. In this chapter changes in the teleconnection with respect to different magnitudes of El Niño only will be used to investigate the linearity.

The main scientific aim of this chapter is to investigate the linearity of the ENSO–ASR teleconnection under El Niño conditions. As seen in Figure 3.16, the potential for Rossby wave propagation to the high southern latitudes may change under different El Niño magnitudes. The linearity of the winter and summer teleconnection are studied separately as the teleconnection mechanism in the two seasons seems to be different.

Turner et al. (2013), found different teleconnection magnitudes between El Niño and La Niña conditions. While it would be ideal to also investigate the linearity of ENSO between El Niño and La Niña conditions, the model does not respond realistically under La Niña when compared to reanalysis data. Hence the focus will be on comparing the teleconnection response across different amplitudes of El Niño.

5.2 Linearity of the teleconnection in austral winter under El Niño conditions

This section will focus on the ENSO–ASR teleconnection linearity under El Niño conditions during JJA. The response of key variables will be discussed in Section 5.2.1. In particular, changes in sea level pressure of the Amundsen sea region, zonal wind of the subtropical jet, RWS anomaly and Rossby wave propagation will be presented. Section 5.2.2 will focus on the combination of the Rossby wave source and propagation via integration. The data comes from the perpetual El Niño timeslice model runs and each El Niño magnitude contains 54 years of data. The El Niño strengths include Niño3.4 temperatures of 0.0 K (baseline), 0.75 K, 1.5 K, 2.25 K and 3.0 K. All results reported refer to these five perturbation experiments.

5.2.1 Response of key variables under various El Niño magnitudes

Sea level pressure

Figure 5.1 shows the SLP anomaly in the ASR under El Niño (0.75 K, 1.5 K, 2.25 K, 3.0 K) conditions. The blue line in the top panel shows the *peak SLP anomaly* in the ASR for the four El Niño HadGEM3 runs. The error bars show two standard errors at the location of the peak anomaly. The maximum SLP anomalies are (3.0 ± 0.7) hPa, (6.1 ± 0.8) hPa, (8.6 ± 0.7) hPa and (7.0 ± 0.7) hPa for the respective El Niño magnitudes in ascending order. The behaviour of the SLP anomaly is perhaps unexpected under the most extreme (3.0 K) El Niño perturbation. While the SLP increases by around 3 hPa in the ASR per 0.75 K Niño3.4 temperature between 0 K to 2.25 K, the SLP anomaly at 3.0 K El Niño breaks away from this linear pattern. It is around 1.5 hPa *weaker* than the SLP anomaly at 2.25 K El Niño. The results of the Rossby wave anomalies indicated the presence of stronger non-linearities at 3.0 K.

To illustrate this non-linearity, the green line in the top panel shows the ‘hypothetical’ linear SLP case, derived using the difference between the baseline case and El Niño of 0.75 K. The SLP anomaly is linear, within statistical significance, up to 2.25 K. At 3 K, there is a statistically significant difference (at the 95% level) between the actual SLP anomaly and the ‘linear’ case. Therefore, the results can be interpreted as being linear within historically observed El Niños in austral winter (0 K–1.5 K) but would not be linear under extreme El Niños that are stronger than historically observed (>2.25 K in JJA).

Figure 5.1 also shows maps of the SLP anomaly for the four different El Niño magnitudes. While most of the gross spatial structure remains similar with a EOF2 PSA-pattern, the magnitudes are different. The maximum strength for the positive SLP anomaly over the ASR can be found in the 2.25 K El Niño run. Structurally, the negative pressure at around 30°S seem to elongate and shift towards the east as El Niño magnitude increases. For example, in 0.75 K, the centre of the negative SLP anomaly is at approximately 150°W while it is around 90–120°W in the 3.0 K El Niño run.

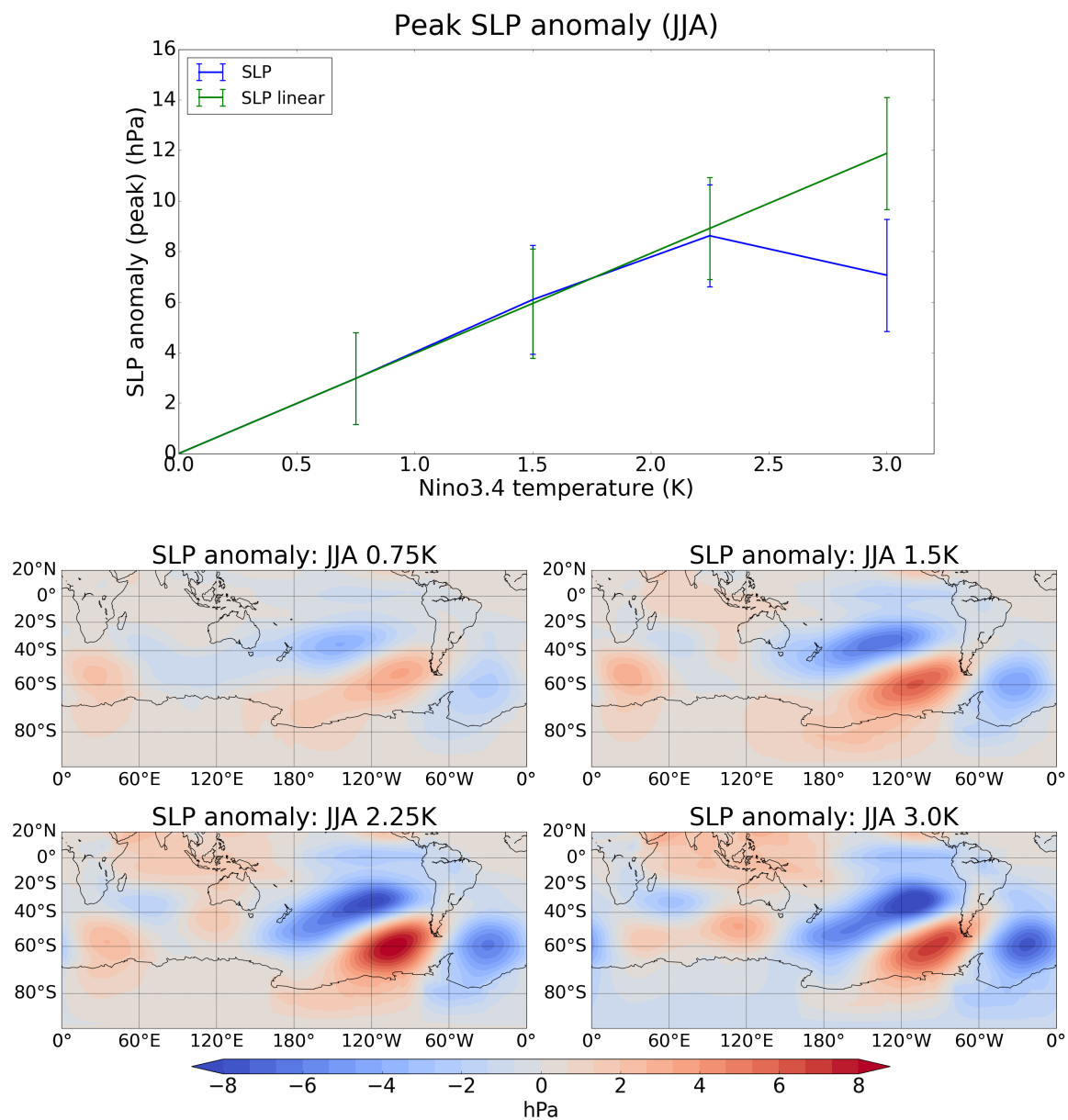


Fig. 5.1 Top: *peak* seasonal time–mean SLP anomaly in the ASR during austral winter (JJA). Blue line shows SLP anomaly, green line shows hypothetical ‘linear’ SLP anomaly. Middle and bottom: seasonal time–mean SLP anomaly maps during JJA. Units are in hPa.

Zonal wind

It was shown in Chapter 3 that the zonal wind plays a significant role in determining both the anomalous RWS and the Rossby wave propagation. Figure 5.2 shows the zonal wind anomalies at 200 hPa under the different El Niño magnitudes. The top panel shows the *maximum* zonal wind anomaly in the region 15–40°S and 190–300°E at 200 hPa. This region is chosen to capture the maximum zonal wind near the STJ. The error bars show two standard errors. The maximum zonal wind anomalies are $(8.7 \pm 0.5) \text{ m s}^{-1}$, $(15.1 \pm 0.4) \text{ m s}^{-1}$, $(18.2 \pm 0.4) \text{ m s}^{-1}$ and $(21.0 \pm 0.4) \text{ m s}^{-1}$ for the respective El Niño magnitudes in ascending order. The increase in zonal wind seems to lessen at the most extreme El Niño case. As expected, the zonal wind anomaly always strengthens as the Niño3.4 temperature increases. This is because the Hadley cell strengthens as warmer surface temperatures are present in the tropical Pacific. So, the decrease in SLP at the 3.0 K does not simply come from decrease in the zonal wind strength.

However, as discussed in Chapter 3, the teleconnection is not only dependent on increasing upper level zonal wind over the Pacific sector but is also due to the eastwards movement of the region of maximum zonal winds. Figure 5.2 shows a latitude–longitude plot of the zonal wind at 200 hPa. The solid contours show the zonal wind in the 0 K baseline run while the coloured contours show anomalies under El Niño conditions. Crosses in these maps indicate the centre of the positive wind anomaly. It can be seen that, the centre of the positive wind anomaly moves eastwards as the El Niño conditions strengthen. As discussed in the following, this eastwards movement will be important for determining the movement of the RWS and the wave reflection zones.

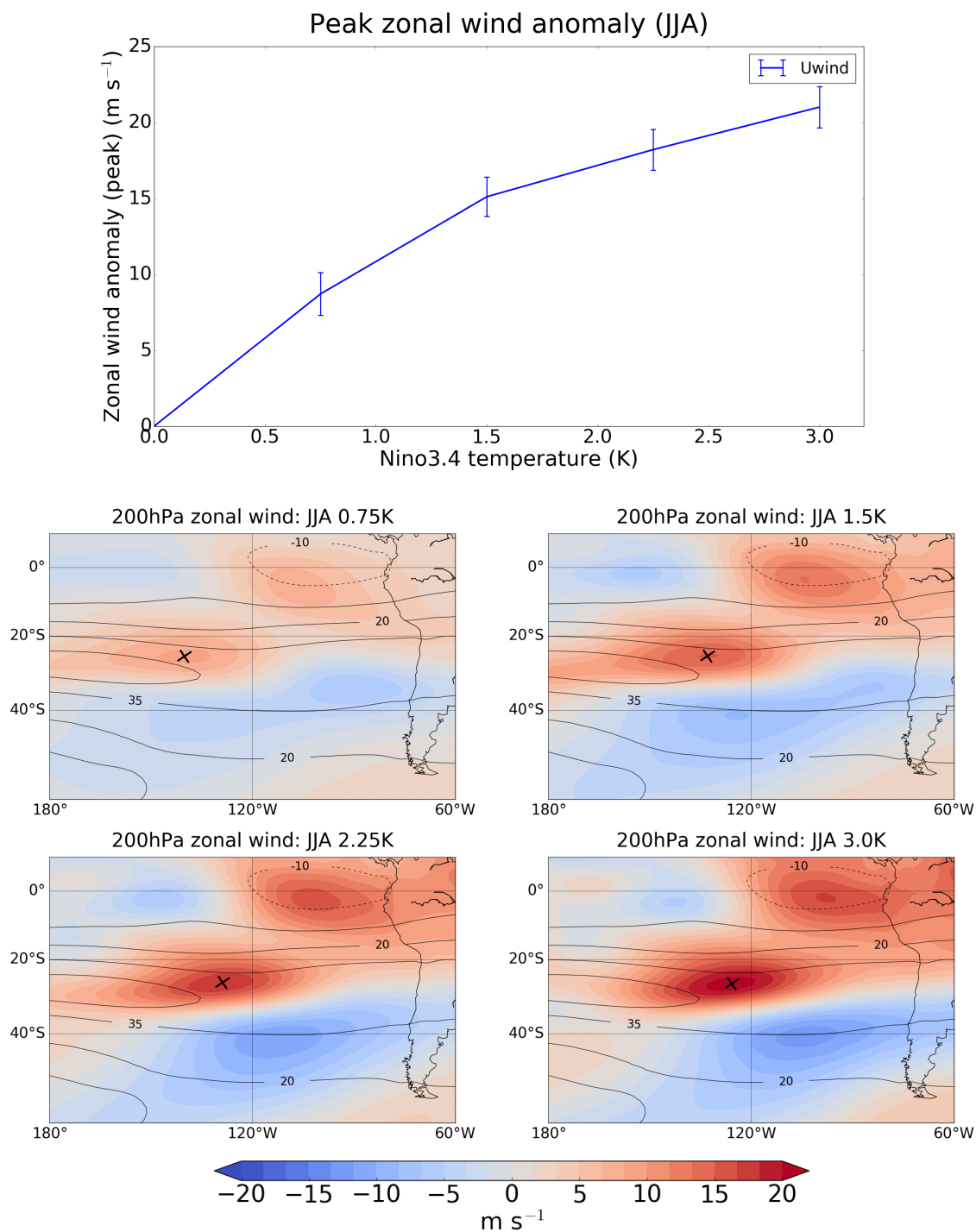


Fig. 5.2 Top: *peak* seasonal time–meaned 200 hPa zonal wind anomaly ($15\text{--}40^{\circ}\text{S}$, $180\text{--}300^{\circ}\text{E}$) during austral winter (JJA). Middle and bottom: seasonal time–meaned 200 hPa zonal wind anomaly maps during JJA. Units are in m s^{-1} .

Rosby wave source

The teleconnection mechanism to the ASR in austral winter (JJA) depends on the Rossby wave source and propagation terms. Therefore, in order to understand why the SLP anomaly is less than expected in the 3.0 K run, it is necessary to look at both the RWS and the propagation characteristic. Figure 5.3 shows the RWS anomaly at 200 hPa. The top panel shows the *peak* RWS anomaly in the southern hemisphere Pacific (between 25–35S and 180–270E) at 200 hPa. This region was chosen to include the maximum RWS anomalies in all 5 runs (1 baseline and 4 El Niños). The maximum RWS anomalies are $3.36 \times 10^{-10} \text{ s}^{-1}$, $5.28 \times 10^{-10} \text{ s}^{-1}$, $6.32 \times 10^{-10} \text{ s}^{-1}$ and $7.49 \times 10^{-10} \text{ s}^{-1}$ for the respective El Niño magnitudes in ascending order. Note the similarity in the patterns of the top panels of Figure 5.3 and Figure 5.2. The RWS increases as El Niño magnitude increases, but the increase in peak RWS is sub-linear with El Niño magnitude. Nevertheless, there is no decrease in the peak RWS anomaly as El Niño increases. Therefore, it is unlikely this explains the reduced SLP anomaly at 3.0 K. Note the similarity between the RWS and the zonal wind is perhaps expected as the RWS is mostly determined by ζD , both of which depend on horizontal wind strength and on horizontal wind gradients.

The maps in Figure 5.3 show the RWS anomalies under the four different El Niño magnitudes. As El Niño strength increases, the RWS dipole (the main positive RWS in the eastern Pacific and the weaker negative RWS in the western Pacific) shifts eastwards and increases in strength. The latitude of the peak RWS anomaly approximately stays the same but the longitude changes from 241°E (0.75 K) to 256°E (3.0 K). This eastwards shift plays a significant role in explaining the decrease in SLP anomaly at 3.0 K, see Section 5.2.2.

It was shown in Chapter 3 that the RWS anomalies are mainly caused by the changes in the absolute vorticity and divergence, ζD . Figure 5.4 shows the divergence, D , absolute vorticity, ζ , and ζD . Note that Figure 5.4 shows the *absolute* values rather than the *anomalies*. From the left column of Figure 5.4, the regions of maximum divergence (convergence) shift² eastwards as El Niño strength increases. This is associated with the eastwards shifting zonal wind, see again Figure 5.2. The middle column shows the absolute vorticity maximum (at around 35°S) strengthening and extending eastwards as the Niño3.4 temperature increases. This is again due to the zonal wind maximum shifting eastwards under El Niño conditions. The result of this is that ζD shifts eastwards as the Niño3.4 temperature increases, see Figure 5.4 right column. Note that none of the variables (D , ζ , RWS) show drastically different responses in their magnitudes and locations changes at 3.0 K compared with the lower temperature changes. While the increase in RWS and the longitudinal movement of

²and extend

the RWS anomaly may differ slightly depending on El Niño magnitude, at no point do they reverse sign at 3.0 K.

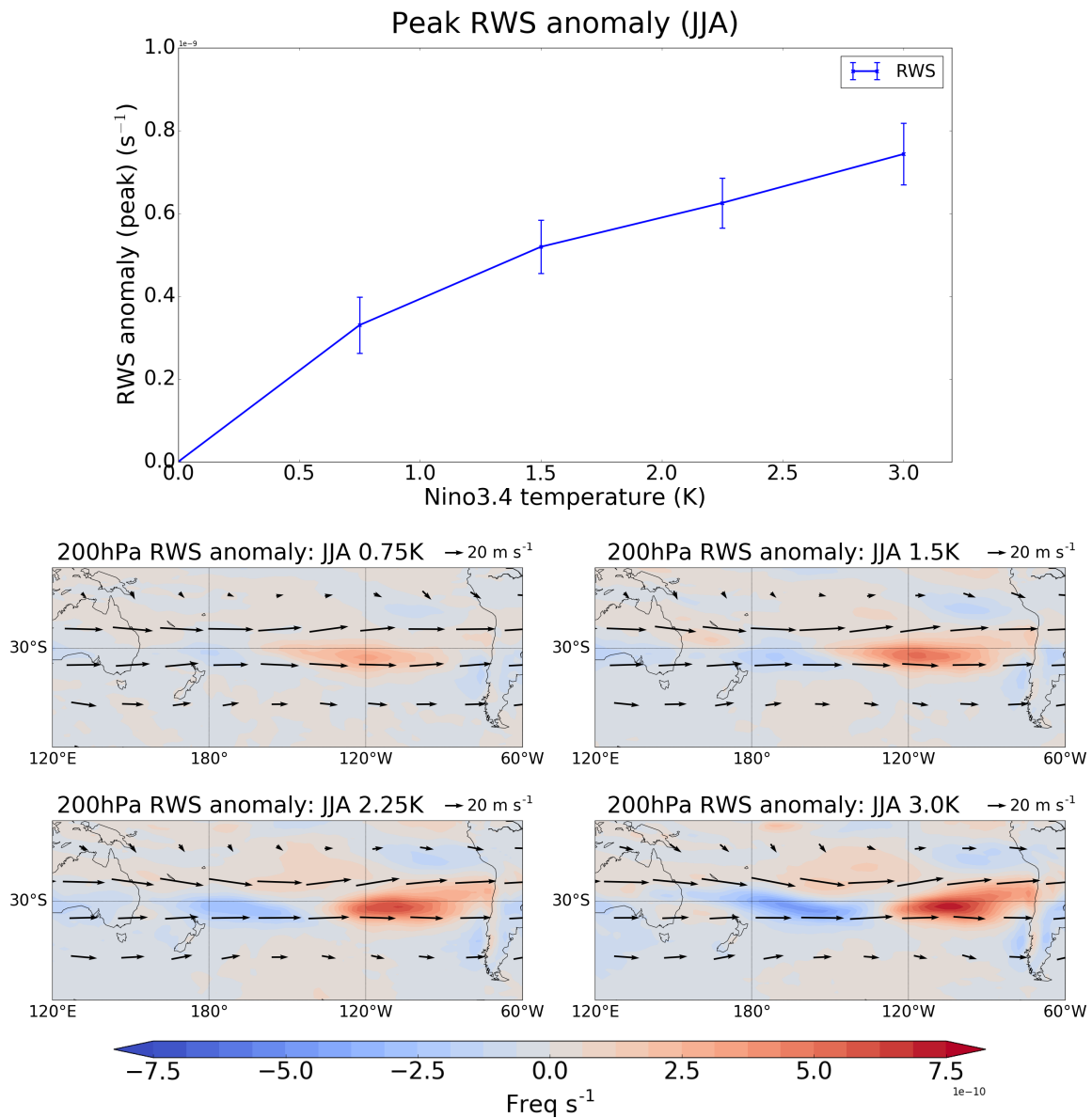


Fig. 5.3 Top: *peak* RWS anomaly (25–35S, 180–270E) in JJA. Middle and bottom: RWS anomaly maps, Units are in s^{-1} . Arrows show the wind direction and speed.

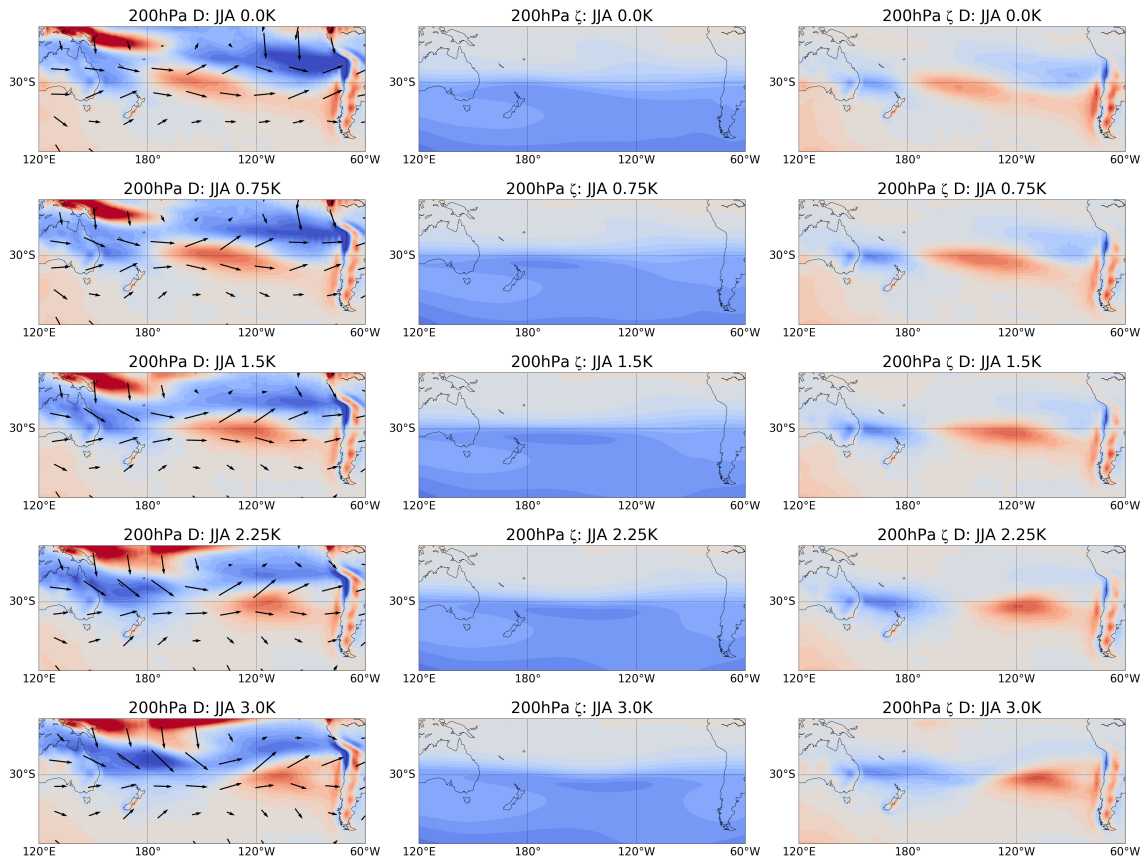


Fig. 5.4 *Absolute* vorticity, divergence and ζD in austral winter (JJA) at 200 hPa. The first column shows the absolute vorticity, the second column shows the divergence and the third column shows ζD . The El Niño magnitude increases as one move down the rows. Arrows on the divergence plots show the wind speed and direction. The meridional wind has been enhanced by a factor of five in these arrows to aid visualisation.

Rossby wave propagation

Figure 5.5 shows examples of Rossby wave ray traces under different magnitudes of El Niño. The top panel shows the percentage of ‘hypothetical’ Rossby waves from ray tracing that make it into and past the ASR, calculated as the rays that pass through 75°S , $170\text{--}290^{\circ}\text{E}$. 50 rays are always initialised from the RWS. Note that, as mentioned in Section 2.5 and Chapter 3, the ray tracing method only provides an qualitative measure of stationary wave propagation under certain simplifying assumptions. In addition, the rays are ‘hypothetical’ and do not have any meaning without the context of the RWS anomaly. In the model runs, the rays initialised at the location of the RWS were spread uniformly apart, see again Section 2.5. This means that the rays do not take into account the strength of the RWS anomaly. For example, the rays initialised at the centre of the RWS will be ‘worth’ more than the rays

initialised at the edge of the RWS. So, Figure 5.5 reflects the percentage change in the number of rays and not the absolute magnitude of the Rossby waves. Therefore, while there is a marked decrease in the percentage of rays at 1.5 K, this does not necessarily mean a marked decrease in the ENSO–ASR response.

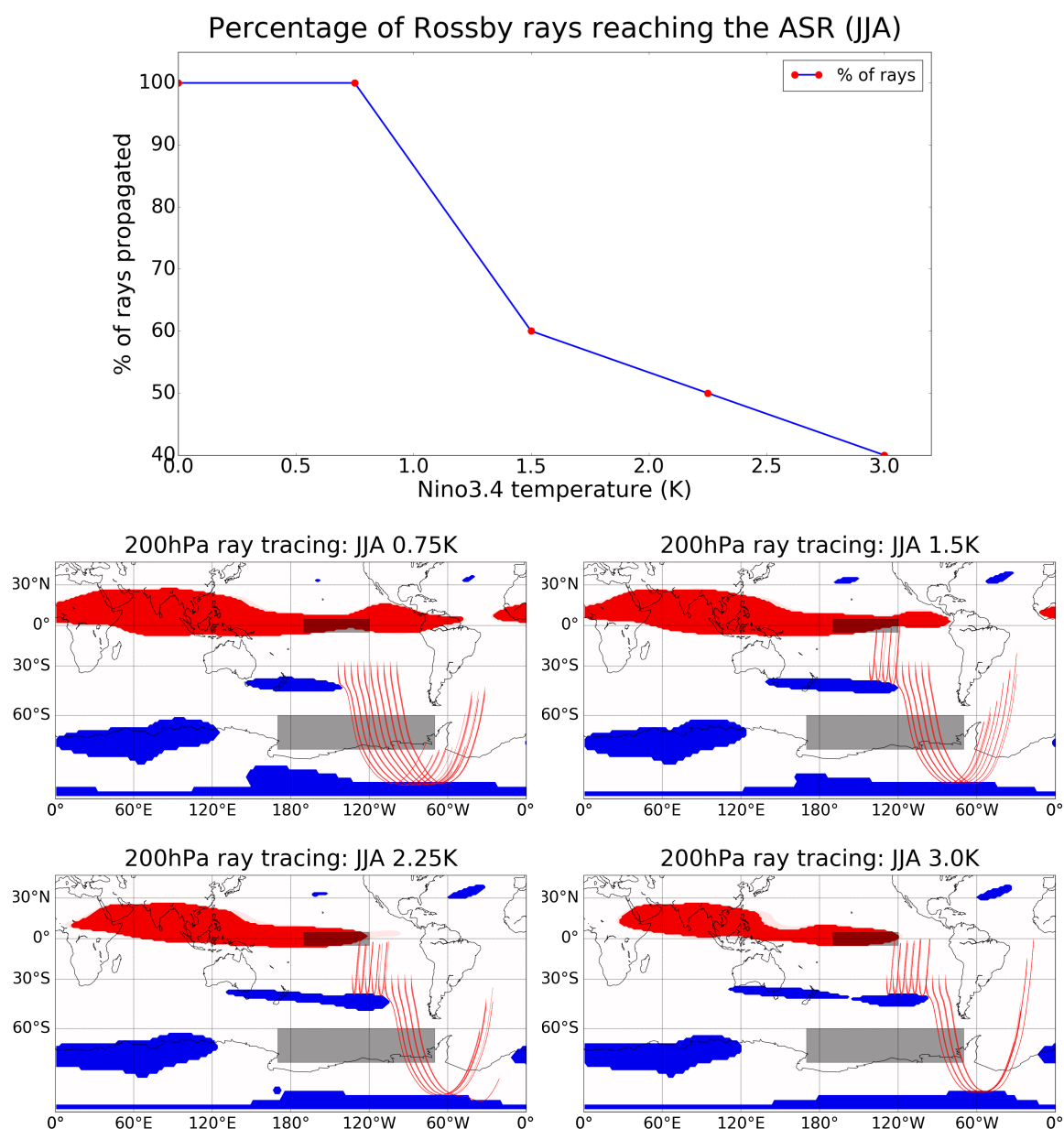


Fig. 5.5 Rossby wave ray tracing in JJA at 200 hPa. Top: percentage of rays that pass through 75°S, 170–290°E. Middle and bottom: Rossby wave ray tracing maps. Rays were initialised at the location of the positive RWS anomaly. Red regions indicate termination, blue regions indicate reflection and white regions indicate propagation regions. The red lines are example paths taken by the hypothetical rays.

From the top panel of Figure 5.5, the relative proportion of the ray traces that propagate through the ASR decreases as the Niño3.4 temperature increases. While this shows that the propensity for wave propagation decreases as El Niño increases in strength, this is not a quantitative measure of Rossby waves in the ASR.

The maps in Figure 5.5 show the Rossby wave ray tracing and the various limiting conditions for propagations. Red denotes wave termination zones and blue the wave reflection zones while white denotes wave propagation zones. As El Niño strength increases, the blue reflection zone at approximately 40°S extends towards the east (and also the west). While it spans the longitudes of approximately 150E–150°W under 0.75 K El Niño, it grows to around 110E–100°W under 3.0 K El Niño. As the RWS lies on the eastwards side of the wave reflection region at baseline, this shift will increasingly ‘block’ the RWS anomaly. As a result, the Rossby waves generated by the RWS anomaly can no longer propagate to the ASR and are reflected at the mid latitudes. However, as both the RWS and the reflection zone shows eastwards movement/extension under El Niño, the propagation is dependent on their relative movements. From the maps in Figure 5.5, it seems that the reflection zones are displaced further eastwards than the RWS anomaly.

Following Chapter 3, the reflection zone is determined by $\beta^* = \beta - U_{yy}$. Figure 5.5 shows that the mid latitude reflection zone in JJA has little latitudinal change under El Niño, β^* will essentially be determined by just U_{yy} as β is constant. The maps in Figure 5.6 shows the *absolute* U_{yy} under different El Niño magnitudes at 200 hPa. A U_{yy} value of $2.7 \text{ m}^{-1} \text{ s}^{-1}$ was empirically identified to be approximately the threshold between regions of wave reflection and propagation at this latitude. There is reflection if U_{yy} is above approximately $2.7 \text{ m}^{-1} \text{ s}^{-1}$ while there is propagation if U_{yy} is under $2.7 \text{ m}^{-1} \text{ s}^{-1}$. Note this value is not derived theoretically but rather is deduced from the model experiments. As seen from the maps in Figure 5.6, the U_{yy} contour extends to the east as El Niño increases in strength which increasingly blocks more rays from passing through the mid latitudes.

The top panel of Figure 5.6 shows the *peak* U_{yy} at each longitude between 30S–45S in the five different experiments. A better understanding of why a ray has been reflected is gained if the focus is placed on the peak value between 30°S–45°S. The reason the ‘peak’ is used is because the ray only needs to hit one grid with a value over $2.7 \text{ m}^{-1} \text{ s}^{-1}$ to reflect. The horizontal dotted line highlights the value of $2.7 \text{ m}^{-1} \text{ s}^{-1}$. The vertical dotted lines show the longitudes where the reflection zone ends for the five model runs. As seen from Figure 5.6, the peak U_{yy} shifts eastwards as El Niño magnitude increases.

Note some caveats: firstly, a reflection zone ending at a certain longitude does not necessarily mean that it would block all Rossby waves at that longitude. This is because, as seen in the ray tracing from Figure 5.5, the rays do not just move latitudinally but also

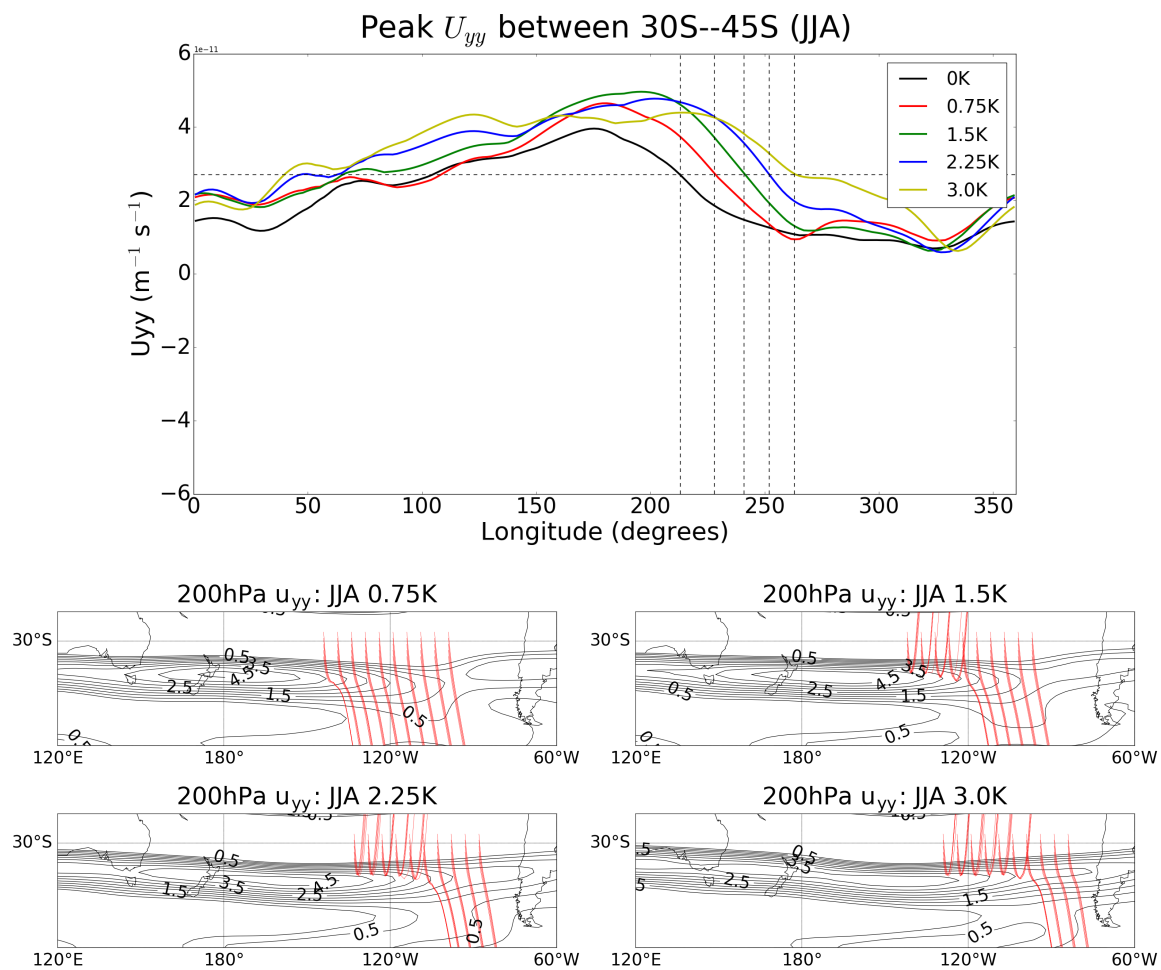


Fig. 5.6 Top: seasonal time-measured 200 hPa U_{yy} (30–45S) during JJA by longitude. Dotted lines show the highest longitude at which the U_{yy} crosses $2.7 \text{ m}^{-1} \text{ s}^{-1}$. $2.7 \text{ m}^{-1} \text{ s}^{-1}$ was chosen as this is approximately the threshold at this latitude in which Rossby waves are reflected. The Rossby waves are reflected if U_{yy} is higher than $2.7 \text{ m}^{-1} \text{ s}^{-1}$ at this latitude. Middle and bottom: seasonal time-measured 200 hPa U_{yy} maps in JJA. The contours in these graphs have a $0.5 \text{ m}^{-1} \text{ s}^{-1}$ spacing. Units are $\text{m}^{-1} \text{ s}^{-1}$.

longitudinally. However, this is a good assumption as the latitudinal movement is usually much greater than the longitudinal movement at this stage of the propagation. Furthermore, although the U_{yy} threshold was chosen as $2.7 \text{ m}^{-1} \text{ s}^{-1}$, this may change due to two reasons. Firstly, $2.7 \text{ m}^{-1} \text{ s}^{-1}$ is merely an approximation and may be slightly off the actual value of the cutoff. Secondly, while the reflection zone does not have much latitudinal movement, it still has *some* movement in the latitudinal direction. This means that β may change slightly which would give a different U_{yy} cutoff.

5.2.2 Combination of the Rossby wave source and propagation

Since neither the strengthening and eastwards movement of the RWS or the changes to the characteristic of wave propagation can explain the changes in SLP anomaly under strong El Niño by itself, these effects need to be combined. The top panel of in Figure 5.7 shows the longitudinal position of the U_{yy} threshold (green line) and *peak* RWS anomaly (blue line) under different El Niño magnitudes at 200 hPa. The U_{yy} threshold is taken from 30–45°S while the peak of the RWS anomaly is taken from 15°S–45°S. As seen in the figure, the U_{yy} threshold is over 10 degrees westwards compared to the location of the RWS anomaly maximum at 0.75 K El Niño. However, the U_{yy} threshold shifts towards the east at a quicker rate than the RWS as El Niño magnitude increases. At 3.0 K El Niño, the U_{yy} threshold is over 5 degrees *eastwards* compared to the location of the peak RWS anomaly which may explain the anomalously low SLP anomaly for the 3.0 K case.

The bottom panel of Figure 5.7 shows the peak RWS anomaly at each longitude between the latitudes of 15–45S at 200 hPa under different magnitudes of El Niños. The coloured dotted lines show the longitude for the U_{yy} cutoff for the respective El Niño magnitudes. At low levels of El Niño (e.g. 0.75 K, red curve), Rossby waves proportional to the area under the red curve on the right of the red dotted line, can propagate to the ASR. This means that the majority of the Rossby waves from the RWS anomaly would reach the ASR. However at high levels of El Niño (e.g. 3.0 K, yellow curve), the majority of the area under the curve is situated on the ‘left’ of the cutoff. Therefore only a small percentage of the Rossby waves generated can reach the ASR.

The total RWS anomalies in the regions where wave propagation is viable could be integrated to give a measure of the potential for significance propagation of anomalous wave activity to high latitudes. To do this, the *peak* RWS anomaly (which is used in the top panel for visualisation simplicity) was not used. Rather, integration³ was summed over all latitudes and longitudes between 15–45S and between the U_{yy} cutoff and 280°E. These coordinates were chosen as they should completely envelope the positive RWS anomaly. Furthermore, in order to distinguish between the background RWS anomaly fluctuations and other weaker positive RWS anomalies from the main RWS anomaly, the contributions from a coordinate are only included if it is higher than $1.68 \times 10^{-10} \text{ s}^{-14}$. This value is approximately half of

³This thesis did not perform a formal ‘integration’. The RWS anomaly values of all grid cells that match these conditions (outside cutoff, in region, above minimal contribution) are summed. As grid cells do not have the same area if latitude is changed, each grid cell have been adjusted with respect to its area before the summation.

⁴There is no contributions from any El Niño magnitudes at the edges of the defined region (15–45°S, 280°E) using this minimal contribution value (of $1.68 \times 10^{-10} \text{ s}^{-1}$). This suggests that the chosen region is large enough and the chosen cutoff is high enough.

the RWS peak anomaly under 0.75 K El Niño. Note that the peak positive RWS anomaly outside of the main source is also approximately of this magnitude, for example see 320°E in Figure 5.7.

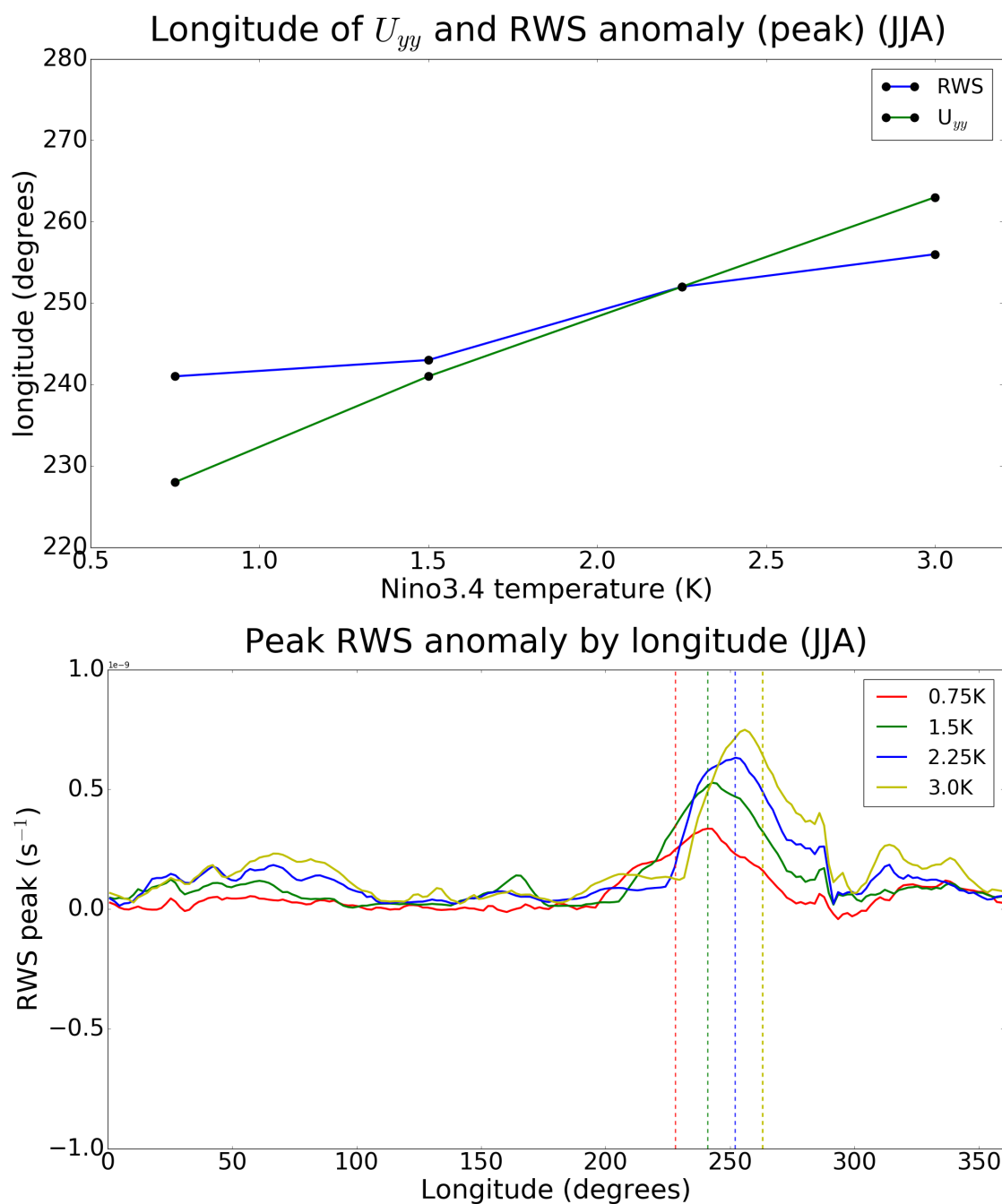


Fig. 5.7 Top: *peak* RWS anomaly (15–45S) during JJA by longitude. Dotted lines show the longitude where the U_{yy} cutoff ($2.7 \text{ m}^{-1} \text{ s}^{-1}$) is situated, see Figure 5.6. Units are s^{-1} . Bottom panel: longitudinal position of the RWS anomaly peak and the U_{yy} cutoff under different El Niño magnitudes

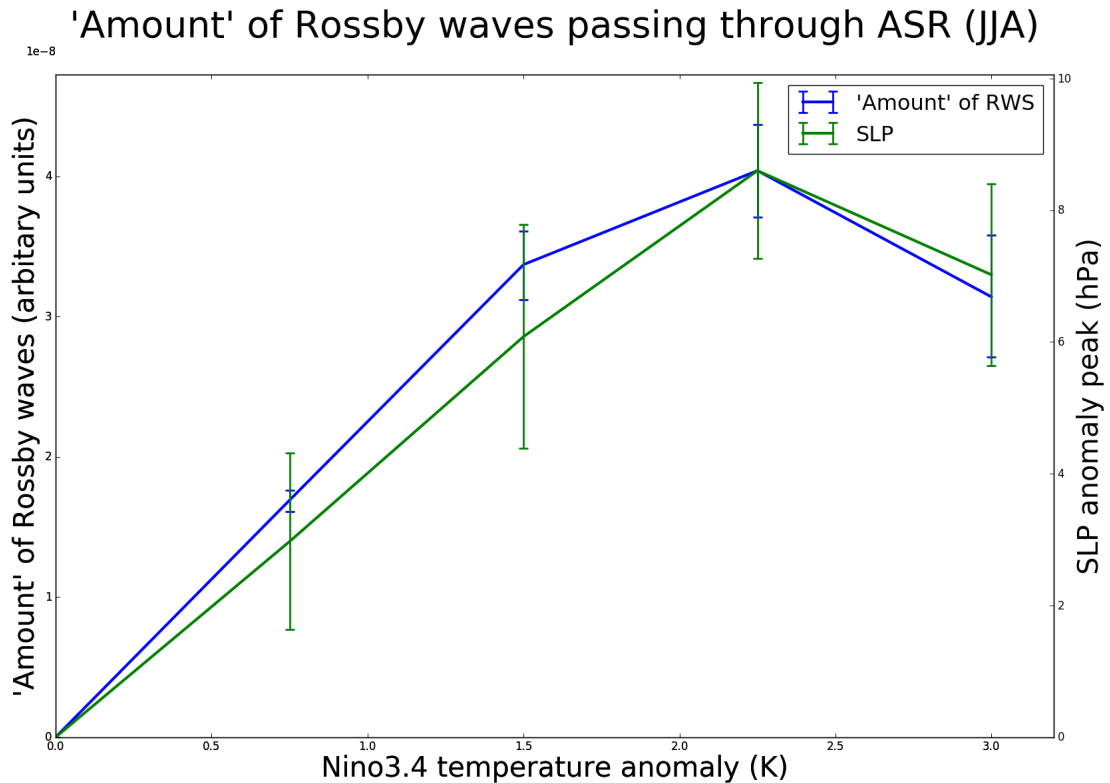


Fig. 5.8 The blue line shows the ‘amount’ of Rossby waves reaching and passing through the ASR in JJA. This is calculated by ‘integrating’ The Rossby wave source that can (not reflected) propagate to the ASR. Simply, it is similar to finding the area under the curve in Figure 5.7 (except the peak RWS is not used). The green line shows the SLP anomaly similar to Figure 5.1.

The blue line in Figure 5.8 shows the ‘integrated’ RWS anomalies under the baseline (0 K) and El Niño (0.75 K–3.0 K) conditions. The error bars shown are the values if one moves the U_{yy} cutoff by one longitude grid in each direction.

The peak SLP anomaly is also plotted in Figure 5.8. The shapes of the two lines are very similar. Similarly to the SLP, the ‘total’ Rossby wave through the ASR (blue line) shows a structure of a linear increase from 0 K to 2.25 K and a decrease at 3.0 K.

From the above, it seems reasonable to conclude that the ‘total amount’ of Rossby waves is controlling the SLP anomaly. This is not unexpected as the proposed teleconnection mechanism (as seen in Chapter 3 and previous literature) is based on the Rossby waves modulating a EOF2 pattern in the SLP. The ‘total amount’ of Rossby waves is controlled by the intensity, location and structure of the RWS anomaly and the longitude location of the U_{yy} cutoff.

However, the method above still implicitly relies on ray tracing for the paths of the rays. As discussed before, caution must be exercised in treating these as the actual paths of the Rossby waves. Therefore, this should only be treated as a qualitative guide.

Summary

This section explored the linearity of the ENSO–ASR teleconnection under El Niño conditions in JJA. The teleconnection is linear up to Niño3.4 temperatures of 2.25 K. At 3.0 K, the linearity breaks down and the SLP anomaly is weaker than the 2.25 K case. Analysis in this section shows that the SLP anomaly is related to the amount of Rossby waves that reaches the ASR. This in turn is related to the competition between the eastwards moving RWS anomaly, the eastwards moving reflection zone and the strengthening RWS anomaly under El Niño conditions. Under extreme El Niño, the eastwards shift of the reflection zone overcomes the RWS strengthening (and movement) which reduces the amount of Rossby waves that reaches the ASR.

5.3 Linearity of the teleconnection in austral summer under El Niño conditions

Attention now turns to the linearity of the ENSO–ASR teleconnection under El Niño conditions during DJF.

Figure 5.9 shows the peak ASR SLP anomaly in DJF under the four El Niño strengths (0.75 K, 1.5 K, 2.25 K, 3.0 K), the DJF counterpart to Figure 5.1.

The top panel shows the *peak* SLP anomaly at each El Niño magnitude. The error bars show two standard errors at the location of the peak. The line shows a linear regression using the five Niño3.4 temperatures. The linear regression lies within the error bars for all the El Niño magnitudes which may suggest that the SLP anomaly in DJF is linear within the estimated errors. Given that the hypothesised teleconnection mechanism in DJF is more direct than JJA, this result might have been anticipated. As discussed in Chapter 3, it is likely that a direct modulation of the PFJ causes pressure changes in the ASR in DJF under El Niño. The maps in Figure 5.9 show the SLP anomalies under the different El Niño magnitudes. Structurally, the SLP seems to remain similar (in a EOF1–like structure) throughout all the El Niño strengths: there is a general positive SLP in the high latitudes with a peak in the ASR.

The maps in Figure 5.10 show the zonal averaged zonal wind by height and latitude under the four different El Niño magnitudes. As the Niño3.4 temperature increases, the positive zonal wind anomaly at around 20–30°S and the negative zonal wind anomaly at around

50–60°S become more intense. However, while the positive anomaly grows more rapidly than the negative anomaly under increasing El Niño, the negative anomaly is nearer to the jet core. The net effect of this is an equatorwards movement of the PFJ and a decrease in the *maximum* jet core speed.

The blue (green) points in the top panel in Figure 5.10 show the *peak* positive (blue) and negative (green) zonal wind anomalies under the four El Niño strengths. The error

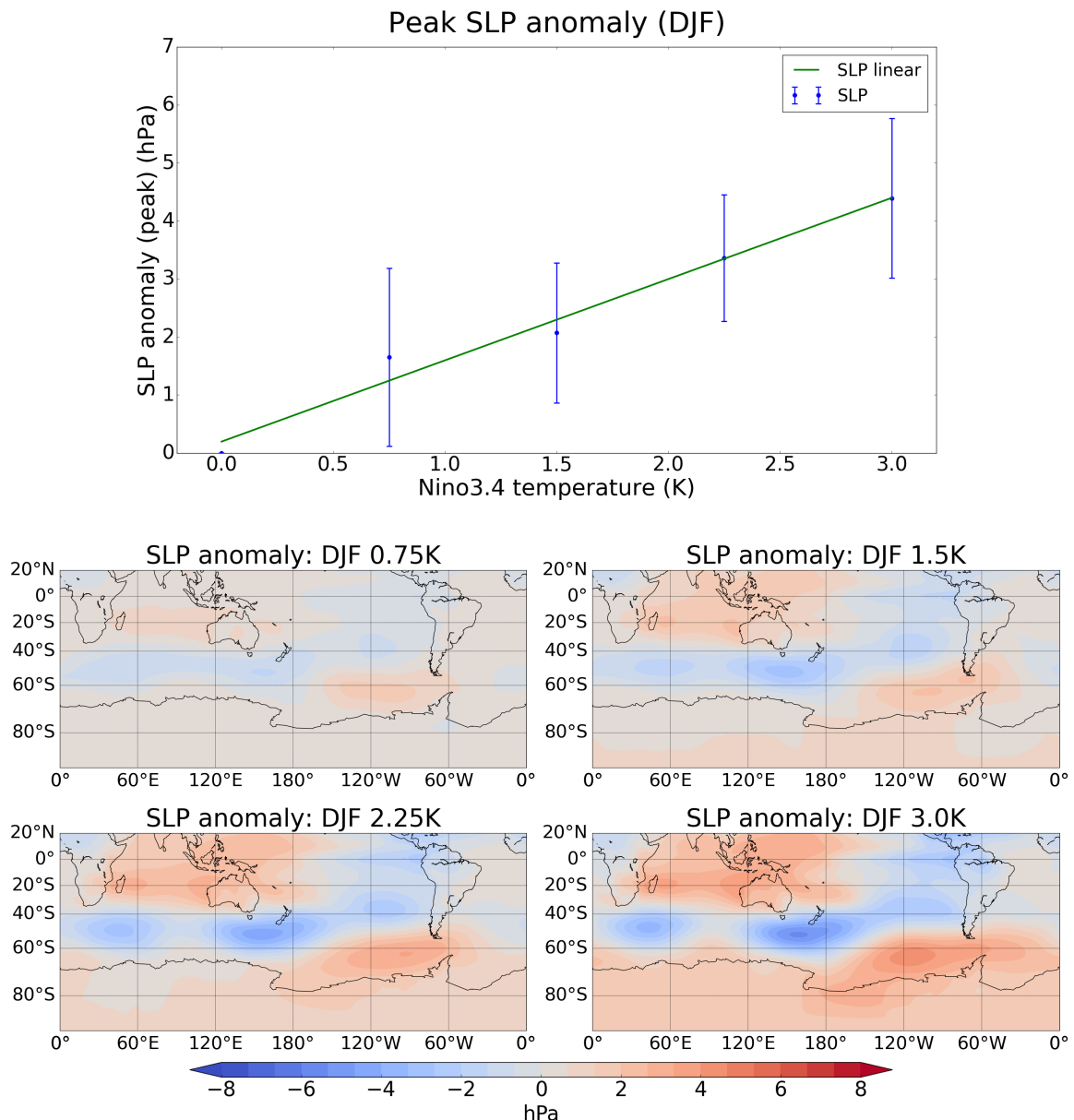


Fig. 5.9 Top: *peak* seasonal time-measured SLP anomaly in the ASR during DJF. Middle and bottom: seasonal time-measured SLP anomaly maps in the four El Niño runs during DJF. Units are in hPa.

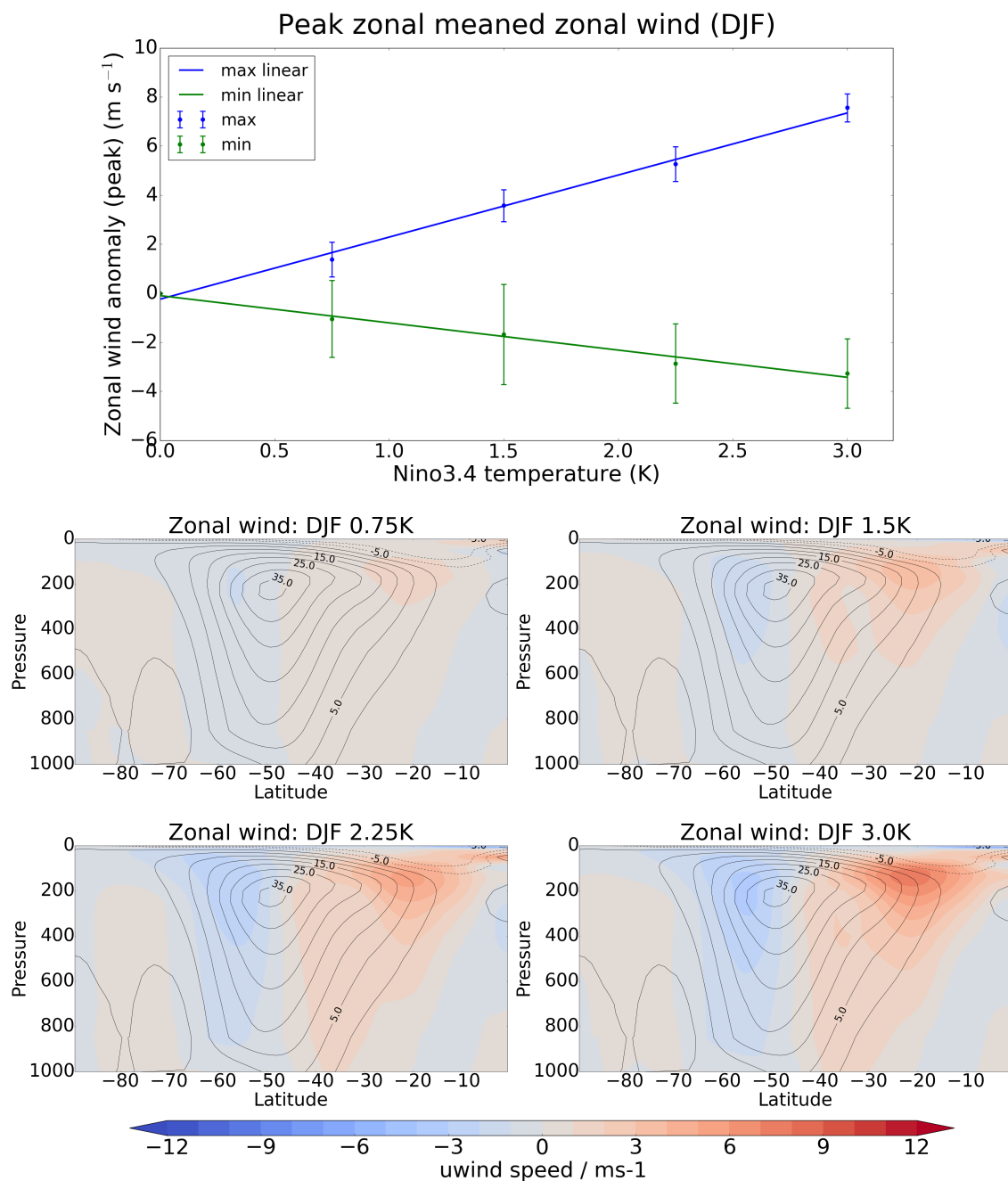


Fig. 5.10 Top: Maximum positive (blue) and negative (green) southern hemisphere zonal mean zonal wind anomaly during DJF. Middle and bottom: zonal mean zonal wind by latitude–height in the four El Niño runs during DJF. Units are in m s^{-1} .

bars show two standard errors at the location of the *peak* anomalies. The blue (green) line shows the linear regression fits of each of the positive and negative anomalies. As both the

weakening and the equatorwards movement of the PFJ⁵ are related to these anomalies, it could be expected that the SLP anomalies in DJF are linear when the zonal wind anomalies changes are also linear.

Summary

This section has explored the linearity of the ENSO–ASR teleconnection under El Niño conditions during DJF. The teleconnection seem to be linear within errors. While this section suggests that the ENSO–ASR teleconnection is linear within errors, the exact feedbacks between the jet and the transient eddies (see, for example Liu et al. (2002)) are not simple and it is not obvious, at least to the author, if this linearity can be expected or anticipated.

5.4 Concluding remarks

This chapter has investigated the linearity of the SLP under different El Niño magnitudes. The results indicate that the peak SLP is linear within errors for El Niño perturbations over the range 0 K–2.25 K. However, at 3.0 K, the peak ASR SLP anomaly is *weaker* than at 2.25 K and deviates, statistically significant at two standard errors, from linearity.

As El Niño increases in strength, the zonal wind anomaly in the Pacific region increases in magnitude and shifts eastwards. This zonal wind anomaly causes a RWS anomaly to be generated. As the RWS is mainly caused by changes in the absolute vorticity and divergence (ζD), the magnitude of the RWS anomaly maps very closely to the zonal wind. However, as the zonal wind anomaly increases in magnitude and shifts, the U_{yy} caused by the jet also increases and shifts. This increased and further eastwards U_{yy} will block additional Rossby waves that are propagating towards the ASR. Therefore there are three competing effects: the RWS magnitude, the RWS longitudinal location and the U_{yy} longitudinal location. These competing effects means that while the RWS anomaly at 3.0 K is stronger than 2.25 K, the potential for wave propagation to high latitudes is actually lower. This explains the reduced SLP anomaly in 3.0 K.

In austral summer (DJF), the teleconnection mechanism arises from modulation of the PFJ. The PFJ weakens and shift equatorwards as the Niño3.4 temperature increases. This is associated with negative SAM which results in an EOF1 like pattern of positive SLP in the high latitudes. The peak ASR SLP response is approximately linear (within error bars) across the entire available spectrum of El Niño magnitudes. As the Niño3.4 temperature increases, a

⁵Note that the movement of the PFJ is not plotted directly, this is because the movement is small compared to the grid size of HadGEM3. The HadGEM3 model used in this thesis has a grid size of 1.25 degrees each while the PFJ only moves around 2-3 grid cells in the extreme El Niño case (3.0 K).

positive (negative) zonal mean zonal wind anomaly develops near 20–30°S (50–60°S). These anomalies seem to get stronger linearly as the Niño3.4 temperature increases.

While these sensitivity experiments point to some non–linearity of the response to El Niño in austral winter at large forcing amplitudes, historically observed El Niños do not reach 3.0 K in JJA. Even in 1997–1998, one of the strongest El Niño events in recent history, the Niño3.4 temperature only reached approximately 3.0 K in DJF and 1.5 K in JJA. Therefore, the conclusion of this chapter is that the ENSO–ASR teleconnection is likely to be linear under historically observed El Niño magnitudes. However, if El Niño strength is higher than historically observed values in JJA, the linearity breaks down.

Naturally, it is impossible to verify these values using observations or reanalysis. However, the mechanism of the non–linearity is only an extension of the eastwards movement of the RWS anomaly and the U_{yy} . Both of these effects are observed in temperatures under 3.0 K. Therefore, it is reasonable to believe that these results are robust.

Chapter 6

Model resolution dependence and the Amundsen Sea Low

This chapter explores the effects of horizontal model resolution on the simulation of the Amundsen Sea low. Section 6.1 provides an overview for the chapter. The effects of horizontal resolution on the climatology of the ASL is explored in Section 6.2. Meanwhile, Section 6.3 investigates the effects of horizontal resolution on the ENSO–ASR teleconnection. The conclusions for the chapter is given in Section 6.4.

6.1 Overview and previous literature

The resolution of climate models may affect the representation of simulated climate (Boville, 1991; Roeckner et al., 2006). For example, changes in model resolution may change the representation of tropical cyclones and storm tracks (Liang et al., 2017; Roberts et al., 2015), tropical circulation (Chemel et al., 2015; Roberts et al., 2009), precipitation (Demory et al., 2014; Schiemann et al., 2014), sea ice (Kirtman et al., 2012), simulation of chemical species (Russo et al., 2015; Stock et al., 2014) and can even affect the large-scale dynamics of the model (Boville, 1991). These changes may also affect the simulation of the ENSO–ASR teleconnection and the ASL itself. For example, Boville (1991) performed a series of experiments with varying horizontal resolutions to examine the effects of resolution on the dynamical aspects of the climate (e.g. winds and eddy fluxes). He ran the NCAR community climate model version 1 (CCM1) at four resolutions: T21, T31, T42 and T63. Boville (1991) found that most variables are better represented at T63 compared with T21. One of the particular foci was the representation of the orography. Obviously, orography is more accurate at higher resolution. For example, the maximum elevation of the Himalayas is

approximately 8848 m. However, this maximum surface elevation is not captured in models due to the finite grid size. The height of the Himalayas is simulated as 4386 m, 4938 m, 5696 m and 5518 m in the four resolutions, respectively (Boville, 1991).

Improved representation of orography could play a strong role in the representation of the ASL because the topography of Antarctica contributes to the enhanced baroclinicity needed for the formation of the low pressure systems in the circumpolar trough (Hosking et al., 2013; Lachlan-Cope et al., 2001; Walsh et al., 2000). Therefore, better horizontal resolution may improve simulation of the ASL.

Turning to the ENSO–ASR teleconnection, while the climatology of the ASL relies heavily on the simulation of local synoptic and subsynoptic low pressure systems, the simulation of the ENSO–ASR teleconnection involves processes from the tropical circulation to the high latitudes. Therefore, it is important for the model to be able to simulate adequately all these components. Increasing resolution has been known to affect simulation of the wider climate. For example, Roberts et al. (2009) found that increasing both atmosphere and ocean resolution in a model can improve the mean statistics of the tropical Pacific atmospheric circulation. In particular, increasing resolution allows the model to better simulate tropical tropospheric instability which allows for a better simulation of the Walker circulation. This is crucial for capturing the effects of ENSO events. Another example is from Schiemann et al. (2014) who found that increasing horizontal resolution in the atmospheric version of the Hadley Centre General Environment Model (HADGAM1) improves tropical circulation and maritime continent precipitation. Improved simulation of precipitation and tropical circulation may be important for the ENSO–ASR teleconnection.

However, it is important to note that increasing resolution does not always improve model performance. For example, Boer and Lazare (1988) found that increasing horizontal resolution did not improve the representation of the large–scale circulation such as winds and eddy fluxes. Palmer et al. (1986) found that the westerly wind bias in the northern hemisphere winter time flow in higher resolution models was worse than the previous coarser resolution model and had to introduce an previously ignored orographic gravity wave drag parametrization¹ to alleviate this problem. Thus, in some cases, representation of climate variables may be improved by higher resolution while others may be worsened.

This chapter presents the changes in both the climatology of the ASL and the ENSO–ASR teleconnection under different horizontal resolutions. The UPSCALE dataset will be used and evaluation of the models will be against the ERA–Interim dataset (Section 2.1). As the prescribed SSTs in UPSCALE are almost identical with ERA–Interim (both are based

¹This is a good example of when increasing model resolution may not always improve performance. The orographic gravity wave drag parametrization was ignored before Palmer et al. (1986). Therefore, sometimes increasing resolution has to be complemented with ‘better’ physics.

on observations), the climatology of the ASL and the ENSO–ASR teleconnection can be compared ‘like–for–like’. The model resolutions explored in this chapter are N96, N216 and N512.

6.2 Model resolution and the climatology of the ASL

In this section, the changes of the climatology of the ASL at different horizontal resolutions are presented. Figure 6.1 shows the climatological SLP in the high latitude southern hemisphere for ERA–Interim (left), N96 (middle left), N216 (middle right) and N512 (right) in austral winter (JJA) while Figure 6.2 shows the root mean squared error (RMSE) of the sea level pressure at various model resolutions when compared with ERA–Interim. As seen from ERA–Interim (left panel, Figure 6.1), the prominent climatological low pressure centres at high latitudes are located at approximately 30°E, 120°E and 200°E longitude along the circumpolar trough. These macro features are mostly captured in all three resolutions in the UPSCALE dataset. However, the structure, location and magnitudes of the three low pressure systems are slightly different in the three resolutions. At N96, the low pressure centre in the ASL is located too far eastwards and its magnitude is weak compared to ERA–Interim². The RMSE in the ASR has a maximum value of 9.84 hPa. The RMSE is especially strong near the Ross sea as the ASL in N96 is too far eastwards.

At the N216 model, the ASL also has a minimum pressure of 985.1 hPa, similarly to at N96. However, the location of the ASL has shifted westwards compared to N96 which brings

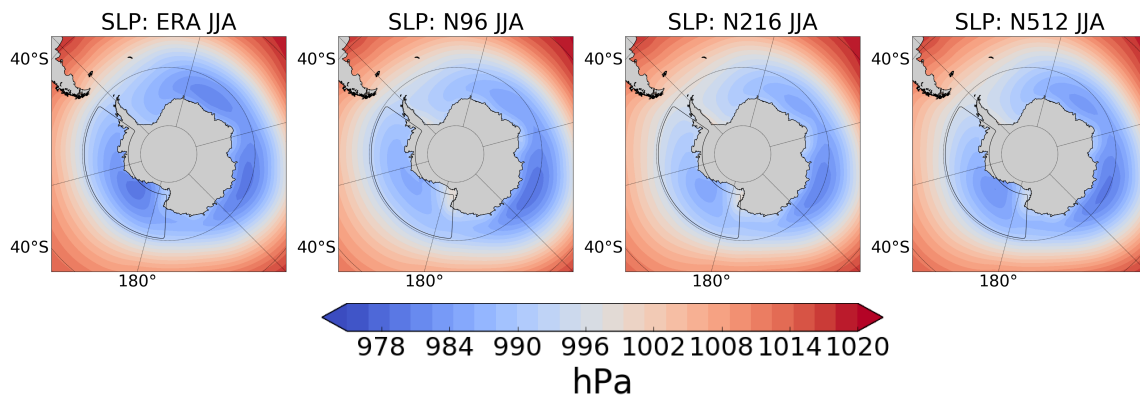


Fig. 6.1 SLP of ERA–Interim (left) and UPSCALE in JJA. Resolution include N96 (middle left), N216 (middle right) and N512 (right). Units are in hPa.

²ASL in ERA–Interim: minimum pressure of 989.7 hPa, -74°S, 208°E. N96 model: minimum pressure of 985.2 hPa, -75°S, 221°E.

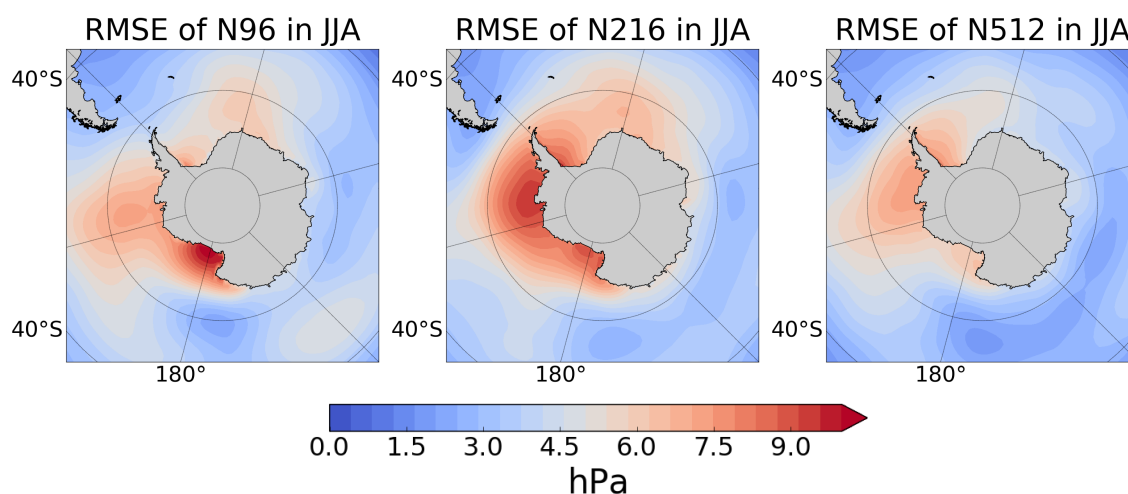


Fig. 6.2 RMSE of the SLP between UPSCALE and ERA–Interim in JJA. Units are in hPa.

the location³ much closer to ERA–Interim. However, as the ASL is still too weak, there is still a relatively large RMSE both eastwards and westwards of the low pressure system. The maximum RMSE in the ASR is 9.50 hPa.

The ASL is deeper at a resolution of N512⁴ compared to the lower resolutions and is the closest to the ERA–interim climatology of the three resolutions. The location is *slightly* more westwards which also brings it closest to ERA–Interim. This is reflected in the lower peak RMSE (Figure 6.2) of 8.09 hPa (maximum). It can be concluded that the climatology of the ASL in JJA is best simulated at N512. However, it is important to note that it is difficult to assess whether the increasing resolution creates a statistically significant improvement in the simulation of the ASL. This is because the ASL is not a fixed pressure system but exhibits significant interannual variability in its depth and location.

Turning to austral summer (DJF), Figure 6.3 shows the SLP in the high latitude southern hemisphere of ERA–Interim and UPSCALE. Comparison between Figure 6.1 and 6.3 shows that UPSCALE generally captures the seasonality of the ASL climatology well. The ASL is located further eastwards in DJF (usually located around the Bellingshausen–Amundsen Sea) than in JJA (usually located near the Ross sea). UPSCALE is based on HadGEM3, which produces a good seasonal climatology for the ASL, so this result might have been expected.

As seen from Figure 6.4, all three resolutions simulate the locations of the ASL well. As resolution is increased, the ASL changes little in its location in DJF. The minimum pressure in the ASR is at 985.5 hPa (N96), 985.7 hPa (N216) and 984.7 hPa (N512). While all three resolutions show higher pressures than ERA–Interim (982 hPa), the central pressure seems to

³-73°S, 212°E.

⁴982.5 hPa

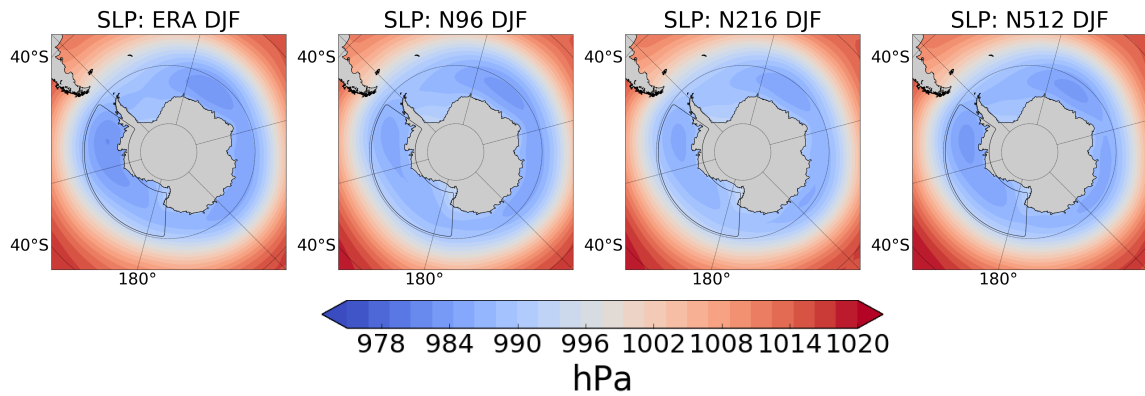


Fig. 6.3 Same as Figure 6.1 but for DJF.

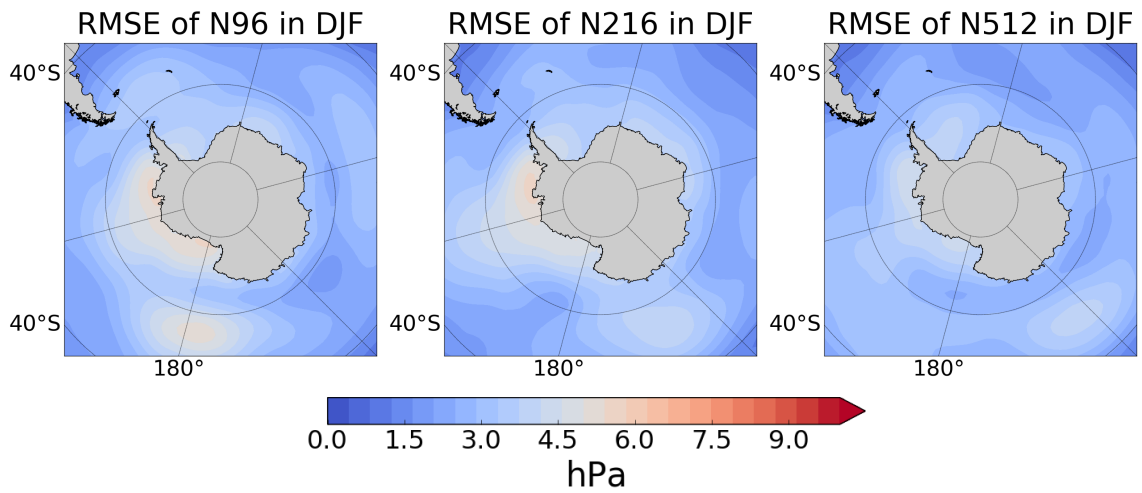


Fig. 6.4 Same as Figure 6.2 but for DJF.

match ERA–Interim best at N512. This is reflected in the RMSE (Figure 6.4). The maximum RMSE in the ASR in N96 (left panel) is 5.65 hPa and 5.61 hPa in N216. However, the RMSE drops in N512 to 4.58 hPa. Therefore, in conclusion, the climatology of the ASL in DJF is marginally better simulated by N512.

Summary

This section has explored the effects of horizontal resolution on the simulation of the ASL climatology. All three resolutions captures the seasonality and climatology of the ASL relatively well. However, the results show that the climatology is best captured in N512 for both austral summer and winter. The simulation at lower resolutions seem to produce

weaker pressures (in DJF and JJA) and incorrect locations (in JJA) for the ASL. However, it is important to note that these changes are not large and may not be statistically significant.

6.3 Model resolution and the ENSO–ASR teleconnection

Section 6.2 has explored the resolution dependence effect on the modeled Amundsen Sea low. This section investigates the effect of horizontal resolution on the simulation of the ENSO–ASR teleconnection. Figures 6.5 and 6.6 shows the SLP composites of El Niño minus neutral seasons in JJA and DJF, respectively. Each composite takes the 26 (1986–2011) years and separates into El Niño seasons (seasonal average Niño3.4 is greater than 0.5 K), neutral seasons (seasonal average Niño3.4 is between 0.5 K and -0.5 K) or La Niña seasons (seasonal average Niño3.4 is less than -0.5 K).

In JJA, there are only five El Niño seasons in ERA–Interim while there are nine El Niño seasons in DJF. As the number of El Niño seasons are small (especially in JJA), caution must be exercised when interpreting the results in anything more than a qualitative fashion.

Figure 6.5 shows the SLP composites in JJA under ERA–Interim and UPSCALE. The ERA–Interim shows the characteristic positive SLP anomaly over the ASR under El Niño and weaker negative anomalies northwards and eastwards of the ASR. UPSCALE N96 shows a structurally similar pattern to ERA–Interim. However, the positive anomaly is *slightly* weaker in UPSCALE N96 (3.38 hPa) compared with ERA–Interim (4.62 hPa). The positive anomaly in the ASR is also further westwards at N96 (242°E) compared to ERA–Interim (266°E). However, these changes may simply reflect the variability as this region is known for its high internal variability (see Section 1.1.1 and 1.4 for details).

The simulation of the ENSO–ASR teleconnection is weaker as resolution increases. At N216, the positive anomaly in the ASR (2.18 hPa) is weaker than N96 and has split into two centres, one centre is located near the Ross Sea with the other near South America. N512 produces a even weaker positive anomaly over the ASR with a value of 1.67 hPa in the Ross Sea. There is even a negative SLP anomaly over the Amundsen sea and the Antarctic peninsula.

As expected from the results of Chapter 3, ERA–Interim in DJF (Figure 6.6) shows a EOF1–like response as opposed to the EOF2–like response in JJA. Superimposed on top of the EOF1–like signal is a weak positive anomaly in the ASR. The maximum pressure change in the ASR in ERA–Interim is 2.42 hPa located at -61°S, 249°E. N96 produces a similar EOF1–like response with the maximum anomaly at 2.27 hPa. The simulation of the ENSO–ASR teleconnection is much weaker in N216 and N512 with a overly weak SLP anomaly of 1.19 hPa and 1.36 hPa, respectively. Furthermore, the EOF1–like signal cannot

be easy seen in the higher resolutions. In conclusion, the ENSO–ASR simulation is best in N96 in both seasons.

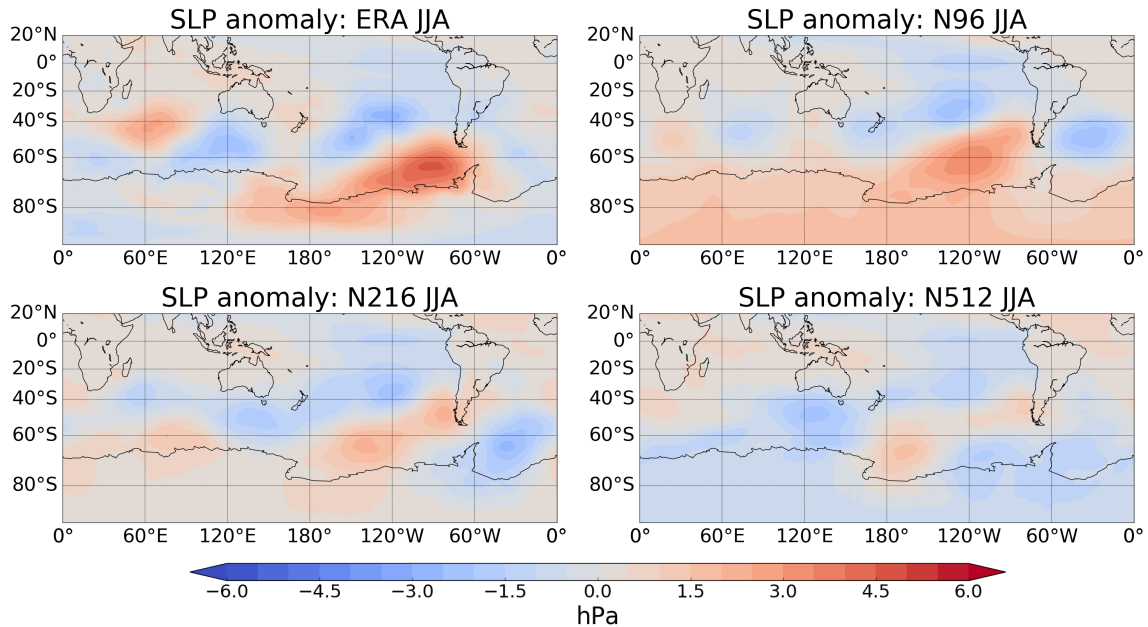


Fig. 6.5 SLP composites of El Niño minus neutral conditions during JJA under ERA–Interim and UPSCALE. ERA–Interim is shown on the left, N96 on the middle left, N216 on the middle right and N512 on the right. Units are in hPa.

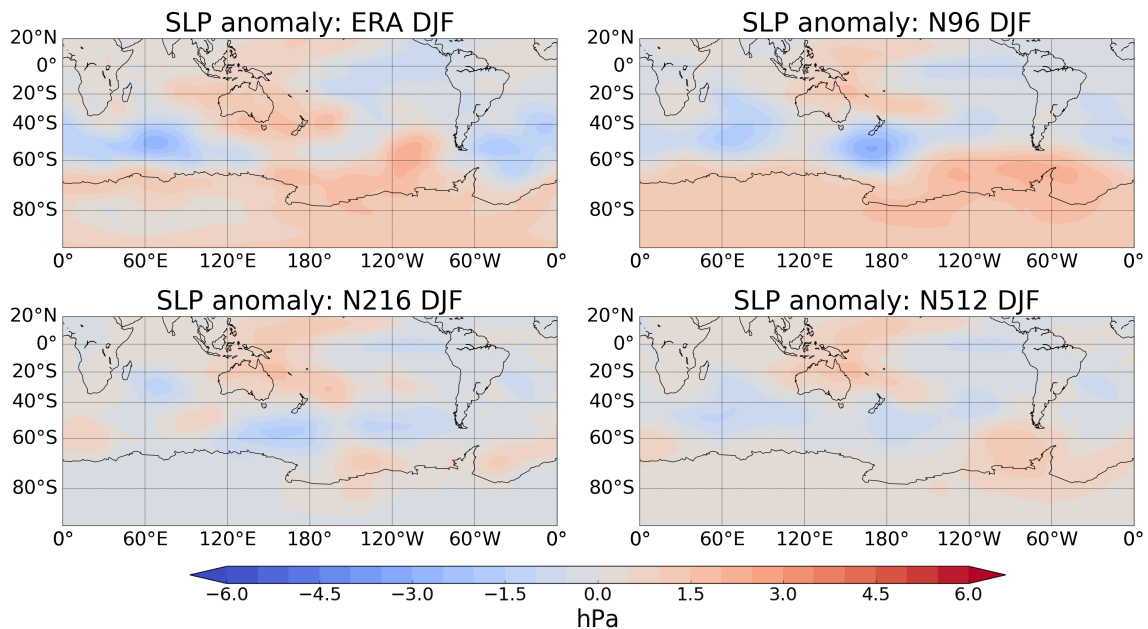


Fig. 6.6 Same as Figure 6.5 but in DJF.

Current analysis has not investigated into the reason for the worsening simulation of the teleconnection as resolution increases. Potential future work to diagnose this is possible. For details, see Section 7.7.

Summary

This section has investigated the simulation of the ENSO–ASR teleconnection under various horizontal resolutions. The results show that the ENSO–ASR teleconnection is best simulated in the N96 model. Both the magnitude and structure are closest to ERA–Interim in the lower resolution model. Furthermore, the seasonality (both magnitude and the EOF structure) is lost in the higher resolution models.

6.4 Concluding remarks

The climatology of the ASL and the simulation of the ENSO–ASR teleconnection has been compared here between ERA–Interim and the UPSCALE dataset, which performs simulations at three horizontal resolutions. The simulation of the seasonality of the ASL climatology is generally good throughout the different resolutions of UPSCALE with a deeper and westwards ASL in JJA and a weaker and eastwards ASL in DJF. However, in JJA, the ASL is slightly too weak and located too far eastwards in the N96 resolution compared to N512. In DJF, the location of the ASL is generally good but is slightly too weak at N96 compared to N512. The high resolution dataset shows marginally better performance in simulating the ASL in both seasons compared to the middle and lower resolution datasets.

However, increasing resolution seems to worsen the simulation of the ENSO–ASR teleconnection signal in both seasons. N96 simulates the ENSO–ASR teleconnection relatively well with an EOF2–like signal in JJA and a EOF1–like signal in DJF. However, in the middle and higher resolution model versions, the SLP anomaly becomes weaker in both seasons and the seasonality of the teleconnection seems to be lost. There is no longer a large difference in the structure (i.e. EOF1 versus EOF2) and the magnitude of the SLP anomaly between the seasons in the highest resolution model. It is important to note that the UPSCALE experiments change horizontal resolution while keeping other model settings and parameters fixed as far as possible. Thus a higher resolution model may be able to capture the ENSO–ASR teleconnection with a high degree of fidelity if its climatology were retuned.

The reason for the worsening simulation in higher resolution models are unknown. Further work is required to gain further insight into this problem, see Section 7.7 for details.

Chapter 7

Conclusions and future work

The HadGEM3 UM model has been used in this thesis to investigate the ENSO–ASR teleconnection. The mechanism behind the seasonality of the teleconnection was explored in Chapter 3. The transient short timescale evolution of the teleconnection was examined in Chapter 4. Chapter 5 dealt with the linearity of the ENSO–ASR teleconnection under El Niño conditions, focusing on the mechanism behind a weakening of the sea level pressure under extreme El Niño conditions. The effect of horizontal resolution on the ASL and the ENSO–ASR teleconnection was explored in Chapter 6. Lastly, brief discussion will be presented in Section 7.5. The following sections summarise the findings of these four chapters and draw conclusions.

This chapter also presents suggestions for future work and possible extensions to the thesis. The future work is separated into two parts. Section 7.6 presents future work that require additional experimental runs involving the HadGEM3 model. Section 7.7 represents future work that requires additional analysis on existing datasets.

7.1 Chapter 3: The seasonality of the ENSO–ASR teleconnection

The aim of Chapter 3 was to understand the mechanism behind the seasonality of the ENSO–ASR teleconnection. In particular, a mechanistic flowchart, inspired by Simpkins et al. (2014), was produced (Figure 3.20) to summarise the mechanism of the ENSO–ASR teleconnection. Runs of the HadGEM3 model were performed in which a perpetual 1.5 K El Niño was imposed to the baseline SSTs. These runs were used to create composites to show the effect of El Niño events on the ENSO–ASR teleconnection.

The response of the tropical circulation was found to be similar between austral winter and summer. The enhancement of the tropical Pacific SSTs causes the Hadley cell to increase in strength and contract in both seasons, which matches previous literature (e.g. Lu et al. (2008)).

The seasonal differences of the ENSO–ASR teleconnection were shown to arise from the seasonality of the zonal large-scale circulation. In DJF, there is usually one jet (PFJ) located at mid latitudes while in JJA, there are usually two jets (PFJ and STJ) but the STJ is dominant (Gallego et al., 2005; Galvin, 2007; Nakamura and Shimpo, 2004). As illustrated in the seasonal split in the flowchart, the seasonal differences of the ENSO–ASR teleconnection arise from this seasonality of the jets.

The teleconnection is propagated by Rossby waves and requires a Rossby wave source (RWS). The RWS anomaly mainly depends in the changes of divergence and absolute vorticity of the winds. As El Niño magnitudes increase, the maximum zonal wind location (MZWL) from the STJ in JJA increases in strength and shifts eastwards. This shift and intensification causes anomalous divergence and absolute vorticity at the new location of the MZWL. A RWS is created at approximately 30°S, 100–120°W. In contrast, there is little change in the divergence and absolute vorticity in DJF as the STJ is weak. This means that there is minimal RWS anomaly in DJF.

The propagation of Rossby waves using ray tracing and wave flux methods was studied next. Rossby wave ray tracing showed that the propagation of the stationary Rossby waves from the tropical Pacific into high southern latitudes is only possible in JJA but not in DJF. The waves in DJF are reflected before reaching deep into the ASR. The reflection zone is consistent with the single polar front jet (PFJ) in DJF. However, the conditions in JJA are more favourable to Rossby wave propagation towards the ASR and then to the Weddell Sea. This is approximately the path of the PSA pattern.

The lack of the anomalous wave source and the inhibition of propagation in DJF mean that the SLP anomaly is weaker than in JJA. Furthermore, the model results suggest that different mechanisms operate in the different seasons. The SLP anomalies in JJA seem to be EOF2–like which matches with the PSA–like pattern that the Rossby waves follow. On the other hand, the SLP anomaly in DJF is EOF1–like which suggests that the DJF teleconnection is from a direct modulation of the latitudinal location and strength of the PFJ via the southern annular mode.

7.2 Chapter 4: Seasonality of the ENSO–ASR teleconnection – transient response

Chapter 4 considered the timescales associated with climate variables connected to the ENSO–ASR teleconnection. There are several reasons as to why it is important to understand the characteristics of the transient response. Firstly, as the mechanistic flowchart (Figure 3.20) is causal, the transient reaction timespans will allow, to a certain degree, confirmation of the flowchart. The variables closer to the tropics can be expected to react quicker than high latitude variables. Secondly, most of the analysis in Chapter 3 uses seasonal mean data. This assumes that the transient nature of the ENSO–ASR teleconnection is shorter than one season. Quantifying the reaction timespans can help confirm this assumption. Finally, understanding the timespans can allow greater insight into the teleconnection mechanism itself.

Two sets of HadGEM3 runs were produced for this chapter. These sets of HadGEM3 runs contain 53 ensemble members each lasting for seven months. In each of the ensemble members, the atmospheric initial conditions were taken from the baseline run in Chapter 3. The anomalous tropical Pacific SSTs (Niño3.4 region) in these ensembles ramped up to +1.5 K over ten days after one month of initialisation. One set of ensemble was initialised in May and the other in November to investigate the JJA and DJF ENSO–ASR teleconnection, respectively.

Two key results were found. Firstly, the time taken for the ENSO–ASR teleconnection to react is less than one season. This means that the use of seasonal data for analysis in Chapter 3 is validated. Secondly, the causal order of the teleconnection flowchart is consistent with the reaction times. However, caution must be exercised due to the large errors in the timescales.

It is difficult to make statements regarding the teleconnections in DJF due to the low signal to noise of the results. Nevertheless, the results in Chapter 4 have reconfirmed that ENSO–ASR teleconnection in DJF are not driven by wave fluxes. This strongly hints towards a separate mechanism for the ENSO–ASR teleconnection in DJF.

7.3 Chapter 5: The linearity of ENSO–ASR teleconnection

The degree of linearity of the ENSO–ASR teleconnection under El Niño conditions is still an open question. Most previous studies (Bertler et al., 2004; Kreuzt et al., 2000; Turner et al., 2013) use reanalysis data to study this teleconnection but there is insufficient observation data to investigate the linearity. Instead, this chapter used the HadGEM3 model to produce simulations of different magnitudes of El Niños. Four different El Niño runs (0.75 K, 1.5 K,

2.25 K and 3.0 K Niño3.4 temperature) and a baseline run were produced. All five runs are 54 years long and all the El Niño runs contain the same idealised perpetual El Niño structure that differs only in magnitude.

The main scientific aim of Chapter 5 was to investigate the linearity of the ENSO–ASR teleconnection under increasingly intense El Niño conditions. In Chapter 3, it was shown that the conditions for Rossby wave propagation may change under different El Niño magnitudes; this could cause non-linearity in the ENSO–ASR teleconnection. Furthermore, as the teleconnection mechanism in the two seasons is different, their linearity must be studied separately.

It was found that the ASR SLP anomaly arising from ENSO is approximately linear for Niño3.4 temperatures up to values found in the historic records, being linear up to approximately 2.25 K in JJA and 3.0 K in DJF. Historically, the strongest El Niños reach ~ 1.5 K in JJA and ~ 3.0 K in DJF. However, during extreme model El Niños (3.0 K), the SLP anomaly in JJA is *weaker* than 2.25 K and deviates (statistically significant at the 95% confidence interval) from linearity. This was due to the eastwards shift of the MZWL causing both the Rossby wave source and wave reflection zone to shift eastwards. As the reflection zone shifted east at a greater rate compared to the RWS anomaly, the potential for wave propagation into the ASR diminishes.

It is important to note that teleconnection that result from El Niño strengths higher than historically observed values cannot easily be verified by reanalysis. However, the mechanism of the non-linearity is simply an extension of the eastwards movement of the RWS anomaly and the changes in U_{yy} which are both observed in the model for temperature anomalies under 1.5 K. Therefore, it is not unreasonable to believe that this is a reflection of changing characteristics of the teleconnection mechanism rather than a model artifact.

In austral summer (DJF), the teleconnection mechanism is hypothesised to be a direct modulation of the location and strength of the PFJ. The PFJ weakens and shifts equatorwards as the Niño3.4 temperature increases which causes a negative SAM anomaly. This is seen as the characteristic EOF1 positive SLP in the high latitudes. The results in Chapter 5 indicate that the SLP anomaly in the ASR in DJF appears linear across the entire available spectrum of El Niño magnitudes explored. As the Niño3.4 temperature increases, a positive (negative) zonal mean zonal wind anomaly appears in 20–30°S (50–60°S) and strengthens linearly. This affects the PFJ linearly which changes the ASR SLP linearly. In conclusion, the ENSO–ASR teleconnection responds linearly to increases in the Niño3.4 temperatures up to historically observed maximum values.

7.4 Chapter 6: Model resolution dependence and the ASL

Chapter 6 investigated the effect horizontal resolution has on the climatology of the ASL and the simulation of the ENSO–ASR teleconnection. The UPSCALE dataset, three sets of ensemble runs at three different horizontal resolutions of N96, N216 and N512 are used. UPSCALE uses an atmosphere–only HadGEM3 with GA3.0 configuration over the period 1985–2011. The chapter compares the three UPSCALE resolutions with ERA–Interim.

The seasonality of the ASL climatology is well simulated throughout the different resolutions of UPSCALE. There is a deeper and westwards ASL in JJA and a weaker and eastwards ASL in DJF. However, the ASL is slightly too weak in lower resolution in for both austral winter and summer. The ASL in JJA is also too far eastwards at N96 resolution. In conclusion, the higher resolution model shows marginally better performance in simulating the climatological ASL in both seasons compared to the lower resolution models.

Perhaps surprisingly, the story is reversed for the ENSO–ASR teleconnection. Increasing model horizontal resolution seems to worsen the simulation of the ENSO–ASR teleconnection in both seasons. N96 simulates the ENSO–ASR teleconnection well with a characteristic EOF2–like (EOF1–like) signal in JJA (DJF). However, in the higher resolutions, both the structure (EOF1 versus EOF2) and the magnitude differences between the seasons are reduced. Moreover, the SLP anomaly is too weak in both seasons at the higher resolution model. In conclusion, the ENSO–ASR teleconnection was found to be best simulated in the lowest resolution (N96) model.

7.5 Overall conclusions and brief discussions

This section will present the overall conclusion to this work and some brief discussions. The main aim of this thesis is to investigate the mechanism behind the seasonality of the ENSO–ASR teleconnection. In conclusion, the seasonal difference in the background state is the dominant control for the structure and magnitude of the ENSO–ASR teleconnection. This is perhaps more important than the strength of the forcing which may explain the strong austral winter ENSO–ASR teleconnection in observations even if ENSO events are stronger in austral summer.

However, it is important to exercise caution in applying the results in this thesis to the real world. The experiments in this thesis contain idealised perpetual ENSO events which are not fully realistic. Additionally, it is difficult, if not impossible, to identify all the causal relationships in the mechanism. One example would be the difficulty in decomposing the changes in the background climatology to the changes in the wave train. While the

background climatology (e.g. the STJ in JJA) is partly affected by the intensification of the Hadley cell, it is also affected by the changing wave train. It is therefore difficult in separating and quantifying the contributions of each of these effects.

7.6 Future work: additional runs

This section will present possible future work requiring additional model runs. Previous literature (Section 1.2.3) showed that different El Niño types have different teleconnections. Section 7.6.1 suggests future work on the difference of the ENSO–ASR teleconnections between eastern Pacific (EP) and central Pacific (CP) El Niños. Section 7.6.2 discusses future work on La Niña–ASR teleconnections. Specifically, additional runs to produce realistic La Niñas are proposed. Section 7.6.3 mentions teleconnections between other tropical regions and the high latitudes. This thesis has predominantly focused on the Pacific ENSO–ASR teleconnections but there are other ENSO–like oscillations in the Atlantic and the Indian Ocean. SST anomalies in these regions have been previously shown (Ashok et al., 2003; Behera et al., 2005; Camberlin et al., 2001; Chan et al., 2008; Li et al., 2015b; Losada et al., 2010; Ping et al., 2006; Yoo-Geun et al., 2013) to produce teleconnections. It is reasonable to expect possible teleconnections from these oceans to the ASR, for details see Section 7.6.3.

The model used in this thesis does not contain interactive chemistry. Details of proposed model runs with interactive chemistry can be found in Section 7.6.4.

7.6.1 Eastern Pacific versus central Pacific El Niños

There are two main types of El Niño events, eastern Pacific and central Pacific El Niños, with differences in the tropical circulation (Kug et al., 2009) and teleconnections (Ashok et al., 2007; Sun et al., 2013) between them. However, the HadGEM3 experiments in this thesis only explore the effects of eastern Pacific El Niños. Additional model experiments could be performed to compare the ENSO–ASR teleconnection under central Pacific El Niño conditions and to compare this to the results in this thesis.

7.6.2 Comparison of real world La Niñas to ‘flipped’ El Niños

As discussed in Section 2.4, the HadGEM3 runs did not capture the observed ENSO–ASR teleconnection under La Niña conditions. One possible reason for the poor performance is due to the unrealistic nature of the idealised imposed La Niña SST anomalies which were structurally the same as the El Niños with a simple sign reversal.

There are several hints in the analysis that suggest the problem may originate from the tropics. Figure 7.1 shows the maximum SLP anomaly in the ASL during DJF (top) and JJA (bottom) over the whole range of Niño3.4 anomalies (-3 K to $+3$ K). The points in Figure 7.1 show the ensemble mean of the peak SLP anomaly while the lines show the linear regression of these points. The blue lines show the linear regression of the points between -3.0 K and 0.0 K while the green lines show the linear regressions of all points between 0.0 K to 3.0 K. The yellow line shows the linear regression of points between 0.0 K and 2.25 K in JJA.

As seen from Figure 7.1, there is a clear split between the SLP anomalies under El Niño and La Niña. The SLP anomaly changes are much stronger in El Niño conditions. This is contrary to previous literature (see Section 1.4) which finds that the ENSO–ASR teleconnection under La Niña are more intense than for El Niño.

The split between El Niño and La Niña can also be seen in the peak zonal wind (STJ, Pacific). Figure 7.2 shows the mean zonal wind at 200 hPa between 25 – 35° S, 240 – 270° E under El Niño and La Niña conditions in DJF (top) and JJA (bottom). The green and red lines show the linear regression for La Niña and El Niño conditions, respectively. The changes under El Niño are also much greater than the changes under La Niña.

This split can even be seen in the tropical circulation. Figure 7.3 shows the peak OLR in the tropical Pacific during DJF (top) and JJA (bottom). Similar to the zonal wind, the changes under El Niño conditions are much greater than the changes under La Niña.

As this discrepancy between the response to La Niña and El Niño conditions happens throughout the variables from the ASR to the tropics, it may suggest that La Niña is having minimal effect on the climate in general. This contradicts results from previous works such as Philander (1985) who found reduced rainfall (and circulation as the ITCZ moves northwards) in the central Pacific during La Niña conditions. This may either be due to a poor implementation of the La Niña (i.e. structure is poor) or the HadGEM3 model being incapable of producing teleconnections from La Niñas. However, as seen in the analysis of UPSCALE, the ENSO–ASR is captured reasonably well in La Niña conditions. So the issue is unlikely to be due to HadGEM3.

Further work would be required to identify the cause. For example, it is possible to run a set of experiments with historic observed La Niña SSTs instead of the idealised anomalies imposed in the current experiments. These experiments could provide useful insight into the cause of the poor ENSO–ASR simulation in the current runs. Composites of historic La Niñas could be used as the forcing. These historic La Niñas could be scaled to have the same Niño3.4 index anomaly as the current La Niña model runs to provide ‘clean’ comparisons.

7.6.3 Atlantic Ocean–ASR and Indian Ocean–ASR teleconnections

This thesis has been solely concerned with ENSO–ASR teleconnection. However, the work could be extended to consider the Atlantic Ocean–ASR and the Indian Ocean–ASR teleconnections. The following provides a short summary on the Atlantic Niño, the Indian Ocean dipole and possible teleconnections to the ASR.

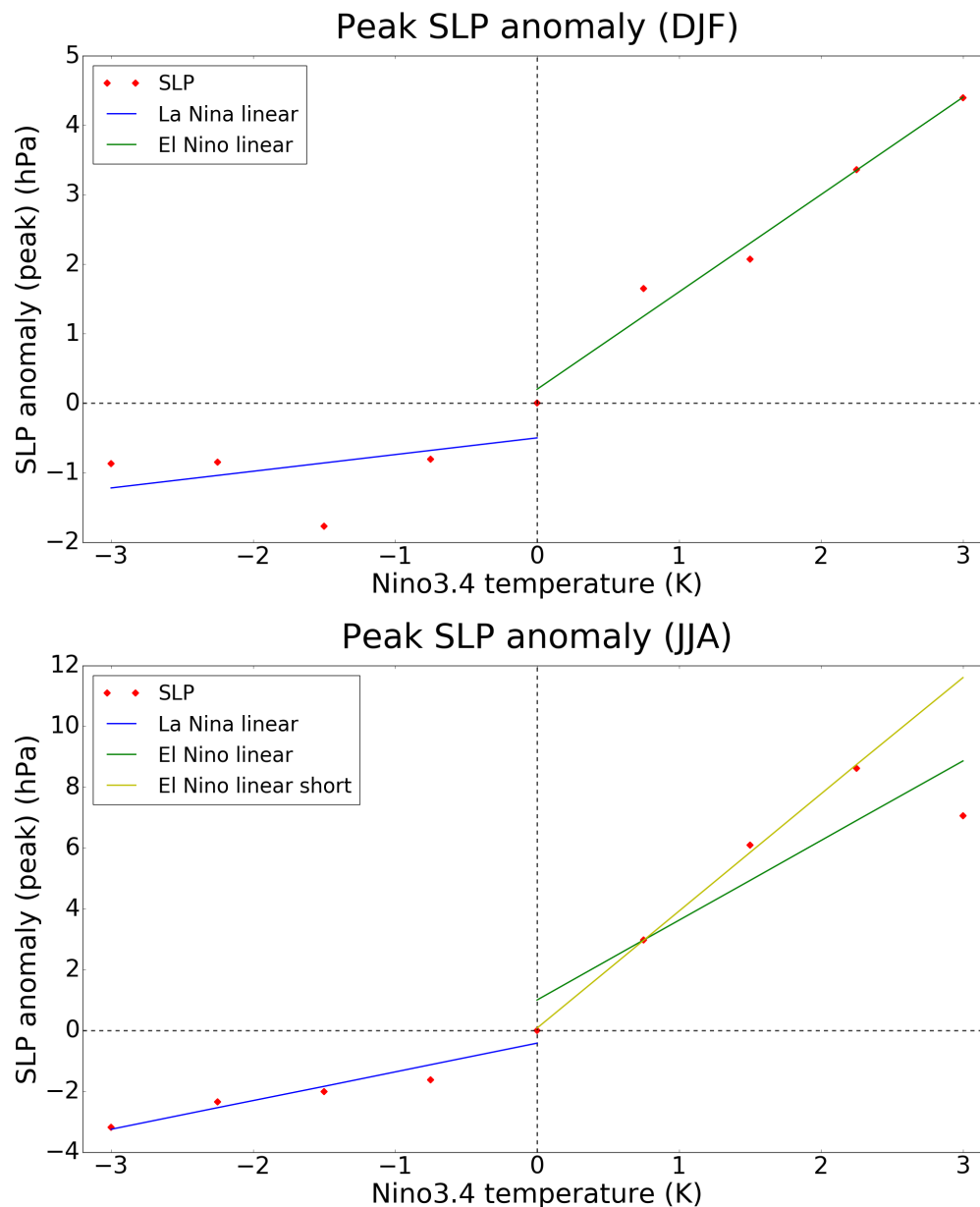


Fig. 7.1 Peak SLP anomaly under El Niño and La Niña conditions in DJF (top) and JJA (bottom). Units are in hPa.

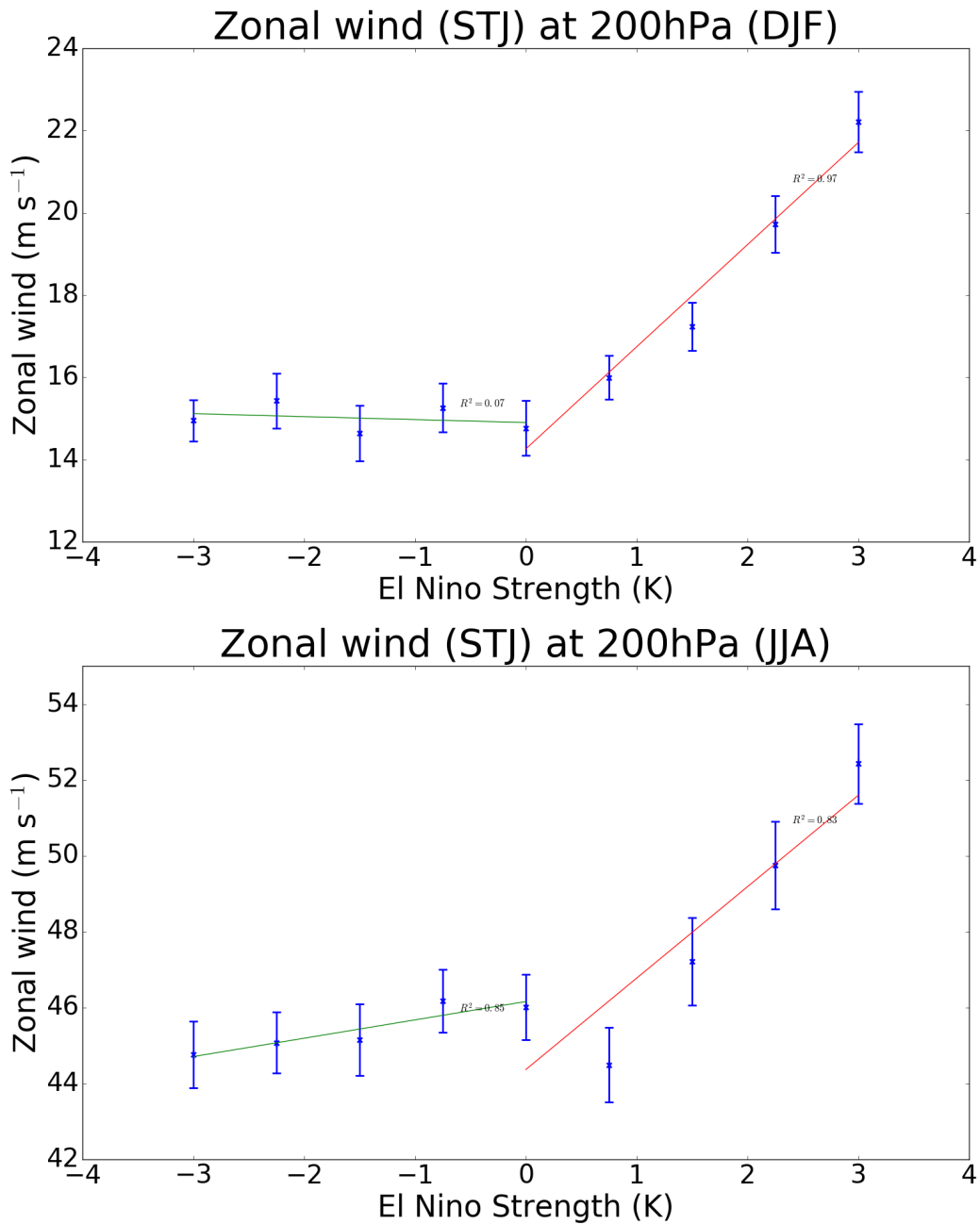


Fig. 7.2 Mean zonal wind at 200 hPa between 25–35°S, 240–270°E under El Niño and La Niña conditions in DJF (top) and JJA (bottom). Units are in m s⁻¹.

It has been known since the 1980s that the tropical Atlantic Ocean displays oceanic and atmospheric conditions that are similar to the tropical Pacific Ocean during El Niño (Carton and Huang, 1994; Philander, 1986). This is usually called the Atlantic Niño or the Atlantic equatorial mode. Observations show that the upper ocean is unusually warm in the eastern part of the basin and rainfall is heavier than usual to the south of the Equator during the warm

phase of the Atlantic Niño (Philander, 1986). The SSTs in the eastern equatorial Atlantic Ocean show warming events of 1–2 degrees every few years (Carton and Huang, 1994). These warming events are usually weaker and have a broader range of scale compared with Pacific ENSO events (Servain, 1991; Ward and Folland, 1991).

Previous work has shown that the Atlantic Niño can have global teleconnection impacts. Some examples include impact on the monsoon (Losada et al., 2010), impact on rainfall

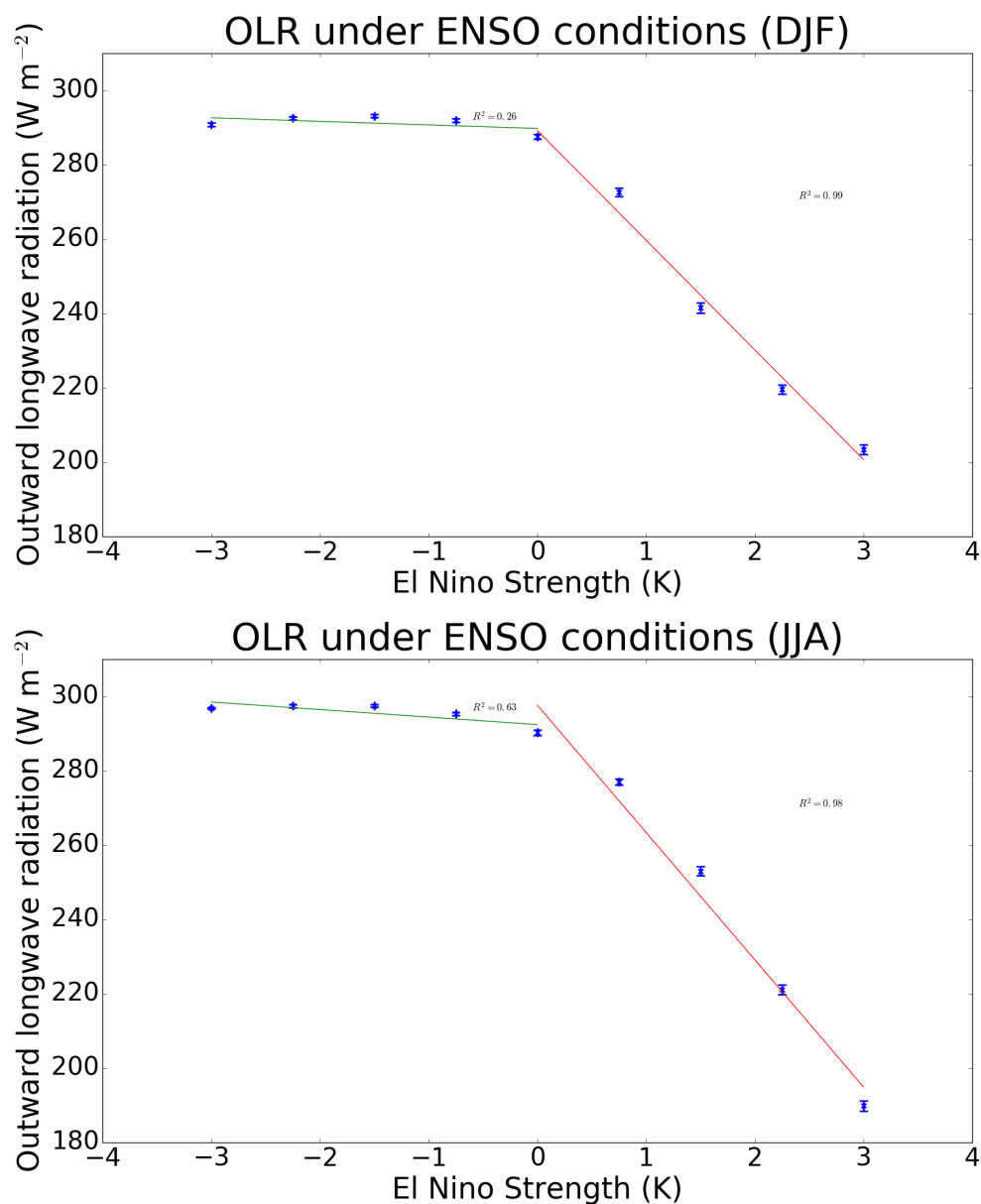


Fig. 7.3 Peak OLR (TOA) under El Niño and La Niña conditions in DJF (top) and JJA (bottom). Units are in W m^{-2} .

in Africa (Camberlin et al., 2001) and even impact on the Pacific ENSO (Ping et al., 2006; Yoo-Geun et al., 2013). Therefore, it would be interesting to understand the impact and seasonality the Atlantic Niño has on the ASR. Li et al. (2015b) may provide insights into the mechanism of the Atlantic Ocean–ASR seasonality. While Li et al. (2015b) do not impose an Atlantic Niño like signal, their imposed heating in the Atlantic showed clear seasonality due to Rossby wave propagation or reflection. A set of HadGEM3 runs consisting of different magnitude Atlantic Niño events (mirroring the ENSO runs in this thesis) could be run to allow for such an analysis.

Turning to the Indian Ocean, it also shows an internal mode of variability similar to the Pacific and Atlantic Oceans (Saji et al., 1999). This is known as the Indian ocean dipole. This dipole is weaker than Pacific ENSO, with a standard deviation of 0.3 K in the dipole mode index (DMI) as opposed to the 0.8 K standard deviation in the Niño3 index (Saji et al., 1999). This ocean dipole accounts for approximately 12% of the SST variability in the Indian Ocean, see again Saji et al. (1999). The Indian ocean dipole is known to show many global teleconnections. Some examples include rainfall in Australia (Ashok et al., 2003), east Africa (Behera et al., 2005) and south America (Chan et al., 2008). Previous work such as Li et al. (2015b) showed the SSTs in the Indian ocean have teleconnections to the high latitudes. Therefore, It may possible for these changes to generate Indian Ocean–ASR teleconnection. This could be investigated by running HadGEM3 model runs with idealised perpetual Indian Ocean dipoles at various magnitudes of the DMI.

7.6.4 Chemistry–interaction with the ENSO–ASR teleconnection

The model used in this thesis does not contain interactive chemistry. However, changes in chemical species, such as ozone, impacts the ASL. Previous studies have found that polar stratospheric ozone may impacts southern hemisphere climate (Gillett and Thompson, 2003; Keeble et al., 2014; Polvani et al., 2011; Thompson and Solomon, 2002b). Thompson and Solomon (2002b) found that changes in geopotential height (and thus the SAM) over radiosonde stations located in Antarctica mapped closely to ozone changes at Halley station (Antarctica). This relationship was reproduced in models by Gillett and Thompson (2003) and in the HadGEM model by Keeble et al. (2014). Additionally, changes in the ozone were found to map to surface variables, including pressure, in Gillett and Thompson (2003) and Keeble et al. (2014). Additionally, Hitchman and Rogal (2010) have also shown that ENSO may influence the ozone in the southern hemisphere. Therefore, it is possible that ENSO may affect the ASL via changes in the SAM and surface variables due to changes in ozone. Future work exploring the three way ozone–ENSO–ASR interactions are possible by repeating some experiments in a chemistry–climate model.

7.7 Future work: additional analysis

This section presents possible future work that uses existing data. Chapter 6 showed that the ENSO–ASR teleconnection is best simulated in the lower resolution model. Section 7.7.1 presents possible future work on investigating the reasons behind this. Inter–model comparison of the ASL climatology was done by Hosking et al. (2013). However, previous works have not investigated the ENSO–ASR teleconnection simulation in different models. Section 7.7.2 presents future work and preliminary results in the inter–model comparison of the ENSO–ASR teleconnection. In Section 7.7.3, future work on the application of machine learning techniques on CMIP5 data will be discussed.

7.7.1 Understanding differences in the ENSO–ASR teleconnection in UPSCALE

In Chapter 6, the effects on the horizontal resolution on the ENSO–ASR teleconnection were presented. However, the majority of the analysis was on the effects of the teleconnection (i.e. SLP). Little analysis has been done on intermediate variables in the ENSO–ASR teleconnection (such as zonal wind changes in the STJ, generation of the RWS anomaly and the propagation of the Rossby waves). As the teleconnection chain is causal, the effect of the teleconnection will be reduced (or non–existent) if any part of the chain is broken. By comparing the effects of horizontal resolution on each part of the chain, it may be possible to find which part of the chain is badly simulated.

7.7.2 Inter–model comparison of the ENSO–ASR teleconnection

The results in this thesis have focused on experiments performed by the HadGEM3 model. However, there are a variety of factors that may lead to differences in the simulated ENSO–ASR teleconnection in other climate models. Inter–model comparisons are therefore important in order to understand how consistently physical phenomena are represented in models.

Previously, Hosking et al. (2013) has investigated the simulation of the climatological ASL across the CMIP5 dataset. The CMIP5 (Fifth phase of the Climate Model Intercomparison Project) is a set of model runs ran by 20 modeling groups from around the world (Taylor et al., 2012). Hosking et al. (2013) found, perhaps unsurprisingly, no one model was best able to simulate both the annual cycle of the longitude and the central pressure of the ASL. Furthermore, they found that biases for ASL pressure and longitude were correlated across the models.

During my PhD project, I began to extend the work of Hosking et al. (2013) by analysing the performance in the simulation of the ENSO–ASR teleconnection in each of the CMIP5 models.

Preliminary results are presented here but could be extended as part of future work. Figure 7.4 and 7.5 shows the regression of the SLP to the Niño3.4 temperature in DJF and JJA, respectively. The models used are from atmosphere only runs (AMIP) and have prescribed observed SSTs and sea ice. The period of analysis spans the dates 1980–2007. Units of the graphs are in hPa K⁻¹.

As seen from Figures 7.4 and 7.5, the models vary in their simulation of the ENSO–ASR teleconnection. For example, CCSM4 seems to capture the SLP anomaly structure in DJF well with a positive pressure anomaly over the Amundsen sea superimposed onto the characteristic EOF1–like pattern around Antarctica. However, the peak magnitude of the SLP anomaly and the EOF1–like signal are weaker than in ERA–Interim. Another example is that CanAM4 seems to produce a stronger peak ASL anomaly over the ASR but the EOF1–like signal is overly weak. However, even though different models seem to perform better in different regions, all models do seem to produce a positive SLP over the ASR. Figure 7.5 shows the SLP regression to the Niño3.4 temperatures in JJA. Similar to the situation in DJF and in Hosking et al. (2013), the different models simulate the ENSO–ASR differently; some perform better than others. For example, MPI–ESM–LR seems to be capturing the EOF2–like signal well with good magnitude and seems to be performing better than models such as GISS–E2–R. These preliminary results suggest there are differences in the fidelity of the CMIP5 models at capturing the ENSO–ASE teleconnection. Future work could explore the causes of these differences using some of the mechanistic analyses performed in this thesis. Note that the regressions containing both El Niño and La Niña are included in Figure 7.4 and 7.5. However, as seen from previous literature, the ENSO–ASR teleconnection behaves differently under El Niño compared to La Niña. Therefore, the analysis of El Niño and La Niña should be carried out separately in the future as well as analysis of the coupled climate models in CMIP5.

7.7.3 Predicting ASR SLP anomaly using statistics and machine learning techniques

Another potential direction for future research would be to build a predictor of the ASL response to ENSO using machine learning techniques. There are two potential applications of machine learning relevant to this project. The first is to be able to predict the maximum SLP anomaly in the ASR. The second is to be able to predict SLP in the ASR (i.e. it becomes

a 2D problem as opposed to a scalar prediction). Towards the end of my PhD, I began to explore the first of these problems.

Regression of SLP onto Niño3.4 temperature: AMIP DJF

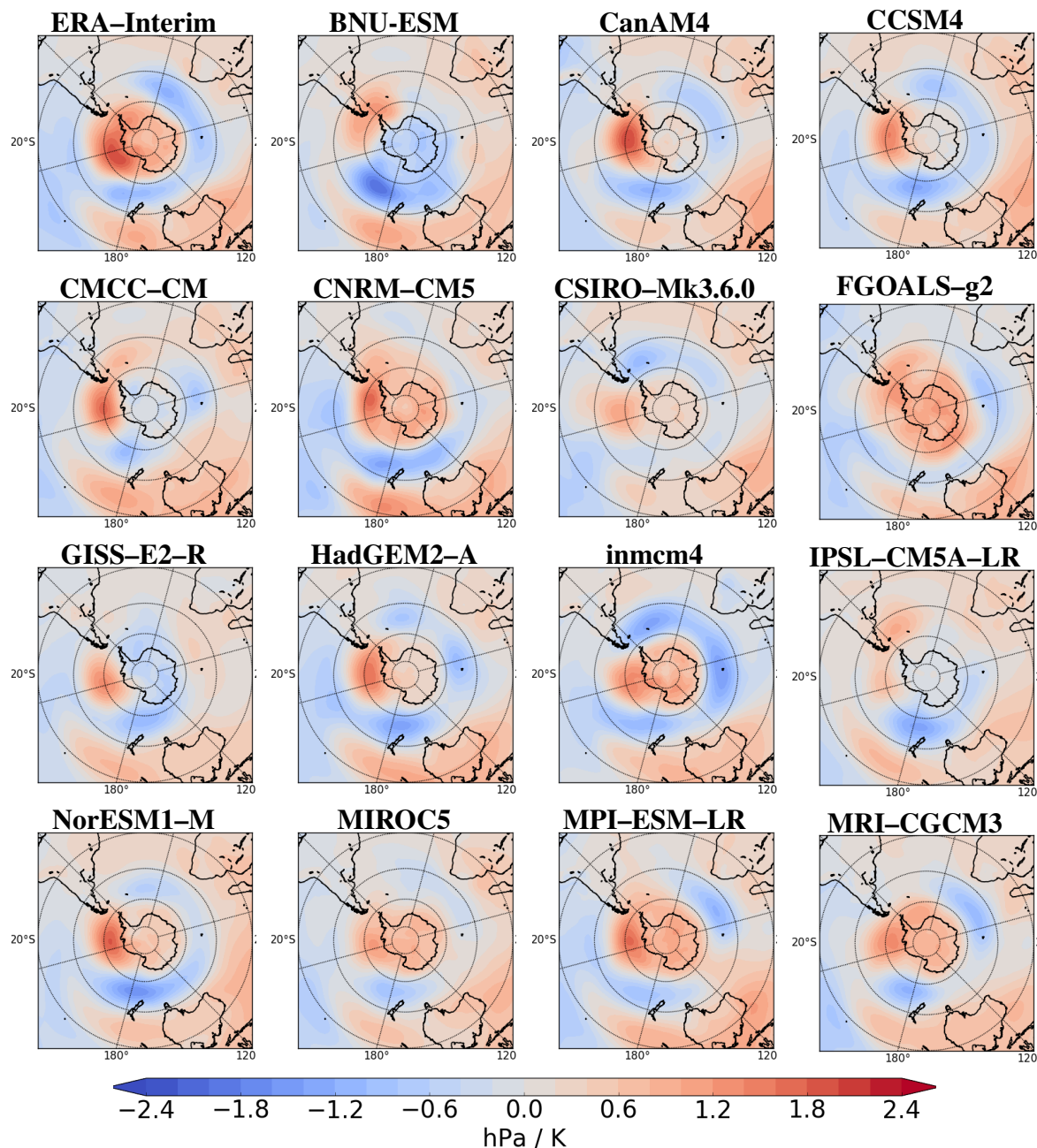


Fig. 7.4 Regression of SLP onto Niño3.4 temperature for the atmosphere only models (AMIP) in DJF. Units are in hPa K⁻¹.

SLP anomaly: AMIP JJA

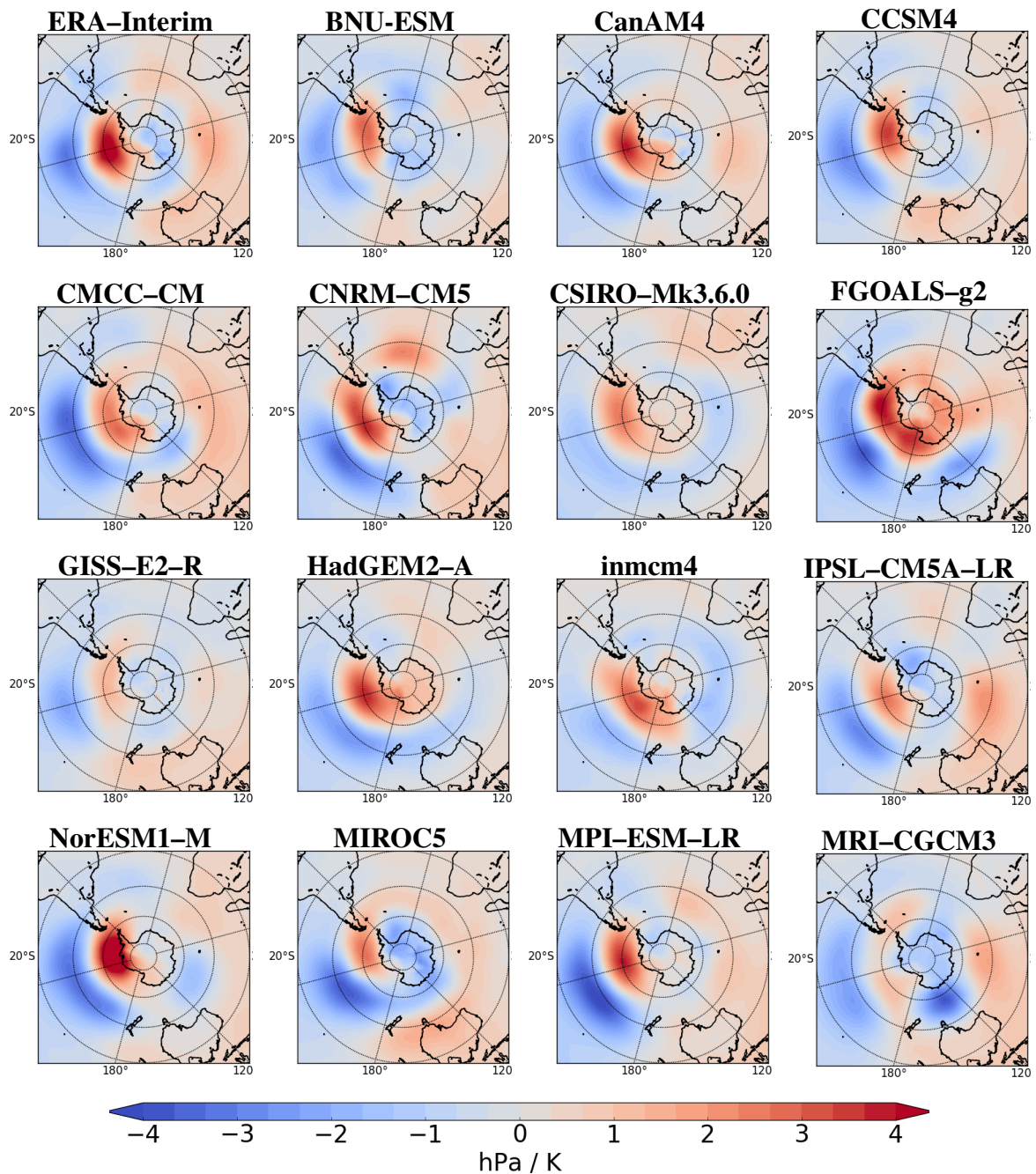


Fig. 7.5 Same as Figure 7.4 but in JJA.

There could be several scientific uses for an ASR SLP anomaly predictor. Firstly, prediction of ENSO events using seasonal to decadal prediction systems has been a focus in recent years. This is perhaps unsurprising as ENSO is the strongest climate variation

on timescales ranging from months to several years (Latif et al., 1998). Furthermore, the teleconnections from ENSO events may cause serious economic losses and pose severe threats to lives. Prediction of ENSO events may allow countries to mitigate the risks associated with these ENSO teleconnections. One of the main goals of the international Tropical Ocean–Global Atmosphere was the development of ENSO forecast models. This goal was achieved as seen by the variety of ENSO prediction models that successfully predicted the low frequency changes in ENSO indices (Latif et al., 1998). If the ASR SLP anomaly predictor only requires the Niño3.4 temperature as input, it could be possible to use future ENSO predictions to effectively predict the ENSO–ASR teleconnection during these future ENSO events. Secondly, it is possible to understand spatial patterns of correlations of between the tropical Pacific SSTs and the SLP anomaly in the ASR. This could provide further insights into the ENSO–ASR teleconnection. For example, if the highest correlations were located in the eastern Pacific, this may hint at greater contributions to the teleconnection from the eastern Pacific SST compared to the central Pacific SSTs. Thirdly, an ASR SLP predictor may help further the understanding to the linearity of ENSO–ASR teleconnection (including La Niña). Comparisons of the performance of linear to non-linear techniques may provide insights into the linearity of the teleconnection.

The use of several statistical and machine learning techniques were explored. Linear regression, lasso regression, K nearest neighbours, decision trees, random forests, boosted trees and neural nets were applied to the CMIP5 preindustrial experiments. There is a growing interest in the application of data mining and machine learning techniques to climate problems, and the application to understanding the ENSO–ASR teleconnection could be explored in the future. For data treatment and preliminary results, see Appendix K.

References

- Abram, N., R. Mulvaney, F. Vimeux, J. Steven, J. Turner, and M. H.E.
2014. Evolution of the Southern Annular Mode during the past millennium. *Nature Climate Change*, 4(7):564–569.
- Ahrens, C. D.
2009. *Meteorology Today*. Belmont: Brooks/Cole, Cengage Learning.
- Amien, I., P. Rejekiingrum, A. Pramudia, and E. Susanti
1996. Effects of interannual climate variability and climate change on rice yield in Java, Indonesia. *Water, Air, and Soil Pollution*, 92(1):29–39.
- Andrews, D.
2010. *An introduction to atmospheric physics*. Cambridge University Press.
- Ashok, K., S. K. Behera, S. A. Rao, H. Weng, and T. Yamagata
2007. El Niño Modoki and its possible teleconnection. *Journal of Geophysical Research: Oceans*, 112(C11):C11007.
- Ashok, K., Z. Guan, and T. Yamagata
2003. Influence of the Indian Ocean Dipole on the Australian winter rainfall. *Geophysical Research Letters*, 30(15):1821.
- Bals-Elsholz, T. M., E. H. Atallah, L. F. Bosart, T. A. Wasula, M. J. Cempa, and A. R. Lupo
2001. The Wintertime Southern Hemisphere Split Jet: Structure, Variability, and Evolution. *Journal of Climate*, 14(21):4191–4215.
- Barnes, E. A. and L. Polvani
2013. Response of the Midlatitude Jets, and of Their Variability, to Increased Greenhouse Gases in the CMIP5 Models. *Journal of Climate*, 26(18):7117–7135.
- Becker, E.
2016. Climatewatch magazine. Downloaded on 20 April 2017.
- Behera, S. K., J.-J. Luo, S. Masson, P. Delecluse, S. Gualdi, A. Navarra, and T. Yamagata
2005. Paramount Impact of the Indian Ocean Dipole on the East African Short Rains: A CGCM Study. *Journal of Climate*, 18(21):4514–4530.
- Bertler, N. A. N., P. J. Barrett, P. A. Mayewski, R. L. Fogt, K. J. Kreutz, and J. Shulmeister
2004. El Niño suppresses Antarctic warming. *Geophysical Research Letters*, 31:L15207.

- Bischoff, T. and T. Schneider
2014. Energetic Constraints on the Position of the Intertropical Convergence Zone. *Journal of Climate*, 27(13):4937–4951.
- Boer, G. J. and M. Lazare
1988. Some Results Concerning the Effect of Horizontal Resolution and Gravity–Wave Drag on Simulated Climate. *Journal of Climate*, 1(8):789–806.
- Boville, B. A.
1991. Sensitivity of Simulated Climate to Model Resolution. *Journal of Climate*, 4(5):469–485.
- Bromwich, D. H., A. N. Rodgers, P. Kallberg, R. I. Cullather, J. W. C. White, and K. J. Kreutz
2000. ECMWF analyses and reanalyses depiction of ENSO signal in Antarctic precipitation. *Journal of Climate*, 13:1406–1420.
- Camberlin, P., S. Janicot, and I. Pocard
2001. Seasonality and atmospheric dynamics of the teleconnection between African rainfall and tropical sea-surface temperature: Atlantic vs. ENSO. *International Journal of Climatology*, 21(8):973–1005.
- Carton, J. A. and B. Huang
1994. Warm Events in the Tropical Atlantic. *Journal of Physical Oceanography*, 24(5):888–903.
- Cavalieri, D. J., C. L. Parkinson, N. DiGirolamo, and A. Ivanoff
2012. Intersensor Calibration Between F13 SSMI and F17 SSMIS for Global Sea Ice Data Records. *IEEE Geoscience and Remote Sensing Letters*, 9(2):233–236.
- Chan, S. C., S. K. Behera, and T. Yamagata
2008. Indian Ocean Dipole influence on South American rainfall. *Geophysical Research Letters*, 35(14):L14S12.
- Chemel, C., M. R. Russo, J. S. Hosking, P. J. Telford, and J. A. Pyle
2015. Sensitivity of tropical deep convection in global models: effects of horizontal resolution, surface constraints, and 3D atmospheric nudging. *Atmospheric Science Letters*, 16(2):148–154.
- Chen, B., S. R. Smith, and D. H. Bromwich
1996. Evolution of the Tropospheric Split Jet over the South Pacific Ocean during the 1986–89 ENSO Cycle. *Monthly Weather Review*, 124(8):1711–1731.
- Chiodi, A. M. and D. E. Harrison
2017. Observed El Niño SSTA Development and the Effects of Easterly and Westerly Wind Events in 2014/15. *Journal of Climate*, 30(4):1505–1519.
- Ciasto, L. M. and M. H. England
2011. Observed ENSO teleconnections to Southern Ocean SST anomalies diagnosed from a surface mixed layer heat budget. *Geophysical Research Letters*, 38(9):L09701.

- Ciasto, L. M. and D. W. J. Thompson
2008. Observations of Large-Scale Ocean–Atmosphere Interaction in the Southern Hemisphere. *Journal of Climate*, 21(6):1244–1259.
- Codron, F.
2007. Relations between Annular Modes and the Mean State: Southern Hemisphere Winter. *Journal of the Atmospheric Sciences*, 64(9):3328–3339.
- Comiso, J. C., C. L. Parkinson, R. Gersten, and L. Stock
2008. Accelerated decline in the Arctic sea ice cover. *Geophysical Research Letters*, 35(1):L01703.
- Cook, K. H.
2003. Role of Continents in Driving the Hadley Cells. *Journal of the Atmospheric Sciences*, 60(7):957–976.
- Cullather, R. I., D. H. Bromwich, and M. L. Van Woert
1996. Interannual variations in the Antarctic precipitation related to El Niño–Southern Oscillation. *Journal of Geophysical Research*, 101(D14):19109–19118.
- Dee, D. P., S. M. Uppala, A. J. Simmons, P. Berrisford, P. Poli, S. Kobayashi, U. Andrae, M. A. Balsameda, G. Balsamo, P. Bauer, P. Bechtold, A. C. M. Beljaars, L. van de Berg, J. Bidlot, N. Bormann, C. Delsol, R. Dragani, M. Fuentes, A. J. Geer, L. Haimberger, S. B. Healy, H. Hersbach, E. V. Hólm, L. Isaksen, P. Kållberg, M. Köhler, M. Matricardi, A. P. McNally, B. M. Monge-Sanz, J.-J. Morcrette, B.-K. Park, C. Peubey, P. de Rosnay, C. Tavolato, J.-N. Thépaut, and F. Vitart
2011. The ERA-Interim reanalysis: configuration and performance of the data assimilation system. *Quarterly Journal of the Royal Meteorological Society*, 137(656):553–597.
- Demory, M.-E., P. L. Vidale, M. J. Roberts, P. Berrisford, J. Strachan, R. Schiemann, and M. S. Mizieliński
2014. The role of horizontal resolution in simulating drivers of the global hydrological cycle. *Climate Dynamics*, 42(7):2201–2225.
- Dickinson, R.
1978. Rossby waves—long-period oscillations of oceans and atmospheres. *Annual Review of Fluid Mechanics*, 10(1):159–195.
- Dima, I. M. and J. M. Wallace
2003. On the Seasonality of the Hadley Cell. *Journal of the Atmospheric Sciences*, 60(12):1522–1527.
- Ding, Q., E. J. Steig, D. S. Battisti, and K. M.
2011. Winter warming in West Antarctica caused by central tropical Pacific warming. *Nature Geoscience*, 4:398–403.
- Ding, Q., E. J. Steig, D. S. Battisti, and J. M. Wallace
2012. Influence of the Tropics on the Southern Annular Mode. *Journal of the Atmospheric Sciences*, 25:6330 – 6348.

- Drake, F.
2001. El Niño 1997–1998: the climate event of the century. *International Journal of Climatology*, 21(11).
- Eichelberger, S. J. and D. L. Hartmann
2007. Zonal Jet Structure and the Leading Mode of Variability. *Journal of Climate*, 20(20):5149–5163.
- Fasullo, J. T. and K. E. Trenberth
2008. The Annual Cycle of the Energy Budget. Part II: Meridional Structures and Poleward Transports. *Journal of Climate*, 21(10):2313–2325.
- Fogt, R. L. and D. H. Bromwich
2006. Decadal Variability of the ENSO Teleconnection to the High-Latitude South Pacific Governed by Coupling with the Southern Annular Mode. *Journal of Climate*, 19(6):979–997.
- Fogt, R. L., D. H. Bromwich, and K. M. Hines
2011. Understanding the SAM influence on the South Pacific ENSO teleconnection. *Climate Dynamics*, 36:1555–1576.
- Fogt, R. L., A. J. Wovrosh, R. A. Langen, and I. Simmonds
2012. The characteristic variability and connection to the underlying synoptic activity of the Amundsen-Bellinghousen Seas Low. *Journal of Geophysical Research: Atmospheres*, 117(D7):D07111.
- Gallego, D., P. Ribera, R. Garcia-Herrera, E. Hernandez, and L. Gimeno
2005. A new look for the Southern Hemisphere jet stream. *Climate Dynamics*, 24(6):607–621.
- Galvin, J. F. P.
2007. The weather and climate of the tropics Part 2 –The subtropical jet streams. *Weather*, 62(11):295–299.
- Genthon, C., G. Krinner, and M. Sacchettini
2003. Interannual Antarctic tropospheric circulation and precipitation variability. *Climate Dynamics*, 21(3):289–307.
- Gillett, N. P. and D. W. J. Thompson
2003. Simulation of Recent Southern Hemisphere Climate Change. *Science*, 302(5643):273–275.
- Gong, D. and S. Wang
1999. Definition of Antarctic Oscillation index. *Geophysical Research Letters*, 26(4):459–462.
- Hansen, J., R. Ruedy, M. Sato, and K. Lo
2010. Global surface temperature change. *Reviews of Geophysics*, 48(4):RG4004.

- Harger, J.
1995. Air-temperature variations and ENSO effects in Indonesia, the Philippines and El Salvador. ENSO patterns and changes from 1866–1993. *Atmospheric Environment*, 29(16):1919–1942.
- Hartmann, D. L. and F. Lo
1998. Wave-Driven Zonal Flow Vacillation in the Southern Hemisphere. *Journal of the Atmospheric Sciences*, 55(8):1303–1315.
- Held, I. M.
1975. Momentum Transport by Quasi-Geostrophic Eddies. *Journal of the Atmospheric Sciences*, 32(7):1494–1497.
- Held, I. M. and A. Y. Hou
1980. Nonlinear Axially Symmetric Circulations in a Nearly Inviscid Atmosphere. *Journal of the Atmospheric Sciences*, 37(3):515–533.
- Hitchman, M. H. and M. J. Rogal
2010. ENSO influences on Southern Hemisphere column ozone during the winter to spring transition. *Journal of Geophysical Research: Atmospheres*, 115(D20):D20104.
- Ho, M., A. S. Kiem, and D. C. Verdon-Kidd
2012. The Southern Annular Mode: a comparison of indices. *Hydrology and Earth System Sciences*, 16(3):967–982.
- Hoerling, M. P., A. Kumar, and M. Zhong
1997. El Niño, La Niña, and the Nonlinearity of Their Teleconnections. *Journal of Climate*, 10(8):1769–1786.
- Hosking, J. S., A. Orr, G. J. Marshall, J. Turner, and T. Phillips
2013. The Influence of the Amundsen–Bellingshausen Seas Low on the Climate of West Antarctica and Its Representation in Coupled Climate Model Simulations. *Journal of Climate*, 26:6633–6648.
- Hoskins, B. J. and T. Ambrizzi
1993. Rossby Wave Propagation on a Realistic Longitudinally Varying Flow. *Journal of the Atmospheric Sciences*, 50(12):1661–1671.
- Hoskins, B. J. and D. J. Karoly
1981. The Steady Linear Response of a Spherical Atmosphere to Thermal and Orographic Forcing. *Journal of the Atmospheric Sciences*, 38(6):1179–1196.
- Hu, S. and A. V. Fedorov
2016. Exceptionally strong easterly wind burst stalling El Niño of 2014. *Proceedings of the National Academy of Sciences*, 113(8):2005–2010.
- Hu, X., S. Yang, and M. Cai
2016. Contrasting the eastern Pacific El Niño and the central Pacific El Niño: process-based feedback attribution. *Climate Dynamics*, 47(7):2413–2424.

- Hubert, L. F., A. F. Krueger, and J. S. Winston
1969. The Double Intertropical Convergence Zone-Fact or Fiction? *Journal of the Atmospheric Sciences*, 26(4):771–773.
- Inatsu, M. and B. J. Hoskins
2004. The Zonal Asymmetry of the Southern Hemisphere Winter Storm Track. *Journal of Climate*, 17(24):4882–4892.
- Jin, D. and B. P. Kirtman
2009. Why the Southern Hemisphere ENSO response lead ENSO. *Journal of Geophysical Research*, 23:101.
- Johannessen, O. M., M. Miles, and E. Bjorgo
1995. The Arctic's shrinking sea ice. *Nature*, 376(6536):126–127.
- Kang, S. M. and J. Lu
2012. Expansion of the Hadley Cell under Global Warming: Winter versus Summer. *Journal of Climate*, 25(24):8387–8393.
- Karoly, D. J.
1989a. Southern Hemisphere Circulation Features Associated with El Niño-Southern Oscillation Events. *Journal of Climate*, 2(11):1239–1252.
- Karoly, D. J.
1989b. Southern Hemisphere Circulation Features Associated with El Niño-Southern Oscillation Events. *Journal of Climate*, 2(11):1239–1252.
- Karoly, D. J. and B. J. Hoskins
1982. Three Dimensional Propagation of Planetary Waves. *Journal of the Meteorological Society of Japan. Ser. II*, 60(1):109–123.
- Karoly, D. J., R. A. Plumb, and M. Ting
1989. Examples of the Horizontal Propagation of Quasi-stationary Waves. *Journal of the Atmospheric Sciences*, 46(18):2802–2811.
- Karumuri, A. and Y. Toshio
2009. Climate change: The El Nino with a difference. *Nature*, 461(7263):481–484.
- Keeble, J., P. Braesicke, N. L. Abraham, H. K. Roscoe, and J. A. Pyle
2014. The impact of polar stratospheric ozone loss on Southern Hemisphere stratospheric circulation and climate. *Atmospheric Chemistry and Physics*, 14(24):13705–13717.
- Kidson, J. W. and M. R. Sinclair
1995. The Influence of Persistent Anomalies on Southern Hemisphere Storm Tracks. *Journal of Climate*, 8(8):1938–1950.
- Kidston, J., J. A. Renwick, and J. McGregor
2009. Hemispheric-Scale Seasonality of the Southern Annular Mode and Impacts on the Climate of New Zealand. *Journal of Climate*, 22:4759 – 4770.
- King, J. C. and J. Turner
2007. *Antarctic Meteorology and Climatology*. Cambridge University Press.

- Kirtman, B. P., C. Bitz, F. Bryan, W. Collins, J. Dennis, N. Hearn, J. L. Kinter, R. Loft, C. Rousset, L. Siqueira, C. Stan, R. Tomas, and M. Vertenstein
2012. Impact of ocean model resolution on CCSM climate simulations. *Climate Dynamics*, 39(6):1303–1328.
- Kreutz, K. J., P. A. Mayewski, I. I. Pittalwala, L. D. Meeker, M. S. Twickler, and S. I. Whitlow
2000. Sea level pressure variability in the Amundsen Sea region inferred from a West Antarctic glaciochemical record. *Journal of Geophysical Research*, 105:4047 – 4059.
- Kug, J.-S., F.-F. Jin, and S.-I. An
2009. Two Types of El Niño Events: Cold Tongue El Niño and Warm Pool El Niño. *Journal of Climate*, 22(6):1499–1515.
- Küttel, M., E. J. Steig, Q. Ding, A. J. Monaghan, and D. S. Battisti
2012. Seasonal climate information preserved in West Antarctic ice core water isotopes: relationships to temperature, large-scale circulation, and sea ice. *Climate Dynamics*, 39(7):1841–1857.
- Kwok, R. and J. C. Comiso
2002. Spatial patterns of variability in Antarctic surface temperature: Connections to the Southern Hemisphere Annular Mode and the Southern Oscillation. *Geophysical Research Letters*, 29(14):50–1–50–4.
- Lachlan-Cope, T. and W. Connolley
2006. Teleconnections between the tropical Pacific and the Amundsen-Bellinghausens Sea: Role of the El Niño/Southern Oscillation. *Journal of Geophysical Research: Atmospheres*, 111(D23):D23101.
- Lachlan-Cope, T. A., W. M. Connolley, and J. Turner
2001. The role of the non-axisymmetric Antarctic orography in forcing the observed pattern of variability of the Antarctic climate. *Geophysical Research Letters*, 28:4111–4114.
- Latif, M., D. Anderson, T. Barnett, M. Cane, R. Kleeman, A. Leetmaa, J. O’Brien, A. Rosati, and E. Schneider
1998. A review of the predictability and prediction of ENSO. *Journal of Geophysical Research: Oceans*, 103(C7):14375–14393.
- Levine, A. F. Z. and M. J. McPhaden
2016. How the July 2014 easterly wind burst gave the 2015–2016 El Niño a head start. *Geophysical Research Letters*, 43(12):6503–6510.
- L’Heureux, M. L. and W. J. Thompson
2006. Observed Relationships between the El Niño–Southern Oscillation and the Extratropical Zonal–Mean Circulation. *Journal of Climate*, 19:276 – 287.
- Li, X., E. P. Gerber, D. M. Holland, and C. Yoo
2015a. A Rossby Wave Bridge from the Tropical Atlantic to West Antarctica. *Journal of Climate*, 28(6):2256–2273.

- Li, X., D. M. Holland, E. P. Gerber, and C. Yoo
2015b. Rossby Waves Mediate Impacts of Tropical Oceans on West Antarctic Atmospheric Circulation in Austral Winter. *Journal of Climate*, 28(20):8151–8164.
- Liang, J., C. Wang, and K. I. Hodges
2017. Evaluation of tropical cyclones over the South China Sea simulated by the 12 km MetUM regional climate model. *Quarterly Journal of the Royal Meteorological Society*, 143(704):1641–1656.
- Limpasuvan, V. and D. L. Hartmann
1999. Eddies and the annular modes of climate variability. *Geophysical Research Letters*, 26(20):3133–3136.
- Lin, J.-L.
2007. The Double-ITCZ Problem in IPCC AR4 Coupled GCMs: Ocean–Atmosphere Feedback Analysis. *Journal of Climate*, 20(18):4497–4525.
- Liu, J., X. Yuan, D. Rind, and D. G. Martinson
2002. Mechanism study of the ENSO and southern high latitudes climate teleconnections. *Geophysical Research Letters*, 29:24.
- Lorenz, D. J. and D. L. Hartmann
2001. Eddy–Zonal Flow Feedback in the Southern Hemisphere. *Journal of the Atmospheric Sciences*, 58(21):3312–3327.
- Losada, T., B. Rodríguez-Fonseca, S. Janicot, S. Gervois, F. Chauvin, and P. Ruti
2010. A multi-model approach to the Atlantic Equatorial mode: impact on the West African monsoon. *Climate Dynamics*, 35(1):29–43.
- Loveday, A.
1985. *The History and Economics of Indian Famines*. Usha Publications.
- Lu, J., G. Chen, and D. M. W. Frierson
2008. Response of the Zonal Mean Atmospheric Circulation to El Niño versus Global Warming. *Journal of Climate*, 21(22):5835–5851.
- Marshall, G. J.
2003. Trends in the Southern Annular Mode from Observations and Reanalyses. *Journal of Climate*, 16(24):4134–4143.
- Marshall, G. J., A. Orr, N. P. M. van Lipzig, and J. C. King
2006. The Impact of a Changing Southern Hemisphere Annular Mode on Antarctic Peninsula Summer Temperatures. *Journal of Climate*, 19(20):5388–5404.
- Marshall, J., A. Donohoe, D. Ferreira, and D. McGee
2014. The ocean’s role in setting the mean position of the Inter-Tropical Convergence Zone. *Climate Dynamics*, 42(7):1967–1979.
- McPhaden, M.
2015. Playing hide and seek with El Niño. *Nature Climate Change*, 5(9):791–795.

- McPhaden, M. J.
1999. Genesis and Evolution of the 1997-98 El Niño. *Science*, 283(5404):950–954.
- Meier, W. N., J. Stroeve, and F. Fetterer
2007. Whither Arctic sea ice? A clear signal of decline regionally, seasonally and extending beyond the satellite record. *Annals of Glaciology*, 46(1):428–434.
- Mizielinski, M. S., M. J. Roberts, P. L. Vidale, R. Schiemann, M.-E. Demory, J. Strachan, T. Edwards, A. Stephens, B. N. Lawrence, M. Pritchard, P. Chiu, A. Iwi, J. Churchill, C. del Cano Novales, J. Kettleborough, W. Roseblade, P. Selwood, M. Foster, M. Glover, and A. Malcolm
2014. High-resolution global climate modelling: the UPSCALE project, a large-simulation campaign. *Geoscientific Model Development*, 7(4):1629–1640.
- Mo, K. C.
2000. Relationships between Low-Frequency Variability in the Southern Hemisphere and Sea Surface Temperature Anomalies. *Journal of Climate*, 13(20):3599–3610.
- Mo, K. C. and J. N. Paegle
2001. The Pacific–South American modes and their downstream effects. *International Journal of Climatology*, 21(10):1211–1229.
- Nakamura, H. and A. Shimpo
2004. Seasonal Variations in the Southern Hemisphere Storm Tracks and Jet Streams as Revealed in a Reanalysis Dataset. *Journal of Climate*, 17(9):1828–1844.
- Naylor, R. L., W. P. Falcon, D. Rochberg, and N. Wada
2001. Using El Niño/Southern Oscillation Climate Data to Predict Rice Production in Indonesia. *Climatic Change*, 50(3):255–265.
- Oort, A. H. and J. J. Yienger
1996. Observed Interannual Variability in the Hadley Circulation and Its Connection to ENSO. *Journal of Climate*, 9(11):2751–2767.
- Palmer, T. N., G. J. Shutts, and R. Swinbank
1986. Alleviation of a systematic westerly bias in general circulation and numerical weather prediction models through an orographic gravity wave drag parametrization. *Quarterly Journal of the Royal Meteorological Society*, 112(474):1001–1039.
- Parkinson, C. and D. Cavalieri
2012. Antarctic sea ice variability and trends, 1979-2010. *The Cryosphere*, 6(4):871.
- Parkinson, C. L. and D. J. Cavalieri
1989. Arctic sea ice 1973–1987: Seasonal, regional, and interannual variability. *Journal of Geophysical Research: Oceans*, 94(C10):14499–14523.
- Parkinson, C. L., D. J. Cavalieri, P. Gloersen, H. J. Zwally, and J. C. Comiso
1999. Arctic sea ice extents, areas, and trends, 1978–1996. *Journal of Geophysical Research: Oceans*, 104(C9):20837–20856.
- Peixoto, J. P. and A. H. Oort
1992. *Physics of Climate*. New York: Springer-Verlag.

- Philander, S. G.
1990. *El Niño, La Niña and the Southern Oscillation*. San Diego: Academic Press.
- Philander, S. G. H.
1985. El Niño and La Niña. *Journal of the Atmospheric Sciences*, 42(23):2652–2662.
- Philander, S. G. H.
1986. Unusual conditions in the tropical Atlantic Ocean in 1984. *Nature*, 322:236.
- Philander, S. G. H., D. Gu, G. Lambert, T. Li, D. Halpern, N.-C. Lau, and R. C. Pacanowski
1996. Why the ITCZ Is Mostly North of the Equator. *Journal of Climate*, 9(12):2958–2972.
- Ping, C., F. Yue, S. R., J. Link, and S. Howard
2006. The cause of the fragile relationship between the Pacific El Niño and the Atlantic Niño. *Nature*, 443:324.
- Plumb, R. A.
1985. On the Three-Dimensional Propagation of Stationary Waves. *Journal of the Atmospheric Sciences*, 42(3):217–229.
- Polvani, L. M., D. W. Waugh, G. J. P. Correa, and S.-W. Son
2011. Stratospheric Ozone Depletion: The Main Driver of Twentieth-Century Atmospheric Circulation Changes in the Southern Hemisphere. *Journal of Climate*, 24(3):795–812.
- Quiroz, R. S.
1983. The Climate of the “El Niño” Winter of 1982–83—A Season of Extraordinary Climatic Anomalies. *Monthly Weather Review*, 111(8):1685–1706.
- Raphael, M. N., G. J. Marshall, J. Turner, R. L. Fogt, D. Schneider, D. A. Dixon, J. S. Hosking, J. M. Jones, and W. R. Hobbs
2016. The Amundsen Sea Low: Variability, Change, and Impact on Antarctic Climate. *Bulletin of the American Meteorological Society*, 97(1):111–121.
- Rasmusson, E. M. and T. H. Carpenter
1982. Variations in Tropical Sea Surface Temperature and Surface Wind Fields Associated with the Southern Oscillation/El Niño. *Monthly Weather Review*, 110(5):354–384.
- Rasmusson, E. M. and T. H. Carpenter
1983. The Relationship Between Eastern Equatorial Pacific Sea Surface Temperatures and Rainfall over India and Sri Lanka. *Monthly Weather Review*, 111(3):517–528.
- Rayner, N. A., D. E. Parker, E. B. Horton, C. K. Folland, L. V. Alexander, D. P. Rowell, E. C. Kent, and A. Kaplan
2003. Global analyses of sea surface temperature, sea ice, and night marine air temperature since the late nineteenth century. *Journal of Geophysical Research: Atmospheres*, 108(D14):4407.
- Riffenburgh, B.
2007. *Encyclopedia of the Antarctic*, volume 1. Taylor & Francis.

- Roberts, M. J., A. Clayton, M.-E. Demory, J. Donners, P. L. Vidale, W. Norton, L. Shaffrey, D. P. Stevens, I. Stevens, R. A. Wood, and J. Slingo
2009. Impact of Resolution on the Tropical Pacific Circulation in a Matrix of Coupled Models. *Journal of Climate*, 22(10):2541–2556.
- Roberts, M. J., P. L. Vidale, M. S. Mizieliński, M.-E. Demory, R. Schiemann, J. Strachan, K. Hodges, R. Bell, and J. Camp
2015. Tropical Cyclones in the UPSCALE Ensemble of High-Resolution Global Climate Models. *Journal of Climate*, 28(2):574–596.
- Roeckner, E., R. Brokopf, M. Esch, M. Giorgetta, S. Hagemann, L. Kornblüeh, E. Manzini, U. Schlese, and U. Schulzweida
2006. Sensitivity of Simulated Climate to Horizontal and Vertical Resolution in the ECHAM5 Atmosphere Model. *Journal of Climate*, 19(16):3771–3791.
- Rogers, J. C. and H. van Loon
1982. Spatial Variability of Sea Level Pressure and 500 mb Height Anomalies over the Southern Hemisphere. *Monthly Weather Review*, 110(10):1375–1392.
- Ropelewski, C. F. and M. S. Halpert
1987. Global and Regional Scale Precipitation Patterns Associated with the El Niño/Southern Oscillation. *Monthly Weather Review*, 115(8):1606–1626.
- Rossby, C.
1939a. Planetary flow patterns in the atmosphere. *Quart. J. Roy. Met. Soc.*, 66:68.
- Rossby, C.
1939b. Relation between variations in the intensity of the zonal circulation of the atmosphere and the displacements of the semi-permanent centers of action. *J. Marine Res.*, 2:38–55.
- Rossby, C.
1945. ON THE PROPAGATION OF FREQUENCIES AND ENERGY IN CERTAIN TYPES OF OCEANIC AND ATMOSPHERIC WAVES. *Journal of Meteorology*, 2(4):187–204.
- Russo, M. R., M. J. Ashfold, N. R. P. Harris, and J. A. Pyle
2015. On the emissions and transport of bromoform: sensitivity to model resolution and emission location. *Atmospheric Chemistry and Physics*, 15(24):14031–14040.
- Saji, N. H., B. N. Goswami, P. N. Vinayachandran, and T. Yamagata
1999. A dipole mode in the tropical Indian Ocean. *Nature*, 401:360.
- Sardeshmukh, P. D. and B. J. Hoskins
1985. Vorticity balances in the tropics during the 1982-83 El Niño-Southern oscillation event. *Quarterly Journal of the Royal Meteorological Society*, 111(468):261–278.
- Sardeshmukh, P. D. and B. J. Hoskins
1987. The Generation of Global Rotational Flow by Steady Idealized Tropical Divergence. *Journal of the Atmospheric Sciences*, 45(7):1228 – 1251.

- Scaife, A. A., R. E. Comer, N. J. Dunstone, J. R. Knight, D. M. Smith, C. MacLachlan, N. Martin, K. A. Peterson, D. Rowlands, E. B. Carroll, S. Belcher, and J. Slingo
2017. Tropical rainfall, Rossby waves and regional winter climate predictions. *Quarterly Journal of the Royal Meteorological Society*, 143(702):1–11.
- Schiemann, R., M.-E. Demory, M. S. Mizieliński, M. J. Roberts, L. C. Shaffrey, J. Strachan, and P. L. Vidale
2014. The sensitivity of the tropical circulation and Maritime Continent precipitation to climate model resolution. *Climate Dynamics*, 42(9):2455–2468.
- Schneider, D. P., Y. Okumura, and D. Clara
2011. Observed Antarctic Interannual Climate Variability and Tropical Linkage. *Journal of Climate*, 25:4048–4066.
- Schneider, T.
2006. The General Circulation of the Atmosphere. *Annual Review of Earth and Planetary Sciences*, 34(1):655–688.
- Schneider, T., T. Bischoff, and G. H. Haug
2014. Migrations and dynamics of the intertropical convergence zone. *Nature*, 513(7516):45–53.
- Servain, J.
1991. Simple climatic indices for the tropical Atlantic Ocean and some applications. *Journal of Geophysical Research: Oceans*, 96(C8):15137–15146.
- Shaffrey, L. C., I. Stevens, W. A. Norton, M. J. Roberts, P. L. Vidale, J. D. Harle, A. Jrrar, D. P. Stevens, M. J. Woodage, M. E. Demory, J. Donners, D. B. Clark, A. Clayton, J. W. Cole, S. S. Wilson, W. M. Connolley, T. M. Davies, A. M. Iwi, T. C. Johns, J. C. King, A. L. New, J. M. Slingo, A. Slingo, L. Steenman-Clark, and G. M. Martin
2009. U.K. HiGEM: The New U.K. High-Resolution Global Environment Model—Model Description and Basic Evaluation. *Journal of Climate*, 22(8):1861–1896.
- Silvestri, G. E. and C. S. Vera
2003. Antarctic Oscillation signal on precipitation anomalies over southeastern South America. *Geophysical Research Letters*, 30(21):2115.
- Simpkins, G. R., L. M. Ciasto, D. W. J. Thompson, and M. H. England
2012. Seasonal Relationships between Large-Scale Climate Variability and Antarctic Sea Ice Concentration. *Journal of Climate*, 25(16):5451–5469.
- Simpkins, G. R., S. McGregor, A. S. Taschetto, L. M. Ciasto, and M. H. England
2014. Tropical Connections to Climatic Change in the Extratropical Southern Hemisphere: The Role of Atlantic SST Trends. *Journal of Climate*, 27(13):4923–4936.
- Stammerjohn, S. E., D. G. Martinson, R. C. Smith, X. Yuan, and D. Rind
2008. Trends in Antarctic annual sea ice retreat and advance and their relation to El Niño–Southern Oscillation and Southern Annular Mode variability. *Journal of Geophysical Research: Oceans*, 113(C3):C03S90.

- Stock, Z. S., M. R. Russo, and J. A. Pyle
2014. Representing ozone extremes in European megacities: the importance of resolution in a global chemistry climate model. *Atmospheric Chemistry and Physics*, 14(8):3899–3912.
- Sun, D., F. Xue, and T. Zhou
2013. Impacts of Two Types of El Niño on Atmospheric Circulation in the Southern Hemisphere. *Advances in Atmospheric Science*, 30(6):1732–1742.
- Taylor, K. E., R. J. Stouffer, and G. A. Meehl
2012. An Overview of CMIP5 and the Experiment Design. *Bulletin of the American Meteorological Society*, 93(4):485–498.
- Thompson, D. W. J. and S. Solomon
2002a. Interpretation of Recent Southern Hemisphere Climate Change. *Science*, 296(5569):895–899.
- Thompson, D. W. J. and S. Solomon
2002b. Interpretation of Recent Southern Hemisphere Climate Change. *Science*, 296(5569):895–899.
- Thompson, D. W. J., S. Solomon, P. J. Kushner, M. H. England, K. M. Grise, and D. J. Karoly
2011. Signatures of the Antarctic ozone hole in Southern Hemisphere surface climate change. *Nature Geosci*, 4(11):741–749.
- Thompson, D. W. J. and J. M. Wallace
1998. The Arctic oscillation signature in the wintertime geopotential height and temperature fields. *Geophysical Research Letters*, 25(9):1297–1300.
- Thompson, D. W. J. and J. M. Wallace
2000. Annular modes in the extratropical circulation. Part I: Month-to-month variability. *Journal of Climate*, 13:1000 – 1016.
- Trenberth, K. E.
1997. The Definition of El Niño. *Bulletin of the American Meteorological Society*, 78(12):2771–2777.
- Trenberth, K. E. and J. M. Caron
2001. Estimates of Meridional Atmosphere and Ocean Heat Transports. *Journal of Climate*, 14(16):3433–3443.
- Trenberth, K. E., J. M. Caron, D. P. Stepaniak, and S. Worley
2002. Evolution of El Niño–Southern Oscillation and global atmospheric surface temperatures. *Journal of Geophysical Research: Atmospheres*, 107(D8):AAC 5–1–AAC 5–17.
- Trenberth, K. E., P. D. Jones, P. Ambenje, R. Bojariu, D. Easterling, A. Klein Tank, D. Parker, F. Rahimzadeh, J. A. Renwick, M. Rusticucci, B. Soden, and P. Zhai
2007. 2007: Observations: Surface and Atmospheric Climate Change. In: *Climate Change 2007: The Physical Science Basis. Contribution of Working Group I to the Fourth Assessment Report of the Intergovernmental Panel on Climate Change*. Cambridge: Cambridge University Press.

- Trenberth, K. E. and D. P. Stepaniak
2001. Indices of El Niño Evolution. *Journal of Climate*, 14(8):1697–1701.
- Turner, J.
2004. The El Niño–Southern Oscillation and Antarctica. *International Journal of Climatology*, 24:1–31.
- Turner, J., J. C. Comiso, G. J. Marshall, T. A. Lachlan-Cope, T. Bracegirdle, T. Maksym, M. P. Meredith, Z. Wang, and A. Orr
2009. Non-annular atmospheric circulation change induced by stratospheric ozone depletion and its role in the recent increase of Antarctic sea ice extent. *Geophysical Research Letters*, 36(8):L08502.
- Turner, J., J. S. Hosking, G. J. Marshall, T. Phillips, and T. J. Bracegirdle
2016. Antarctic sea ice increase consistent with intrinsic variability of the Amundsen Sea Low. *Climate Dynamics*, 46(7):2391–2402.
- Turner, J., T. Phillips, J. S. Hosking, G. J. Marshall, and A. Orr
2013. The Amundsen Sea low. *International Journal of Climatology*, 33:1818–1829.
- Van Heerden, J. and J. J. Taljaard
1998. *Africa and Surrounding Waters*, Pp. 141–174. Boston, MA: American Meteorological Society.
- Viñas, M. J.
2017. Sea Ice Extent Sinks to Record Lows at Both Poles. Downloaded on 8 May 2017.
- Vincent, D. G.
1998. *Pacific Ocean*, Pp. 101–117. Boston, MA: American Meteorological Society.
- Waliser, D. E. and C. Gautier
1993. A Satellite-derived Climatology of the ITCZ. *Journal of Climate*, 6(11):2162–2174.
- Walsh, K. J., I. Simmonds, and M. Collier
2000. Sigma-coordinate calculation of topographically forced baroclinicity around Antarctica. *Dynamics of Atmospheres and Oceans*, 33(1):1–29.
- Walters, D. N., K. D. Williams, I. A. Boutle, A. C. Bushell, J. M. Edwards, P. R. Field, A. P. Lock, C. J. Morcrette, R. A. Stratton, J. M. Wilkinson, M. R. Willett, N. Bellouin, A. Bodas-Salcedo, M. E. Brooks, D. Copsey, P. D. Earnshaw, S. C. Hardiman, C. M. Harris, R. C. Levine, C. MacLachlan, J. C. Manners, G. M. Martin, S. F. Milton, M. D. Palmer, M. J. Roberts, J. M. Rodríguez, W. J. Tennant, and P. L. Vidale
2014. The Met Office Unified Model Global Atmosphere 4.0 and JULES Global Land 4.0 configurations. *Geoscientific Model Development*, 7(1):361–386.
- Ward, M. N. and C. K. Folland
1991. Prediction of seasonal rainfall in the north nordeste of Brazil using eigenvectors of sea-surface temperature. *International Journal of Climatology*, 11(7):711–743.
- Whetton, P. and I. Rutherford
1994. Historical ENSO teleconnections in the eastern hemisphere. *Climatic Change*, 28(3):221–253.

- Williams, L. N., S. Lee, and S.-W. Son
2007. Dynamics of the Southern Hemisphere Spiral Jet. *Journal of the Atmospheric Sciences*, 64(2):548–563.
- Wolter, K.
1989. Modes of Tropical Circulation, Southern Oscillation, and Sahel Rainfall Anomalies. *Journal of Climate*, 2(2):149–172.
- Wolter, K. and M. Timlin
1998. Measuring the strength of ENSO events: How does 1997/98 rank? *Weather*, 53(9):315–324.
- Woollings, T., A. Hannachi, and B. Hoskins
2010. Variability of the North Atlantic eddy-driven jet stream. *Quarterly Journal of the Royal Meteorological Society*, 136(649):856–868.
- Yang, X. and E. K. M. Chang
2007. Eddy–Zonal Flow Feedback in the Southern Hemisphere Winter and Summer. *Journal of the Atmospheric Sciences*, 64(9):3091–3112.
- Yoo-Geun, H., K. Jong-Seong, P. Jong-Yeon, and J. Fei-Fei
2013. Sea surface temperature in the north tropical Atlantic as a trigger for El Niño/Southern Oscillation events. *Nature Geoscience*, 6:112.
- Yuan, X. J.
2004. ENSO-related impacts on Antarctic sea ice: a synthesis of phenomenon and mechanisms. *Antarctic Science*, 16(4):415–425.
- Zickfeld, K., A. Levermann, M. G. Morgan, T. Kuhlbrodt, S. Rahmstorf, and D. W. Keith
2007. Expert judgements on the response of the Atlantic meridional overturning circulation to climate change. *Climatic Change*, 82(3):235–265.
- Zubair, L.
2002. El Niño–southern oscillation influences on rice production in Sri Lanka. *International Journal of Climatology*, 22(2):249–260.

Appendix A

The ITCZ and the ‘energy flux equator’

Schneider et al. (2014) argued that the ITCZ should lie near the ‘energy flux equator’. This is where the atmospheric meridional energy flux changes sign.

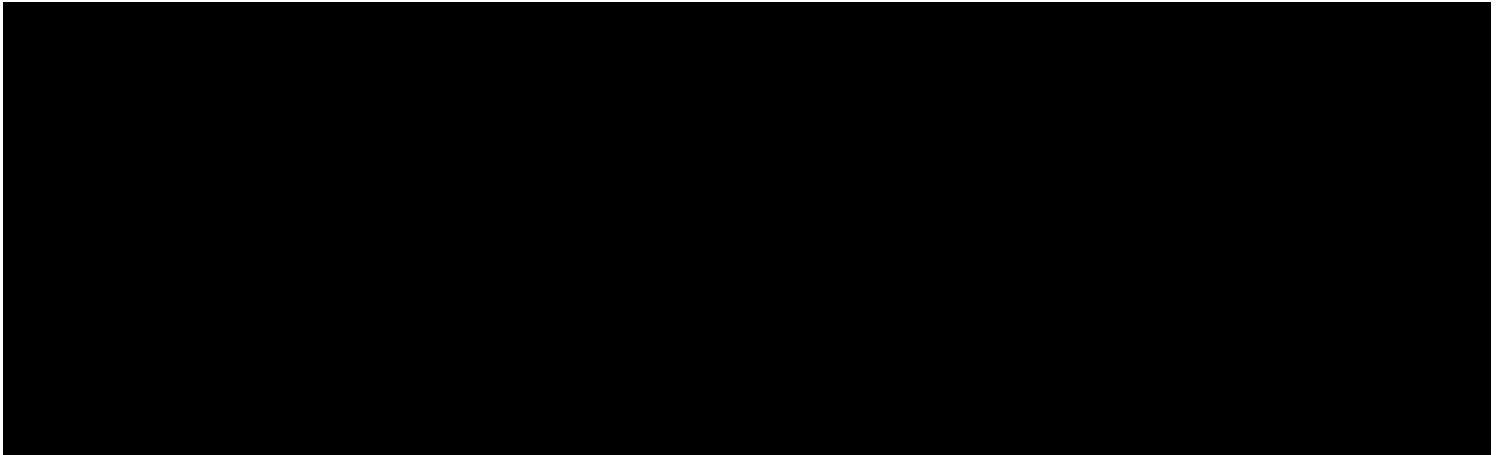


Fig. A.1 Monthly changes in latitude of the ITCZ. The maximum precipitation (a proxy for the ITCZ) is marked with the red line while surface winds are given as arrows. Data is from daily TMPA data averaged over 1998–2012. Figure taken from Schneider et al. (2014).

The atmospheric energy balance (Peixoto and Oort, 1992; Schneider et al., 2014) is expressed as

$$\nabla \cdot F = S - L - O, \quad (\text{A.1})$$

where F is the energy flux, S is the net downwards shortwave radiation at the top of the atmosphere (TOA), L is the outwards longwave radiation (TOA), O is the energy uptake by the ocean. By expanding the meridional energy flux F to first order in latitude and solving, a relationship between the latitude (where the energy flux equator is) and energy

contributions (Bischoff and Schneider, 2014; Schneider et al., 2014) can be obtained.

$$\delta \approx -\frac{1}{a} \frac{F_0}{S_0 - L_0 - O_0}, \quad (\text{A.2})$$

where δ is the latitude for the energy flux equator, a is the radius of the Earth, the subscripts indicate latitude. The atmospheric heat transport across the equator is $0.2PW$ northwards (Marshall et al., 2014). The net equatorial energy is 18 W m^{-2} (taking values of $S_0 \approx 323 \text{ W m}^{-2}$, $L_0 \approx 251 \text{ W m}^{-2}$ and $O_0 \approx 54 \text{ W m}^{-2}$) (Fasullo and Trenberth, 2008). Using (A.2), the energy flux equator lies somewhere near 4°N latitude (Schneider et al., 2014), so that

$$\delta \approx -\frac{1}{6371000m} \frac{(0.3 \times 10^{15}W)/(2 * \pi * 6371000m)}{(323 - 251 - 54)Wm^{-2}} \approx 0.0654 \text{ radians} \\ \approx 4^\circ N.$$

It is important to note that any small changes in S_0 , L_0 and O_0 can result in large movements in the ITCZ (Schneider et al., 2014). For example, reducing S_0 or increasing L_0 and O_0 by 6 W m^{-2} can lead to the energy flux equator moving by a factor of 1.5 polewards.

There are many factors that may lead to ITCZ migrations. The main interest in this thesis lies in how the ITCZ reacts to ENSO events. The following discussion mainly follows Schneider et al. (2014). During El Niño, the mean global temperature rise by approximately 0.1K . However, there is a hemispheric difference: the northern hemisphere warms around 0.08K more than the southern hemisphere (Hansen et al., 2010). Therefore, the ITCZ would be expected to shift north. However, during El Niño, the ITCZ actual migrates south. This is because O_0 is around 15 W m^{-2} less during El Niño compared to La Niña (Schneider et al., 2014; Trenberth et al., 2002). This is more than enough to overcome the ITCZ shift due to the northern hemisphere warming. In reality, during extreme El Niño conditions such as 1982–1983 and 1997–1998, the ITCZ shifts by around 5° .

Appendix B

Extreme historical El Niño events

Figure B.1 shows the seasonal SST maps of the three largest El Niño from 1950s (2015–2016, 1997–1998, 1982–1983) from era interim data. Figure B.2 shows the evolution of the ONI and SOI for the three El Niños. The ranking of El Niños since 1950 in terms of October–December Niño3.4 temperature anomaly is shown in Figure B.3.

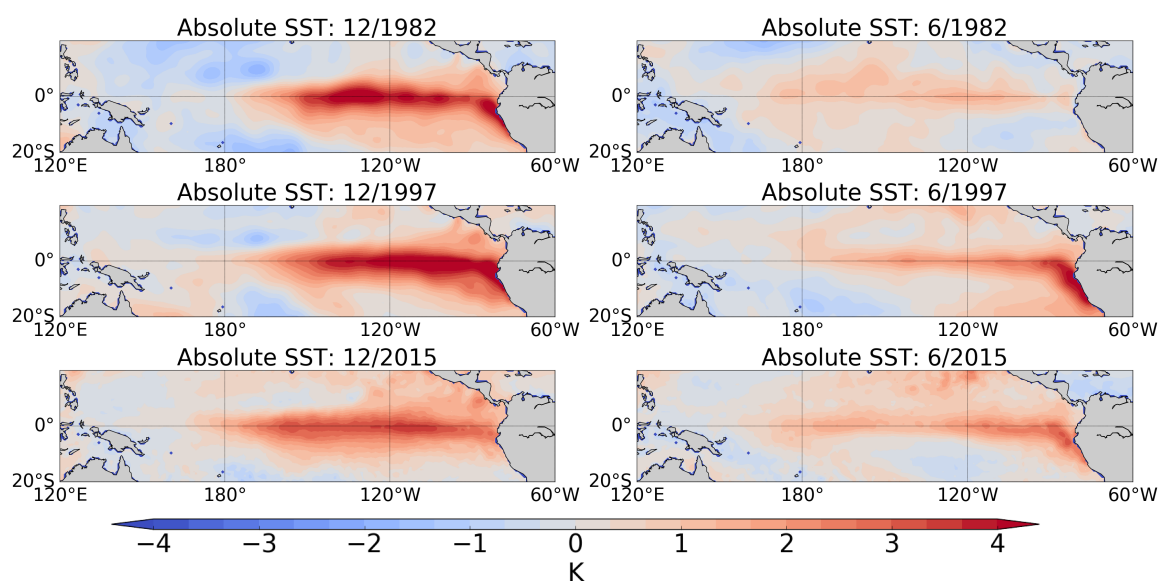


Fig. B.1 The SST anomalies during December and July for the three historical extreme El Niños (1982–1983, 1997–1998, 2015–2016). The data used was ERA-interim by the European Centre for Medium-range Weather Forecasts.

2015–2016 El Niño

The 2015–2016 El Niño is one of the strongest El Niño historically, reaching +2.38 K above average in the Niño3.4 region at its peak (Becker, 2016). This El Niño is of particular

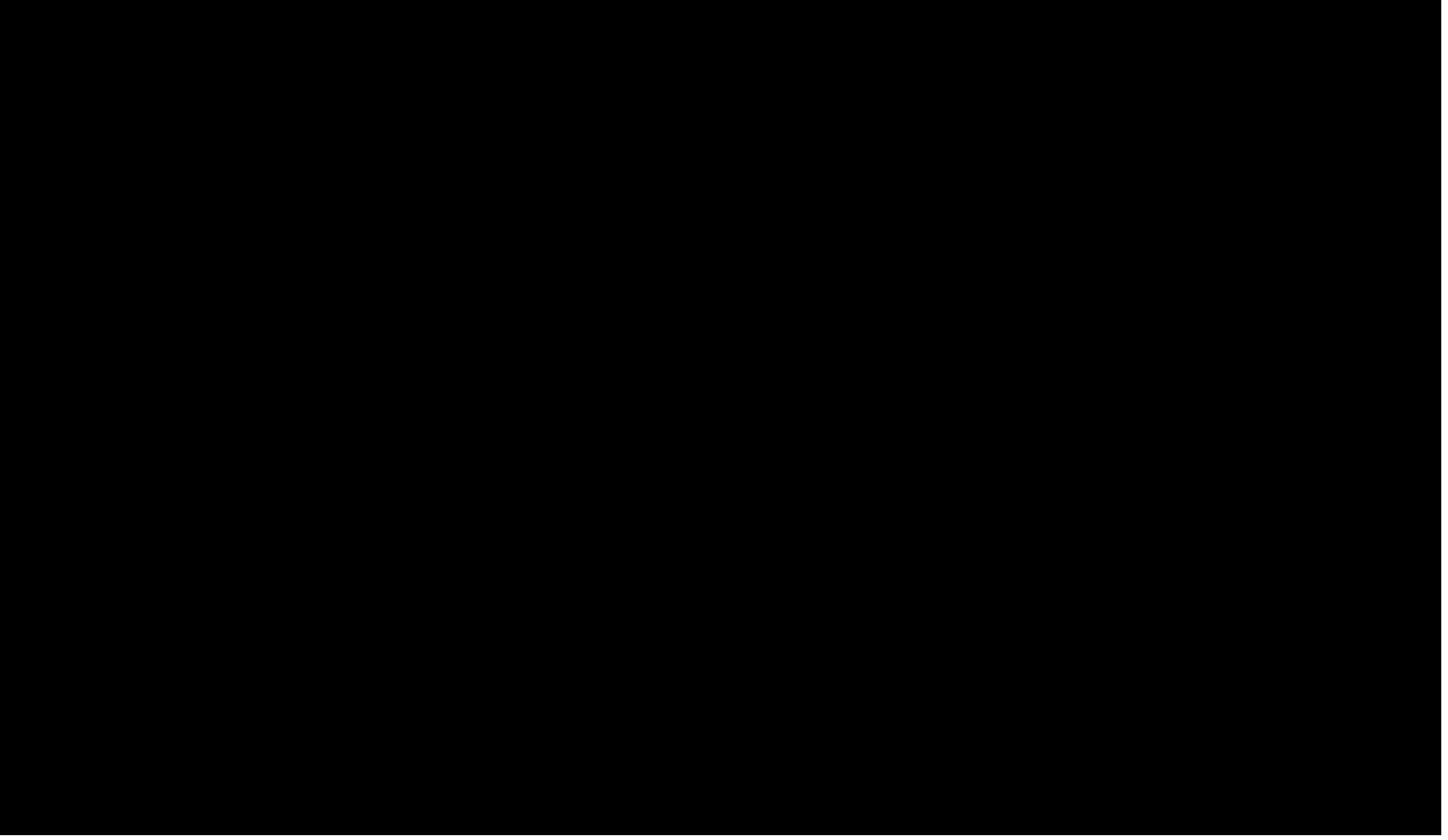


Fig. B.2 The evolution of the ONI and the SOI for the three extreme historic El Niños (1982–1983, 1997–1998, 2015–2016). The graphs look at the indices for every three month averages starting at June–August–September for the year before the El Niño starts and ending with October–November–December. This figure was taken from <https://www.climate.gov/news-features/understanding-climate/2015-state-climate-el-ni%C3%B1o-came-saw-and-conquered>

interest to the ENSO community due to several reasons. Firstly, it is an extreme El Niño that happened recently: El Niños on the scale of the 1997–1998 (and 2015–2016) El Niño only happens around once every 15–20 years (McPhaden, 2015). There are only three El Niños over 3.0 K ONI from 1950 till now, see Figure B.3. This provides El Niño scientists with a rare opportunity to study extreme El Niño events and to collect data. Secondly, the evolution of the 2015–2016 El Niño is quite unusual: initially, at the start of 2014, an El Niño was predicted to occur that year. However, the El Niño never managed to develop in 2014 but rather developed the year after in 2015 (Hu and Fedorov, 2016; McPhaden, 2015). Thirdly, this provides an insight into our El Niño predictions and why the prediction failed in 2014. Many centres such as the National Oceanic and Atmospheric Administration (NOAA) expected an El Niño at the end of 2014 and announced an ‘El Niño watch’ in March 2014 (Hu and Fedorov, 2016). The National Aeronautics and Space Administration (NASA) suggested in May 2014 that the May El Niño may be similar in strength with the 1997–1998 El Niño.

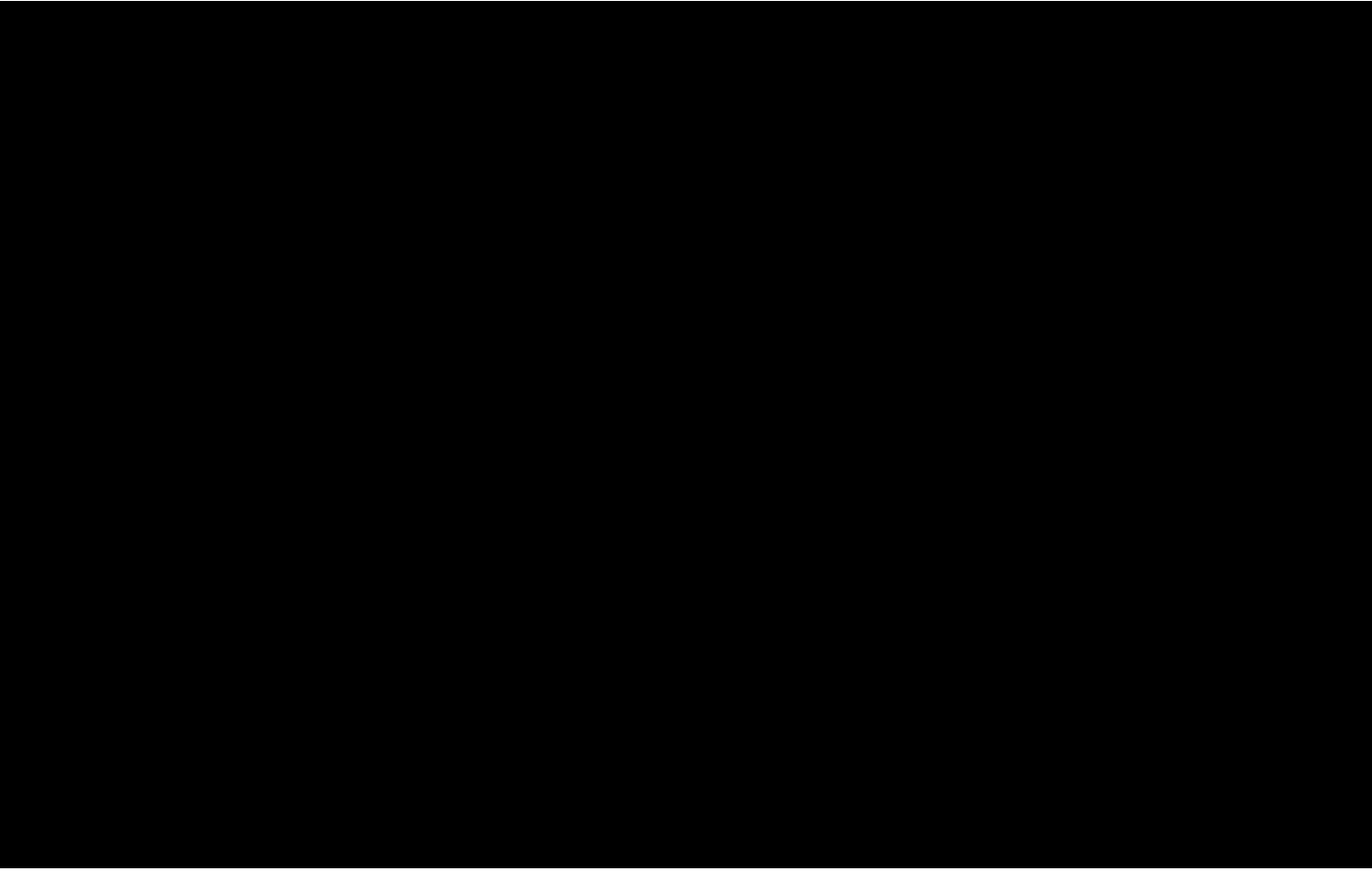


Fig. B.3 The ranking of October–December El Niño episodes since 1950 by ONI. As seen from the figure, there are only three El Niño that are over 2 K ONI since the 1950. The three strongest El Niños are 1997-1998, 2015–2016 and 1982–1983 in order of magnitude. Note that this ordering is not absolute, a different index or different time period may change the order of the El Niños. This is especially true for the 1997-1998 and the 2015–2016 El Niño as their magnitudes are very similar. This figure was taken from <https://www.climate.gov/print/808265>

Eventually the 2014 El Niño was just short of being classified as an El Niño, see again Hu and Fedorov (2016). It was classified as an neutral year by conventional indices.

I mainly follow the works of McPhaden (2015) and Hu and Fedorov (2016) for the following overview on the failure of the El Niño in 2014 and the development and peak of the El Niño in 2015. The conditions of early 2014 resembled 1997. The equatorial Pacific in early 2014 had positive SSH which indicated it was heat charged. The built up heat content may indicate at El Niño conditions towards the end of the year. This ‘primes’ the ocean to El Niño conditions, awaiting the Westerly winds bursts (WWBs) needed to initialise the El Niño. The WWB can be looked as a weakening of the trade winds. In January and February, there were two strong WWBs due to a paired tropical cyclone that formed at opposite sides of the equator. Subsequently, weaker WWBs followed the two strong WWBs which excited

downwelling Kelvin waves in April. In May, the Niño3.4 region has reached +0.5 K (Chiodi and Harrison, 2017). However, the subsequent WWBs were weaker than expected and there was even a strong Easterly wind burst in June: this Easterly wind started in May and reached peak strength in mid-June. Figure B.4 shows the dates and strengths of the WWBs and Easterly wind bursts (EWBs) in 2014 and 2015. There were two strong EWB occurring in days 154 (early June) and 185 (early July). These EWB had significant impacts to the dynamics in the area. The EWB excited a strong upwelling Kelvin wave that approximately canceled out the initial warming. The SSTs anomalies began to decay at the middle of 2014 and was only left with a very weak warming at the end of 2014 that was stretched across the Pacific.

I follow the works of McPhaden (2015), Chiodi and Harrison (2017) and Levine and McPhaden (2016) for the following overview on the development of the El Niño in 2015. There was a series of WWBs in the first half of 2015 that renewed the El Niño development, see Figure B.4. The WWB was from some unusual cyclone activity that occurred over the prevailing warm water over the Western Pacific. Thus the ‘failed’ El Niño in 2014 helped to reignite the El Niño. By June 2015, the anomalous SSTs in the Niño3.4 region has reached one degree. This is the second highest Niños3.4 temperature (highest being 1997) recorded since 1950s, see Figure B.2 for the ONI. By this point, NOAA predicted greater than 90% chance that El Niño will occur that year. There are three main points in hindsight of why the 2015 El Niño occurred while the 2014 El Niño ‘failed’. Firstly, the 2014 El Niño failure prevented any discharge of the built up heat content in the ocean. There was even a reverse (further build up) of heat content due to the failed El Niño in 2014. This helped push the 2015 El Niño to extreme magnitudes. Secondly, the WWB that occurred in the first half 2015 were stronger than first half of 2014, see Figure B.3. This was due to anomalously warm water from the failed El Niño. Thirdly, the EWB in 2015 was of much lower magnitude than 2014. For example, the EWB in day 165 of 2015 (mid June) is less than half the magnitude of the EWB in June 2014.

1997–1998 El Niño

The 1997–1998 El Niño has been hailed as the ‘El Niño of the century’ (Wolter and Timlin, 1998). It is approximately the strongest (or second strongest) El Niño in recent history, see Figure B.2 and B.3 for the comparison of Niño3.4 temperature, ONI and SOI. For more details, see Wolter and Timlin (1998).

The following overview on the development of the 1997–1998 El Niño is adapted from McPhaden (1999). The trade winds weakened and reversed in the Western and Central equatorial Pacific in the early 1997. This led to the development of positive anomalous SSTs



Fig. B.4 The list of EWBs and WWBs of 2014 and 2015 with dates, longitudes and the amplitude scale factors. Figure taken from Chiodi and Harrison (2017)

in the Central Pacific. The warm waters in the Western Pacific migrated East due to the lack of trade winds. There was then a series of WWBs of increasing intensity from the start of 1997 until the end of 1997. The El Niño developed very quickly from June to December. The SST anomalies averaged around four degrees in the cold-tongue region at the peak of the El Niño. The thermocline in the Eastern Pacific was depressed by more than 90m in late 1997 which favoured the development of warm surface waters due to the lack of cold water upwelling. The trade winds abruptly resumed at around mid-May 1998 which caused the SSTs to drop rapidly. At one location, the SSTs dropped more than eight degrees in 30 days due to the resumption of the trade winds. This effectively terminated the El Niño.

The event is important scientifically due to several reasons (Drake, 2001). Firstly, in 1997, it was the largest and warmest El Niño to develop in the last 100 years. Secondly, scientists were able to predict climate conditions of the winter six months in advanced with the knowledge of the incoming El Niño. Thirdly, the predictions on teleconnections allowed scientists to inform decision makers to take action.

1982–1983 El Niño

The 1982–1983 El Niño is perhaps the strongest El Niño from 1900–1982, see Quiroz (1983) and Sardeshmukh and Hoskins (1985). The following overview on the evolution of the El Niño in 1982–1983 is adapted from Quiroz (1983). The SOI started to fall in April–June 1982 and was coincidental with the collapse of the Easterly trades in the Western Pacific. By January 1983 (approximately at the peak of the El Niño), the SOI has reached a minimum value of 3.5 standard deviations below normal. This is the lowest value on record from 1935 to 1983. The December SST anomalies in the Eastern equatorial Pacific reaching six degrees above average in certain locations.

Appendix C

Seasonality of the southern annular mode

The southern annular mode (SAM) is the first EOF in SLP or low level geopotential height in the southern hemisphere (often taken polewards of 20°S) using monthly data, see for example (Ho et al., 2012; Thompson and Wallace, 2000). The SAM is dependent on the meridional excursions of the jet and thus the first principal component changes seasonally. However, the general structure of the SAM remains generally similar throughout the seasons. For example, Thompson and Wallace (2000) found that ‘in the SH (southern hemisphere), the spatial structures for the warm and cold seasons are both nearly zonally symmetric, with similar amplitude and similar meridional scale, and they resemble the leading mode of variability based on all calendar months shown in Thompson and Wallace (2000, Figs. 1 and 3).’ This is unlike the northern annular mode (NAM) which have larger amplitude and meridional scale in the cold season. This agrees with the work of Rogers and van Loon (1982) who found that ‘The first eigenvectors of SLP and 500 mb (hPa) height in Rogers and van Loon (1982, Figs. 2 and 3) change little from winter to summer.’ They attributed this to the high zonal symmetry of land and sea in the mid to high latitude southern hemisphere and the seasonal invariance of Antarctica being a heat sink and the ocean at the mid latitudes being a heat source.

Figure C.1 shows the first and second EOFs for 500hPa geopotential height between 20°–90°S. The data is from the HadGEM3 baseline timeslice run. As seen from the figure, the structure of both EOF1 and EOF2 are similar between DJF and JJA. In both seasons, the EOF1 (SAM) shows positive geopotential height at the mid latitudes and negative geopotential height at the higher latitudes. For EOF2 (PSA1), there is a wavetrain of alternating geopotential height from the mid latitude pacific to the Amundsen sea region (ASR).

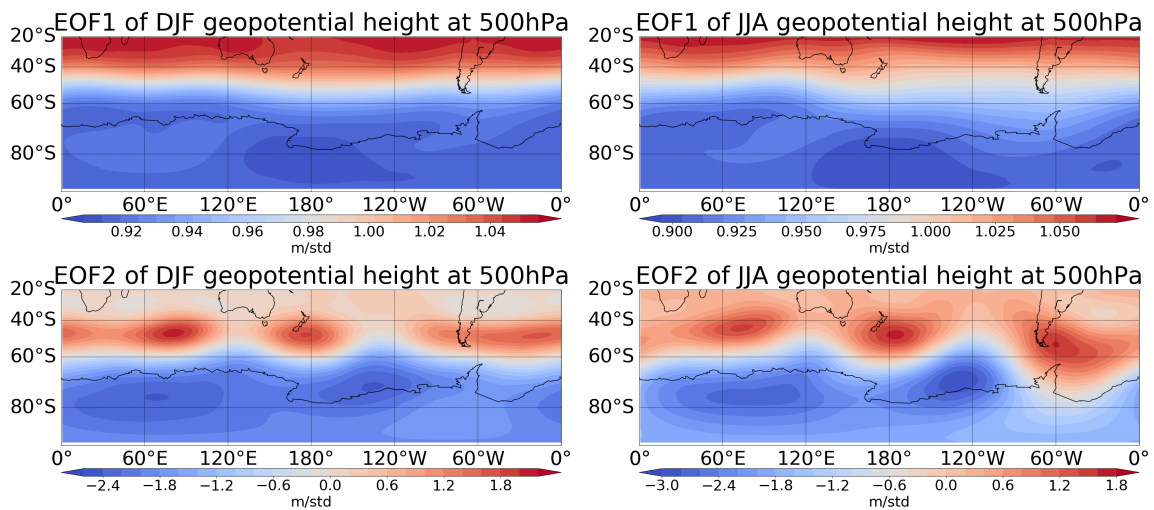


Fig. C.1 First and second EOFs in HadGEM3 for DJF and JJA. 500hPa geopotential height from 20°–90°S used. Units are in metres per standard deviation of the principal component.

Appendix D

Limitations of implementing Rossby wave ray tracing

There are several important limitations and issues to consider when performing Rossby wave ray tracing and interpreting its results. Firstly, the width of the 2-D Gaussian filter is somewhat arbitrary. However, halving or doubling the width of the filter seem to make little difference to the results. Another limitation is that ray tracing attempts to address the question of whether hypothetical Rossby waves can propagate from A to B. It does not take into account the magnitude (or even presence) of a RWS. Therefore the number of ‘rays’ reaching the destination is no indication of the energy propagated or the frequency of the Rossby wave due to a stronger source. As an extreme example, if the rays were propagated from an area without any Rossby wave source, then even if large amounts of these hypothetical rays show propagation to a given destination, it would not mean anything physically as this would not provide a source for waves in the first place.

The choice of the wavenumber, k , also requires consideration. While it is conventional to choose the wavenumber 3 in ray tracing, other wavenumbers still play a role in the teleconnection. However, this problem is addressed in Chapter 3 when ray tracing was performed for different wavenumbers.

Various minor problems can also occur during the implementation of the ray tracing. For example, there could be cases where the ray becomes ‘trapped’ between two reflection surfaces and bounces between them rapidly (in an unrealistic way), see Figure D.1 panel one. There can also be unwanted reflections due to the finite grid size of the model, see Figure D.1 panel two. Note that reducing the grid size (i.e. running a higher resolution model) or decreasing the step size will not help with this problem. This is because no matter how fine the grid cell is, the ray still is highly likely to hit between lattice points. Another example

is rays not being able to exit the reflection zone if the reflection–propagation boundary is too steep, see Figure D.1 panel three.

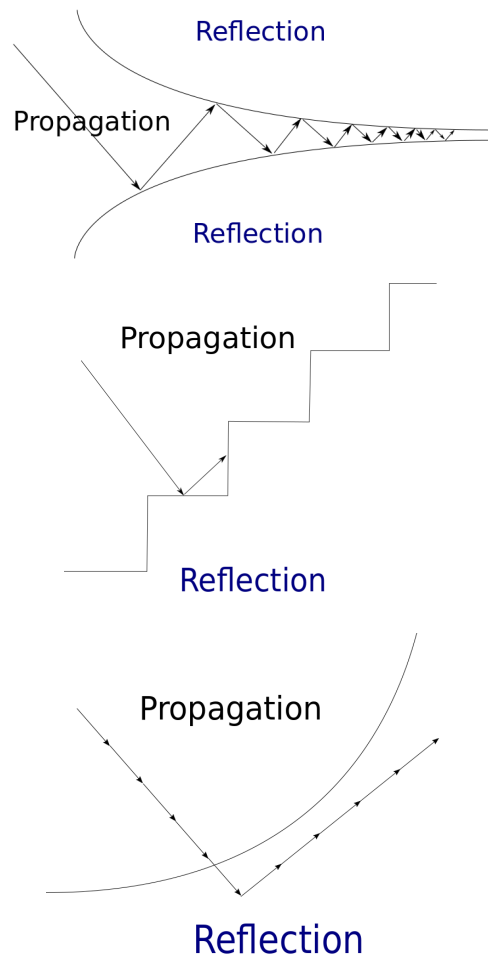


Fig. D.1 These schematics illustrate some of the potential technical problems of implementing ray tracing.

Appendix E

Rossby wave ray tracing using different wavenumbers

Figure E.1 shows the Rossby wave ray tracing at 200hPa at wavenumber 2 (top row) and 4 (bottom row). All other parameters such as step size, filter size and maximum step number were kept the same. The overall structure of the reflection, termination and Rossby ray paths stays similar (with minor changes) under the different wavenumbers. In austral summer (DJF), the Rossby rays are reflected at $\sim 60^\circ\text{S}$ in wavenumbers 2, 3 and 4. The rays then terminate near the equator. In austral winter (JJA), the rays are allowed to pass into the ASR for all three wavenumbers. They all follow (approximately) a similar path to the PSA. Note that, in the bottom right panel of Figure E.1, the waves are cut off in JJA wavenumber 4 at the Weddell Sea due to reaching the maximum number of steps in the code. This is a programming effect rather than any physical phenomenon. In conclusion, the wavenumber does not change the overall story as long as the wavenumber is kept near wavenumber 3. However, if the wavenumber is set to an extremely high value (e.g. wavenumber 20), as expected, the overall structure does changes significantly.

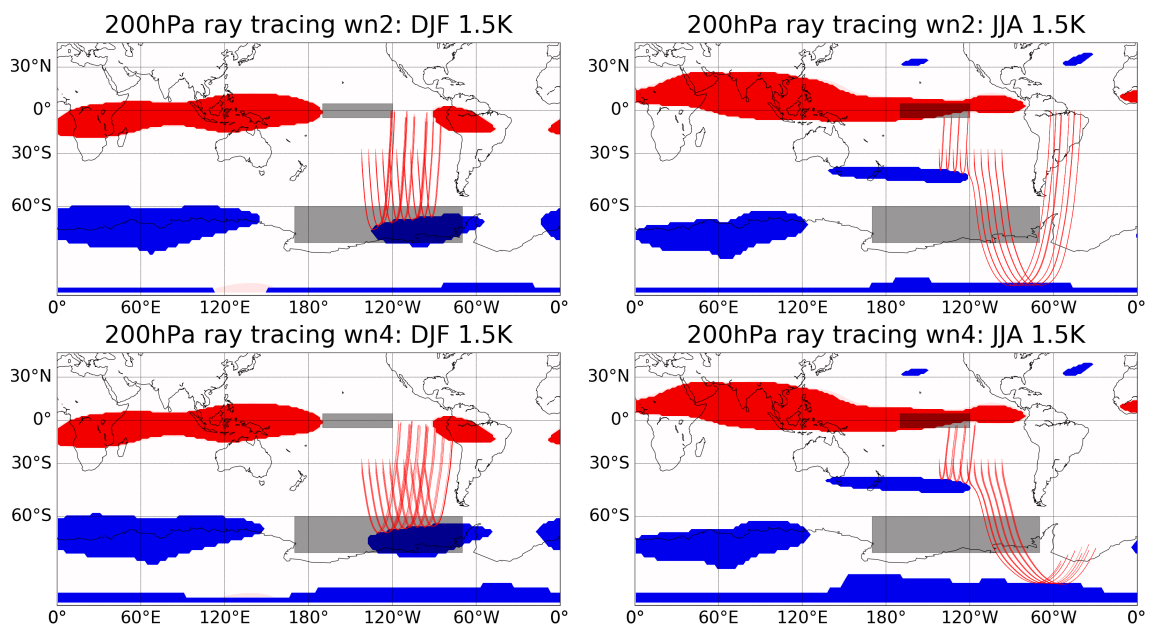


Fig. E.1 Rossby wave ray tracing performed on the 1.5K El Niño run for austral summer (DJF) and austral summer (JJA) for wavenumber 2 and 4.

Appendix F

Rossby wave ray tracing using different radius of filters

Li et al. (2015a,b) used a 2-D Gaussian filter is used on the β^* and U fields while Scaife et al. (2017) used a a 60° sectoral zonal averaging to filter the background circulation. In this appendix, the sensitivity of the filter radius on ray tracing will be tested.

Figure F.1 shows examples of 1.5K Rossby wave ray tracing performed with different sizes of Gaussian filters. Zonal filter sizes of approximately 21 degrees, 30 degrees, 39 degrees, 51 degrees and 60 degrees are tested. As seen from the figure, there is little change in the path of the rays as long as the filter sizes are sensibly decided¹. The seasonality of the waves (reflection in DJF and mostly propagation in JJA) is unchanged.

Figure F.2 shows examples of 3.0K Rossby wave ray tracing performed with these various sizes of Gaussian filters. As seen from the figure, while there are minute changes in DJF (a few rays on the edges managed to propagate through) under a 60 degrees filter, there is still little change in the seasonality of the waves (reflection in DJF and mostly propagation in JJA).

¹i.e. on the order of thousands of km

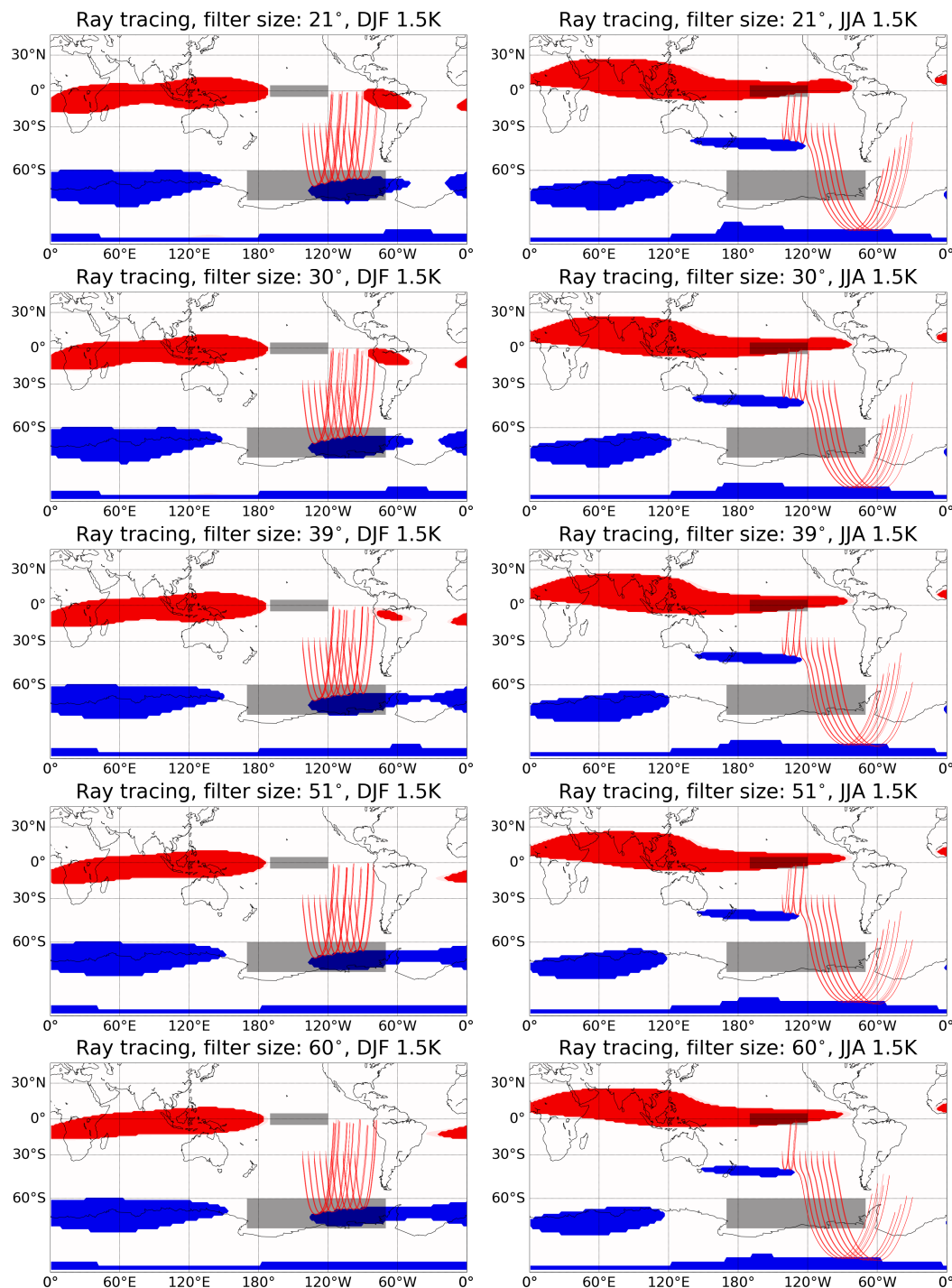


Fig. F.1 Rossby wave ray tracing performed on the 1.5K El Niño run for austral summer (DJF) and austral winter (JJA) with zonal filter sizes of approximately 21 degrees, 30 degrees, 39 degrees, 51 degrees and 60 degrees.

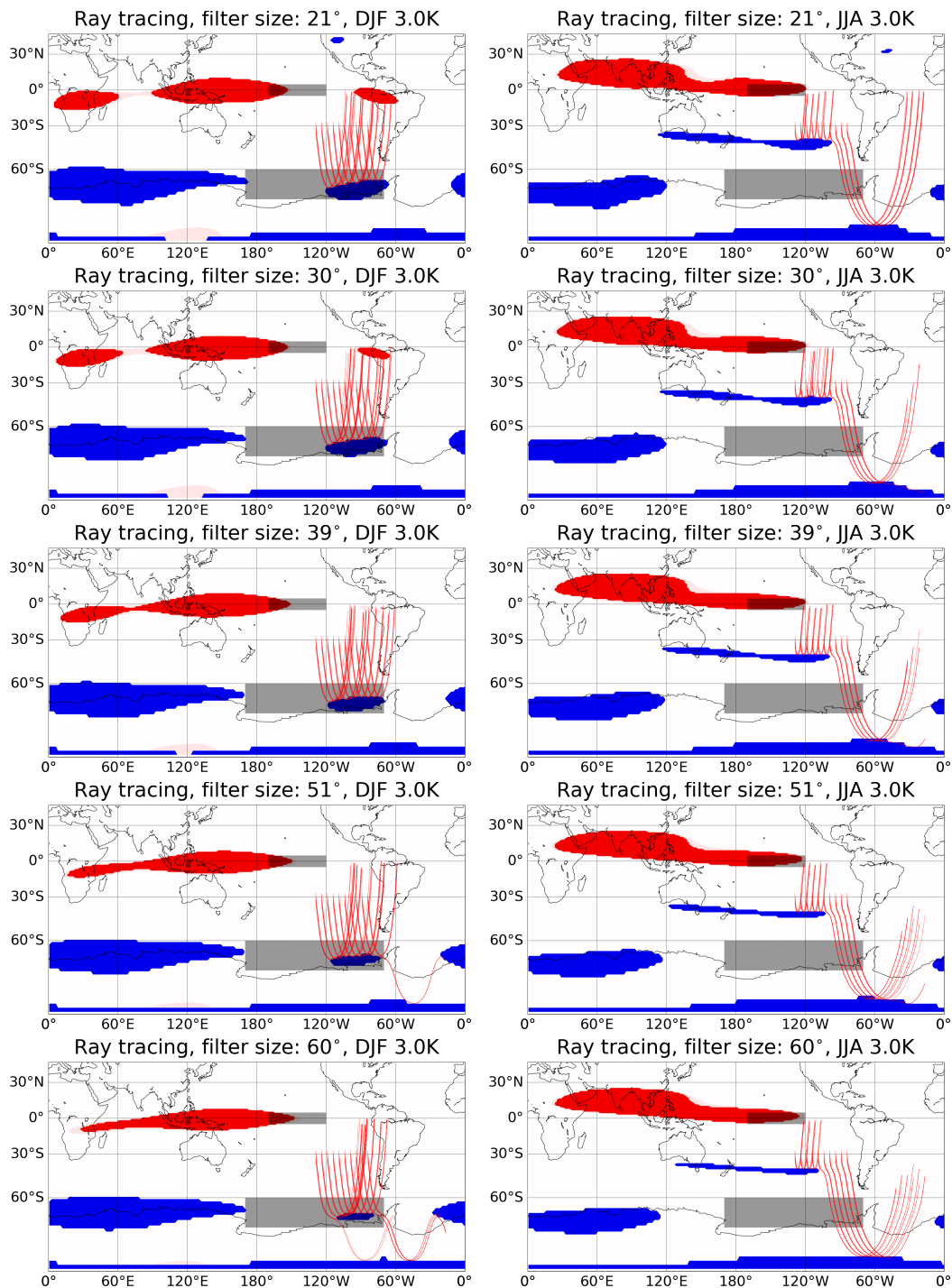


Fig. F.2 Same as Figure F.1 but for 3.0K.

Appendix G

Tropical circulation changes and clouds

Figure G.1 shows the annual time-mean bulk cloud fraction averaged over the tropical Pacific. It is useful to look at the bulk cloud fraction with respect to height. This is in order to understand the changes in cloud top height (CTH), cloud bottom height (CBH) and the maximum bulk cloud fraction. The CTH/CBH can indicate the height of the tropical circulation while the maximum bulk cloud fraction can provide a general idea of the strength of the tropical circulation. In Figure G.1, only clouds within 10°S – 10°N and 180°E – 60°W are included. Any clouds higher than 20 km is disregarded (as there is very little cloud over this height). In the baseline model run (blue curve, Figure G.1), there are three ‘layers’ of clouds at ~ 2 km, ~ 5 km and ~ 8 – 15 km. The analysis will only focus on the high clouds (~ 8 – 15 km) near the upper troposphere. There are two reasons for concentrating on these high clouds. Firstly, these are likely the clouds formed due to the upwelling of the Hadley cell as the Hadley cell is approximately 10–15 km in height. Secondly, the amount of clouds in this ‘layer’ is much greater than the lower clouds.

As El Niño increases, the circulation strengthens and the cloud fraction increases from around 0.32 (peak) to 0.45 (peak) in the 3.0 K El Niño model run. Furthermore, the CTH (of the high clouds) increases while the CBH (of the high clouds) decreases under El Niño conditions. This can be seen from the widening of the curve (increased full width at half maximum of the high clouds). This suggests that the circulation cell is growing in size and height under El Niño conditions. Note that, the seasonal bulk cloud fraction (not shown) shows little differences between the seasons. This is perhaps expected as there is little seasonality in the tropics. Another common proxy for the circulation is the outwards longwave radiation (OLR) at the top of the atmosphere (TOA). Clouds tend to absorb OLR and reemit it in all directions, therefore, the net effect is that clouds tend to reduce the OLR at TOA. Therefore the OLR is a good proxy for circulation strength as it indicates the total cloud amount in that area. Note that increased OLR (TOA) also indicates higher and colder

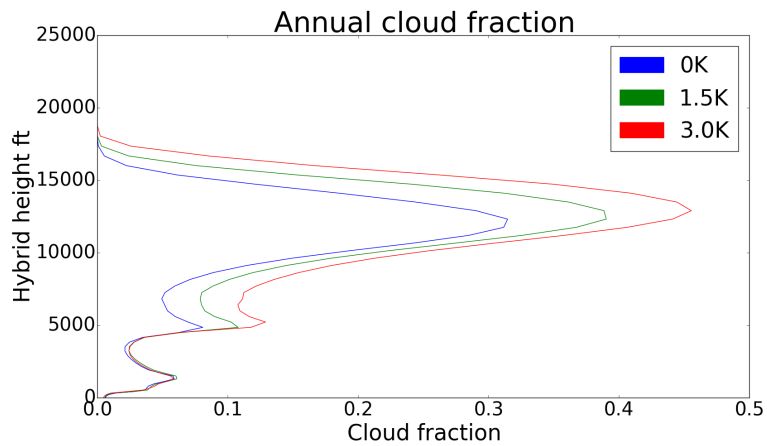


Fig. G.1 *Absolute* time–meaned (over 54 years climatologies) annual bulk cloud fraction under baseline (0.0 K) and (1.5 K and 3.0 K) El Niño conditions. The region averaged is approximately the tropical Pacific: 10°S–10°N and 180°E–60°W. The bulk cloud fraction is the fraction of a grid that is covered in clouds. For example, a number of 0.5 would signify that half the grid at that height level would have clouds.

cloud tops. This is because these colder and higher clouds emit much less radiation into space.

Appendix H

Absolute wave flux

The absolute wave flux for the 1.5 K El Niño experiment for DJF and JJA are shown in Figure H.1. Similar to the anomalies found in Figure 3.19, there is a lack of wave flux in the high latitudes in DJF but the presence of wave flux in JJA.

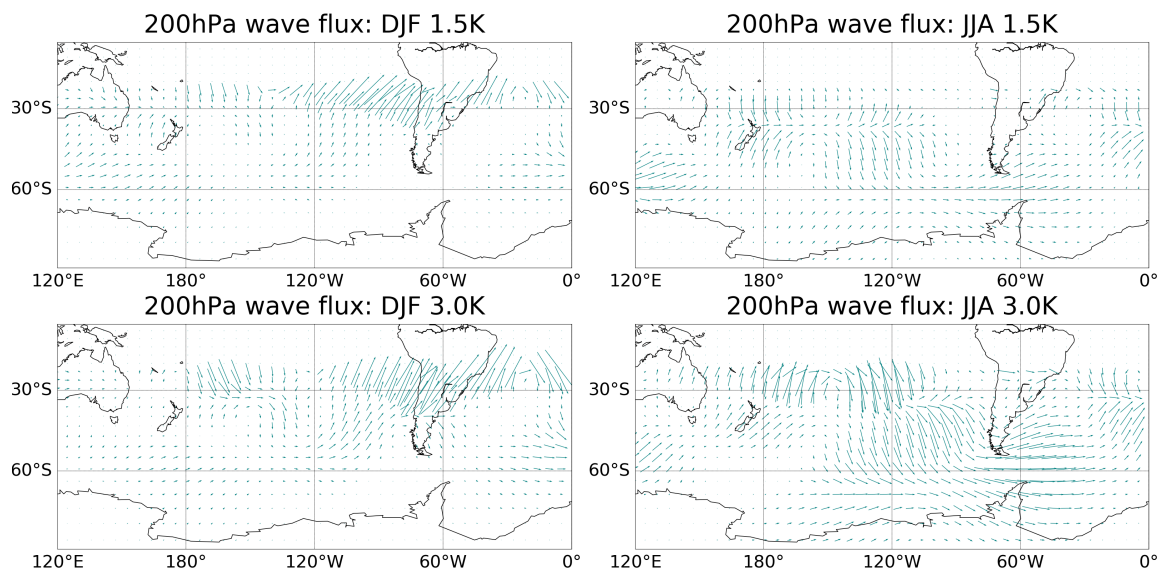


Fig. H.1 Absolute wave flux anomaly following Plumb (1985) under El Niño (1.5 K) conditions in austral summer (DJF) and austral winter (JJA).

Appendix I

Comparison of wave flux between ERA-40 and Karoly et al. (1989)

This appendix presents figures that reproduces the waveflux analysis as seen in Karoly et al. (1989, Fig. 2). ERA-40 data was used instead of the southern hemisphere dataset used in Karoly et al. (1989). Following Karoly et al. (1989), a 10 year mean winter (JJA) from 1973 to 1982 was created from daily geopotential data at 300hPa. The zonal and meridional winds were calculated using the geostrophic wind equation from the geopotential. The top left panel of Figure I.1 shows the zonal removed geopotential height from ERA-40 while the bottom left panel shows the zonal removed geopotential height as seen in Karoly et al. (1989, Fig. 2, left panel). The top right panel of Figure I.1 shows the wave flux calculation from ERA-40 while the bottom right panel shows the wave flux calculation as seen in in Karoly et al. (1989, Fig. 2, right panel). As seen from the figure, both the geopotential height and the wave flux patterns are very similar between Karoly et al. (1989) and ERA-40.

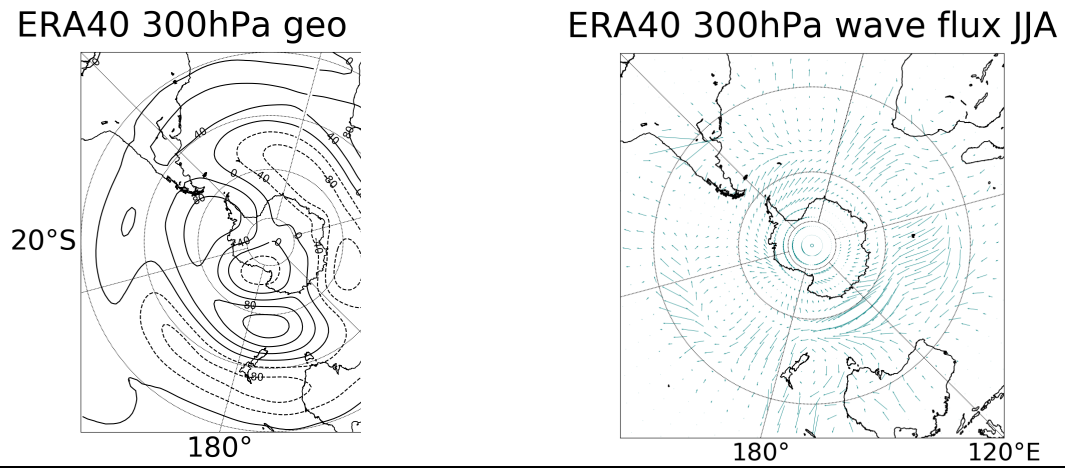


Fig. I.1 Geopotential height and absolute wave flux anomaly from ERA-40 (top) and Karoly et al. (1989) (bottom).

Appendix J

Ray tracing from the weaker negative RWS anomaly

There are two RWS anomalies in the Pacific region, see again Figure 3.11. While the rays are propagated from the strongest RWS anomaly (positive) located at around 30°S , $100\text{--}120^{\circ}\text{W}$ in Figure 3.16, there is also a weaker (negative) RWS anomaly at around 30°S , $150\text{--}180^{\circ}\text{W}$. The negative RWS *anomaly* is, at least partially, due to the eastwards shift in the *absolute* RWS. This negative RWS *anomaly* can be seen as the ‘previous’ location of the *absolute* RWS before its eastwards movement. Therefore, Rossby waves should be propagated from this location. Figure J.1 shows the propagation of the Rossby waves using ray tracing from the negative RWS anomaly under the 1.5K El Niño run. The teleconnections are reflected by the reflection zone at $\sim 40^{\circ}\text{S}$. The lack of propagation and the weakness of this negative RWS anomaly (compared to the positive RWS anomaly) means that it is reasonable to ignore this RWS as it does not seem to play a significant role in the ASL teleconnection.

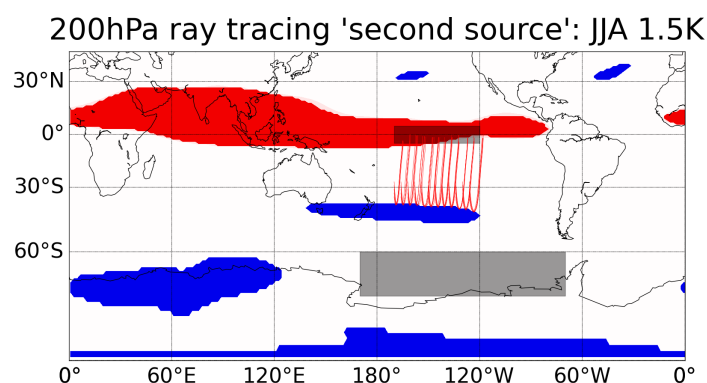


Fig. J.1 Rossby wave ray tracing performed on the 1.5K El Niño run for austral summer (DJF) and austral summer (JJA). The rays were initialised approximately at the location of the negative RWS anomaly (‘second source’) found in JJA.

Appendix K

Preliminary results using machine learning techniques

Each model grid¹ within the Niño3.4 is treated as one input variable. Analysis has only been carried out for JJA currently. The data is split randomly into 60% training data, 20% cross validation data and 20% test data. The training data is used to train the various machine learning techniques, the 20% cross validation data is used to tune the parameters of the machine learning techniques and the 20% test data is used to check the performance of the results. Initially, only one of the CMIP5 models was used² and the minimum absolute SLP was regressed directly onto the Niño3.4 region after scaling to a mean of zero and standard deviation of one. The results (from all methods) tend to show a R^2 of less than 0.05. In hindsight, this is perhaps unsurprising as it is more difficult to predict the minimum ASL depth compared with the maximum ASR anomaly. This is due to the large movements of the ASL affecting its coupling with the ENSO–ASR pressure anomaly. In the future, the *maximum* SLP anomaly will be regressed to the Niño3.4 temperatures. One possible method of obtaining the SLP anomalies is by subtracting each SLP entry (with respect to time) with the seasonal climatological mean. In addition to this, analysis using all CMIP5 datasets (together) has been attempted. The initial analysis showed a suspiciously high R^2 value of $\sim 0.6-0.7$ (highest was from neural net). This is suspicious as only the Niño3.4 temperature is fed into the neural net as an input variable. It is unlikely the Niño3.4 temperature alone can produce such a high R^2 in such a variable region. It turns out that the neural net was predicting *which* CMIP5 model the test data was from using the biases in the models. This is because each CMIP5 model has its own biases in the SLP. This problem needs to be solved

¹All models are re-gridded to the same resolution

²multiple singular CMIP5 models were used

before further analysis. A potential solution is to normalising each CMIP5 dataset³ before use.

³to ERA-Interim